Using Atomic Force Microscopy to Analyse the Geomechanical Properties of Organic Rich Rocks

Thomas David Fender

Thesis submitted for the degree of

Doctor of Philosophy



School of Natural and Environmental Sciences

Newcastle University

Newcastle upon Tyne

United Kingdom

November 2020

Declaration

I hereby certify that this is my own work, except where otherwise acknowledged, and that it has not been submitted for a degree at this, or any other university.

Thomas D Fender

Acknowledgements

I thank the collaborative efforts of Newcastle University (Dr. Mohamed Rouainia, Dr. Cees Van Der Land, Dr. Martin Jones, Dr Matthew German and Sam Graham), the British Geological Survey (Dr. Chris Vane and Dr. Jan Hennissen) and Heriot-Watt University (Prof. Thomas Wagner and Dr Jim Buckman) for their input, feedback and contributions throughout.

Thank you to the funders (NERC Centre for Doctoral Training Oil and Gas scheme) and Newcastle University.

Thank you in advance to the internal and external examiners for giving up their time to read this thesis.

Thank you to the past and current employees and members of NERC CDT Oil and Gas, who helped broaden my knowledge base and put this project into perspective as well as provided a great distraction in times of need.

On a more personal note, I would like to thank Dr Jack Walker, Claire McGhee, Sam Graham and Katie Gilmour for helping and supporting me during the good and bad times.

And lastly and most importantly thank you to my mother and the rest of my family, for all the support, especially during the last nine months in the midst of the COVID-19 pandemic. Without your sacrifices, submitting this thesis would not have been possible!

Abstract

Climate change will have a major impact on society in the 21st century and beyond, unless the right measures are taken in the next decade. These measures require a drastic decrease in carbon dioxide emissions to reduce the concentrations of CO_2 in the atmosphere most likely through sequestration into geologic formations. Organic matter has a key role in two major types of carbon sequestration play; as a key component of a shale seal in many conventional reservoirs, and comprising the majority of coal reservoirs. As such recent research has focused on the mechanical properties of this organic component, with the Atomic Force Microscope and Nanoindentation used to measure Young's modulus at the nanoscale. This research is expand upon by investigating the trends in organic matter Young's modulus within marine shales, and compare an immature marine shale (Tarfaya) to a lacustrine equivalent (Green River) using the AFM. The results of this study indicate that there is a clear trend of marine shales exhibiting a bimodal distribution in modulus, with a soft phase centered around 5-9GPa and a stiffer phase centered around 18-24GPa. ^{13}C NMR spectroscopy indicates that the increase in stiffness is tied to an increase in aromatic carbon, which could indicate increases in modulus across all organic matter with maturity.

Here AFM is used on a suite of coal macerals from different depositional environments and maturities to assess if there are common trends. The results of this highlight that the modulus distribution of coal macerals is generally unimodal, and softer than that in shales, with all modal values <10GPa. There is however, a similar trend in terms of a stiffening with maturity, with all macerals stiffer in the mature Northumberland Coal than in the immature cannel or paper coals. Thermal modelling suggests that differential strain is more likely in immature coals, where there is a greater difference moduli of liptinite and inertinite macerals. This problem is reduced in the mature coal, with little difference between the maceral moduli, suggesting that deeper mature coal seams are better targets for CCUS than shallower less mature seams.

Machine learning can be used to maximise already collected data by making inferences on samples where information is limited, using the trends from a larger dataset. Here the first

attempt at using machine learning on SEM, EDX and AFM data is documented, using data collected from the Eagle Ford and Green River shales, with the goal of making mineralogic and geomechanical predictions. A variety of supervised and unsupervised machine learning methods were used, including; Multi-Layer Perceptron, KNN and Random Forest. The accuracies of these models on the test/training data is generally above 85%, and in the case of the KNN and Random Forest above 95%. However, when the model are used on an unrelated dataset, the accuracy decreases significantly. This research indicates that if machine learning is to be used, the training dataset and model should be selected with the end result in mind, whilst acquiring the datasets using a similar technique to a similar quality.

Contents

1 Introduction and Thesis Objectives **1**

1.1 Introduction 1

1.2 Aims and Objectives 7

2 The Assessment of Organic Matter Young's Modulus Distribution with Depositional Environment and Maturity **10**

2.1 Introduction 10

2.2 Depositional Environment and Geological Setting of Studied Samples 15

2.2.1 Barnett Shale 15

2.2.2 Bowland Shale 16

2.2.3 Eagle Ford Shale 18

2.2.4 Tarfaya Shale 18

2.2.5 Green River Shale 19

2.3 Methods 21

2.3.1 Samples 21

2.3.2 Preparation and Analysis 22

2.3.3 Organic Matter Chemical Characterisation 22

2.3.4 Palynofacies 23

2.3.5 Nanomechanical Measurements 24

2.3.6 Modulus Data Analysis 26

2.3.7 Deconvolution 28

2.4 Results . . . 29
2.4.1 Organic Content Typing and Analysis . . . 29
2.4.2 Organic Matter Young's Modulus . . . 32
2.4.3 Deconvolution . . . 40
2.5 Discussion . . . 43
2.5.1 Depositional Environment . . . 44
2.5.2 Maturity . . . 46
2.5.3 Kerogen Type I vs Kerogen Type II . . . 53
2.5.4 Water Content . . . 55
2.6 Conclusions . . . 56
2.7 Contributions . . . 57

3 Geomechanical Properties of Coal Macerals; Measurements Applicable to Modelling Swelling of Coal Seams During CO_2 Sequestration 58

3.1 Introduction . . . 58
3.1.1 Maceral Analysis . . . 62
3.2 Methods and Samples . . . 63
3.2.1 Samples and Sample Preparation . . . 63
3.2.2 Maceral analysis . . . 64
3.2.3 Atomic Force Microscopy Quantitative Imaging . . . 65
3.2.4 Mercury Injection Porosimetry . . . 68
3.2.5 Nanoindentation . . . 68
3.3 Results and Discussion . . . 70
3.3.1 Coal Petrography . . . 70
3.3.2 Vitrinite Reflectance . . . 72
3.3.3 Young's Modulus of Coal Macerals . . . 72
3.3.4 Organic Matter Distribution Analysis . . . 81
3.3.5 Mean Analysis . . . 85
3.3.6 CO_2 Injection Modelling . . . 88

3.3.7 Nanoindentation Comparison . . . 93
3.3.8 Comparisons Between AFM and Nanoindentation Results . . . 95
3.3.9 Limitations of this Nanoindentation Dataset . . . 97
3.4 Conclusions . . . 99
3.5 Contributions . . . 101

4 An Assessment of the Viability of Different Machine Learning Algorithms for Predicting Shale Young's Modulus Data 102

4.1 Introduction . . . 102
4.1.1 Previous uses of Machine Learning Algorithms for Rock/Mineral Classification . . . 104
4.1.2 Machine Learning for Geomechanical Prediction . . . 107
4.1.3 Aims of this Study . . . 107
4.2 Shale Data and Depositional Environment . . . 108
4.2.1 Posidonia Shale . . . 109
4.2.2 Shale Data Acquisition (Techniques and Methods) . . . 110
4.3 Methods and Models . . . 110
4.3.1 Data Preparation . . . 110
4.3.2 Segmentation . . . 113
4.3.3 Machine Learning Models . . . 115
4.3.4 Model Training . . . 124
4.4 Results and Discussion . . . 127
4.4.1 Individual Shale Accuracies . . . 127
4.4.2 Overall Mean Accuracy . . . 137
4.4.3 Model Validation . . . 139
4.4.4 Validation Young's Modulus Analysis . . . 147
4.4.5 Overall Modulus Prediction . . . 155
4.4.6 Four-Phase Classification . . . 156
4.5 Conclusions . . . 160

4.6 Contributions 163

5 Conclusions and Future Work **164**

A Appendix 1: Well Logs **171**

A.1 Barnett Lake Davis Well 172

A.2 Barnett TP Sims Well 173

A.3 Bowland Preese Hall #1 174

A.4 Eagle Ford Cinco Saus 175

A.5 Eagle Ford Carol 176

A.6 Tarfaya, S57 177

List of Figures

2.1 A map of the base of the Barnett Shale and associated maturity, indicating the major tectonic elements in the deposition. The TP Sims II and Lake Davis well are indicated. This figure has been adapted from Montgomery et al. (2005). As can be seen the maturity is anomalously high proximal to the Mineral Wells Fault, which has impacted the sample taken from the TP Sims well. 16

2.2 A location map of the Bowland Shale adapted from Walker (2020); Waters et al. (2009). The map indicates the major fault network in the area along with the major depo-centre (grey) and the carbonate shelf (blue). 17

2.3 A map summary of the Eagle Ford Shale and the associated maturity. The map indicates the location of the San Marcos Arch paleohigh. As can be seen the Carol Well has been drilled into the Eagle Ford near the San Marcos Arch and is therefore likely to comprise more terrestrial and oxidised organic matter. The Cinco Saus well is located in Maverick County, which is much lower maturity and within the Maverick Basin. 19

2.4 A map indicating the location of the Tarfaya sample taken, with the paleo-shoreline and shelf indicated. Adapted from Kolonic et al. (2005); Beil et al. (2018). 20

2.5 A location map of the Green River Shale, indicating the extent of the Mahogany Zone and the approximate sample location from this study. The geographical information for the Mahogany Zone outcrop used here was acquired from the USGS and is available at `https://certmapper.cr.usgs.gov/data/apps/oil-shale-data/` 21

2.6 The working mechanics of an AFM. The initial phase involves oscillating the tip near to the sample (a), where adhesive forces bring the tip onto the sample surface (b). After this a set amount of force is applied (c). It is on this gradient that the Young's modulus is measured (red line). The amount of displacement ($d - d_0$) is then measured at the largest force (F). After which the tip is removed from the surface by the oscillation of the cantilever (d). 25

2.7 An example of the filtering procedure for the raw AFM data. The initial data is put through a 30GPa and 0.1GPa filter to remove these values. It is then compared to SEM images (centre) to identify the maximum value of Young's modulus for organic matter. Then if required the data is filtered for fracture data whereby, modulus values believed to relate to fractures are removed (Stage 2). . 27

2.8 Scanning Electron Microscopy images of the shales studied. a.) are two scans showing the different morphology of organic matter in the Barnett Shale Lake Davis sample, b.) is indicative of organic matter in the Barnett Shale TP Sims well, c.) shows the lenses of organic matter in the Bowland Shale, d & e.) indicate the organic matter mainly associated with fecal pellets in the Eagle Ford Carol and Cinco Saus respectively and f.) shows the large amounts of organic matter both within the matrix and associated with fecal pellets in the Tarfaya. g.) indicates the different appearance of the Green River shale, with the organic matter as a component of the matrix, the clasts are dominated by calcite, quartz, and dolomite. Quartz, clay, pyrite, organic matter, calcite and dolomite are indicated at their first occurrence. 33

2.9 ^{13}C Solid State NMR results. Sample plots are shown maturity order, a. Bowland Shale, b. Barnett TP Sims, c. Eagle Ford Carol, d. Barnett Lake Davis, e. Eagle Ford Cinco Saus, f. Tarfaya and g. Green River. Aliphatic kerogen is the dominant phase in immature samples. In shales in the oil window the proportion of aromatic kerogen dominates, whilst still retaining a significant portion of aliphatic kerogen ($\sim$ 30%). The kerogen of the most mature shales (Barnett TP Sims and Bowland) is dominated by aromatic bonds with <15% aliphatic compounds. 34

2.10 Kernel Density Estimate distributions for each shale. a.) corresponds to the Barnett Shale Lake Davis sample, b.) the Barnett Shale TP Sims sample, c.) the Bowland Shale sample, d.) The Eagle Ford Carol sample, e.) the Eagle Ford Cinco Saus sample, f.) the Tarfaya Shale sample and g.) the Green River Shale sample. The blue and grey shading represent the 95% confidence interval for each shale, the number in blue or black refer to the amount of AFM scans used to create the distribution once filtered. There appears to be two distributions for the Barnett Lake Davis and Eagle Ford Cinco Saus shales, which are at peak and early oil window maturities respectively. 36

2.11 Examples of an AFM QI^{TM}scan per shale. a.) corresponds to the Barnett Shale Lake Davis sample, b.) the Barnett Shale TP Sims sample, c.) the Bowland Shale sample, d.) The Eagle Ford Carol sample, e.) the Eagle Ford Cinco Saus, f.) the Tarfaya Shale sample and g.) the Green River Shale sample. 37

2.12 Young's modulus values for an individual scan of Barnett Lake Davis and Eagle Ford Carol calculated using different values for Poisson's ratio. A variation of Poisson's ratio from almost incompressible to almost infinitely compressible. This yields a variation of approximately 4GPa in the modal value of Young's modulus. 38

2.13 The resulting phase distributions of a two phase deconvolution on each shale distribution both with Constraint B in place (Constrained) and Constraint B relaxed (Unconstrained). The distribution of the phases in constrained and unconstrained deconvolution is identical using Normal distributions. There is a large disparity of fit between the constrained and unconstrained Gamma distributions. The Gamma distribution appears to poorly fit the Tarfaya shale in all cases, whilst the Normal distribution only fits poorly for the stiffer phase indicating that this may not be present in the Tarfaya. 41

2.14 The root-mean-squared error associated with the deconvolution of each shale using Normal and Gamma distributions into two phases, both constrained using Constraint B in equation 2.6 (Constrained) and without this constraint (Unconstrained). 43

2.15 An adaptation of the T-Max/HI plot from Peters (1986) indicating kerogen type and maturity. The distributions above are arranged in order of maturity, showing the evolution of Young's modulus distribution in a Type II kerogen from Tarfaya shale dominated by soft organic matter, to the Bowland dominated by a stiffer component. 46

2.16 A Representation of the composition of kerogen at immature ($\sim$0.5%R_o), oil window mature ($\sim$0.8%R_o) and gas window maturity ($\sim$1.3%R_o) after the models of Behar and Vandenbroucke (1987); Vandenbroucke and Largeau (2007). The length of aliphatic chains, number of NSO compounds and general heterogenity decrease with increasing thermal maturty, until all that remains are aromatic rings with short aliphatic side chains. These compositions are similar to those within the Tarfaya (immature), Barnett Lake Davis & Eagle Ford Cinco Saus (oil window) and Barnett TP Sims & Bowland (gas window). 50

3.1 An indication of the scale in which coals can be analysed by triaxial, Vickers microhardness tests, nanoindentation and AFM. The black box is the area in which a 9x9 nanoindentation grid would be situated. The red box is the area of one AFM scan within this study, containing over 250,000 measurements. 61

3.2 A graphical indication of the process of acquiring an AFM measurement. Initially the tip starts away from the sample surface (a), once the tip is brought towards the surface of the sample Van Der Waals forces adhere the tip to the surface (b), at the point of maximum adhesion (c) a force is exerted onto the sample surface, until at a point (d) the preset maximum force is exerted. At this point (d) the tip is allowed to leave the sample surface. The reduced Young's modulus is calculated along the extend curve (red) using the Hertz-Sneddon equation (Equation 3.1). . 67

3.3 A grahpical representation of the load and unload curve of a single nanoindentation indicating the displacement and force applied, along with the measurements used to calculate the slope S. 69

3.4 Photomicrograph of the Coal macerals studied. Photos show cutinite (a,b,e), sporinite (c,d), bituminite (f) and inertinite (g-l) studied. The left column are from the Paper coal, the middle column from the Cannel coal and right column from the Northumberland coal. 71

3.5 Probability distributions of each of the macerals studied, (a) is the distributions of immature cutinite from the Paper coal, (b) is the distributions of immature sporinite form the cannel coal, (c) is the distributions of inertinite in all three coals and (d) is a composite chart of all macerals studied. Block lines are from immature coals (paper and cannel), dashed lines are from the Northumberland Coal. Boxes indicate the modal value of each distribution, circles are the locations of the mean values from each distribution. In the immature shales the liptinite macerals have a lower modulus than their inertinite counterpart, a relationship which inverts with maturity. Liptinite macerals increase in stiffness drastically with maturity, as well as becoming more Normally distributed. Inertinite also becomes stiffer with maturity, although to a lesser extent than liptinite, which may be due to the oxidized state in which the inertinite was deposited. n.b. ^{I} denotes immature macerals, ^{M} denotes mature macerals. 73

3.6 A selection of AFM Young's modulus scans including (a) immature cutininte from the Paper coal, (b) immature sporinite from the Cannel coal and (c) mature cutinite from the Northumberland Coal. Areas of white in the scans are places where the reduced Young's modulus is greater than 30GPa. It is obvious from both these scans and Figure 3.5 that there is far more heterogeneity associated with immature cutinite (a) than either the immature sporinite (b) or mature cutinite (c). 75

3.7 A comparison of the AFM distribution with the optimum Normal, Gamma and Lognormal Distribution for immature cutinite (a), sporinite (B), immature inertinite (c), Bituminite (d), mature Cutinite (e) and mature inertinite (f). The Gamma distribution appears to be the best fit for all macerals apart from immature inertinite. The Normal distribution is the next best fit visually aside from the immature cutinite distribution. The Lognormal distribution is the poorest fit for each distribution and is particularly poor for sporinite. 83

3.8 The Root-Mean-Squared-Error associated with fitting each distribution on all the macerals studied. The Gamma distribution has a low error value for each maceral and a relatively small standard deviation in error. The Lognormal error is high, partly due to the poor fit on Sporinite. 84

3.9 The distribution of mean values for AFM when analysed at $25\mu m^2$ increments. This gives a total of 361 mean measurements for each $50\mu m \times 50\mu m$ area. The left of the figure indicates the approximate area of influence for a nanoindentation scan 100nm deep, which is a hemisphere of radius $\sim 5\mu$m. The figure on the right indicates the probability distributions of the means. Each of the modal values are greater than those in the overall local AFM population (Figure 3.5), the modal value of the immature cutinite means is significantly greater than the local AFM distributions indicated in Table 3.2. n.b. ^{I} denotes immature macerals, ^{M} denotes mature macerals. 85

3.10 A comparison of the mean distributions of AFM from this paper with nanoindentation values from other literature, at the maturities measured. The means of the AFM distributions are within the range of literature values acquired from nanoindentation at the maturities measured. The mean of the immature cutinite may be marginally above the literature reported but is most likely due to the interaction with mineral matter/groundmass. 88

3.11 Gas injection pressure comparison with linear strain generated on each of the coal macerals using the Pan and Connell (2007) model and data from Table 3.5. The modal value of modulus was used to compute the results The strain related to each maceral from CH_4 (a), CO_2 (b) indicates that a lower Young's modulus causes greater linear strain upon injection. (c) and (d) are CH_4 and CO_2 injection into the macerals defined by their effective Young's modulus modal values (Table 3.2) from the 5μm mean analysis. 91

3.12 Probability density functions of Nanoindentation data collected on each coal maceral. Figure a indicates the modulus distribution of cutinite in the immature and mature coals, b indicates the distribution of sporinite within the paper coal, c, the distribution of inertinite measured and d, the overall distribution of all macerals across each coal. ^{I} and ^{M} indicate immature and mature coals macerals. 94

3.13 Young's modulus distributions of each maceral when analysed with AFM (spotted line), AFM 5μm^2 area (dashed line) and nanoindentation (solid line). The scans recorded are a.) immature sporinite, b.) immature cutinite, c.) immature inertinite, d.) mature bituminite, e.) mature cutinite and f.) mature inertinite. . 96

3.14 Young's modulus distributions of macerals analysed through nanoindentation. The distributions are coded in the form of initial nanoindentation (dashed line), which include the inertinite and Cutinite10 scans from the paper coal and the scans undertaken on the Northumberland coal during an MSc project. The solid line scans are undertaken at a later date and are much stiffer than the nanoindentation results from earlier. The cause of this unknown but is most likely due to either damage to the indenter tip or the machine used to run the nanoindentation. 98

4.1 SEM and EDX images of the Posidonia scans used in this study. Scan *a* is referred to as 24/2-007, Scan *b* referred to as 24/2-010 and Scan *c* is referred to as 29/2-008 in later sections of this study. There is a notable lack of Calcite in scan *a* and *b*, whilst scan *c* shows an a few calcite crystals in the scan. Scan *c* is notably less clear than the other scans. 109

4.2 Analysis of the possible scaler distributions for use with this data. The graphs show the mean boundaries of each phase on each of the scalers. The standard scaler and robust scaler are similar apart from the outlier in the organic matter upper phase boundary on the robust scaler. Feldspar was not included in this as it did not appear in every SEM scan. Organic matter and porespace are combined as organics, due to having a similar greyscale value under SEM. 113

4.3 Relative brightness in ranks of segmentation and mineral enrichment for classification 114

4.4 An indication of one single stem in the Decision Tree used for this study. Ten separate branches are shown with the alternate path for one branch also indicated. The sorting criteria for each node is also shown along with the entropy. 119

4.5 The Multi Layer Perceptron used in this study, comprising of two hidden layers with eight neurons in each. In this study ϕ_1 is the tanh function (Equation 4.14) and ϕ_2 is the softmax function (Equation 4.5). Black dashed lines represent the travel of data in the feedforward loop in Equation 4.16, blue arrows indicate the back propagation of the error in Equation 4.17. 121

4.6 A diagram of 5-fold cross validation. The train/test data is split into 5 composite parts each of 500,000 points, which are tested with each hyperparameter to be tuned, using each dataset as the test data once and a part of the train data 5 times. 126

4.7 An SEM image (a) of the Green River shale with the equivalent initial segmentation (b). The images below indicate the predicted phases of the Green River scan from each of the six machine learning models. Models shown are trained on 2,000,000 random training data (Random Seed Test Data) or trained on 2 scans of each shale as mentioned previously in Figure 4.10 (2x Each Shale). 128

4.8 An SEM image of the Eagle Ford Shale Carol Well with the equivalent mask. The images below indicate the predicted mask of the Green River scan from each of the six machine learning models. Models shown are trained on 2,000,000 random training data (Random Seed Test Data) or trained on 2 scans of each shale as mentioned previously in Figure 4.10 (Shale Split Test Data). 131

4.9 An SEM image of the Eagle Ford Shale Cinco Saus Well with the equivalent mask. The images below indicate the predicted mask of the Green River scan from each of the six machine learning models. Models shown are trained on 2,000,000 random training data (Random Seed Test Data) or trained on 2 scans of each shale as mentioned previously in Figure 4.10 (Shale Split Test Data). . . 134

4.10 A bar plot indicating the mean accuracy of each method across the entire database. The different colours represent different random seeds of the 2,500,000 train/test data for model initialization in the red, blue and green. The results in yellow were from models trained and tested on data from 2 scans of each shale (Eagle Ford Cinco Saus, Eagle Ford Carol and Green River Shale). The grey dashed line is the minimum possible accuracy of any model, i.e. the accuracy acquired if the model selected the same mineral for every pixel on every scan. The black lines at the top of each bar represents the standard deviation. 137

4.11 Bar graph indicating the accuracy associated with each model on the Posidonia shale scans. These accuracies are obtained with models trained on random seeded 2,000,000 datapoints as mentioned in section 4.3.4. It is notable that the accuracy of all models when fitting the scan from sample 29-2 is at double the scale in order to show bars with lower accuracies. The accuracy of each model is included above the bar on the chart. 141

4.12 Bar graph indicating the accuracy associated with each model on the Posidonia shale scans. These accuracies are obtained with models trained on two scans of each shale as mentioned in section 4.3.4. It is notable that the accuracy of all models when fitting the scan from sample 29-2 is at double the scale in order to show bars with lower accuracies. The accuracy of each model is included above the bar on the chart. 141

4.13 An indication of the accuracy of each model when predicting data on the Posidonia 29-2-Scan008. 142

4.14 Indications of the accuracy of each model when predicting the data on the Posidonia scan 24-2-Scan007. 144

4.15 Indications of the accuracy of each model when predicting the data on the Posidonia scan 24-2-Scan010. 145

4.16 Probability density functions of Young's modulus for each of the major mineral phases from Posidonia shale sample 24-2 Scan007 as classified as the initial segmentation and each of the machine learning models used. 149

4.17 Probability density functions of Young's modulus for each of the major mineral phases from Posidonia shale sample 24-2 Scan010 as classified by the initial segmentation and each of the machine learning models used. 151
4.18 Probability density functions of Young's modulus for each of the major mineral phases from Posidonia shale sample 29-2 Scan008 as classified by the initial segmentation and each of the machine learning models used. 154
4.19 Accuracies for learning in a four phase system. The dashed line represents the minimum possible guess which in this case would be guessing everything to be intermediate-stiff phase 156
4.20 Accuracy of each model on the validation dataset under a four-phase system when trained with the random seed method. 158
4.21 Accuracy of each model on the validation dataset under a four-phase system when trained with the two scan from each shale method 159

List of Tables

2.1 A list of the samples used in this study, with a representative depth, log location and sample type. The logs for these samples are included within Appendix 1 at the end of this thesis. 22

2.2 Rock Eval pyrolyisis results for the shale samples analysed. 30

2.3 Shale maceral and palynofacies characterisation. The majority of organic matter within the samples studied was amorphous organic matter, with terrestrial macerals (inertinite & vitrinite) only above 2% in the Bowland Shale. Spores were observed in only the Bowland Shale. The Green River unsurprisingly is the only shale to contain freshwater algae, although only at 1 count per 300. 30

2.4 Organic matter Young's moduli reported in the literature, with respective thermal maturities where available. The range in Young's moduli using nanoindenation is approximately 20GPa, with AFM providing a range of 30GPa. Results from this study are in accordance with other studies using AFM, with some subtle heterogeneity. The mature Barnett shale and Bowland shale have the largest ranges of Young's modulus values, with the smallest range observed for the Tarfaya shale. Analysis of these results indicate that at the scale of nanoindentation, increasing maturity decreases the kerogen Young's modulus, whereas increasing maturity generally increases the AFM measured Young's modulus. 35

2.5 Root-Mean-Squared-Error for each distribution fit for each Shale. The mean value for the normal distributions are shown along with the modal values for the Gamma distributions on each shale. [1]This is an unrealistic second phase in the Tarfaya due to being stiffer than the maximum stiffness in moduls, the curve itself as observed in Figure 2.13 has a frequency of <0.001. [2]There is no modal value in the Tarfaya due to the non fit of the data. The Tarfaya single phase indicates the error associated with fitting a single Normal and Gamma distribution to the curve. 42

2.6 List of contributors to this chapter 57

3.1 Mean measured vitrinite reflectance values for the coals studied based on 100 point counts. 65

3.2 Modal an mean values of AFM QI^{TM}on each coal maceral. *Values for Alginite are affected by the interaction of the alginite/tip with the resin. 72

3.3 Mercury injection porosimetry derived total porosity and mean pore radius size values for each coal. 80

3.4 Root-Mean-Squared-Error for each distribution fit for each Maceral. ^{I} denotes from an immature coal, whilst ^{M} denotes from a mature coal 84

3.5 Input parameters used in this study for Equation 3.7. E_s values are the modal modulus value of each maceral within this study. The remaining mechanical and thermodynamic properties are adopted from Scherer (1986); Levine (1996); Pan and Connell (2007). 89

3.6 List of contributors to this chapter 101

4.1 The number of pixels associated with each shale sample set, the Eagle Ford is common and comprises over 75% of the training dataset, whereas the validation dataset is small in comparison. 111

4.2 The total number of datapoints classified as each phase post segmentation. There is an obvious enrichment in calcite and clay within the training dataset, which is different to the large amount of quartz in the validation dataset. 111

4.3 The criteria for segmentation for each mineral 114
4.4 Optimal hyperparameters from 5-fold cross validation testing. Further detailed information on these hyperparameters can be found in sklearn/ tensorflow documentation (Pedregosa et al., 2011; Abadi et al., 2015) 127
4.5 A description of the capacity of each machine learning algorithm's ability to predict each of the phases in Green River Shale Sample 129
4.6 A description of the capacity of each machine learning algorithm's ability to predict each of the phases in Eagle Ford Carol Sample 132
4.7 A description of the capacity of each machine learning algorithm's ability to predict each of the phases in Eagle Ford Cinco Saus sample 135
4.8 A description of the capacity of each machine learning algorithm's ability to predict each of the phases in Eagle Ford Cinco Saus sample 143
4.9 A description of the capacity of each machine learning algorithm's ability to predict each of the phases in the Posidonia 24-2-Scan007 sample 145
4.10 A description of the capacity of each machine learning algorithm's ability to predict each of the phases in the Posidonia 24-2-Scan010 sample 145
4.11 List of contributors to this chapter 163

Chapter 1

Introduction and Thesis Objectives

1.1 Introduction

"The moment of crisis has come", is a quote by Sir David Attenborough (Shukman) regarding the effects of climate change on the world. This is in response to the average global temperature has increased by nearly a degree in the last thirty years (NASA, 2019b), caused by carbon dioxide emissions into the atmosphere, triggering a greenhouse effect. The concentration of carbon dioxide in the atmosphere has increased by approximately one sixth in the last thirty years, and still continues to rise (NASA, 2019a; Oceanic and Adiministration, 2019). In response to this the Paris agreement was signed by 197 world leaders in 2016, as a basis for reducing the CO_2 in the atmosphere and moving towards a future with less dependence on hydrocarbons for energy (Protocol, 1997). However, it has been noted as long ago as 2012 that reducing emissions alone is not enough to reverse the effects of climate change (Scott et al., 2013). Following this Carbon Capture and Utilisation Storage (CCUS) has been proposed as viable method for sequestering large amounts of liquid and gaseous carbon dioxide in subsurface reservoirs.

The most obvious candidate for sequestering CO_2 are depleted conventional oil and gas reservoirs, due mostly to the detailed knowledge of conditions and reservoir quality, which is a major requirement during the prospecting and production of any conventional hydrocarbon play. The first major CCUS project was in the Norwegian North Sea, with the Sleipner Field, which initiated in 1996 and has successfully sequestered 16M tonnes of CO_2 as of 2017 (Furre

et al., 2017).

Whilst requiring significant knowledge of the reservoir quality and chemistry, the integrity of the seal is the most important aspect of a successful CO_2 sequestration play. Therefore accurate prediction of the seal properties across the play, are vital in determining the viability of a conventional reservoir for CO_2 storage. The integrity of the seal in most traditional oil and gas plays is not as well studied as the reservoir conditions, especially with any changes to seal integrity during production and abandonment. The capacity of a seal is determined by the maximum column height of the sealed fluid that the caprock can maintain without a significant breach. Mudrocks, being the most common caprock in most conventional oil plays, are a major sealing target, due to their chemical stability under injection of high volumes of CO_2.

Although counter intuitive, unconventional hydrocarbons can also be used to reduce the carbon footprint of energy in some countries, as natural gas is a considerably cleaner fuel than coal. The concepts for a caprock shale in CCUS are also similar for an unconventional shale gas play, as information gained on the properties of the shale for seal integrity, are some of the same parameters that govern the potential of a shale unit for unconventional production, namely, thickness, mineralogy, porosity and geomechanical properties.

The proliferation of unconventional hydrocarbon production and in particular, shale gas in north America has led to much of the research into shale geomechanics over the two decades. Major shale gas production in the USA commenced in late 1990s with the development of improved proppant and horizontal drilling, making previously noncommercial plays, financially viable (Zhiltsov and Semenov, 2016). This was facilitated by an increase in oil price as the industry moved toward plays which were more complex, in deeper water, or were more mature. This increase in oil and gas price incentivzsed the exploitation of the source rock for some of the common simple subsurface gas plays in the USA, e.g. the Eagle Ford Shale as the source rock for the Austin Chalk petroleum play.

One of the first plays to be drilled extensively for shale gas was the Barnett Shale, produced by Mitchell Energy(Wang and Krupnick, 2015; Zhiltsov and Semenov, 2016). The proven method of extracting the tight oil and gas using hydraulic fracturing, caused many more operators to move to the large shale plays of the USA. This meant that by 2010 shale gas accounted for 23.1%

of all US natural gas production. The major fields explored during this time were the Eagle Ford, Marcellus, Bakken, Woodford, Fayetteville and Haynesville(Wang et al., 2014). As such many of the techniques that have been developed, including those used in this research project have been helped by the availability of high quality core from these shale gas operations.

With the economic change and shifting public attitudes toward hydrocarbons, it is unlikely that shale gas production in the USA or any other country will hit the levels of the mid-late 2000s. However, natural gas will play a key role in the movement forward into a net-zero society by 2050, and the legacy of the technical improvements made possible by the rise of US shale gas will continue to help with capturing and safely storing both carbon dioxide and hydrogen.

Mudstones are fine grained, fissile, laminated, clastic sedimentary rocks, generally comprised of a mixture of quartz, calcite, dolomite, clay minerals, organic matter and porespace (Aplin and Macquaker, 2011). The majority of porespace in shales is located between minerals, as well as within clay minerals and organic matter (Jennings et al., 2013; Klaver et al., 2015; Yang et al., 2015). The organic matter, related to key porespace within these caprock shales, evolves substantially with maturity, changing in abundance, physical appearance and chemistry (Curtis et al., 2012; Mathia, 2015; Milner et al., 2010). The properties of the organic matter also evolve depending on the reservoired liquid, particularly noticeable with the greater affinity between organic matter and CO_2 than either water or hydrocarbons (Pan et al., 2018; Zeng et al., 2018). It is therefore imperative to understand the effects of CO_2 injection on the mechanical properties of the organic matter at porescale.

The Young's modulus, a key mechanical property, that controls the relationship between stress and elastic strain, has been studied on shales at the microscale previously through indentation testing (Bobko and Ulm, 2008; Zargari et al., 2011; Kumar et al., 2012). However, it's only in the last five years that organic matter has been tested with a resolution capable of highlighting changes that may occur in individual particles (which may be $<1\mu m^2$ in area) (Eliyahu et al., 2015; Emmanuel et al., 2016, 2017; Goodarzi et al., 2016; Li et al., 2019; Khatibi et al., 2018). Testing Young's modulus at this resolution is important to understanding the heterogeneity which exists down the wellbore or across strata. Testing at this resolution, also informs upscaling models how any potential changes in effective stress will impact the shale

seal/ unconventional reservoir, and thus where the most likely planes of weakness are within the sample. The planes of weakness within the sample control the propagation of fractures. Whilst it is useful to measure the mechanical properties of a unit at the resolution of wireline sonic logs and triaxial tests, it is also incredibly important to understand the micro-scale properties directly impacting on these lower resolution tests to determine whether the intrinsic heterogenity will impact any potential sealing capacity.

Sub-micron testing has been undertaken thanks to the development of Atomic Force Microscopy (AFM), in particular the Bruker PeakForce^{TM} machine. This technique, which involves the oscillation of a tip, approximately 10nm in radius, onto the sample surface, allowing measurements of Young's modulus at the resolution of the tip, in a fast, non destructive manner, which enables the first insights into the Young's modulus variance in microscale organic particles. Previous work using AFM has been undertaken on a range of shales, from a Cretaceous shale from southern USA (Emmanuel et al., 2016), a Jurassic shale from the USA (Eliyahu et al., 2015), along with the Devonian/ Mississippian Bakken shale from North Dakota (Li et al., 2018a; Khatibi et al., 2018) and the Cretaceous aged Posidonia shale from Germany (Goodarzi et al., 2016). Initial trends indicate a maximum modulus of approximately 30GPa in the organic matter and a bimodal distribution observed by some authors (Emmanuel et al., 2016, 2017). A bimodal distribution contains two non-overlapping peaks, indicative of two separate distributions, each with a modal value. As such the distribution cannot be defined by its mean or standard deviation.

The bimodal distribution of Young's modulus has been shown to evolve and become dominated by a stiffer phase with maturity (Emmanuel et al., 2016). Alongside the AFM, traditional nanoindentation has been used by many studies to give an initial understanding of the Young's modulus of organic matter, with results suggesting a much lower maximum value (approximately 20GPa) (Zeszotarski et al., 2004; Zargari et al., 2016; Kumar et al., 2012; Wilkinson et al., 2015; Shukla et al., 2013).

Whilst it is convenient to use depleted oil and gas reservoirs for CCUS, not all countries across the world have a long history of conventional oil production, with two of the highest CO_2 emitting economies also being two of the largest net importers of petroleum (China & India)

and thus relatively lacking in depleted conventional reservoirs for sequestration (Barron; PTI). It therefore is prudent to look at other solutions for storing CO_2. One heavily developed method is using saline aquifers in a similar manner to depleted oil & gas reservoirs, generally due to their similar characteristics (size, structure, reservoir and caprock) to well known petroleum plays (Kongsjorden et al., 1998; Bentham and Kirby, 2005; Chadwick et al., 2008). However, another less explored avenue is to use the large coal deposits in these countries to sequester CO_2 (Wang et al., 2017; Datta and Krishnamoorti, 2019). As mentioned previously, organic material has a greater affinity for CO_2 than either water or hydrocarbons, and coals by nature are the most organic rich rocks in the crust- a coal is defined as being at least 50% organic matter by weight (Schopf, 1956). Coal can also have extremely large porosity, with up to 56% reported (Rodrigues and De Sousa, 2002), giving this previously "dirty" fuel the possibility of a second life as a viable CCUS reservoir, as well as being a natural seal. Another advantage of coal is that owing to the past use as a fuel and reuse of coal bearing land for development, a lot is known about the macromechanics of coal seams in the civil engineering industry. This combined with a recent history of numerous publications focusing on the thermodynamics of coals and the effect of CO_2 injection, indicates that coal may be an ideal candidate for CO_2 storage (Busch and Gensterblum, 2011, and references therein).

However, despite the well constrained geomechanical properties of coal, it is known to soften significantly with a higher moisture content (Poulsen et al., 2014). This becomes relevant when injecting CO_2 as the coal itself will act more like a sedimentary rock than a homogeneous organic solid, with coals made up of macerals, porespace and mineral matter. The fracture-like porespace (cleats) in coal would act as the initial primary target for sequestration, which would allow diffusion into and adsorption onto the coal surface. Due to this, there have been a large number of studies on the physical effects of CO_2 sorption on coals (e.g. Busch and Gensterblum, 2011; Goodman et al., 2005; Karacan, 2007; Gensterblum et al., 2010). It is therefore important to understand how the individual maceral components of a coal will respond mechanically to the injection pressures, and the change in pore fluid. Some studies have already been undertaken on the Young's modulus of these macerals using indentation techniques (Kossovich et al., 2016; Borodich et al., 2015). Most recently nanoindentation has been used to study the modulus

distributions of coal macerals, but similar to the organic matter in shale, some of these macerals cannot be adequately quantified by means of nanoindentation. The first study of AFM on coal macerals was undertaken by Li et al. (2020), indicating that this technique is effective at classifying coal macerals, which in turn may allow for greater insight and understanding at the resolution required to investigate the true effect of CO_2 sequestration.

Whilst it would be convenient to collect core samples of all wells for CO_2 injection and hydraulic fracturing, due to the monetary constraints, it is commonplace to collect only cuttings from the caprock. Nanoindentation and AFM make the most of these cuttings but they are not readily comparable to corescale measurements, let alone play or regional scale. However, in the last decade machine learning has been adapted by the oil and gas industry to attempt to make classification faster and assist in the upscaling and prediction of results (Tang et al., 2017; Wu et al., 2019; Duarte-Coronado et al., 2019; Su et al., 2020). This allows the industry to make advanced statistical interpretations where datasets are incomplete or absent completely using machine learning. This same approach could be useful on the limited data obtained from shale cuttings. Machine learning has already been used on SEM data with Artificial Neural Networks (ANN), Convolutional Neural Networks (CNN) and Random Forest proving the most useful algorithms to infer conclusions, such as grain boundaries and mineralogy, from basic backscatter SEM (Saporetti et al., 2018). Machine learning has also been used to predict mechanical properties from wireline data (Chen and Zhang, 2020), suggesting there is scope to combine mechanical properties with SEM identification into one model.

The advantage of having a single model that could measure and predict the mineralogy and geomechanical properties of a shale from SEM, is the ability to add this data to an upscaling model. Currently homogenization methods are applied using the deconvolution of a nanoindentation distribution for the mechanical phases and a few SEM scans on similar areas to represent the grain sizes and mineralogical phases (Goodarzi et al., 2017). However, machine learning through pattern recognition could easily allow larger areas to be analysed creating more complex and accurate homogenizations schemes. The machine learning algorithms would automatically segment the main mineral phases, allowing accurate measurements of mineral proportions and mean grain size. This ability to quickly determine mineralogy on a larger area, can then be

combined with AFM data in a machine learning model, to give predictions on the distribution of each phase. This allows for a greater insight into the geomechanical interactions of separate phases. For example, machine learning would be able to quickly identify if the shale is matrix or mineral supported and therefore, which of the phases Young's modulus distributions would be more important for modelling deformation.

Despite the vast array of literature on micro/nanoscale geomechanical properties of rocks and coals, there are some obvious gaps in knowledge:

- Does all marine derived organic matter have a similar Young's modulus distribution, and do the changes in modulus occur similarly in all marine shales?
- Is the bimodal Young's modulus distribution exhibited by marine organic matter, similar in lacustrine or terrestrially derived organic matter?
- Are there any trends in the Young's modulus distribution of coal macerals, and as such do they have a trend with maturity similar to the organic matter in shales?
- Can coals, which are generally more homogeneous at the micrometer scale than shales, be upscaled between AFM and nanoindentation measurements to give a similar modal modulus for further upscaling?
- Can SEM/EDX/AFM data be used by machine learning algorithms to make accurate predictions of the mineralogy and geomechanical properties of an individual shale, and further a unseen shale, dissimilar from those used to train the algorithm
- Further from this, which is the best machine learning algorithm to determine the composition of a shale from the SEM/EDX/AFM data?

1.2 Aims and Objectives

The main motivation of this study is to build upon the initial investigations into the geomechanical properties of organic matter, and systematically analyse if the initial observations from a single shale can be applied to other shales and organic rich rocks. The background for this, as

mentioned previously, is to enhance predictions in the subsurface for CCUS, hydraulic fracturing and Enhanced Coal Bed Methane (ECBM) recovery. A principal aim in this study is to identify if the trends in organic matter geochemistry, which are well documented between kerogen types and with maturity, are also the primary influence on the trends in organic matter geomechanics. These geochemical processes are prevalent in both shale organic matter and coalified organic matter, and so investigating the extent to which these processes influence the the geomechanical properties of the respective organic matter types, is integral to building a conceptual model of how all organic matter evolves with maturity.

Chapter 2: A comparison of organic matter Young's modulus from different depositional environments and maturities

Nanoscale measurements using atomic force microscopy are the only method to adequately determine the Young's modulus distribution of organic matter in shales, an important variable in their CO_2 sealing potential as well as determining frackability. Previous literature has focused on assessing shales on a case by case basis. Chapter 2 assesses the potential trends in modulus distribution with maturity across several marine shales, from different depositional environments and time periods. The results of this study indicate that there is a bimodal distribution in all marine shales, with a softer peak and a stiffer peak. This distribution evolves with maturity, whereby the stiff peak begins to dominate after the early oil window. Chapter 2 also demonstrates that their is a difference between the modulus distributions of Type II kerogen and Type I kerogen.

Chapter 3: An investigation into the Young's modulus distributions of different coal macerals with maturity

Whilst the AFM has been used extensively to look at the Young's modulus of organic matter in shales, it has been relatively unused on coals. In Chapter 3, three coals and one shale from different maturities with different maceral combinations are used to assess the impacts of maturity and provenence on the modulus distribution. The findings indicate a modal modulus of <15GPa in all macerals, there is no bimodal distribution in the coal macerals, with the maceral distributions more closely alligned to a Gamma distribution. These modulus distributions are also compared to nanoindentation data on the same macerals, and a basic upscaling between

the AFM and nanoindentation. The results of this are applied to the Pan and Connell (2007) model to indicate the difference in swelling based strain for each maceral.

Chapter 4: Use of Machine Learning techniques to predict mineral composition and modulus distribution of shales

It is very expensive to collect core samples to undertake geomechanical testing for caprock analysis. It is therefore prudent to gain as much understanding as possible from previously collected core and the cuttings which are returned during drilling. Machine learning is a key development in utilising large datasets for prediction. In Chapter 4, twenty SEM/EDX/AFM scans totalling over 25 million datapoints, are used to identify the most accurate machine learning models for mineral prediction. The mineral predictions are also compared with the equivalent modulus predictions indicating that mineral and modulus prediction capacity is based on having a well-rounded, detailed training dataset, where accuracy decreases massively when used on a dissimilar dataset.

Chapter 2

The Assessment of Organic Matter Young's Modulus Distribution with Depositional Environment and Maturity

Research from this chapter are published within the Journal of Geophysical Research-Solid earth and are available at https://doi.org/10.1029/2020JB020435

2.1 Introduction

Quantification of mudrock geomechanics has become increasingly important in order to inform the design of hydraulic fracturing treatments (Iferobia and Ahmad, 2020). This is driven by the need to reduce economic risk and balance environmental impact, by ensuring that production is achieved with as little fracture fluid possible. Additionally, in order to assess the suitability of conventional oil and gas reservoirs along with saline aquifers for storage of carbon dioxide, geomechanical models are required to constrain the conditions under which the top seal may begin to fail through fracturing (Ingram and Urai, 1999). Laboratory measurements and geomechanical modelling becomes paramount as production from reservoirs causes changes in the effective

stress regime, triggering seismicity and inducing new fractures and fault reactivation, potentially compromising seal integrity. In an effort to minimize risk and improve understanding, there has been a drive to improve the complexity and reliability of subsurface geomechanical models for both unconventional resources and potential carbon storage. This has yielded benefits of better constraining 'sweet spots' in the unconventional plays, where the shale is oil or gas window mature, and of the right mineralogic composition (Dehua and Fangzheng, 2012; Khair et al., 2013), along with improvements in models for the large scale geologic storage of CO_2 (Zoback, 2010; Rutqvist, 2012). Over the last five years numerous new approaches have been taken to model mechanical properties and fracture propagation in shales such as Eagle Ford (Morales et al., 2016) and Woodford (Bennett et al., 2015).

However, despite further improvements to geomechanical models, recovery from gas shales is still low and the decline rate of unconventional reservoirs is still concerning (Baihly et al., 2015). One reason for this unfavorable situation is the uncertainty in modelling the propagation of the fracture tip and aperture, within shales. Fractures are most likely to propagate along or reactivate existing planes of weakness and within minerals with the lowest values of Young's, shear and bulk moduli (Sone and Zoback, 2013). Young's modulus is therefore a first order control on the capacity of a shale to propagate hydraulic fractures, with a value of 20GPa deemed the minimum for a prospective shale gas play. Shales with Young's moduli below this are more anisotropic and prone to proppant embedment, leading to further increases in the complexity of fracture propagation (Britt et al., 2009).

A large proportion of shale geomechanical modelling has been dedicated to predicting bulk rock properties. The majority of hydrocarbons are however stored in interparticle pores within the matrix, or within intraparticle pores associated with the organic matter (Wang et al., 2009). The most likely migratory route is through these pores for non-fracture related seal release. The degree of anisotropy within whole rock shale models is in a direct correlation with the organic matter content, which is expected to have a key control in geomechanical properties (Sone and Zoback, 2013). The bulk matrix properties of a shale can be determined from triaxial testing or high load nanoindentation tests. Due to the limited resolution of these experiments (greater than $5cm^3$ and $5\mu m^2$ respectively), and the size of interspersed organic matter (which can be less than

1μm in diameter), obtaining representative measurements of organic matter Young's modulus is challenging and relies on measurements of larger organic particles. Although organic matter may only represent 1-5% of a potential CCUS seal by volume, the occurrence of this organic matter within the shale matrix may cause preferential fractures to occur between relatively soft organic matter and stiffer matrix components e.g. calcite and quartz. Knowledge of the mechanical properties of interspersed matrix kerogen becomes important as during deformation kerogen has been observed to begin to flow with strain (Rybacki et al., 2015). Until this thesis, no efforts have been made to analyse the mechanical properties of the matrix kerogen, with other studies focusing on larger "lumps" (Emmanuel et al., 2016; Eliyahu et al., 2015; Goodarzi et al., 2016). Therefore, novel techniques must be applied to determine the mechanical properties of these individual components.

The Young's modulus of organic matter has previously been measured by means of nanoindentation and Atomic Force Microscopy (AFM), with results indicating a range of 1-32.2GPa (Table 2.4). Nanoindentation studies have found a range of values of approximately 1-20GPa for kerogen Young's modulus (Table 2.4 and references therein). The aforementioned limited resolution of nanoindentation preclude it from being used to resolve the mechanical properties of most dispersed bitumen along with the majority of internal heterogeneity in kerogen. To further complicate the interpretation of nanoindentation measurements, organic matter porosity has been inferred to cause variability in the Young's modulus (Kumar et al., 2012), since porosity will cause a reduction in Young's modulus relative to a solid unit (Bobko and Ulm, 2008). Sub-micron scale organic porosity is abundant in organic matter across the maturity range (Loucks et al., 2009; Curtis et al., 2012), but generally increases with maturity.

Kerogen undergoes both chemical and physical changes with maturity, becoming increasingly aromatic, losing a large proportion of its thiophenes, amines and other nitrogen, sulphur, oxygen (NSO) compounds. This is coupled with kerogen becoming increasingly porous whilst also reducing in overall volume (Okiongbo et al., 2005; Curtis et al., 2012; Suwannasri et al., 2018). Pores within the kerogen are primarily nanometer intraparticle pores, with secondary porosity created where the kerogen volume has decreased (Bernard et al., 2012). Several studies have identified that organic matter develops secondary porosity with maturity, which can range to

nanoscale intraparticle circular pores (Bernard et al., 2012) or interparticle elongate fissures (Allan et al., 2014, 2016; Suwannasri et al., 2018). This secondary porosity accounts for the majority of porosity increase within shale samples with maturity and can comprise up to by 6-7% volume (Suwannasri et al., 2018). The onset of this porosity increase occurs during the oil window, with a large proportion already generated by the wet gas window. Modelling work by Goodarzi et al. (2017) shows that porosities up to 20% are possible at the scale of a nanoindent and could reduce the measured Young's modulus by up to 60% of its solid value, which was supported by nanoindentation measurements across a series of maturities by Zargari et al. (2016).

AFM studies mainly using Bruker's AFM PeakForce^{TM} QNM^{TM} have measured a maximum organic matter Young's modulus of 32.2GPa (Table 2.4 and references therein). Organic matter has been shown on occasion to comprise a stiff outer coating with a softer porous centre (Eliyahu et al., 2015; Emmanuel et al., 2016). Even at the resolution of AFM some of the nanoporosity observed within organic matter cannot be resolved and could account for the variability in Young's modulus values observed (Curtis et al., 2012).

Effective elasticity is affected directly by porosity in studies using both acoustic wave velocity (Allan et al., 2014, 2016; Suwannasri et al., 2018) and nanoindentation, whereby derived organic matter Young's modulus decreases from 20GPa to 7-12GPa with increasing porosity (Zargari et al., 2016). However, in higher resolution studies using AFM, an increase in organic matter Young's modulus is observed with maturity (Emmanuel et al., 2016; Goodarzi et al., 2017; Li et al., 2018a).

Further variability in organic matter Young's modulus has been identified using AFM, with a bi-modal distribution forming at higher maturities, believed to reflect the difference between the stiff kerogen component and softer bituminous component (Emmanuel et al., 2016). This phenomenon was also observed using nanoindentation of artificially matured Bakken shale by Zargari et al. (2011), who attributed a significant amount of Young's moduli values below 10GPa to bitumen formed during hydrous pyrolysis.

In this study Atomic Force Microscopy Quantitative Imaging (AFM QI^{TM}) is used for nanomechanical measurements. The benefit of this technique is both the increased resolution (10-50nm vs 1μm) compared with nanoindentation measurements and the non-destructive na-

ture of AFM QI^{TM}. This allows imaging with scanning electron microscopy after measurements have been acquired. The range of Young's modulus values in AFM nanomechanical studies of organic matter show greater heterogeneity, both between organic particles and also within an individual organic particle, resulting in a greater variance than that obtained through nanoindentation (1-32.2GPa vs 1-11.1GPa, see Table 2.4), and thus more likely represents the true variability of organic matter Young's modulus.

As mentioned previously, the degradation of organic matter with progressive thermal maturation (burial) is well understood and documented, it progresses from an aliphatic rich organic mélange into a better structured aromatic complex. The rate of this degradation is dependent on the primary composition of the organic matter, which in turn is a function of depositional environment and preservation efficiency (Pepper and Corvi, 1995a; Pepper and Dodd, 1995; Pepper and Corvi, 1995b). This raises the question of whether the rate and extent of thermal modification during maturation is determined by organic precursor input and if this could affect the mechanical properties of organic matter? Although several studies note that geochemical maturity changes also impact Young's modulus (Eliyahu et al., 2015; Emmanuel et al., 2016, 2017), little research has been focused on the impact of different geochemical input characteristics on Young's modulus.

It is possible that geochemical variability from subtle differences in depositional environment and thermal maturity cause intrinsic patterns within the Young's modulus distribution of organic matter. Using this technique we are able to investigate trends in Young's modulus that represent the transition of organic matter through different thermal maturities. These distributions may allow for increased realism in microscale geomechanical models, which will assist in the interpretation of fracture tip propagation in the subsurface. This is a first order control on the fracture mechanics of organic pores, which are known to house the hydrocarbons or CO_2 enabling increasingly cost effective hydraulic fracturing and CCS seal integrity studies.

2.2 Depositional Environment and Geological Setting of Studied Samples

In order to conduct this study, shale samples were chosen from a range of marine depositional environments, which include some of the most prolific black shale depo-types known in the petroleum industry.

2.2.1 Barnett Shale

The Mississippian Barnett Shale Formation was deposited by hemipelagic processes in a shallow epeiric sea (Pollastro et al., 2007) covering the majority of north and central Texas. The Barnett Shale is, at its maximum ∼300m of relatively homogenous black shale, except for a debris flow deposit in the centre (Ellenburger), itself with a maximum thickness of 120m in the north east of the basin. The Barnett Shale was deposited at approximately 14μm/year (Loucks and Ruppel, 2007) and has average TOC content of 2.5-3.5% (Jarvie et al., 2005). Studies into the sedimentary structures in the Barnett Shale suggest a shallow paleo water depth; below 120m (Loucks and Ruppel, 2007).

The Barnett shale was suited for this study as a classical shale composed almost entirely of hemipelagic deposits giving rise to a characteristic Type II kerogen (Jarvie et al., 2007). The Barnett shale also has a maturity signature not completely dominated by present day overburden. The Barnett is anomalously mature in the north east and south east of the Fort Worth Basin, due to the impact of hydrothermal fluids during the time of the Ouachita Thrust in the Late Carboniferous-Early Permian (Bowker, 2007). This allows an insight into the shale at similar depositional ages, from an almost identical environments but at different levels of thermal maturity. Samples in this study were selected accordingly (Table 1); from the Lake Davis Well from Hamilton county in the east of the Newark East Field and the TP Sims II Well from Wise county in the north east of the Newark East Field. The Lake Davis sample is believed to have a vitrinite reflectance (VR_o) value of $\sim 1.0\%$, with the TP Sims sample have a VR_o value of $\sim 1.3\%$, due to being proximal to the hydrothermal influence of Mineral Wells Fault (Pollastro et al., 2007). This is demonstrated in Figure 2.1 adapted from Montgomery

et al. (2005) indicating the influence of the Mineral Wells Fault and associated hydrothermal system

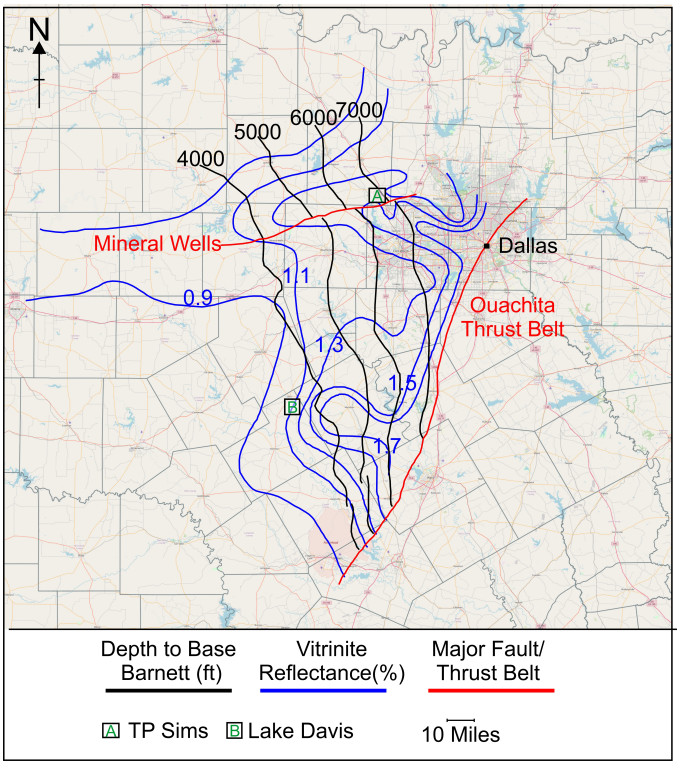

Figure 2.1: A map of the base of the Barnett Shale and associated maturity, indicating the major tectonic elements in the deposition. The TP Sims II and Lake Davis well are indicated. This figure has been adapted from Montgomery et al. (2005). As can be seen the maturity is anomalously high proximal to the Mineral Wells Fault, which has impacted the sample taken from the TP Sims well.

2.2.2 Bowland Shale

The Bowland Shale in England is also of Mississippian age and deposited in the Bowland Basin (covering large parts of north-west Lancashire- Figure 2.2), which is one of a series of small basins occupying tilted fault blocks formed during rifting in the late Devonian/ mid Chesterian. These fault blocks were tectonically inactive during the deposition of the Bowland Shale in the middle Mississippian (Fraser et al., 1990). The Bowland Shale is mainly composed of hemipelagic deposits, although a southwards prograding pro-delta, responsible for deposition of the Millstone Grit (Pennsylvanian), meant an increase in terrestrial organic matter present. Facies changes within the Bowland are related to basin topography during the Late-Mississippian/

Early-Pennyslvanian, which is observed in either orbitally-driven gradual changes or abrupt gravity slump deposits (Gawthorpe, 1987). The Bowland Shale interval studied here is from the Lower Bowland Shale (mid-Mississippian) and represents a maximum flooding surface, where anoxia is believed to be widespread within the basin (Gawthorpe, 1987). This choice of interval maximises the potential of measuring organic matter during nanomechanical testing, with the range of TOC of the Bowland in the Preese Hall-1 well sampled being from 0.5-6.1wt% (Fauchille et al., 2017), compared to 6.47wt% in the sample tested (Table 2.2). Records suggest that the Lower Bowland shale within the Bowland Basin is oil to gas window mature (Andrews, 2013).

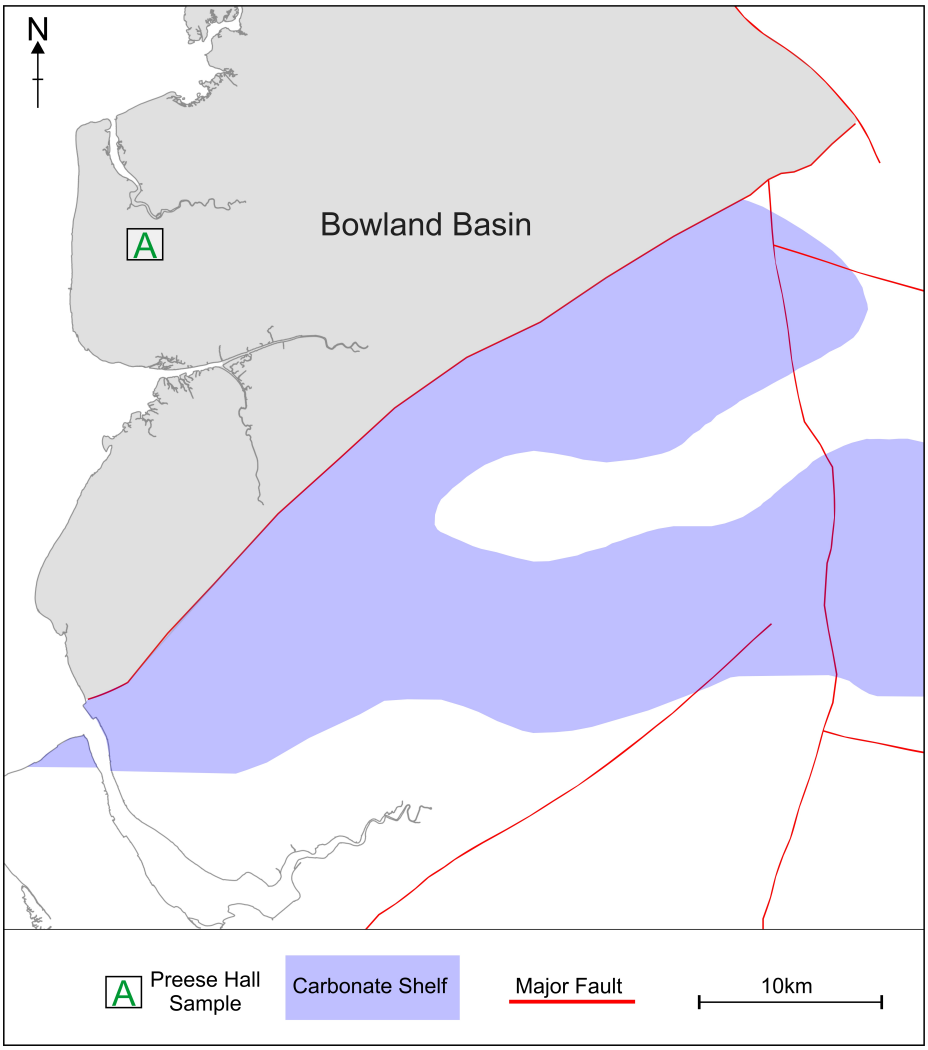

Figure 2.2: A location map of the Bowland Shale adapted from Walker (2020); Waters et al. (2009). The map indicates the major fault network in the area along with the major depo-centre (grey) and the carbonate shelf (blue).

2.2.3 Eagle Ford Shale

The Eagle Ford Shale was deposited during the Cenomanian-Turonian Ocean Anoxic Event (OAE II), in the Western Interior Seaway ranging from Canada across the majority of the western USA to Mexico. The Eagle Ford was deposited in three major depocentres; one to the east, and one to the west of the San Marcos Arc paleohigh (Figure 2.3), along with a further depocenter in the rapidly subsiding Maverick Basin (Condon and Dyman, 2006). This study focuses on samples of marginally mature Eagle Ford from the Cinco Saus well in the north of the Maverick Basin, and mature Eagle Ford shale from the Carol Well in Lavaca County from high on the west limb of the San Marcos Arch, south of the Karnes trough (Condon and Dyman, 2006; Fan et al., 2011). These samples represent different thermal maturities but also subtly different deposition environments, with the Eagle Ford deposited closer to the shore in the Carol well, which is consistent with the increased Type III kerogen content reported in the Eagle Ford around the San Marcos Arch (Condon and Dyman, 2006), which is a similar depositional environment to the Bowland Shale.

2.2.4 Tarfaya Shale

Like the Eagle Ford, the Tarfaya shale was also deposited during the Cenomanian-Turonian OAE II, and is composed primarily of fine grained calcareous material. The Tarfaya shales were however, deposited in warm upwelling nutrient rich water off north west Africa, (Figure 2.4) enhancing primary productivity and are generally richer in organic matter (Sachse et al., 2011) but this is highly variable at orbital time scales (Kolonic et al., 2002; Wagner et al., 2013). The studied interval shows strong biomarker and trace metal evidence support of temporal fluctuations in bottom water and photic zone euxinia (Kolonic et al., 2002). The Tarfaya shale is immature in the samples studied but makes an excellent potential source rock further off-shore where it is mature, with organic matter concentrations of up to 16% (Sachse et al., 2011), and with the majority of TOC contents falling between 3-9% for the section sampled from (Kolonic et al., 2005). The organic matter within the Tarfaya is highly labile and known to be sulphurised, fitting into the characteristic Type IIS region of a pseudo-Van Krevelen diagram with HI values

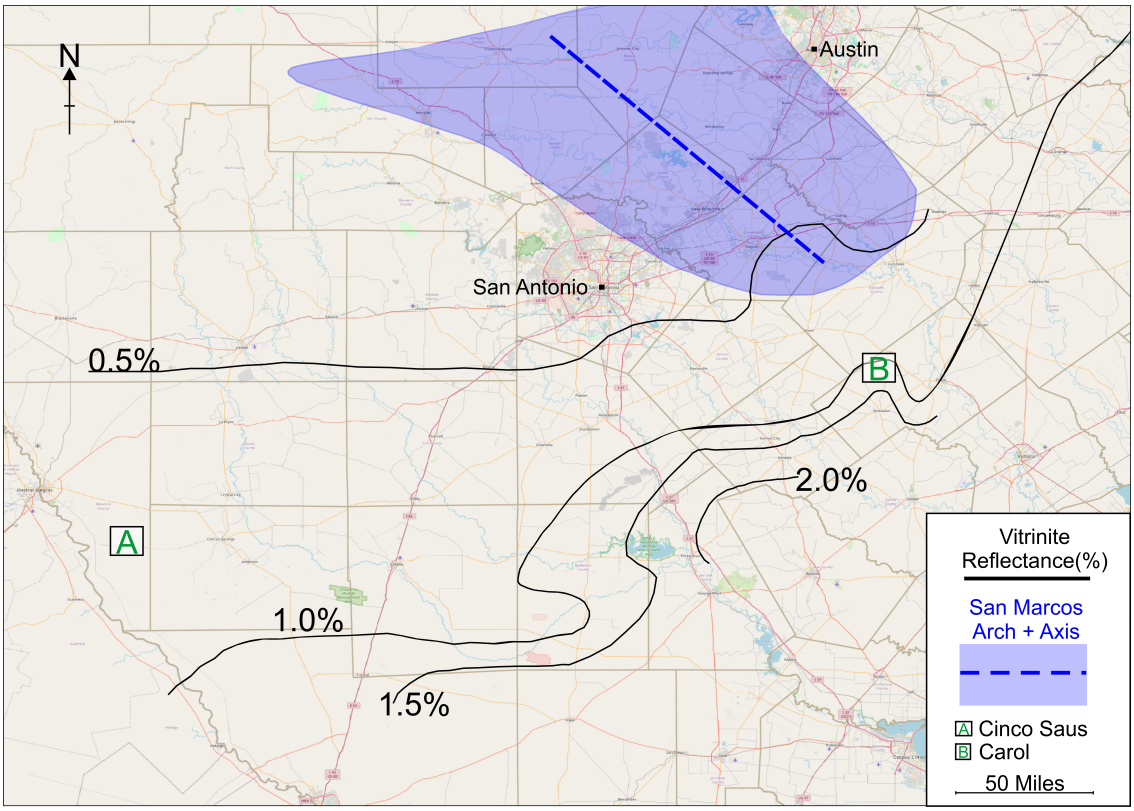

Figure 2.3: A map summary of the Eagle Ford Shale and the associated maturity. The map indicates the location of the San Marcos Arch paleohigh. As can be seen the Carol Well has been drilled into the Eagle Ford near the San Marcos Arch and is therefore likely to comprise more terrestrial and oxidised organic matter. The Cinco Saus well is located in Maverick County, which is much lower maturity and within the Maverick Basin.

of between 400 and 800mgHC/gTOC reported (Kolonic et al., 2005; Sachse et al., 2011). Organic matter is reported to be predominantly amorphous, with minor concentrations of alginite in the form of lamalginite (Sachse et al., 2011).

2.2.5 Green River Shale

The lacustrine Green River shale was deposited in a playa lake (Lake Gosiute/Lake Unita) setting during the Eocene, and comprises organic enriched shales representing wet periods where the lake expanded, alternating with dolostones representing dryer periods where the lake sides may have been exposed sub-aerially (Bradley, 1964). The sample studied is from an interval known as the Mahogany Zone (Figure 2.5), famed for its exceptionally high preservation and high stratification, evident from the presence of Gammacerane (Collister et al., 1992). During

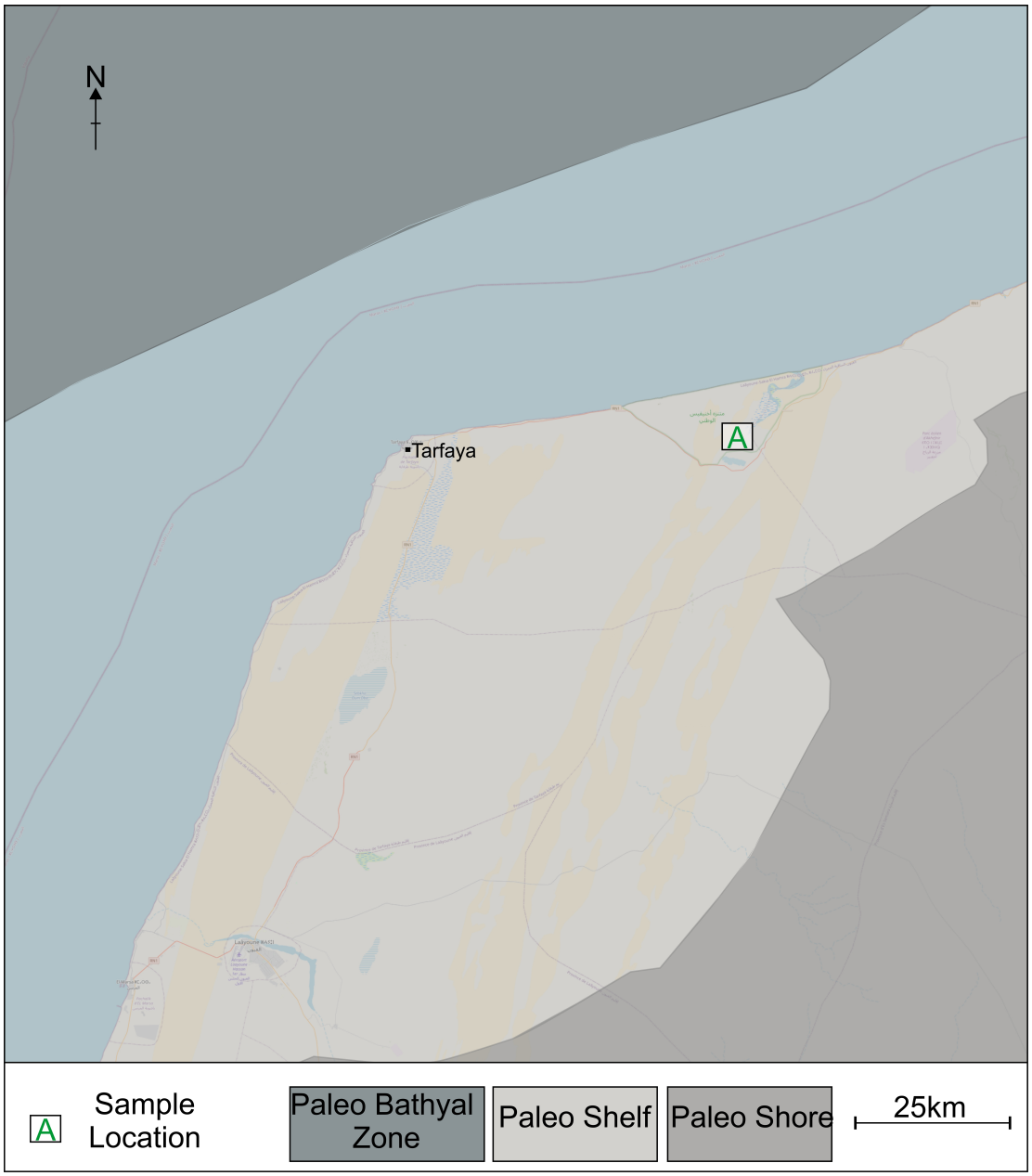

Figure 2.4: A map indicating the location of the Tarfaya sample taken, with the paleo-shoreline and shelf indicated. Adapted from Kolonic et al. (2005); Beil et al. (2018).

these periods it is hypothesized that Lake Gosiute was completely stratified. Previous research indicates that the stratified sections of the Green River are composed primarily of Type I kerogen (bacterial OM) (Horsfield et al., 1994). This represents a fundamentally different kerogen type and organic type to the rest of this study. The thermal maturity of the Green River sample used for testing here is reported to be immature (Table 2.4).

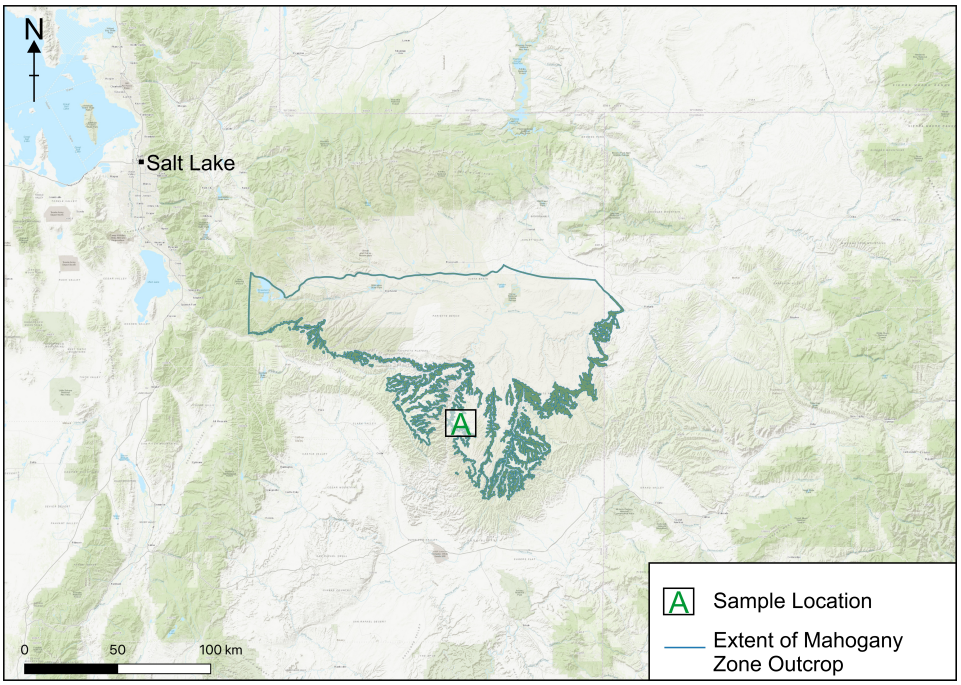

Figure 2.5: A location map of the Green River Shale, indicating the extent of the Mahogany Zone and the approximate sample location from this study. The geographical information for the Mahogany Zone outcrop used here was acquired from the USGS and is available at `https://certmapper.cr.usgs.gov/data/apps/oil-shale-data/`

2.3 Methods

2.3.1 Samples

Samples of each shale, approximately $10cm^3$ in volume were collected from wells of the Barnett, Bowland, Eagle Ford and Tarfaya. The Green River shale sample was collected from an outcrop of the Mahogany Zone in Utah. Details on the sampling regime and location are included in Table 2.1 below. Geological logs for each of the boreholes sampled are included within Appendix 1 at the end of this thesis.

Shale	Location/Well	Sample Depth (mbgl)	Sample Type
Barnett Shale	Lake Davis Well, Wise County, Texas	1262.75	Sample from core
	TP Sims II Well, Hamilton county, Texas	2326.55	
Bowland	Preese Hall-1, Lancashire	2081.7	Sample from core
Eagle Ford	Carol Well, Lavaca County, Texas	3724.00	Sample from core
	Cinco Saus Well, Maverick County, Texas	1222.50	
Green River	Mahogany Zone, Utah	N/A	Outcrop sample
Tarfaya	S57 Well, Tarfaya, Morocco	51.60	Sample from core

Table 2.1: A list of the samples used in this study, with a representative depth, log location and sample type. The logs for these samples are included within Appendix 1 at the end of this thesis.

The sampling strategy for each of the shales was slightly different. In general samples were taken from locations which appeared to be un-oxidised and therefore slightly enriched in organic matter. The sample from the Bowland shale was taken from a zone known to be enriched in organic matter, located within a Marine Band. The reason for this was to ensure that an adequate amount of organic matter could be analysed on the AFM from the sample. Total organic carbon values of <1% were deemed insufficient to acquire a representative dataset on the AFM.

2.3.2 Preparation and Analysis

Shale samples, prepared as thin sections perpendicular to bedding were analysed using scanning electron microscopy (SEM), with a FEI Quanta FEG 650 SEM. The microscope was operated under low vacuum conditions (0.82 Torr), at between 15-20kV, allowing a resolution of <100nm on the uncoated samples.

2.3.3 Organic Matter Chemical Characterisation

Total Organic Carbon (TOC) and Rock Eval Pyrolysis measurements were conducted to assist in maturity analysis and organic matter typing. Rock Eval analysis was undertaken using a Rock-Eval 6 configured in standard mode, with a heating rate of 25^oC/min between 300^oC and 600^oC in an inert N_2 atmosphere, and the residual organic matter was then oxidised from 300^oC to 850^oC at 20^oC/minute. The hydrocarbons released during pyrolysis were measured using a flame ionisation detector, and the CO_2 and CO measured using an infared detector. Oil

saturation index (OSI), Hydrogen Index (HI) and Oxygen Index (OI) were calculated using the following equations (2.1):

$$OSI = \frac{S1 \times 100}{TOC}, \;\; HI = \frac{S2 \times 100}{TOC}, \;\; OI = \frac{S3 \times 100}{TOC} \tag{2.1}$$

The values of S1, S2 and S3 were measured by the integration of the respective peaks, with S1 representing in-situ hydrocarbons, S2 representing the cracking of organic matter to hydrocarbons during heating, and S3 representing the organic matter analysed as CO_2 and CO when burned. Further details of this method are found in Słowakiewicz et al. (2015).

Solid-State ^{13}C NMR spectroscopy was undertaken on powdered samples to help characterise the organic composition of each shale. The spectra were recorded at a frequency of 100.62MHz using a Bruker Advance III HD spectrometer and 4mm magic angle spinning probe. The spectra were recorded at ambient temperature, using cross-polarisation and TOSS spinning sideband suppression with a 1ms contact time, 2s recycle delay and at a sample spinning rate of 10 kHz. 100-165mg of sample was used for each NMR analysis. The spectral referencing was obtained by using neat tetramethylsilane carried out by setting the high-frequency line from adamantane to 38.5 ppm. The absolute value of signal varied between each sample, which was a reflection of the variable organic carbon content across the range of shales sampled.

NMR spectra were analysed using chemical ranges from Chadwick et al. (2004), whereby aliphatic hydrocarbons exist primarily of the spectral range of 0-55ppm, and aromatic hydrocarbons over 95-170ppm. Although solid-state NMR is not absolutely quantitative it can be considered a semi quantitative method of characterising organic composition.

2.3.4 Palynofacies

Palynofacies preparation was undertaken on approximately 5g of sample from each shale using hydrochloric acid and hydrofluoric acid to remove carbonate and silicates. The kerogen fraction was then filtered through a 10μm sieve and strewn-mounted on microslides. Palynofacies analysis was undertaken on a Leica DM2700 P polarising microscope at 400x magnification, equipped with a PetrogLite motorized stage. 300 randomly selected particles analysed following the

palynofacies classification of Tyson (2012) and McArthur et al. (2017). Slides were also studied in blue light excitation following the standard recommendations for epifluorescence on palynological slides (Tyson, 2006, 2012).

2.3.5 Nanomechanical Measurements

The bedding-normal shale samples were prepared for nanomechanical measurements using a GATAN Precision Etching and Coating System (PECS^{TM}) II- Argon Broad Ion Beam Mill on to reduce shale topography. The central 28mm^2 of the sample sections were polished for 90 minutes using a 4kv ion beam to achieve maximum results without excess spluttering. This milling is unlikely to have affected the surface organic matter maturity, as this method was similar to that used in (Mastalerz and Schieber, 2017), which indicated a negligible increase in VR_o.

A JPK NanoWizard 3 (now Bruker JPK BioAFM^{TM}) was used to generate nanomechanical measurements using QI^{TM}. This technique along with its sister technique PeakForce^{TM} QNM^{TM} has successfully obtained mechanical measurements of biological materials (Chopinet et al., 2013), cements (Trtik et al., 2012) and shales (Goodarzi et al., 2017). Recent research suggest that these two techniques are similar when measuring moduli in the range expected for organic matter (Graham et al., 2020). The AFM QI^{TM} was used with the following settings: Force applied: 500nN, Z Length: 750nm, speed: 253μm/s. Silicon Nitride RTESPA-525 tips were selected, which are the latest variant of the TAP-525 used by Emmanuel et al. (2016). These tips are indicated to have a nominal working range of between 0.1GPa and approximately 20GPa (Pittenger et al., 2014). However, Emmanuel et al. (2016) measured Young's modulus values of up to 32GPa using similar TAP-525 tips, suggesting that there is flexibility to measure Young's moduli in this region with the RTESPA-525 tips.

The general method for acquiring AFM mechanical measurements involves oscillating a tip/cantilever assemblage onto a less stiff sample surface. The oscillation occurs at a frequency below the resonance frequency with a set force. Movement of the tip-surface interaction is measured by deflection of a lazer on a photo-diode using beam theory. More information on the QI^{TM}is described in "QI^{TM}mode-quantitative imaging with the NanoWizard 3 AFM" (JPK-

Instruments, 2011) and in Figure 2.6.

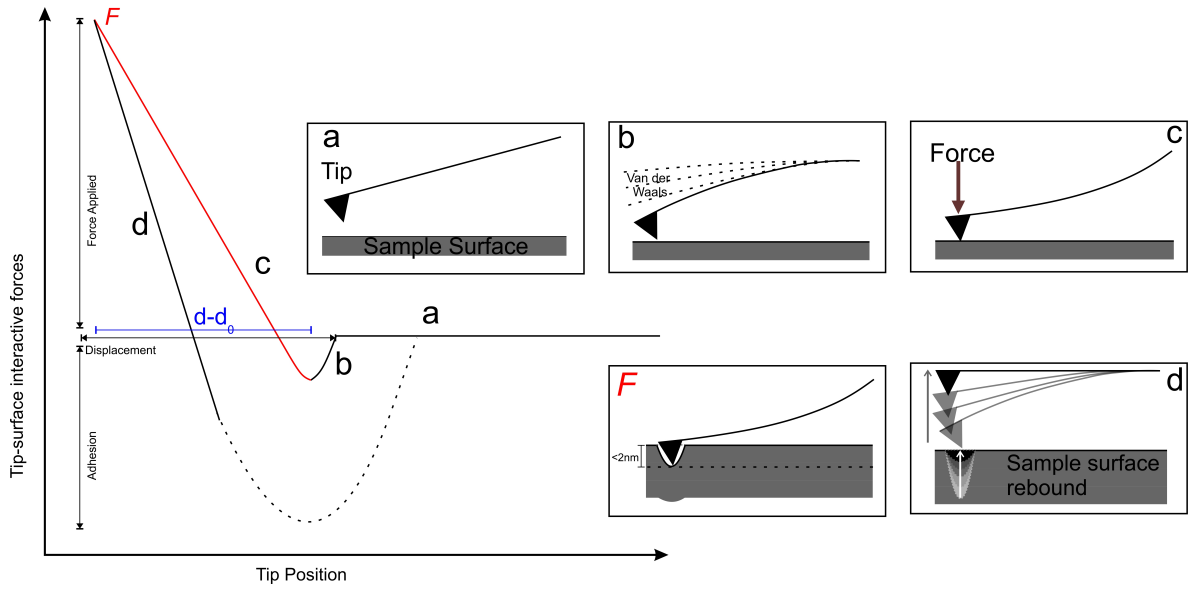

Figure 2.6: The working mechanics of an AFM. The initial phase involves oscillating the tip near to the sample (a), where adhesive forces bring the tip onto the sample surface (b). After this a set amount of force is applied (c). It is on this gradient that the Young's modulus is measured (red line). The amount of displacement ($d - d_0$) is then measured at the largest force (F). After which the tip is removed from the surface by the oscillation of the cantilever (d).

New tips were used per 4-8 scans due to tip wear, or sooner if the tip was believed to be damaged during a scan. Spring constants and sensitivities were calculated using contact-free calibration, whereby the tip is oscillated away from the sample and the flextural movement of the cantilever is recorded before use. This is the method suggested by Bruker and in a comparison with contact-mode calibration with a sapphire standard produced more realistic spring constants and sensitivities. Young's modulus calibration was obtained before scanning with a new tip by scanning a sample of Highly Ordered Pyrolitic Graphite (HPOG-12M), adjusting sensitivities and the spring constants to obtain a value of 18GPa +/-0.5GPa.

Random areas of each shale were scanned within the 28mm^2 ion beam milled area to ascertain the Young's modulus of organic matter. Areas scanned were generally 250μm^2 at a resolution of 512 $\times$ 512 pixels. Each sample was successfully scanned a minimum of 10 times. This approach has been chosen as a means of upscaling measurements of individual organic matter particles from literature (Emmanuel et al., 2016; Goodarzi et al., 2017; Khatibi et al., 2018), and attempt to align the high resolution data from the AFM with other bulk sample measurements (Rock

Eval). To locally upscale, some AFM scans were meshed together to form a larger $1000\mu m^2$ area. Whilst this only reflects a small proportion of the $28mm^2$ milled area, the total area scanned of approximately $2500\mu m^2$ may offer the first insights into upscaling AFM results and measuring organic matter as a matrix, rather than a grain.

An advantage of the AFM QI^{TM}is the user has a constant feedback of force curves, which allows understanding of tip functionality. If during scanning a tip was thought to be damaged, the tip was replaced immediately and the area rescanned if possible.

Once the force curve has been produced, the reduced Young's modulus is derived from the fitting of the extend curve, in accordance with the operation manual for the Bruker BioFilm AFM QI^{TM}. This discounts the minor amounts of adhesion on the samples (adhesion is corrected for in processing of results). These samples were then analysed using the Hertz-Sneddon Model (Sneddon, 1965);

$$\begin{aligned} F &= \frac{4}{3}E'\sqrt{R\ (d-d_0)^2} \\ E' &= \left(\frac{1-\nu_s^2}{E_s}\ +\ \frac{1-\nu_{tip}^2}{E_{tip}}\right)^{-1} \end{aligned} \tag{2.2}$$

Where F is the peak force, E' is the reduced Young's modulus, R is the tip radius (approximately 10nm for RTESPA-525 tips) and $(d-d_0)$ is the sample displacement (Figure 2.6). Using Equation 2.2 Young's modulus can be calculated from the reduced Young's modulus, using the Poisson's ratio of the sample (ν_s) and tip (ν_{tip}) along with the Young's modulus of the tip-cantilever array (E_{tip}).

2.3.6 Modulus Data Analysis

A four step approach was undertaken in the processing of the raw AFM QI^{TM}data (Figure 2.7.

- The initial reduced Young's modulus data was processed through a 30GPa cut-off, which represents the reported absolute limit of the tip from Emmanuel et al. (2016) (stage 1 in Figure 2.7). At this stage any data below reported lower limit of the tip is removed (0.1GPa: Pittenger et al. (2014)).

- The residual data is then checked for a maximum value of organic matter Young's modulus, achieved by comparing the AFM QI^{TM}scans with their equivalent SEM scan and EDX data obtained. This was undertaken first by enhancing the SEM through colour thresholding using the method proposed by Camp (2013). The pixel values of the enhanced SEM are then manually compared with visible values for organic matter and porosity. The mask created is combined with a mask of the colours associated with the peak carbon values from EDX (stage 2 Figure 2.7). This allows removal of dark colours in the SEM which are associated porosity, as these values will show no peak in carbon on the EDX.

- The data is then put through an adhesion filter, which removes values where adhesion is greater than 5% of the total force exerted. This level of adhesion makes the value suitable for the Derjaguin-Muller-Toporov model (Derjaguin et al., 1975), which includes adhesion as part of the Young's modulus calculation.

- Lastly any areas of topographic variability above 5° are filtered out in all shales apart from the Tarfarya, in which the requisite polish from ion beam mill couldn't be achieved due to the high proportion of organic matter and contrast with calcite.

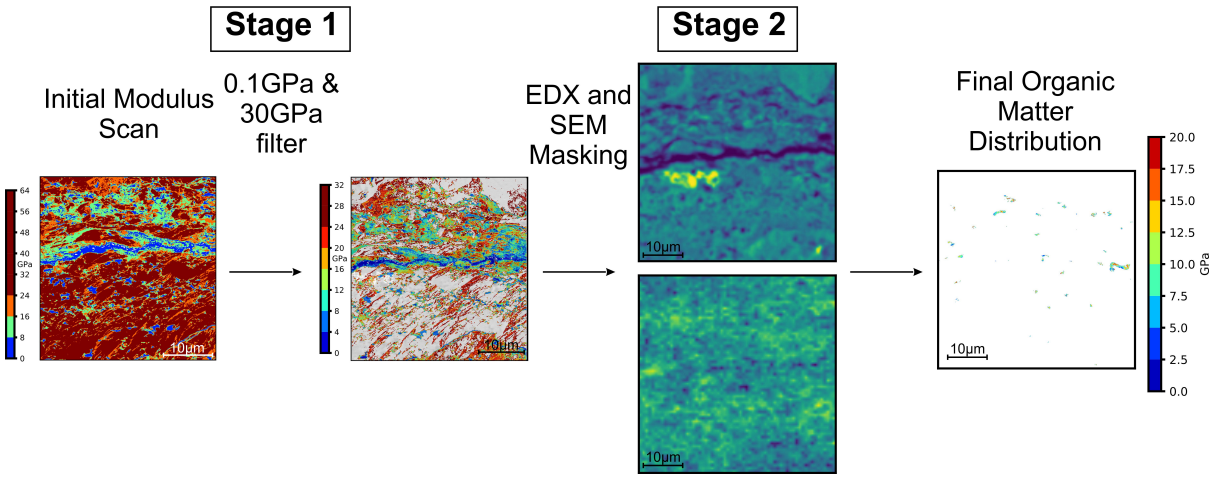

Figure 2.7: An example of the filtering procedure for the raw AFM data. The initial data is put through a 30GPa and 0.1GPa filter to remove these values. It is then compared to SEM images (centre) to identify the maximum value of Young's modulus for organic matter. Then if required the data is filtered for fracture data whereby, modulus values believed to relate to fractures are removed (Stage 2).

Upon filtering the Young's modulus data of each scan and each shale, the results were

visualised as a Kernel Density Estimate (KDE) plot in order to identify trends using GetDist (Lewis, 2019), which has inbuilt functionality to undertake boundary correction on KDEs. This is relevent for some of the shales, whose modal results are close to the limit of the organic matter phase identified using SEM/EDX.

2.3.7 Deconvolution

The deconvolution technique-first described by (Bobko and Ulm, 2008) has been used frequently to understand the complex distributions in nanoindentation data. This technique uses the central limit theorem, whereby, the distributions of a series of means will always be normally distributed (Bauer, 2011). In the case of nanoindentation, each indent measures a mean Young's modulus across the indented area ($\sim 1-5\mu\text{m}^2$). Therefore once a series of nanoindentation results are plotted, the resulting probability density function represents a composite of the normal distributions for each mechanically active phase.

These phases can be described by their proportion on the surface, along with their mean and standard deviation. This technique is useful when dealing with effective moduli, such as at the scale of a single nanoindent. However, it requires some adjusting when downscaling the measurements to local moduli values, which are not necessarily normally distributed.

Here we use the deconvolution technique to understand the potential different distributions within the organic matter Young's modulus. Initially the experimental cumulative distribution function (ECDF) of the organic matter Young's modulus data is calculated using Equation 2.3.

$$F_E\ (E_i) = \frac{i}{N} - \frac{1}{2N} \tag{2.3}$$

where, N is the number of datapoints in the modulus dataset, sorted into ascending order and i is an incremental point on the dataset. Firstly the ECDF is compared to a two phase normally distributed system, the CDF of which is generated using Equation 2.4.

$$F\left(E_i; \mu_n^j, \sigma_n^j\right) = \frac{1}{\sigma_n^j\sqrt{2\pi}} \int_{-\infty}^{E_i} e^{\frac{-\left(u-\mu_j^E\right)^2}{2\left(\sigma_j^E\right)^2}} du \qquad j \in [1; n] \tag{2.4}$$

Where, μ is the mean and σ is the standard deviation. The superscript ^{j} reprents the j'th phase

in the system.

The CDFs generated of the two phases are minimised for the smallest root-mean-squared-error (RMSE) against the ECDF using equation 2.5.

$$\min \left[\sum_{i=1}^{N} \left(\sum_{j=1}^{n} f_j F\left(E_i; \mu_j^E; \sigma_j^E\right) \; - \; F_E\left(E_i\right) \right)^2 \right] \tag{2.5}$$

In this each phase (F) occupies a fraction(f) of the sample surface. This minimisation is constrained by the sum of all phases equating to one (Constraint A) which represents a physical constraint on the model. A second analytical constraint (Constraint B) is selected to avoid overlapping phases. This is important in systems whereby the mechanical phases are unrelated. However, in this deconvolution we present results with both this constraint in place but also relaxed, as the phases of organic matter may be fundamentally related (kerogen hosting bitumen, or aliphatic and aromatic end members of carbon).

$$\sum_{j}^{n} f_j = 1 \text{ (Constraint A)} \quad \mu_j^E + \sigma_j^E \leq \mu_{j+1}^E + \sigma_{j+1}^E \text{ (Constraint B)} \tag{2.6}$$

Previous research suggests (Fender et al., 2020) that the normal distribution may not be the most suitable fit for coal macerals, which are similar in structure to the organic matter in shales. As such, in accordance with those results, minimization has been undertaken using the CDF for the Gamma distribution (Equation 2.7) to indicate if this prevails within organic matter within shales.

$$F\left(E_i; k_n^j; \theta_n^j\right) = \int_{-\infty}^{E_i} \frac{\gamma\left(k, \frac{E_j}{\theta}\right)}{\Gamma\left(k\right)} \quad j \in [1; n] \tag{2.7}$$

2.4 Results

2.4.1 Organic Content Typing and Analysis

Table 2.2 presents the TOC values for each shale. Samples of the Bowland and Eagle Ford Carol were selected across intervals known to have elevated TOC in order to ensure that a

representative amount of organic matter Young's modulus data could be obtained during the AFM QI^{TM}analysis. TOC values in general fall between 4-7% of the total rock weight, indicating that ∼10-15% of the shale surfaces scanned should be organic matter.

The TOC of the Tarfaya shale sample is the highest observed at 17.5%, which is indicative of a TOC rich layer in this section (Poulton et al., 2015). The Bowland shale TOC value, which at 6.5% is also amongst the richest intervals in the entire section logged (0.51-6.1%wt reported in Fauchille et al. (2017)).

Shale	Kerogen Type	Maturity (Literature)	Pyrolysis Measurements				
			Total Organic Carbon (wt%)	HI ($mgCO_2/gTOC$)	OI ($mgCO_2/gTOC$)	Tmax °C	Oil Saturation
Barnett Lake Davis	Type II	∼1.0% R_o	5.0	143	1.0	445	41.8
Barnett TP Sims	Type II	∼1.3% R_o	3.9	13	4	453	7.5
Bowland	Type II/III	Oil/Gas Window	6.5	63	2	464	16.1
Eagle Ford Carol	Type II/III (increased Type III relative to Cinco Saus)	Wet Gas Window	3.7	106	3	457	156.8
Eagle Ford Cinco Saus	Type II/III (increased II relative to Carol)	Oil Window	5.6	198	10.5	443.5	76.7
Tarfaya	Type IIS	Immature	17.5	598	35	408	23.5
Green River	Type I	Immature	6.1	776	30	430	37.0

Table 2.2: Rock Eval pyrolyisis results for the shale samples analysed.

The inherent variability between shales is demonstrated in mineralogy evident in Figure 2.8, with the Tarfaya and Eagle Ford displaying the characteristics of a marl rather than the typical black shale, with significantly more matrix calcite than the other shales. Tmax values indicate that the Tarfaya and Green River samples are thermally immature (<435°C), while the Bowland has a Tmax greater than 460°C indicative of the gas window. The Barnett TP Sims has been reported to be in the gas window (Zhang et al., 2014) and although the Tmax is below 460°C, the low S2 and Oil Saturation Index values suggest that this sample is also within the gas window. The Eagle Ford Carol shale is at approximately late oil maturity, represented by high OSI, due to little expulsion. The Barnett and Cinco Saus Eagle Ford shales have reached marginal oil window maturity (Tmax 445 and 443.5^{o}C respectively).

Shale	Amoprhous Organic Matter (%)	Inertinite (%)	Vitrinite (%)	Spores (%)	Acritarch (%)	Freshwater Algae (%)
Barnett Lake Davis	100.0	-	-	-	-	-
Barnett TP Sims	100.0	-	-	-	-	-
Bowland	93.4	3.3	2.0	1.0	0.3	-
Eagle Ford Carol	98.3	0.7	1.0	-	-	-
Eagle Ford Cinco Saus	98.6	0.7	0.7	-	-	-
Tarfaya	100.0	-	-	-	-	-
Green River	98.7	0.7	-	0.3	-	0.3

Table 2.3: Shale maceral and palynofacies characterisation. The majority of organic matter within the samples studied was amorphous organic matter, with terrestrial macerals (inertinite & vitrinite) only above 2% in the Bowland Shale. Spores were observed in only the Bowland Shale. The Green River unsurprisingly is the only shale to contain freshwater algae, although only at 1 count per 300.

Palynofacies characterisation (Table 2.3) supports previous depositional environment assignments. The Barnett and Tarfaya samples comprised solely of amorphous organic matter, typical of algal dominated hemipelagic deposition (Loucks and Ruppel, 2007; Kolonic et al., 2002). The Bowland sample contained the most terrestrially derived organic matter with 2% vitrinite and 3.3% inertinite. Both the Eagle Ford samples contained similar maceral compositions with the Carol slightly enriched in vitrinite (3 counts per section compared to 2). The proportion of terrestrial organic matter in the Carol and Bowland samples may be lower than anticipated due in part to sampling from organic rich intervals of the core, representing periods of less continental runoff and increased preservation of marine organic matter. The Green River shale sample has a similar abundance of inertinite to the Eagle Ford samples, and considerably less than that in the Bowland, but does contain the only occurrence measured of freshwater algae. This suggests that the Green River sample may not be from a period of large amounts of fluvial input into Lake Gosuite, due to the low abundances of inertinite, vitrinite and spores.

SEM imaging perpendicular to bedding indicates a subtle difference in the appearance of the organic matter between the shales studied (Figure 2.8). The grain fabric in the Barnett Lake Davis sample (Figure 2.8a) appears to be random, and the organic matter distribution is almost entirely bimodal and occurs either amongst clay-rich interlayers or as scarce single agglomerations within the well cemented quartz rich layers. The organic matter within the TP Sims (Figure 2.8b) is subtly different to that of the Lake Davis sample and occurs as either larger ($\sim$50μm) or smaller ($\sim$10μm) irregularly shaped lenses. The fabric of TP Sims sample shows little lamination within the organic matter or other minerals, similar to the Lake Davis sample, indicative of possible early cementation.

The organic matter in the Bowland sample (Figure 2.8c) appears to be either in the form of large (>10μm) spores or smaller lenses of AOM, distributed parallel to bedding. Across the Bowland the organic matter appears to be strongly laminated with the fabric.

The habit of organic matter within the Eagle Ford is similar in both the Carol sample (Fig.2.8d) and the Cinco Saus sample (Fig. 2.8e). Organics generally appear as either as 10-40 μm clumps within a fecal pellet, or as thinner wispy lamellae within the matrix of the micrite interlayers.

The organic matter appearance in the Tarfaya is similar to the Eagle Ford; both are primarily formed from fecal remains (Fig.2.8f). Whilst similar in morphology of organic matter, the Tarfaya has a significant proportion existing as $\sim$10μm lamellae. The Tarfaya is also finer grained and has an organic dominated matrix with interspersed micrite.

The organic matter occurrence within the Green River shale is similar to the Tarfaya, in the sense that it comprises as large amount of the matrix interspersed between larger clasts. The clasts in the Green River samples comprise mainly quartz, dolomite and calcite. There is a notable amount of clay within the matrix although, this has not been quantified in this study. The organic matter itself appears as whispy and globular occurances within the shale matrix, commonly associated next to pores and in places interspersed between clays as indicated in Figure 2.8.

Results from Solid State NMR spectroscopy, displayed in Figure 2.9, show the proportion of aliphatic to aromatic hydrocarbons within the kerogen of each shale. The proportion of aliphatic to aromatic kerogen within each shale has been determined by integrating the values at 0-55ppm and 90-145ppm respectively from the NMR results. The thermally immature Tarfaya and Green River shale samples are significantly enriched in aliphatic carbon (70% & 77%) compared to aromatic carbon within the kerogen results shown in Figure 2.9. The Cinco Saus, Carol and Barnett Lake Davis all comprise approximately 68-69% aromatic kerogen, whereas the Bowland and Barnett TP Sims contain >80% aromatic kerogen.

2.4.2 Organic Matter Young's Modulus

The Young's modulus values obtained within this study along with other studies, Table 2.4, which indicate that the range of values found within this study are similar to other AFM studies. Table 2.4 also shows modulus values from different maturities showing a clear increase in maximum Young's modulus values with maturity in shales measured by AFM.

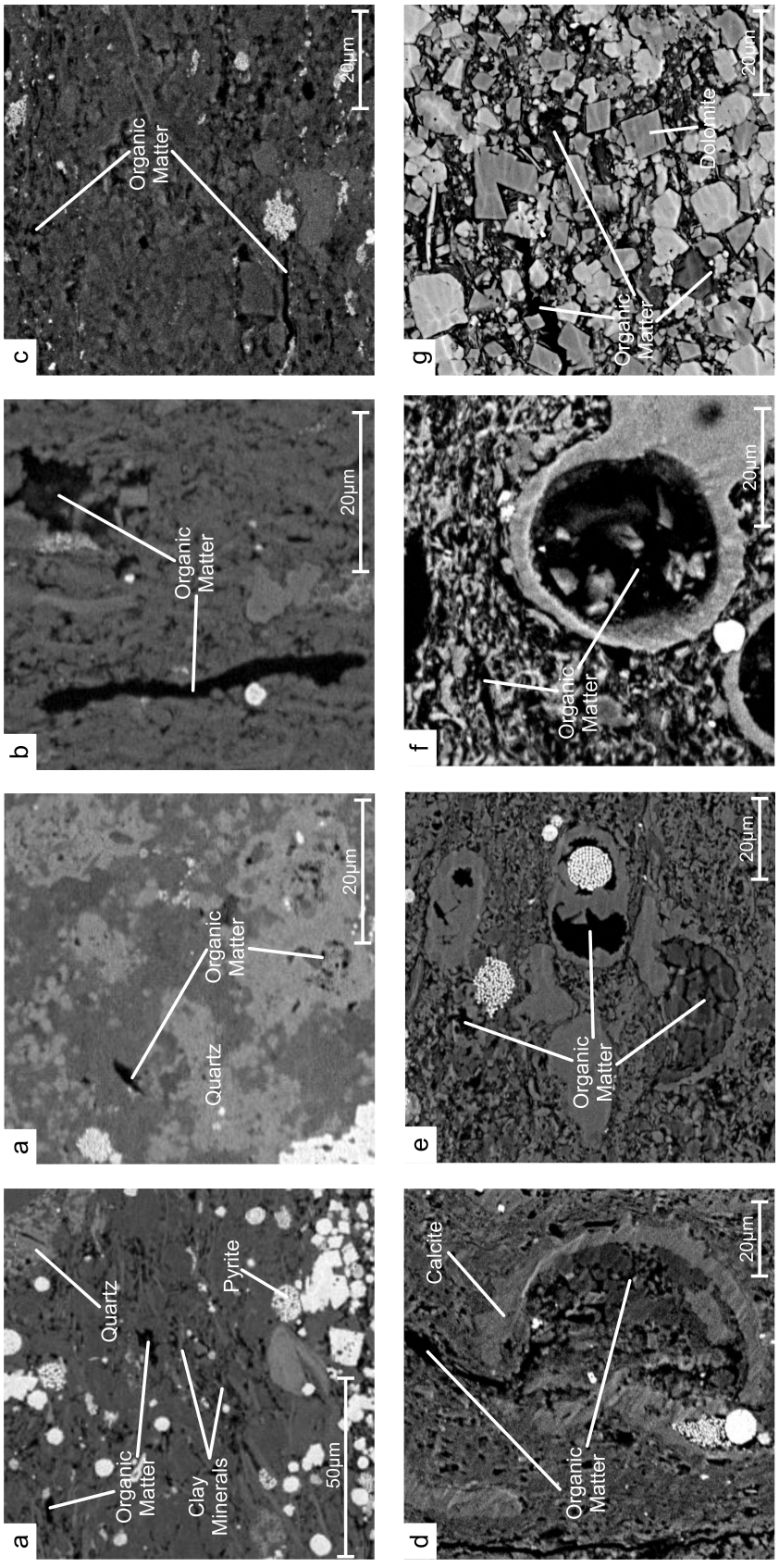

Figure 2.8: Scanning Electron Microscopy images of the shales studied. a.) are two scans showing the different morphology of organic matter in the Barnett Shale Lake Davis sample, b.) is indicative of organic matter in the Barnett Shale TP Sims well, c.) shows the lenses of organic matter in the Bowland Shale, d & e.) indicate the organic matter mainly associated with fecal pellets in the Eagle Ford Carol and Cinco Saus respectively and f.) shows the large amounts of organic matter both within the matrix and associated with fecal pellets in the Tarfaya. g.) indicates the different appearance of the Green River shale, with the organic matter as a component of the matrix, the clasts are dominated by calcite, quartz, and dolomite. Quartz, clay, pyrite, organic matter, calcite and dolomite are indicated at their first occurrence.

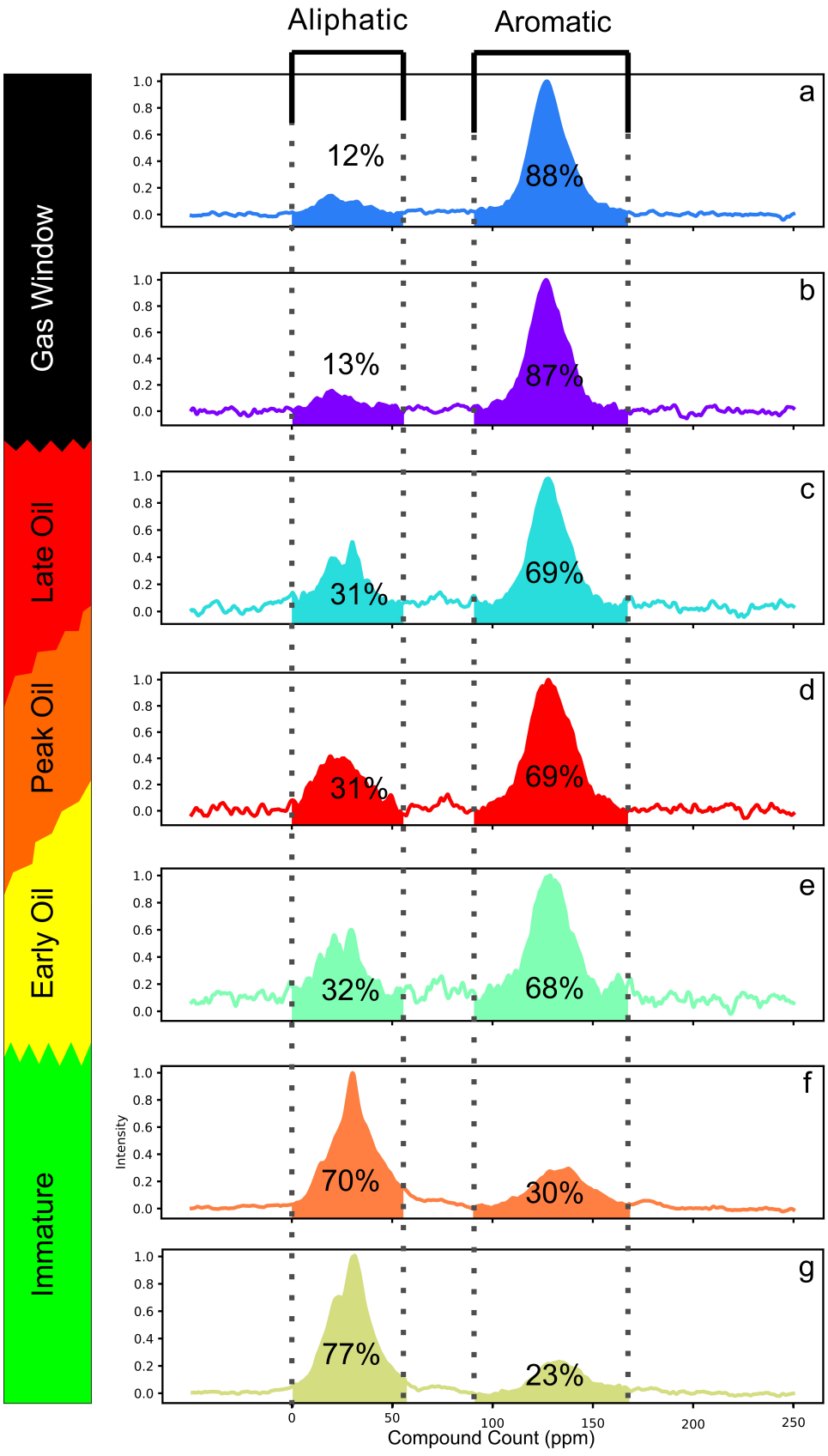

Figure 2.9: ^{13}C Solid State NMR results. Sample plots are shown maturity order, a. Bowland Shale, b. Barnett TP Sims, c. Eagle Ford Carol, d. Barnett Lake Davis, e. Eagle Ford Cinco Saus, f. Tarfaya and g. Green River. Aliphatic kerogen is the dominant phase in immature samples. In shales in the oil window the proportion of aromatic kerogen dominates, whilst still retaining a significant portion of aliphatic kerogen ($\sim$ 30%). The kerogen of the most mature shales (Barnett TP Sims and Bowland) is dominated by aromatic bonds with <15% aliphatic compounds.

Author	Shale	Reported Organic Matter Young's Modulus	Maturity	Technique
Kumar et al. (2012)	Woodford	7-9GPa 7.6±1.3GPa 6.2GPa	0.5-0.9%VRo 1.61%VRo 471°C Tmax	Nanoindentation
Shukla et al. (2013)	Woodford (low porosity) Woodford (high porosity) Kimmeridge Wolfcamp	8.7GPa 2GPa 5.6GPa 8.5GPa 7.3GPa 6.1GPa	0.54%VRo 0.37-0.53%VRo 421°C Tmax 455°C Tmax 451°C Tmax	Nanoindentation
Zeszotarski et al. (2004)	Woodford	10.5-11.1GPa	421°C Tmax	Nanoindentation
Wilkinson et al. (2015)	Bakken	10GPa	N/A	Nano-DMA
Zargari et al. (2016)	Bakken	15-20GPa 7-10GPa 7-12	Immature Peak Oil Window Gas Window	Nano-DMA
Goodarzi et al. (2016)	Posidonia	5.9GPa 10.35GPa	0.53%VRo 0.89%VRo	AFM PeakForce QNM
Eliyahu et al. (2015)	Upper Jurassic Source Rock	0-25GPa	2.1%VRo	AFM PeakForce QNM
Emmanuel et al. (2016)	Cretaceous Source Rock	3.2-7.8GPa 7.7-29.2GPa (kerogen) 6.2-10.1GPa (bitumen) 9.3-29.9GPa (kerogen) 5.4-17.1GPa (bitumen)	0.4%VRo 0.82%VRo 1.25%VRo	AFM PeakForce QNM
Emmanuel et al. (2017)	Cretaceous Source Rock	1.4-14.4GPa*	0.8/1.25%VRo	AFM PeakForce QNM
Li et al. (2018a)	Bakken	1.32-22.34GPa	428 – 450°C Tmax	AFM PeakForce QNM
Khatibi et al. (2018)	Bakken	2.5GPa 16.0GPa	0.38%VRo 0.94%VRo	AFM PeakForce QNM
This Study	Barnett Bowland Eagle Ford Tarfaya Green River	0.1-23GPa 0.1-24GPa 0.1-20GPa 0.1-14GPa 0.1-20.0GPa	445 – 453°C Tmax 464°C Tmax 443.5 – 457°C Tmax 408°C Tmax 430°CTmax	Bruker Biofilm (AFM QI^{TM})

Table 2.4: Organic matter Young's moduli reported in the literature, with respective thermal maturities where available. The range in Young's moduli using nanoindenation is approximately 20GPa, with AFM providing a range of 30GPa. Results from this study are in accordance with other studies using AFM, with some subtle heterogeneity. The mature Barnett shale and Bowland shale have the largest ranges of Young's modulus values, with the smallest range observed for the Tarfaya shale. Analysis of these results indicate that at the scale of nanoindentation, increasing maturity decreases the kerogen Young's modulus, whereas increasing maturity generally increases the AFM measured Young's modulus.

Random areas of each shale sample were scanned using the AFM QI^{TM}and the overall reduced Young's modulus results are displayed in Figure 2.10 with examples of an AFM scan from each sample displayed in Figure 2.11. The conversion of E' to E from equation 2.2 has been used on a scan from the Barnett Shale Lake Davis and Eagle Ford Carol samples (Figure 2.12), with a change in Poisson's raio (ν) resulting in a maximum difference in modal Young's modulus values of approximately 4GPa. Previous authors have used a set value of Poisson's ratio to convert from reduced modulus (Eliyahu et al., 2015; Li et al., 2018a), but it is likely that Poisson's ratio will vary in a similar manner to Young's modulus between shales, between organic particles and within organic particles. Therefore further work must be undertaken to better constrain the Poisson's ratio of organic matter and because of this we have chosen to report our distributions in terms of reduced Young's modulus (E'). Poisson's ratio estimates of organic matter from coal indicate that a likely Poisson's ratio range from 0.20-0.48 (Gentzis

et al., 2007), which includes a range of maturities and geological strength indices, suggesting that a similar range would occur in the range of shale organic matter tested here.

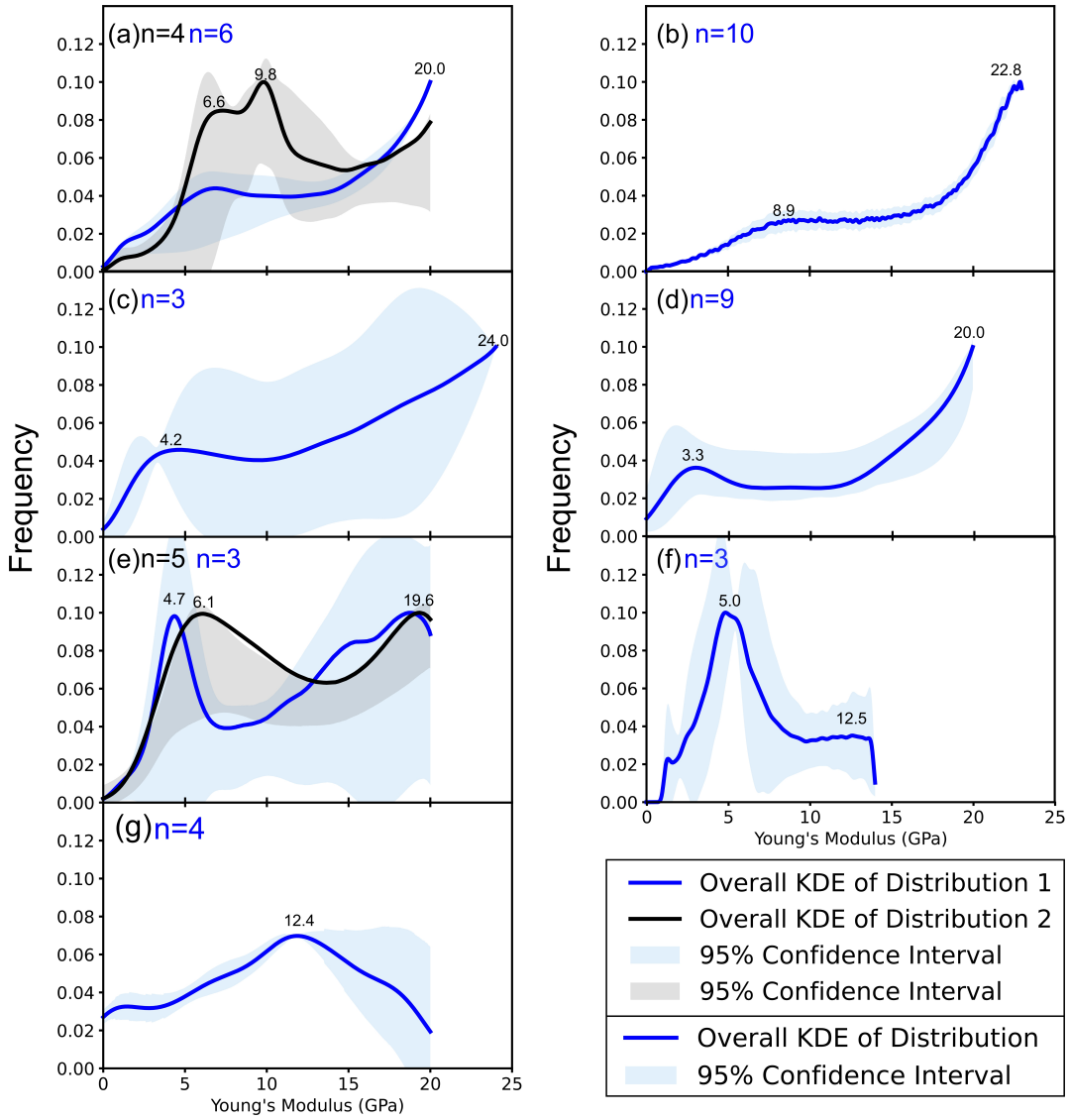

Figure 2.10: Kernel Density Estimate distributions for each shale. a.) corresponds to the Barnett Shale Lake Davis sample, b.) the Barnett Shale TP Sims sample, c.) the Bowland Shale sample, d.) The Eagle Ford Carol sample, e.) the Eagle Ford Cinco Saus sample, f.) the Tarfaya Shale sample and g.) the Green River Shale sample. The blue and grey shading represent the 95% confidence interval for each shale, the number in blue or black refer to the amount of AFM scans used to create the distribution once filtered. There appears to be two distributions for the Barnett Lake Davis and Eagle Ford Cinco Saus shales, which are at peak and early oil window maturities respectively.

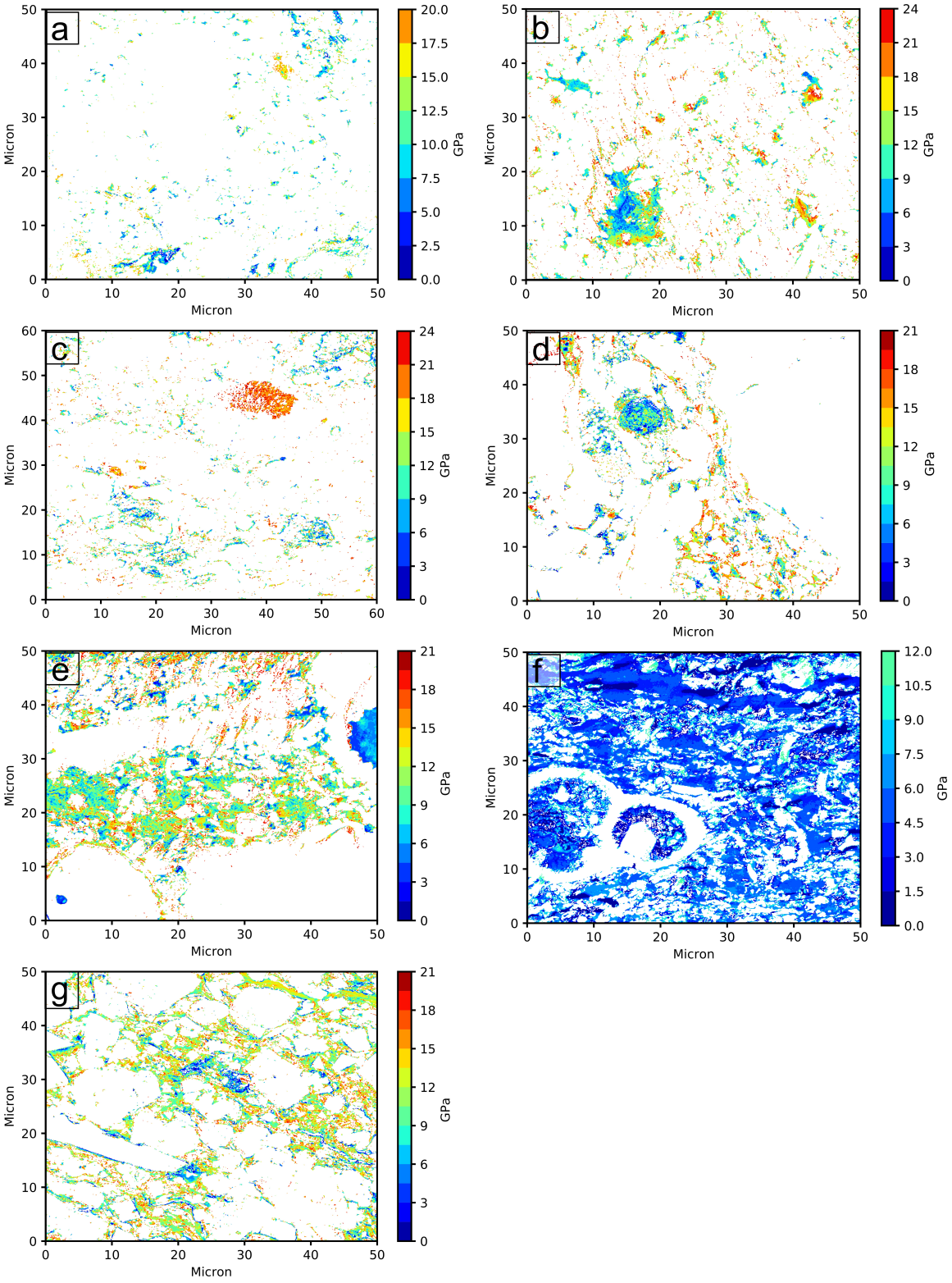

Figure 2.11: Examples of an AFM QI^{TM}scan per shale. a.) corresponds to the Barnett Shale Lake Davis sample, b.) the Barnett Shale TP Sims sample, c.) the Bowland Shale sample, d.) The Eagle Ford Carol sample, e.) the Eagle Ford Cinco Saus, f.) the Tarfaya Shale sample and g.) the Green River Shale sample.

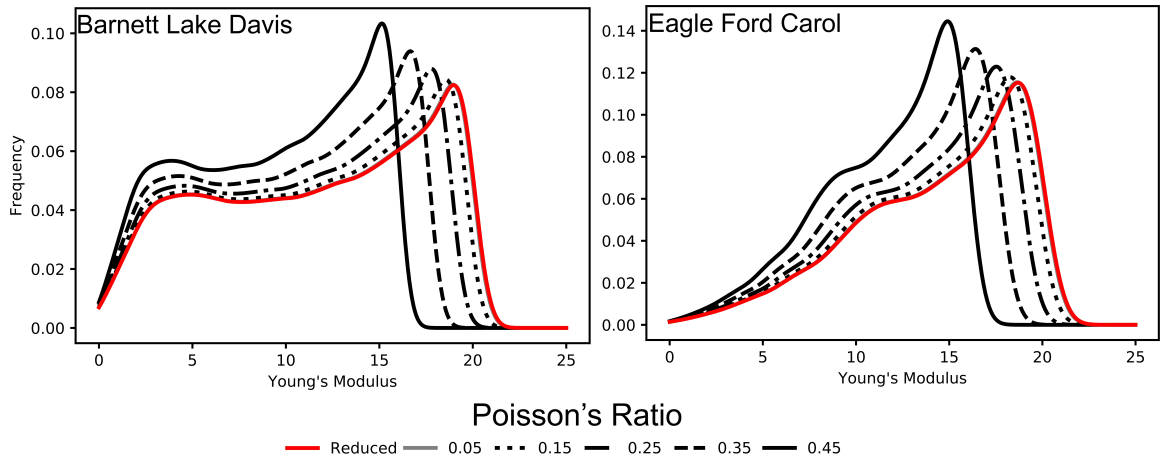

Figure 2.12: Young's modulus values for an individual scan of Barnett Lake Davis and Eagle Ford Carol calculated using different values for Poisson's ratio. A variation of Poisson's ratio from almost incompressible to almost infinitely compressible. This yields a variation of approximately 4GPa in the modal value of Young's modulus.

The modulus distributions in Figure 2.10 show the average across each shale sample and 95% confidence interval. Even though a minimum of 10 AFM scans have been undertaken on each shale not all scans were suitable for use after filtering, owing to topographic issues or large amounts of adhesion. Thus the number of scans are included in Figure 2.10 at the top of each distribution. As can be seen, the Bowland and Tarfaya were most affected by adhesion and topography, with the Bowland showing significant adhesion believed to be from clay mineral interactions. The Tarfaya samples also showed moderate adhesion within areas dominated by organic matter, along with a polishing issue mentioned previously.

The reduced Young's modulus range of the Barnett shale was between 0.1 and 23GPa. The Lake Davis scans (Figure 2.10a) exhibit two different probability distributions; Distribution 1.) bimodal with peaks at 6.0 and 20.0GPa, but with the stiffer distribution dominant, Distribution 2.) bimodal with the initial distribution showing a sub peak at 6.6GPa but a major peak at 9.8GPa and a second distribution with a modal value of 20.0GPa. This distribution has a high proportion of values within the less stiff (9.8GPa mode) peak. The Barnett TP Sims sample also exhibits a bimodal distribution, but with a significantly lower proportion of values less than 10GPa, centred on a modal value of 8.9GPa.The modulus peak in the stiffest phase is at 22.8GPa. The TP Sims organic matter also has a greater maximum stiffness and appears to be

more uniformly distributed than the organics in the Lake Davis, with a small 95% confidence interval (Figure 2.10b).

The Bowland shale Young's modulus distribution ranges from the cutoff minimum (0.1GPa) to 24GPa, and comprises two main peaks, with a small proportion of organic matter data situated around a modal value of 4.6GPa, and another more significant peak at 24.0GPa (Figure 2.10c). The Bowland appears less bimodal than the Barnett, with a less well defined initial peak than exhibited in the TP Sims distribution.

Scans of the Carol well of the Eagle Ford shale indicate organic matter Young's modulus values from 0.1GPa to 20GPa (Figure 2.10d). The Carol, similar to the Bowland and Barnett TP Sims displays a bimodal distribution in the main dominated by a stiff peak with a modal value of 20.0GPa and a lesser peak at 3.3GPa. This value is below the lower modal value in the Bowland and TP Sims. The most significant peak in the Carol well organic matter is centred on a modal value of 20.0GPa contributing approximately 42% of the overall data. The Cinco Saus well of the Eagle Ford has a different distribution to the Carol and the other aforementioned distributions with an equant bimodal distribution (Figure 2.10d), with a similar number of values within soft and stiff sub-distributions; 43.7% of data >10GPa, 56.3% of data<10GPa . This is represented in Figure 2.10e as the two distributions and accompanying 95% confidence intervals. The modal values for the softer distribution are between 4.7 and 6.1GPa (Figure 2.10e) and modal values of the stiff distribution are between 18.6 and 19.6GPa.

The Tarfaya shale has a distribution dominated by a peak centred around a modal value of 4.6-6.0GPa (Figure 2.10f), which was different from the other distributions observed. This probably corresponds to the stiffness of the organics within both the shale matrix and the fecal pellets, suggesting that these two phases of organic matter are geomechanically similar. There is a second small peak centred around 12.7GPa, which may be the start of a bimodal distribution, although only represents 17.74% of the data.

The Green River shale has a broad unimodal distribution (Figure 2.10g), which is unilike any of the other scans which all show some evidence of bimodality. The Green River also has a modal modulus value of 12.4GPa, which dissects the common bimodal peaks at around 5-8GPa and 19-24GPa. The peak of the Green River is at a similar modulus to the second

sub-peak of the Tarfaya distribution. It is notable that the modal modulus frequency value is low (approximately 0.07) and similar to those exhibited by the Barnett Lake Davis and Eagle Ford Cinco Saus, which have both have multiple distributions. This is combined with the unimodal distributions indicates that the modulus distribution of the Green River is relatively heterogeneous.

2.4.3 Deconvolution

The deconvolution results indicate that the two phase system cannot be described perfectly as a combination of two Normal or two Gamma distributions (Figure 2.13). However, the Normal distribution deconvolution leads to lower RMSE than the Gamma (Figure 2.14, Table 2.5), and appears to fit the data better. Both the Normal and Gamma distributions identify two definitive peaks; a first peak with a modal value of between 5-13GPa and a second with a modal value of between 16-22GPa in the deconvolution constrained by non-overlapping means (Figure 2.13).

Analysis of the phases in Table 2.5 demonstrate that the Gamma distribution has a lower modal value than the equivalent Normal distribution for each of the fractions, which is most likely due to the different shape of these distributions. The difference in modal value for the Gamma and Normal distributions are greater in the softer phase (mean difference = 2.47GPa) than the stiffer phase (mean difference = 0.79GPa).

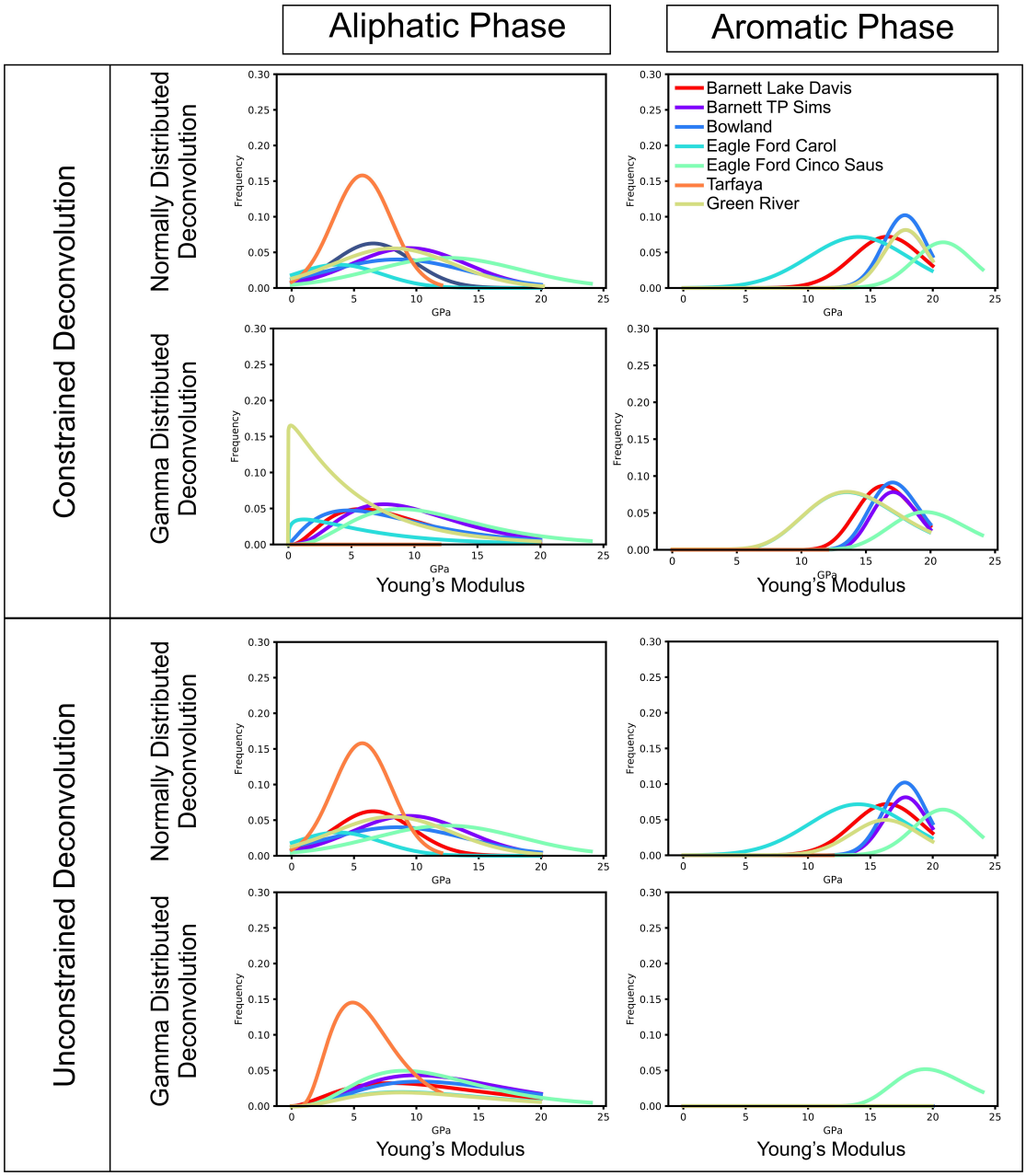

Figure 2.13: The resulting phase distributions of a two phase deconvolution on each shale distribution both with Constraint B in place (Constrained) and Constraint B relaxed (Unconstrained). The distribution of the phases in constrained and unconstrained deconvolution is identical using Normal distributions. There is a large disparity of fit between the constrained and unconstrained Gamma distributions. The Gamma distribution appears to poorly fit the Tarfaya shale in all cases, whilst the Normal distribution only fits poorly for the stiffer phase indicating that this may not be present in the Tarfaya.

Shale	Constrained Normal Error	Constrained Gamma Error	Unconstrained Normal Error	Unconstrained Gamma Error
Barnett Lake Davis	0.012	0.016	0.012	0.052
Barnett TP Sims	0.014	0.021	0.014	0.021
Bowland	0.012	0.018	0.012	0.019
Eagle Ford Cinco Saus	0.015	0.015	0.015	0.048
Eagle Ford Carol	0.017	0.022	0.017	0.079
Tarfaya	0.022	0.289	0.022	0.013
Green River	0.021	0.013	0.021	0.048
Tarfaya Single Phase	0.030	0.024		
Shale	Constrained Normal Phase Means (GPa)	Constrained Gamma Phase Modes (GPa)	Unconstrained Normal Phase Means (GPa)	Unconstrained Gamma Phase Modes(GPa)
Barnett Lake Davis	9.41, 17.83	7.57, 16.38	9.41, 17.83	10.02, 20.04
Barnett TP Sims	12.77, 21.08	10.37, 20.49	12.77, 21.08	10.32, 20.39
Bowland	12.48, 20.83	8.87, 19.59	12.48, 20.83	9.02, 19.44
Eagle Ford Cinco Saus	6.54, 16.37	5.76, 16.38	6.54, 16.37	8.02, 20.04
Eagle Ford Carol	8.48, 17.76	4.76, 17.08	8.48, 17.76	10.72, 20.04
Tarfaya	5.66, 20.00[1]	N/A[2]	5.66, 20.00[1]	4.91, 20.04[2]
Green River	10.58, 19.07	1.04, 10.91	10.58, 19.07	3.38, 20.00[1]

Table 2.5: Root-Mean-Squared-Error for each distribution fit for each Shale. The mean value for the normal distributions are shown along with the modal values for the Gamma distributions on each shale. [1]This is an unrealistic second phase in the Tarfaya due to being stiffer than the maximum stiffness in moduls, the curve itself as observed in Figure 2.13 has a frequency of <0.001. [2]There is no modal value in the Tarfaya due to the non fit of the data. The Tarfaya single phase indicates the error associated with fitting a single Normal and Gamma distribution to the curve.

The mean RMSE associated with the use of the Gamma distribution on the constrained data is greater than the RMSE associated with the Normal distribution (Table 2.5). This average trends towards a similar value when the Tarfaya shale is removed (Normal RMSE=0.014, Gamma RMSE=0.018). Neither of the deconvolution methods successfully fit the Tarfaya shale to the same accuracy as the other shales, however the fit is significantly less accurate using a Gamma distribution leaving an RMSE of ~ 0.29 (Figure 2.14, Table 2.5); this appears as a flat line with a frequency of zero in Figure 2.13. Minimization using one phase deconvolution leads to errors in Gamma fit of the same order of magnitude of the other errors. The Gamma distirbution fit of the Green River shale is also poor, generating a large peak with a modal value of approximately 1GPa in the Constrained fit, which causes an increased error on the fit of this shale. The error associated with each other shale is relatively similar with no obvious other outliers.

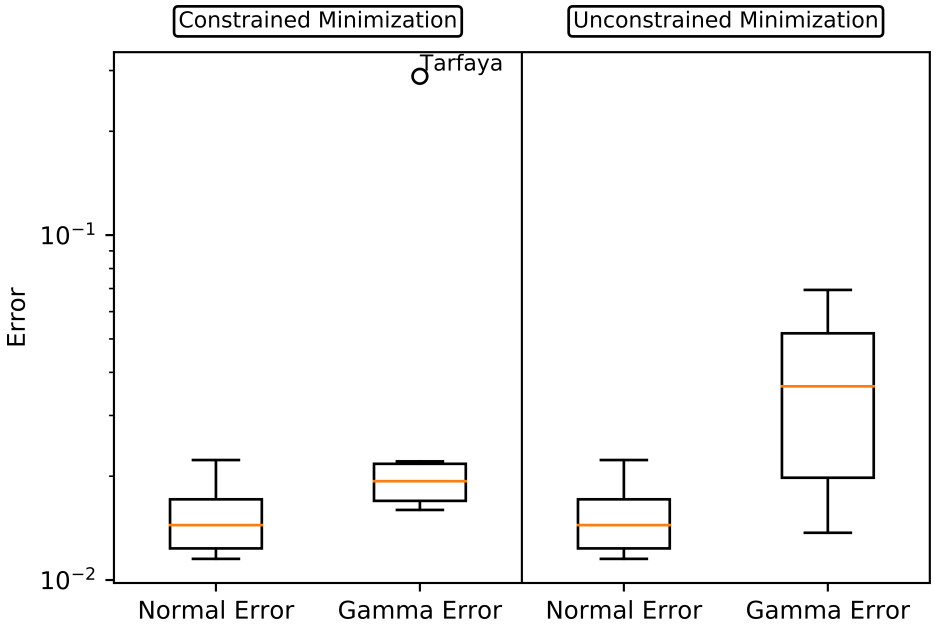

Figure 2.14: The root-mean-squared error associated with the deconvolution of each shale using Normal and Gamma distributions into two phases, both constrained using Constraint B in equation 2.6 (Constrained) and without this constraint (Unconstrained).

Deconvolution has also been undertaken relaxing Constraint B (Equation 2.6), which indicates an identical result when deconvolving into two Normal distributions (Figure 2.14, Table 2.5). The error associated with unconstrained means on a Gamma based deconvolution yields a poorer average RMSE but does allow a better fitting of the Tarfaya and Green River shales with a smaller error. The unconstrained Gamma fitting also results in many values not deviating from the initial estimate of 20.0GPa, which may be due to the model finding a local minima.

2.5 Discussion

The organic matter Young's moduli values found within this study have two defining characteristics: a range of 0.1 to 24GPa, fitting within the limits of the RTESP-525 tip, and for most shales a degree of bi-modality. A similar range of Young's moduli has been reported by various studies using AFM (Eliyahu et al., 2015; Emmanuel et al., 2016; Goodarzi et al., 2017; Li et al., 2018a) using single observations of individual samples, wells or formations. We find that this trend of bimodality and Young's moduli <30GPa is ubiquitous amongst shales from different formations and maturities, and reflects the distribution of organic matter in the shale matrix.

The lowest absolute values of organic matter modulus reported here are less than that observed by the aforementioned other literature, which may be due to this study measuring matrix organic matter, which may have more associated porespace than larger isolated organic clumps, or it could be due to a minimum cut-off in other studies due to the AFM.

The total organic carbon levels in these samples is relatively high, which is a necessity in order to gain a representative amount of Young's modulus measurements in each sample, given the area which can be scanned is approximately $1000\mu m^2$. However, in some cap rocks the overall volume of organic matter may be <5%. In spite of this, the distribution of that organic matter is most likely to be in the form of organic rich layers, such as marine bands, or in organic rich intervals. As such, whilst the TOC of the overall caprock may be low, some bands may have significantly elevated organic contents. Within any caprock the organic matter is proven to be the lowest Young's modulus phase. These organic rich layers may act as a natural plane of weakness, which may help propagate fractures and reduce the material strength of the shale (Ambrose, 2014; Cardott et al., 2015). Understanding the reason behind the internal heterogenity within these layers is paramount for modelling any fracture propagation which would occur at core scale (Ambrose, 2014).

The strength of a shale sample is likely to be limited by these organic rich layers, which may help to inform upscaling models of CCUS seals, where sequence stratigraphy can be well established. It is likely that marine bands, and the associated highstand periods are likely to comprise layers of weakness within the strata. These may be modelled from the insight gained using techniques such as AFM to describe the well known organic geochemical changes in terms of geomechanical properties.

2.5.1 Depositional Environment

Analysis of organic matter Young's modulus according to depositional environment is relatively difficult in these samples, and would be in many other shales, as the main organic component is amorphous organic matter. The most terrestrially influenced shale (Bowland) within this study comprises ∼95% AOM, with all other shales composed of at least 98% AOM. The scanned regions of each shale in this study contained only AOM and thus it is difficult to ascertain

the depositional environments from AFM scans alone. Vitrinite and inertinite macerals within these shales had a long axis range of approximately 10-55μm, which would comprise an entire AFM scan if found. Thus it may not be prudent to select visible macerals to undertake AFM measurements due to the capacity to misrepresent the organic population as a whole.

However, AOM can be sub characterized based on its organic precursor (Tyson, 2012). The AOM within Barnett, Bowland, Eagle Ford and Tarfaya has been mostly derived from a planktonic algal marine precursor, which appears to be relatively uniform in its modulus pattern, with a bimodal distribution centered around peaks of 4-9GPa and 14-20GPa. The variance in distribution appear to be more heavily influenced by thermal maturity, with the Barnett Shale data from the Lake Davis and TP Sims wells comprising a similar palynolofacies but with a difference in the proportion of modulus values within each peak determined by the difference between peak oil and late oil/ early gas window maturiy (Figure 2.15). This implies that although the depositional environment may be important, amongst AOM it is adequate to use Rock Eval pyrolysis measurements to describe organic matter Young's modulus, rather than more time intensive analytical techniques such as palynofacies analysis.

Although geochemically the AOM within each of the shales may be similar, there are subtle differences in Young's modulus distribution. When deconvolving the modulus data it appears that the softer phase, has a lower Young's modulus (between 5.5GPa and 8.5GPa) in the marly, calcite-rich shales of the Tarfaya and Eagle Ford, than the equivalent peak (between 9.4GPa and 12.8GPa) in the more siliceous Barnett and Bowland shales. This may be reflection of the different appearances of organic matter within these two different facies, as fecally derived organic matter appears less stiff than whispy organic lamellae. This could be due to the carbonate coating and early cementation of the fecal remains, reducing the amount of compaction related stiffening in the organic matter.

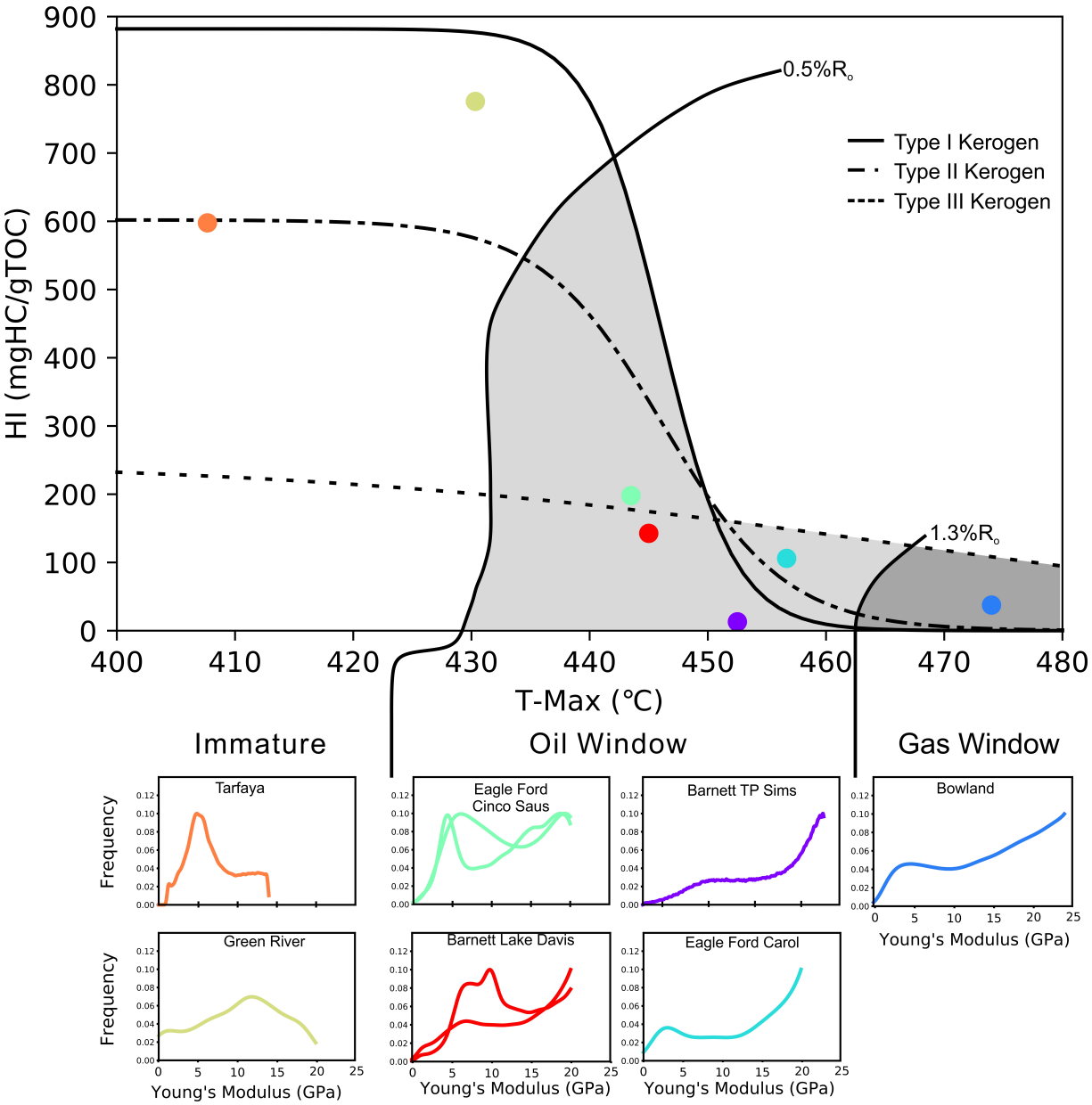

Figure 2.15: An adaptation of the T-Max/HI plot from Peters (1986) indicating kerogen type and maturity. The distributions above are arranged in order of maturity, showing the evolution of Young's modulus distribution in a Type II kerogen from Tarfaya shale dominated by soft organic matter, to the Bowland dominated by a stiffer component.

2.5.2 Maturity

The evolution of organic matter Young's modulus with maturity has been previously identified by AFM on individual shales (Emmanuel et al., 2016; Khatibi et al., 2018). This evolution is exhibited in an increase in the maximum and modal values of Young's modulus (Emmanuel

et al., 2016). The data presented here suggests that this is ubiquitous across Type II marine kerogen rich shales. The lowest modal value and maximum value of Young's modulus within this study is found within the Tarfaya shale, which is thermally immature. The modal values and maxima in Young's modulus increase through the oil window and are at their highest within the gas window, exhibited by the distributions of the Barnett TP Sims and Bowland samples, which have a maxima of approximately 23GPa and 24GPa, respectively. These maximum values appear to reflect similar values to those found by Khatibi et al. (2018), but are lower than those in Emmanuel et al. (2016). The transition from a soft dominant to a stiff dominant distribution occurs within the early/peak oil window, demonstrated within the scans of the Eagle Ford Cinco Saus and Barnett Lake Davis samples, which have an equant distribution and a Tmax in the early oil window (Figure 2.15).

Although the maximum value of organic matter Young's modulus increases with maturation, the increase is rather modest, reflecting an increase of only 4GPa from early oil to peak gas window. The distribution of modulus values appears to represent the change through maturity more clearly, becoming increasingly dominated by a peak with a modal value of between 19-24GPa with maturity, after the early oil window (Figure 2.15).

Whereas previous interpretations suggests that this bimodal distribution and evolution is simply due to kerogen and bitumen (Emmanuel et al., 2016), this may be too simplistic a description of the observations presented. Two other factors must be taken into consideration; organic porosity created by the migration of bitumen from the system as petroleum, and the overall chemical change to the organic phase (bitumen and kerogen).

Nanoindentation studies on shales with maturity suggest that there is a reduction in 'effective' Young's modulus with increased maturity (Shukla et al., 2013; Zargari et al., 2016) caused by the development of organic intraparticle pores from bitumen generation and migration. The 'effective' Young's modulus is the modulus of the organic matter and the associated porespace which cannot be separated at the resolution of a nanoindent. If the development of porosity was the only influence on the organic matter reduced Young's modulus distribution, it would be expected that the proportion of higher modulus values and overall modulus values would decrease with maturity. This is not exhibited either within this study or in AFM literature (Emmanuel

et al., 2016, 2017; Khatibi et al., 2018). This important observation indicates that one should be cautious when comparing AFM and nanoindentation derived mechanical measurements. It is most likely that the created pores within the organic matter are resolvable by the AFM, (>10nm in diameter), but not by the nanoindentor tip (<1μm in diameter). The AFM therefore allows insight into how the load-bearing organic matter changes in modulus once pores are created, demonstrating a Young's modulus increase that counteracts any decrease in effective Young's modulus due to porespace generation with maturity. Although this concept has been proposed by Suwannasri et al. (2019) using data driven modelling, this is the first instance of observations of the general increase in solid organic matter Young's modulus with maturity.

Porosity development is dependent on maceral composition (Mastalerz et al., 2013; Cardott et al., 2015; Ko et al., 2018), which has been identified in samples of Woodford, Eagle Ford and Barnett shale. Organic matter porespace increases with maturity, but is initially infilled with liquid or gaseous bitumen during the oil window (Ko et al., 2016, 2018). Research on the pores within the Eagle Ford and Barnett by Ko et al. (2016, 2018) indicate that these pores should be resolvable by the AFM, as the majority of pores are >10μm in size (Ko et al., 2016).

Further research into the evolution of organic porosity with maturity indicates that the overall porosity increases within marine shales from immature to the gas window(Loucks and Reed, 2014; guo; Song et al., 2020). Research by guo indicates that the micro-porosity and meso-porosity both increase during this period, however, the volume increases in microporisty is less than the equivalent volume increase of mesopores during maturation(guo). These micropores are unlikely to resolved by the AFM tip, and thus could contribute towards the bimodal distribution observed. There is indicated to be a short period at the start of the oil window, whereby the micropore volume decreases with the infilling of bitumen (Wang and Guo, 2019).

Under surface pressures and temperatures, any bitumen in the Eagle Ford Cinco Saus sample may have solidified, but most likely exists as a liquid. It is therefore unclear as to whether the bitumen may be included within the Young's modulus distributions presented here. If it were a liquid, the modulus would be below the 0.1GPa cut-off used to process these results.

With organic porosity unlikely to be the cause of the increasing bimodality in AFM results, chemical transformations of the organic matter are likely to be the cause in the observed

trends. The results of the solid-state NMR undertaken on the kerogens indicate that there is a sharp increase in aromatic structures with maturity (Figure 2.9), this trend towards an ordered graphite-like composition away from an organic melange could be the driver for the increase in modal modulus. Statistical tests however between the two distributions in the form of student T-Tests and Kolmogorov-Smirnov tests indicate little correlation. This is perhaps not unsurprising as the Young's modulus plots do not readily deconvolve into two separate phases using the technique applied in Section 2.3.7, which inhibits the use of statistical tests dependent on normal distributions. Secondly the NMR spectra do not readily distinguish between bitumen and kerogen, which further complicates this interpretation, given the changes in bitumen composition during maturation (Liu et al., 2018). Though the relatively low abundance of bitumen in immature shales (1-2% of overall organic matter in Tarfaya Rock Eval results) and large proportion of Young's modulus values within the lower modulus phase indicate that attributing this peak to bitumen alone is incorrect.

It appears that the Young's modulus distributions and evolutions observed within Type II kerogen are heavily dependent on the kerogen composition at the sample interval. The increases in aromatic kerogen observed by NMR (Figure 2.9), coincide with the increase in the proportion of higher modulus phase (Figure 2.10). Raman spectroscopy by Khatibi et al. (2018) on the Bakken shale indicates there may be a correlation between the increase in aromatic hydrocarbons and Young's modulus values, which is further substantiated by the results of the NMR to Young's modulus comparison here.

Hydrocarbon chain length must also play a key role in the Young's modulus distribution, with lower chain length compounds likely to have a lower Young's modulus, whereby it may be that short chain aromatic compounds may overlap with long chain aliphatic compounds. During the early stages of the oil window most of the C-N and C-S bonds and some of the C-O or bonds are broken and the resulting hydrocarbon side chains are lost (Tissot and Welte, 1978). This causes the kerogen to become significantly less enriched in aliphatic components by the mid oil window (Figure 2.9), with a large variability in chain length. Retained bitumen and hydrocarbons generated in the oil window have been shown to exist as a complex mix of aromatic and aliphatic compounds with variable chain lengths (Cornford et al., 1983). This

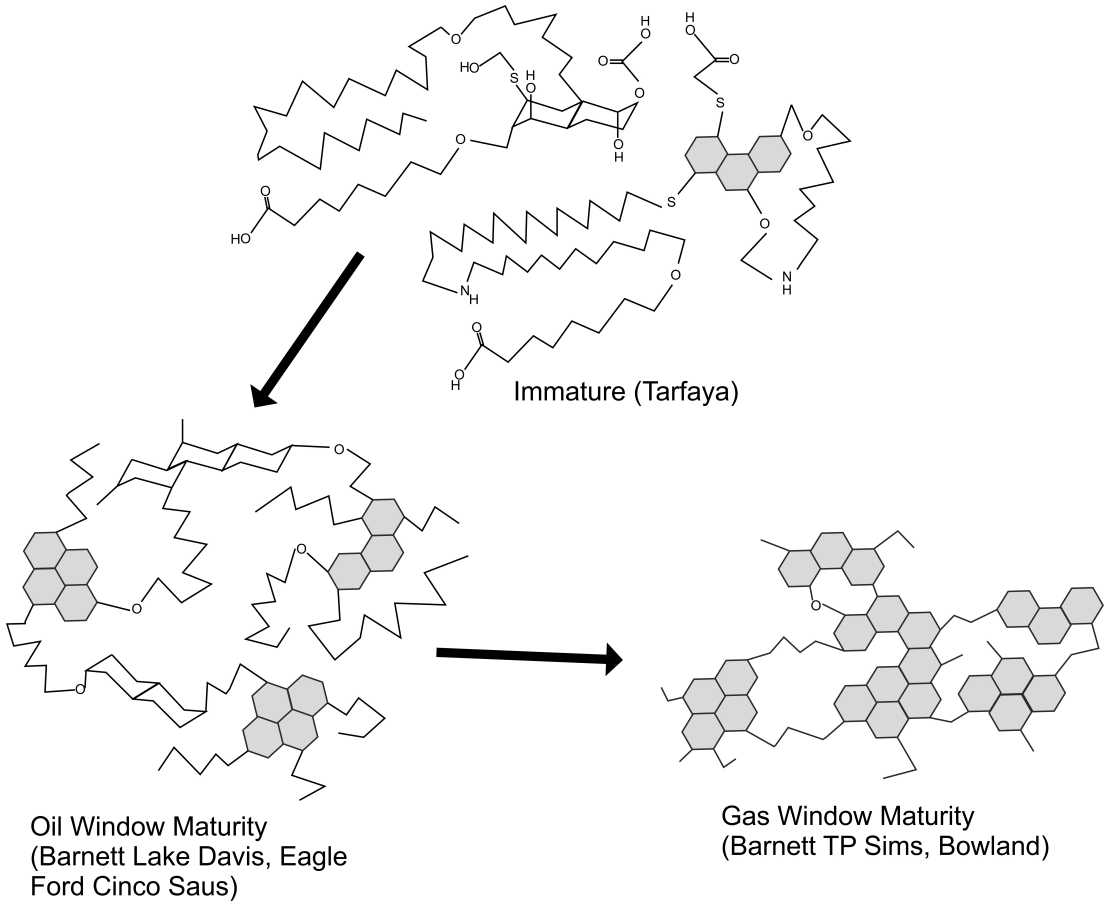

Figure 2.16: A Representation of the composition of kerogen at immature ($\sim$0.5%R_o), oil window mature ($\sim$0.8%R_o) and gas window maturity ($\sim$1.3%R_o) after the models of Behar and Vandenbroucke (1987); Vandenbroucke and Largeau (2007). The length of aliphatic chains, number of NSO compounds and general heterogenity decrease with increasing thermal maturty, until all that remains are aromatic rings with short aliphatic side chains. These compositions are similar to those within the Tarfaya (immature), Barnett Lake Davis & Eagle Ford Cinco Saus (oil window) and Barnett TP Sims & Bowland (gas window).

complex mixture of bitumen and kerogen may manifest as the equal bimodal distributions in the Barnett Lake Davis and Eagle Ford Cinco Saus (Figure 2.9), which appears as a kerogen composition similar to Figure 2.16b. This most likely has an adsorbed bituminous phase which may significantly alter the strength of the aromatic kerogen and cause the complex Young's modulus distributions in 2.10. It is difficult to comment on the exact nature of the bitumen within each shale, due to the changes in bitumen composition with maturity; the likelihood is that the bitumen will decrease in aliphatic carbon with maturity (Craddock et al., 2015), becoming more aromatic, though probably to a lesser extent than the load bearing kerogen at the equivalent maturity.

Deconvolution of the peaks into two phases supports this kerogen distribution, in which the model identified two peaks, but was unable to fit a normal distribution to each of them. This is caused by overlap between the two phases which make up the peaks, and in the softer phase a large standard deviation. The inability to determine two separate phases could be due in part to the complex melange of organic compounds and polymeric material within the kerogen and bitumen. Whilst the kerogen becomes enriched in aromatic components with maturity, these are most likely connected to aliphatic structures with side chains and branches. This would form a complex distribution with little homogeneity but two peaks representing broadly aliphatic and aromatic rich compounds, which we see in Figure 2.9. This deconvolution technique has been used successfully on many other minerals and composites (Constantinides and Ulm, 2007; Vandamme and Ulm, 2009), but mainly with defined stoichiometry, which is not present in the organic matter.

Although, we believe that the two phases here are mechanically interlinked, relaxing Constraint B (Equation 2.6) does not improve the fit in either the Normal or Gamma distributions. This suggests that the two phases are intrinsically mechanically different. The inability to deconvolve the Tarfaya may suggest that in an immature shale, the organic matter is too mixed to deconvolve and requires the breaking of hydrocarbon chains to clearly separate out aliphatic and aromatic carbon. The NMR results suggest that the Tarfaya has very little aromatic carbon, which may be either be the small sub-peak in the 12-14GPa range or be lost within the large soft aliphatic peak.

During the gas window the majority of long chain aliphatic components have either been lost or are cracked to short chain gas hydrocarbon compounds ($<C_5$) during catagenesis (Tissot and Welte, 1978). This leads to a more ordered, aromatic rich structure (Figure 2.16.C), exhibited by the aromatic dominance in the NMR results (87% in Barnett TP Sims and 88% in Bowland) in Figure 2.9. Any bitumen present at this maturity would most likely exist as highly volatile condensate, unlikely to contribute significantly to organic matter Young's modulus, or as pyrobitumen. Whilst we cannot rule out the contribution of pyrobitumen (generated as a residue from the in-situ cracking of bitumen to less dense components) to the organic matter Young's modulus distribution of the samples in question, no pyrobituminous organic matter was identi-

fied or scanned during this study. It is most likely that although pyrobitumen is characterised geochemically with bitumen, due to their common provenance as products of during thermal cracking, geomechanically pyrobitumen is most akin to kerogen, due to the polymeric nature of its composition.

Whilst the vitrinite reflectance and T-max values presented in Table 2.2 indicate the maximum maturity reached by these samples, some of the shales have been uplifted. Whilst uplift bears no impact on the chemical composition of organic matter, as chemical transformations are irreversible within organic matter, it is unclear as to what impacts uplift has on the physical properties of organic matter. Little research has been undertaken on the effects of uplift and overpressure on organic matter geomechanics, or the physical appearance of organic matter. It is likely that due to the irreversible nature of the chemical changes, that physical changes would be limited. Clay minerals transform with burial and uplift, which causes physical transformations (Boles and Franks, 1979; Curtis, 1985; Pytte and Reynolds, 1989; Bjørlykke and Aagaard, 1992), however, this is only possible due to nature of the chemical transformations. Future research may seek to gain an understanding if the physical transformations of organic matter at different burial depths, possibly by utilising coal as a proxy, or undertaking triaxial tests on samples utilising different confining pressures. This however, would be difficult due to the sporadic nature of organic matter within most black shales, it therefore would be prudent to use a sample from a location such as the Mahogany Zone of the Green River Shale, where TOC values are >25%. Future research in this area could also comprise utilising shale samples from similar plays/fields which have undergone different burial histories, most likely due to their proximity to a thrust belt. Samples of Barnett Shale proximal to the Oachita Thrust Belt, and samples from further to the west could be tested for differences in the distribution of organic matter Young's modulus.

These findings provide further complexity to modelling of hydraulic fracture tip and homogenization (Goodarzi et al., 2016), as models can be adapted for a dependence on both depositional environment and maturity. By correlating organic geochemical properties with geomechanical properties for the first time, we suggest the modelling of previously expensive to measure mechanical properties through an adaptation of relatively inexpensive techniques such as Rock-Eval pyrolysis. This linkage between geochemistry and geomechanics could be readily improved by

undertaking geochemical measurements and AFM scans on cuttings obtained from wellbores of both carbon capture and storage seals and unconventional reservoirs.

The research presented here in combination with the thermodynamics of hydrocarbon generation may offer valuable insight into the initial migration of hydrocarbons from the organic matter host. The amount of pore pressure created during maturation is fundamentally linked to the mechano-chemistry of the organic matter, whereby the internal generation of significant amounts of hydrocarbons may cause a pore-pressure unsustainable by the host organic matter. The extent to which the organic matter within a shale can accommodate increases in stresses, is determined by the mechanical properties and are influenced heavily by Young's modulus. The results here indicate that by the onset of generation of significant quantities of hydrocarbons (early-peak oil window), a bimodal distribution of Young's modulus is already established (Eagle Ford Cinco Saus and Barnett Lake Davis). Therefore further investigation may be necessary to determine which of the two distributions plays the major role in the formations of microfractures, enhancing primary migration of hydrocarbons out of the organic phase. Using the trends in the data within this study, this problem may be approached in a stochastic manner.

2.5.3 Kerogen Type I vs Kerogen Type II

Comparative analysis between two kerogen types proves relatively difficult with only one sample of Type I kerogen (Green River shale) and one sample of kerogen Type II (Tarfaya shale) from a similar maturity level. However, there does appear a clear difference in the modulus distributions of the organic components of these two shales. The Green River shale has a considerably lower amount of organic matter, which occupies a portion of the matrix in this clast dominated mudstone (Figure 2.8g). The Tarfaya is petrologically different, where the organic matter is distributed through the matrix, with relatively small amounts of clay as observed in Figure 2.8f. This difference in organic matter is more subtle in the bulk geochemistry data, whereby the hydrogen index of the Green River is higher than that of the Tarfaya, probably representing increased algal/bacterial input. A higher hydrogen index is indicative of increasing amounts of aliphatic carbon, which is actually not observed in the NMR results, where the Green River and Tarfaya have similar levels of aliphatic compounds (77% and 70% respectively; Figure 2.9). This

subtle difference in geochemistry and morphology is represented in a large difference in Young's modulus distribution, with the Green River having a unimodal distribution, in comparison to the bimodal distribution observed in all of the Type II kerogen shales (Figure 2.10). The modal modulus value of the Green River is also much higher than that in the Tarfaya (Figure 2.10), and similar to the softer peak in the oil window mature Type II kerogen shales (Barnett Lake Davis and Eagle Ford Cinco Saus).

The reasons for this difference in modulus are not immediately apparent, with both shales comprising mainly amorphous, highly labile organic matter, although the Tarfaya is notably enriched in sulphurised organic matter in comparison to the Green River (Kolonic et al., 2002, 2005). The chemical composition of the oils produced from Green River Shale Mahogany Zone are dominated by linear alkanes with a bimodal distribution with peaks at/ around $C_9 - C_{10}$ and $C_{25} - C_{27}$, indicative of a mixed algal and higher plant sources, as the $C_9 - C_{10}$ are believed to be the pyrolisate of longer chains (Ingram et al., 1983). A study by Horsfield et al. (1994) on whole rock and kerogen isolate samples to have a peak in the region of C_{10} and also C_{17}, indicative of algal organic matter. The kerogen pyrolisate composition of the Tarfaya shale at the interval studied is reported to be very different and dominated by alkylthiophenes, alkenylthiophenes and alkybenzothiophenes, with a smaller concentration of n-alkanes/alkenes (Kolonic et al., 2002). This is mostly due to the euxinic conditions at time of deposition, which, although shared by the depositional environment of the Green River Shale during periods of deposition of the whole unit, at the time of deposition of the interval studied here, the environment is likely too hypersaline to support large scale euxinic organic deposition (Mason and Surdam, 1992), evident by the abundant dolomite in the SEM images from Figure 2.8.

These geochemical differences most likely play the major role in the difference in organic matter Young's modulus. An interesting point is that although geochemically, the organic matter in the Green River is bimodal due to two different sources (algal and terrestrial), the modulus is not, suggesting that long and short chain aliphatic components may resolve to a similar modulus, and may contribute to the large unimodal peak in the Green River. It appears that the sulphurization of the organic matter in the Tarfaya may be the cause of the lower modulus and narrower modulus peak, although further work entailing a detailed organic

geochemical study would confirm this.

2.5.4 Water Content

It is notable that the Young's modulus values in this study were recorded on samples of shale not fully water saturated, and with unknown water contents. The water content of a shale affects its mechanical properties, reducing strength and stiffness considerably (Hebblewhite and Lu, 2004; Josh et al., 2012; Lai et al., 2016). However, organic rich intervals of shale have generally a lower water content than other shale layers (Josh et al., 2012), and the samples analysed in this study are all relatively organic rich with TOC values all in excess of 3.5%.

The amount of porewater sorption onto the organic matter within these shales in the reservoir is unknown. The volume of porewater has been demonstrated to increase during the oil window and then decrease in the condensate and gas window (Cheng et al., 2019) indicating that porewater volumes will vary across the samples collected.

The amount of porewater adsorbed onto the organic matter in most of these shales is considered to be low, as porewater generally adsorbs onto the clay minerals within a shale, hence the lower water content of the organic rich layers. Water doesn't readily adsorb onto mature organic matter due to the unreactive nature of the oxygen functional groups in mature organic matter (Gensterblum et al., 2010, 2013; Merkel et al., 2015). Therefore, the AFM derived Young's moduli are likely similar to those at reservoir water saturations, on the more mature shales (Eagle Ford, Barnett and Bowland). However, there may be effects of water adsorption on the Tarfaya and Green River organic matter. It is difficult to quantify these affects as the water saturation is dependent on the reservoir conditions, but also the organic composition of the shale, and the proportion of active hydroxyl or carboxylic groups within the organic matter. This study has collected no data on the absolute chemical composition of the organic matter in these samples as such, it is difficult to suggest the likely magnitude of any potential reduction in organic matter moduli, from porewater saturation. Further research could focus on assessing the Young's modulus of organic matter in a sample at full water saturation, and then in a dry sample to demonstrate the likely difference between these two end members. Huaqing et al. (2018) found that hydration does little to affect the morphology or position of pores within the

organic matter, so the influence of water content on organic matter Young's moduli may be low.

2.6 Conclusions

Shale geomechanical properties are a key factor in the economic viability of an unconventional shale gas play and play a major role in determining the column height of CO_2 that can be housed in a conventional reservoir. As such, knowledge of these properties is important. Much is known about the mechanical properties of common minerals present in shale. However, the organic matter which acts as the host for the hydrocarbons in place, and a diffusive path for the CO_2 is less well understood.

Analysis of the Young's modulus of organic matter in four prolific black shales, with subtly different marine depositional environments and thermal histories, was undertaken on a nano-scale using AFM QI^{TM}, a similar technique to the PeakForce QNM ^{TM}used in other studies (Eliyahu et al., 2015; Emmanuel et al., 2016, 2017; Li et al., 2018a). The results of this analysis indicate a bimodal distribution of organic matter Young's modulus in all of the shales studied, with a maximum value of 24GPa.

Differences in depositional environments between marine shales has relatively little impact on the organic matter Young's modulus. The Young's modulus of marine organic matter evolves with maturity, initially dominated by values <10GPa centred on a peak of ∼5-6GPa whilst immature, which is believed to represent the aliphatic-rich heterogenous mixture in immature kerogen. At the oil window, the distribution evolves to become equally distributed between a peak at 5-6GPa and a second, tighter distribution around 19-20GPa, believed to represent the more aromatic kerogen. With increasing maturity into the gas window, this peak around stiffer values increases in maximum stiffness up to 24GPa and contributes to 70-80% of the organic matter distribution, reflecting the dominance of aromatic structures within the organic matter in the gas window. This allows modelling of the Young's modulus in a Type II kerogen as a series of bimodal distributions that trend from a soft dominated to stiff dominated distribution with increasing maturity.

The Young's modulus distribution of organic matter in most samples cannot be explained

using normal Gaussian distributions and so future research should attempt to determine the Young's modulus distribution of these complex organic phases. Future studies should also investigate different types of organic matter, i.e. different assemblages of heterogenous and homogenous amorphous organic matter along with other major macerals and maceral types e.g. spores vitrinite and inertinite.

This modelling of other macerals, combined with future studies on the evolution of Type I kerogen with maturity, will assist in overall modelling of organic matter Young's modulus in both cap rocks and unconventional reservoirs by allowing further correlation between the trends well known as part of source rock geochemistry and trends that occur within source/cap rock geomechanics.

2.7 Contributions

The contributors to this chapter are as follows.

Name/ Institution	Contribution
Chris Vane (British Geological Survey)	Rock Eval Pyrolysis
Ian Chaplin (Durham University)	Thin section and polished block sample preparation
Matthew German (Newcastle University)	Atomic Force Microscopy assistance and advice
Cees Van Der Land (Newcastle University)	Academic support
Mohamed Rouainia (Newcastle University)	Academic support
Martin Jones (Newcastle University)	Academic support
Thomas Wagner (Heriot-Watt University)	Academic support

Table 2.6: List of contributors to this chapter

Chapter 3

Geomechanical Properties of Coal Macerals; Measurements Applicable to Modelling Swelling of Coal Seams During CO_2 Sequestration

Research from this chapter are published within the International Journal of Coal Geology and are available at https://doi.org/10.1016/j.coal.2020.103528

3.1 Introduction

As civilization moves forward toward a net-neutral carbon environment, further emphasis has been put on undertaking carbon capture and its underground storage. Advances have been made in re-purposing former conventional hydrocarbon reservoirs in the Norwegian Continental Shelf with the Sleipner storage facility (Bickle, 2009; Cavanagh and Ringrose, 2014), the Weyburn oilfield, Canada(Zaluski et al., 2016, and references therein) and Al Salah, Algeria (Ringrose et al., 2009; Mathieson et al., 2010), amongst others. Meanwhile recoveries from many current conventional and unconventional hydrocarbon reservoirs are being enhanced with CO_2 injection across the world. This technique has proven successful in the Permian Basin of North America,

helping to both extract residual oil and offset the carbon footprint of a major conventional oil play (West, 2014).

Such conventional oil and gas reservoirs make appropriate locations for storage of CO_2 underground due to preexisting knowledge of their geological conditions as well as reservoir production data obtained during the field's lifetime. Deep coal deposits represent another potential target for storage of supercritical liquid and gaseous CO_2. In the past two decades, CCUS has been undertaken within deep coal seams within the San Juan Basin, USA (Weber et al., 2012); in Alberta, Canada (Gentzis, 2000); and the Qinshui Basin (Wang et al., 2016) and Yaojie Coalfield (Li et al., 2013) in China.

Coal has a natural CO_2 storage capacity, with an intrinsic affinity for adsorbing CO_2 onto its porous surfaces, with pore volume as high as $50cm^3/g$ (Laxminarayana and Crosdale, 1999). Sorption of CO_2 into coal has been widely studied (Liu et al., 2010; Masoudian, 2016; Ranjith and Perera, 2012) with coal seams acting as naturally fractured reservoirs, combining both fracture porosity with the natural micro and meso porosity that exist within the coal matrix itself (Espinoza et al., 2015).

Whilst the effects of injecting supercritical CO_2 into conventional clastic reservoirs are relatively well understood, the intrinsic problems with swelling of coals can complicate matters greatly. During injection the pore pressure within coal seams increases, which may lead to increased permeability through increasing cleat aperture. However, coals are also known to swell under CO_2 injection (Levine, 1996; Robertson, 2005), which may cause the coal to swell into the cleats and thus reducing cleat and microfracture aperture, decreasing overall permeability (Pan and Connell, 2007; Pan et al., 2010).

When attempting to model the impact of injecting of CO_2 into coals, several mechanical properties are integral to our understanding of how this poro-elastic framework works. The most frequent mechanical properties required are Young's modulus, Poisson's ratio and Bulk modulus (Pan and Connell, 2007; Palmer et al., 1996; Shi and Durucan, 2004); all of which can be calculated through mechanical property testing (e.g. triaxial testing).

Triaxial measurements of coal Young's modulus and Poisson's ratio are widely variable and are influenced greatly by pore-pressure and the associated changes in effective stress (Gentzis

et al., 2007; Pan et al., 2010; Espinoza et al., 2015), whilst Alexeev et al. (2004) suggest that triaxial tests undertaken on steeply dipping coals should be conducted under a non-uniform stress state, to compensate for the inclined bedding direction. The water content of coal has been observed to affect triaxial and nanoindentation derived Young's modulus greatly (Alexeev et al., 2004; Zhang et al., 2018c), with coal strength decreasing with water content. Thus techniques that help elucidate the complex relationships that exist between coal mechanical properties, strain and permeability are worthy of investigation.

Triaxial testing whilst keeping either a constant pore water pressure or constant mean effective stress has been used to derive the stress/strain and pore water pressure/strength relationships, allowing for modelling of these relationships under different CO_2 injection pressures (Pan et al., 2010; Espinoza et al., 2015). Triaxial experimental results and modelling indicate a non-linear relationship between effective stress and strain/ shear strength. Poisson's ratios have been reported in the region of $0.22 - 0.48$ from triaxial testing and sonic velocities (Zheng et al., 1991; Gentzis et al., 2007; Ranathunga et al., 2016). Reported Young's modulus values of coal from triaxial experiments vary greatly, with values usually appearing to be within the region of as 50-90MPa reported (Viete and Ranjith, 2006) for coals with significant water content; however, Gentzis et al. (2007) report moduli as high as 5.07GPa in water saturated coals.

Vickers hardness testing is higher resolution than triaxial testing (mm^3 rather than cm^3) (see Figure 3.1), ignoring larger cleats and fractures, while the reduced Young's modulus (E') of individual macerals is an order of magnitude higher than the values obtained by most triaxial testing; Stach et al. (1982) reported a variation between $240 - 382$MPa on vitrinite. Other Vickers hardness testing on coals report an increase in hardness with coal rank and carbon content. Vickers microhardness tests account for both plastic and elastic behavior, and coals have a reported hardness of 20-100kp/mm^2 (Hower et al., 2008, and references within),whilst vitrinite hardness is reported to be between 24.5-36.6kp/mm^2 (Stach et al., 1982).

Higher resolution ($\sim$ 10s of microns^3) nanoindentation studies (Figure3.1) have been undertaken on coals, and report a variety of Young's moduli and hardness values, between 3.02GPa and 9.04GPa, with many authors reported modulus values of 4-7GPa (Yu et al., 2018; Borodich et al., 2015; Epshtein et al., 2015; Kossovich et al., 2016; Zhang et al., 2018c). This variation

in moduli accounts for a variation in vitrinite reflectance of 0.4%-1.52%R_o. The resolution of nanoindentation is in the order of $1 - 15\mu m^3$ and thus removes the effects of cleats and larger fractures, allowing increased accuracy in measurements of undamaged coal matrix effective modulus.

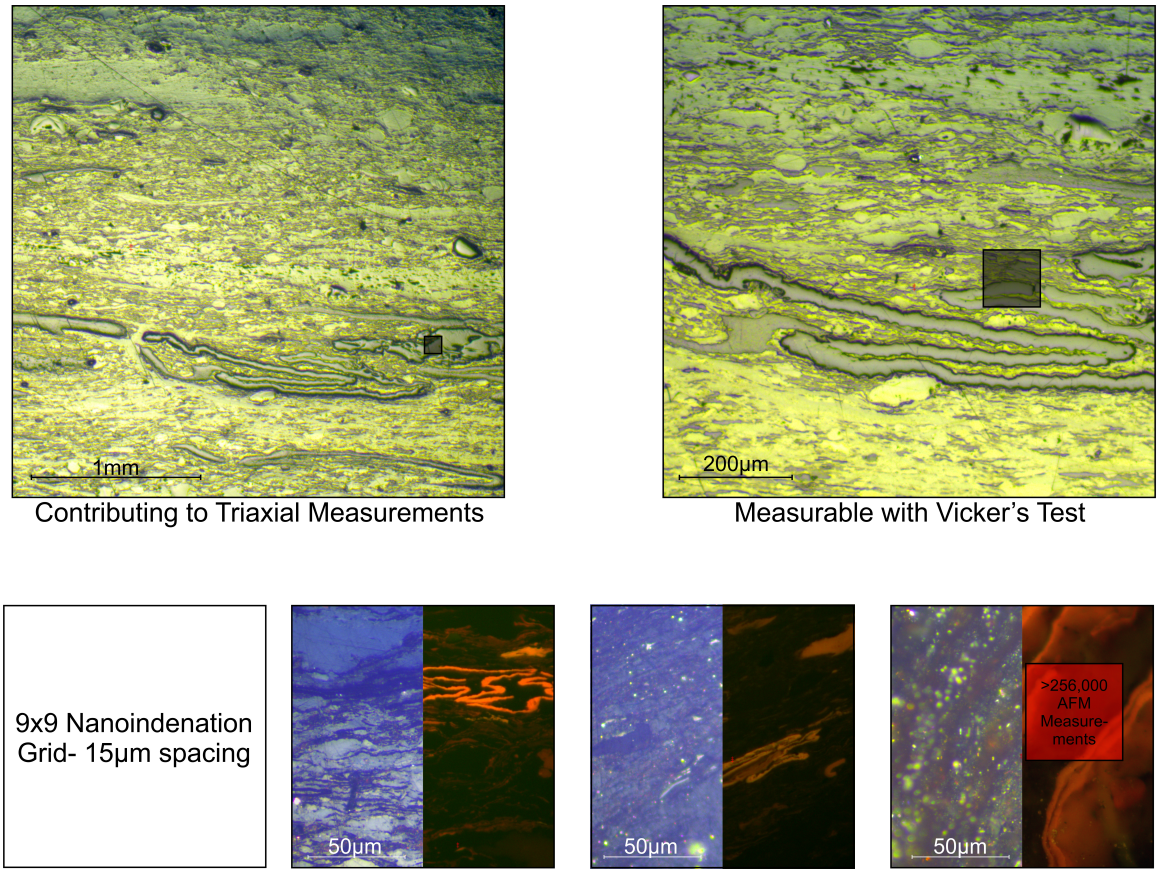

Figure 3.1: An indication of the scale in which coals can be analysed by triaxial, Vickers microhardness tests, nanoindentation and AFM. The black box is the area in which a 9x9 nanoindentation grid would be situated. The red box is the area of one AFM scan within this study, containing over 250,000 measurements.

Obtaining local elastic modulus of coal and coal macerals proved to be relatively difficult due to the size of some macerals and the distribution of nano and micro-porosity. However, technical advances in atomic force microscopy (AFM) in the last few years, now allow increased insight into these properties and enable thousands of high resolution measurements in a timely manner (Figure 3.1). One of the first studies using AFM to understand coal at higher resolutions was undertaken by Li et al. (2020) using a PeakForce^{TM}QNM^{TM}AFM. Those results

indicated a Young's modulus distribution with peaks at 8GPa, 11GPa and 14GPa, with a bi-modal distribution found in one sample, but normally distributed in others. The occurrence of a bimodal distribution was assumed to be due to mineral matter, with a softer pure organic peak and stiffer organic/mineral peak (Li et al., 2020). This represented the first acquisition of true non-effective, local Young's moduli of coal.

Mechanical properties-although not as readily important for the injection of CO_2 in conventional reservoirs, become important properties of the shales that cap most appropriate conventional CCUS reservoirs (Armitage et al., 2011). The mechanical properties of coals and shales are therefore a first order control on the feasibility of CO_2 injection and long term storage within most conventional and unconventional targets.

AFM has been used for the last five years to obtain Young's modulus results at the resolution required for coal maceral analysis on shale organic matter indicating a variation from <1GPa to $\sim$ 32GPa as well as identifying a bimodal distribution in organic matter, and a stiffening with maturity (Eliyahu et al., 2015; Emmanuel et al., 2016; Goodarzi et al., 2017; Li et al., 2018a; Khatibi et al., 2018). Here we undertake a similar approach to identify trends within selected macerals in varying rank coals and organic-matter rich shales.

3.1.1 Maceral Analysis

Coals and organic rich shales are compositionally made of mineral and organic phases. In coals the mineral phase is generally less than 50% of the sample by weight, while the organic phase in shales tends to be between 1 and 10% of the whole rock by weight (Stephen and Passey, 1993; Jarvie et al., 2004).

Organic matter in shales is commonly categorised by provenance (e.g. terrestrial/ marine/ lacustrine) or kerogen type derived from Rock Eval pyrolysis (Type I, Type II, Type III, Type IV), whereas in coals this classification differs in that it is based more heavily on the organic precursor (e.g. cutin, lignin). Whilst it is convenient to describe organic matter in shales in terms of provenance, shales can also be described in terms of precursor. It may offer insight into the relationships between depositional processes and their geomechanical response to define the organic matter in shales by the same classifications as those for coal, more specifically into the

three main maceral groups summarised in Stach et al. (1982).

Liptinite (formerly termed exinite) is derived from plant and algal remains rich in hydrogen. Vitrinite is sourced from hydrogen lean structural components of plant remains, whilst inertinite is oxidised or biochemically altered liptinite and vitrinite (O'Keefe et al., 2013). Each of these maceral groups can be further subdivided, however, only liptinite can be subdivided based on precursor material (Stach et al., 1982), whereas inertinite and vitrinite are mainly divided based on the preservation of cell structure and the extent of oxidation. In low rank coals, liptinite macerals are recognised by low relief and high fluorescence (Stach et al., 1982; Teichmüller, 1989).

Shales can contain macerals that are present in coal but the organic matter in them is usually dominated by amorphous organic matter (AOM), that can occur as layers or granular material admixed into the matrix. However, alginite can also be a key component in some of the most organic-rich shales (e.g. Green River Shale: Ingram et al. (1983)).

Coal macerals can be less than 100μm in size and because of this size limitation very little effort has been made to study how these individual components of a coal influence the overall mechanical properties (Borodich et al., 2015). It is important to establish whether these structured components are load supporting. Here we present some of the first work to classify coal and shale macerals mechanical properties. This provides insight into the interactions between macerals upon increased stress from CO_2 injection and the associated swelling.

3.2 Methods and Samples

3.2.1 Samples and Sample Preparation

Three coal samples and one shale sample were selected for this study due to being rich in a particular maceral. The paper coal is rich in cutinite, the cannel coal rich in both alginite and sporinite, the New Albany Shale is rich in alginite and the coal from the Northumberland Coal Field is rich in both vitrinite and inertinite.

The paper coal and cannel coal come from the eastern part of the Illinois Basin, and are Pennsylvanian in age. Both samples are associated with the Upper Block Coal Member in

Indiana and were likely deposited in deltaic-fluvial dominated environment (DiMichele et al., 1984).

The Northumberland coal was deposited in the Northumberland basin in the North East of England also during the Pennsylvanian. A sample of coal from the Top Plessey seam, which is part of the Pennine Middle Coal Measures (cf. Bullock et al., 2018) was collected in-situ from the exposed seam at the Shotton Surface Mine, Cramlington. Reported vitrinite reflectance measurements for this seam are between 1.3-1.6%R_o (Bullock et al., 2018), indicating that this coal is of a rank between medium-low volatile bituminous coal (Stach et al., 1982).

The New Albany Shale sample is Upper Devonian and comes from a core (543m depth) drilled in Daviess County, Indiana. The New Albany Shale contains Type II kerogen and ranges in maturity from immature to post-mature (Strapoc et al., 2010). The studied sample has R_o of $\sim 0.65\%$, thus representing thermal maturity corresponding to the early oil window (Mastalerz et al., 2016). New Albany shale has been selected for this study due to the high concentrations of alginite reported (Barrows and Cluff, 1984; Strapoc et al., 2010).

Samples from the paper and cannel coal were then crushed and mounted in epoxy resin before being polished using 0.5μm alumina powder as the final step (Taylor et al., 1998). The Northumberland Coal was cut perpendicular to bedding and mounted in epoxy resin and polished using the same technique. The sample of New Albany Shale was prepared as a kerogen isolate slide. The crushed shale sample was treated with hydrochloric acid and hydrofluoric acid to remove carbonate and silicates (cf. Rexer et al., 2014), then filtered through a 10μm sieve and strewn-mounted on microslides coated in resin.

3.2.2 Maceral analysis

Maceral identification was undertaken initially without immersion oil due to the possibility of remnant oil on the surface interfering with the AFM QI^{TM}analysis. A Leica DM2700 P^{TM}polarising microscope at 400× and 630× magnification was used to identify the macerals. Slides were also studied in blue light excitation following the standard recommendations for epifluorescence on coal polished blocks (Taylor et al., 1998). These images were initially used to identify areas of potential macerals for analysis on the AFM. The macerals selected within this

study were generally larger than $250\mu m^2$ in area due to the resolution of the microscope when used without immersion oil. Once scanned with the AFM, final images of each maceral were taken at 500× magnification under immersion oil for analysis of AFM scan location.

Vitrinite reflectance was measured on the samples of cannel, paper and Northumberland coal using the Leica DM2700 P at 500× magnification. This was undertaken using reflectance standards at 0.42, 0.69 and 0.91%R_o on 100 individual particles of vitrinite for each coal(Taylor et al., 1998). The mean values are reported in Table 3.1 removing any perceived outliers. Vitrinite reflectance measurements were conducted in accordance with the ASTM method presented in D2798-11a (2014).

Coal	Mean Vitrinite Reflectance (%)
Cannel Coal	0.38
Paper Coal	0.39
Northumberland Coal	1.56
New Albany Shale	0.65

Table 3.1: Mean measured vitrinite reflectance values for the coals studied based on 100 point counts.

As previously mentioned, the samples chosen for this study were selected due to the high abundance of a respective maceral for ease of identification with the limited microscopic capacity of the AFM. Thermally immature coals were chosen owing to the obvious difference between the vitrinite, inertinite and liptinite macerals. The cannel and paper coals presented here are too immature to target for ECBM. However, similarly mature samples are beyond the threshold of approximately 800m-1km deep required for CO_2 sequestration(Rubin and De Coninck, 2005), if at their maximum burial depth in a typical or cool geothermal gradient ($< 35°C/km$ (Middleton, 1982; Suggate, 1998).

3.2.3 Atomic Force Microscopy Quantitative Imaging

Atomic Force Microscopy Quantitative Image^{TM}(AFM QI^{TM}) was undertaken on a JPK Nano Wizard 3 in QI^{TM}mode (JPK-Instruments, 2011). RTESPA-525 silicon nitride tips were selected for this experimental set-up, with a reported working range of <1GPa- $\sim$ 25GPa (Pittenger et al., 2014), however, accurate measurements of up to 30GPa have been reported using the previous

generation of these tips by Emmanuel et al. (2016).

The mechanism of AFM QI^{TM}involves the oscillation of a tip onto the sample surface by a cantilever at a frequency below its resonance frequency. The force applied to the sample is set (in this case to 500nN), and the displacement is in the order of 1-3nm. This is measured by a current generated from the deflection of a laser beamed off the head of the tip onto a photo-diode. The radii of the tips used in this study are reported to range between 8-12nm, although 10nm was used as the average tip radius for processing of Young's modulus data.

One cycle of AFM QI^{TM}scanning is described in Figure 3.2, in which the tip is brought towards the sample from a point 150nm away, until a point (b) where adhesive Van Der Waals forces cause the tip to flex onto the sample surface. At a point of maximum adhesion (c) a force is imparted onto the sample surface by the tip. The deflection measured at the point (d) of maximum force (500nN). The extend curve of force vs deflection is used to calculate the reduced (Indentation) Young's modulus (E') based the Hertz Sneddon model Equation 3.1 (Sneddon, 1965):

$$F = \frac{4}{3}E'\sqrt{R\ (d-d_0)^3} \tag{3.1}$$

where R is tip radius, F is force applied and $d - d_0$ is the displacement.

Each measurement of load/displacement was made in 6ms. Further information on the QI ^{TM}is available in "QI^{TM}mode-quantitative imaging with the NanoWizard 3 AFM" (JPK-Instruments, 2011).

The AFM QI^{TM}was first calibrated in non-contact mode; a method suggested in the JPK documentation (JPK-Instruments, 2011). In this method the cantilever is flexed, whilst measuring the movement of the laser beam from the deflection of the tip, the movement of the tip is known from the spring constant of the cantilever, and this allows calibration of the photo-diode sensitivity. Further calibration is undertaken a by scanning a standard of Highly Ordered Pyrolysed Graphite, with a known modulus of 18GPa. The sensitivity and spring constant were then adjusted to give a reading within a standard deviation of 18GPa.

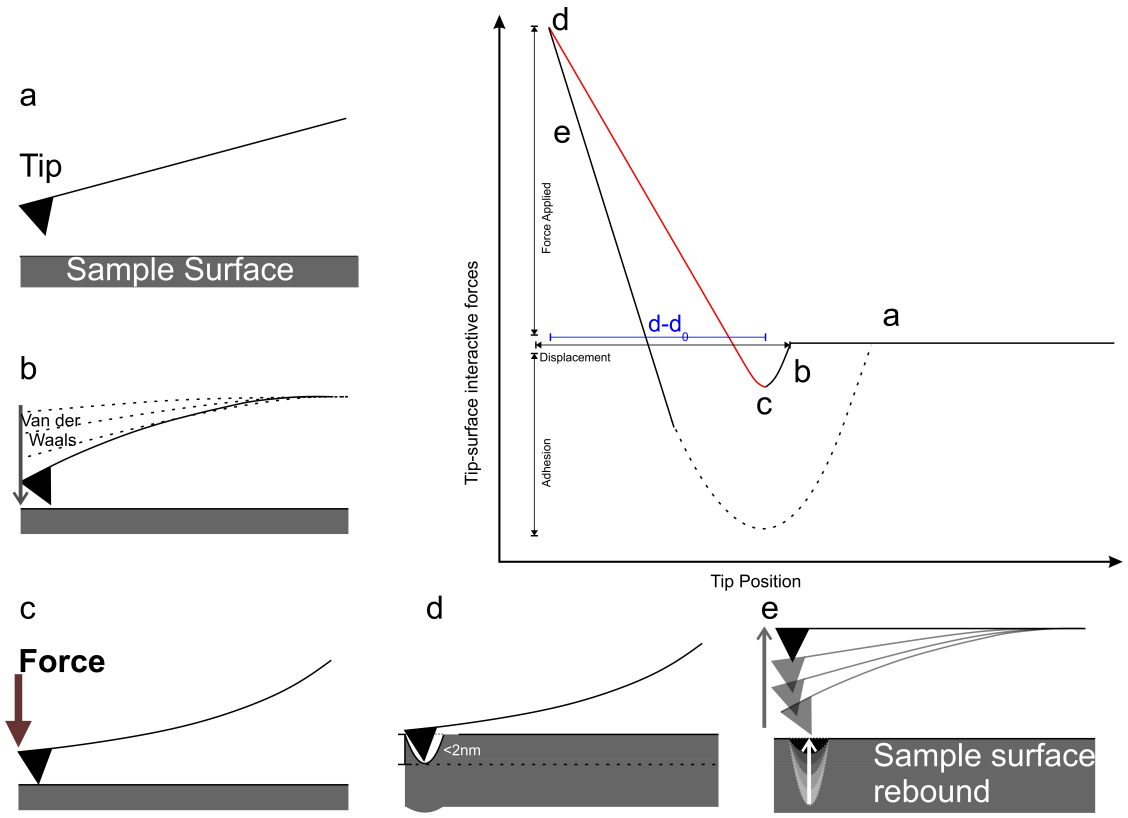

Figure 3.2: A graphical indication of the process of acquiring an AFM measurement. Initially the tip starts away from the sample surface (a), once the tip is brought towards the surface of the sample Van Der Waals forces adhere the tip to the surface (b), at the point of maximum adhesion (c) a force is exerted onto the sample surface, until at a point (d) the preset maximum force is exerted. At this point (d) the tip is allowed to leave the sample surface. The reduced Young's modulus is calculated along the extend curve (red) using the Hertz-Sneddon equation (Equation 3.1).

AFM QI^{TM}scans were generally 512 × 512 pixels on an area of 250μm^2. A minimum of four scans were undertaken per cutinite and sporinite maceral, which were generally on adjacent areas to give a representative overall distribution of each maceral, with two macerals (eight scans) scanned per coal sample. These macerals were located using microscope images obtained prior to the AFM. The AFM areas were oriented to reduce the likelihood of scanning other adjacent macerals during analysis. A total of twelve inertinite scans were obtained across the three coals- four scans per coal. Due to the larger particle size of the inertinite (>250μm^2), a minimum of two not necessarily adjacent scans were collected on each inertinite maceral, giving a total of six inertinite macerals analysed. For the same reason as inertinite, a minimum of two scans were obtained on the bituminite and cutinite within the Northumberland coal. Measuring

Poisson's ratio of coal macerals at this length scale proves challenging, and as such all Young's modulus values are reported in reduced modulus (E'), which is also the case for values obtained from nanoindentation where Poisson's ratio is unavailable.

3.2.4 Mercury Injection Porosimetry

Pore size distribution and total porosity analysis was undertaken on the samples of coal only using the mercury injection capillary pressure technique. It was not undertaken on the New Albany Shale sample due to the difference in porosity associated with bulk shale and isolated kerogen. The mercury injection analysis was conducted at Aberdeen University, using a Micrometrics Autopore IV 9500. Samples of $\sim 2.5\text{cm}^3$ in size from each coal were selected. The pore size distribution is acquired from the pressure required to overcome capillary entry pressure by the Washburn equation (Equation 3.2).

$$P_c = \frac{-2\gamma \cos\theta}{r} \tag{3.2}$$

Where P_c is the capillary entry pressure, γ is the surface tension of mercury (480 dyne/cm), θ is the contact angle between the wetting and non-wetting phases (142° for air and mercury) and r is the pore throat radius. Using the Washburn equation, curves of mercury injection pressure vs max pore radius were calculated. Mercury injection capillarity porosimetry has a working range of approximately 2.0-100.0nm.

3.2.5 Nanoindentation

Nanoindentation has been undertaken on all coal samples using a Berkovic triangular pyramid diamond indenter tip at Newcastle University. The principles of nanoindentation were first documented by Oliver and Pharr (1992), in which a stiff indenter is used to punch an indentation into the sample surface, and the elastic properties of the surface can be measured. The principal of nanoindentation is relatively simple with the elastic displacement is related to the load applied by two constants, one of which is related to the shape of the indenter and one to the property of the fit.

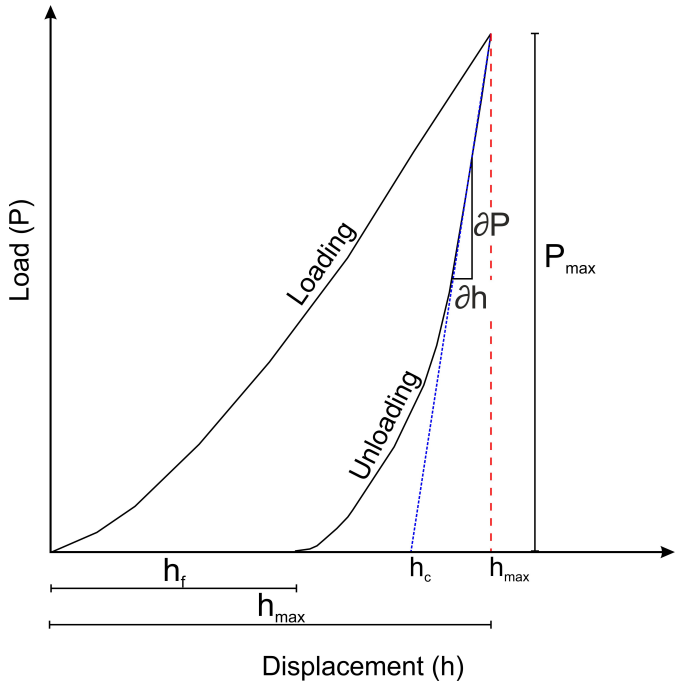

Figure 3.3: A grahpical representation of the load and unload curve of a single nanoindentation indicating the displacement and force applied, along with the measurements used to calculate the slope S.

When using nanoindentation in more practical terms this law fits as equation 3.3, where h_{max} is the maximum displacement and h_c is the residual non elastic displacement after indentation. m is a constant related to the shape of the indenter, which will have a value of between one and two, and α is a power law constant.

$$E' = \alpha(h_{max} - h_c)^m \tag{3.3}$$

Using equation 3.3 the initial unloading phase of the indentation can be fit to give the contact stiffness ($S = \frac{\partial P}{\partial h}$), Figure 3.3. This stiffness in turn allows measurement of the reduced Young's modulus (E') using equation 3.4

$$E' = \beta \frac{\sqrt{\pi}}{2} \frac{S}{\sqrt{A}} \tag{3.4}$$

Where A is the contact area of the indenter, β is a correction factor related to the tip geometry, and has as value of 1.034 for the Berkovic indentor used here (Kumar et al., 2012). In order to compare and corroborate with the AFM measurements made in this study, results are reported

in reduced Young's modulus.

The nanoindentation in this study was undertaken in grids of 20 x 20 measurements with a load of 5mN to enable a comparison between macerals and with the AFM data collected. The unload curve fit was accomplished using scipy.least_squares to enable an estimate of the slope and power law values (Virtanen et al., 2020). Probability density functions of the 400 points were generated to assist in comparisons between the macerals and allow a direct comparison with the AFM data collected.

3.3 Results and Discussion

3.3.1 Coal Petrography

Twelve individual macerals have been scanned using AFM QI^{TM}for this study from three different coals and one shale. These can be seperated into categories; immature sporinite, immature cutinite, immature alginite, mature cutinite, mature bituminite and inertinite.

The sporinite within the cannel coal (Figure 3.4c,d) is the finest grained of any of the macerals existing as fluorescing doubled over structures approximately 10-50μm along axis, which either exist in clumps or more occasionally as individual spores. The spores are in general relatively well-preserved. The inertinite within the cannel coal is large compared to the other macerals present (Figure 3.4i,j), appearing generally as laminated blocks up to 500μm along axis parallel bedding.

The macerals within the paper coal are generally larger than the those in the cannel coal. For example, the cutinite within the paper coal appear as 100-400μm long and approximately 10-20μm thick laminae which are readily distinguishable under blue light exitation (Figure 3.4a,b). Similar to the sporinite, these liptinite macerals show little evidence for oxidation. The inertinite within the paper coal appears as a relatively minor constituent and similar to the cannel coal, appears as large clasts; the matrix of the coal appears to be relatively inertinite lean.

In contrast, the Northumberland coal has a very different appearance to the other two studied coals: it is richer in vitrinite and inertinite, indicative of a more oxidising depositional environment. The bituminite in the Northumberland coal appears as millimeter long bands

oriented parallel to bedding and has a low fluorescence under incident blue light. The occasional sporinite macerals in the Northumberland coal are slightly oxidised and broken, with a low fluoresence. Cutinite macerals within this coal appear as the most fluorescent component but are much smaller than the equivalent in the Paper coal. The abundant inertinite within this coal appears as large bands similar to the other coals but also within the coal matrix (Figure 3.4f).

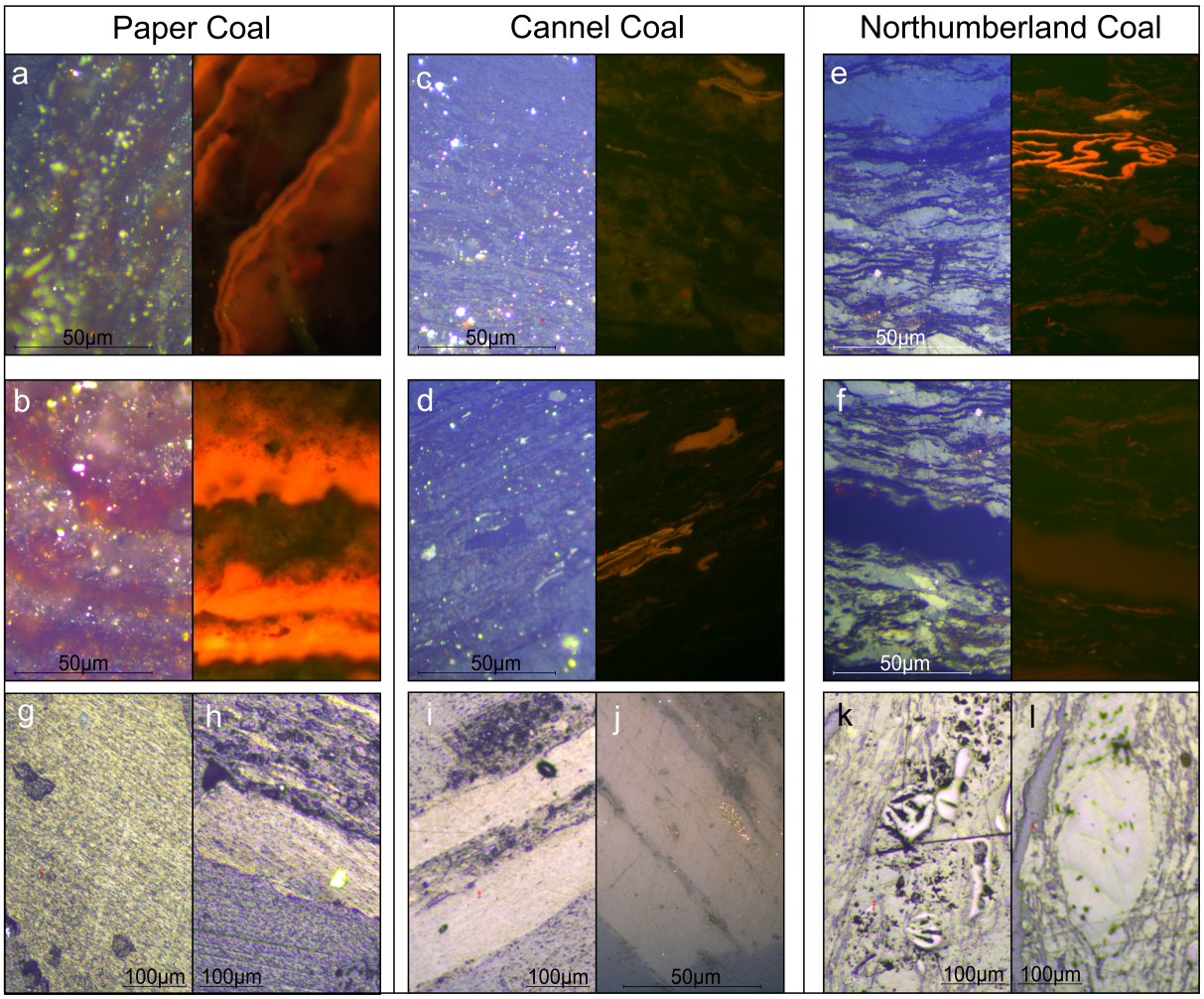

Figure 3.4: Photomicrograph of the Coal macerals studied. Photos show cutinite (a,b,e), sporinite (c,d), bituminite (f) and inertinite (g-l) studied. The left column are from the Paper coal, the middle column from the Cannel coal and right column from the Northumberland coal.

3.3.2 Vitrinite Reflectance

Vitrinite reflectance analysis of these coals confirms the difference in maturity identified by the difference in fluorescence of the liptinite macerals. The analysis showed that the cannel and paper coals are 0.38% and 0.39%R_o, respectively, with the Northumberland coal being more more mature at 1.56%R_o. Maturity analysis was not undertaken on the New Albany Shale sample, though results from other studies on samples from the same location indicate an approximate R_o of 0.65% (Mastalerz et al., 2016).

3.3.3 Young's Modulus of Coal Macerals

The kernel density estimates and the mean and modal values of Young's modulus for alginite, sporinite, cutinite, bituminite and inertinite from mature and immature coals are shown in Figure 3.5. The mean and modal Young's modulus values of the macerals studied are also given in Table 3.2. Due to the resolution of each measurement ($\sim$ 10nm), we believe that this reflects a true local modulus of an individual phase rather than the effective modulus obtained from nanoindentation. Macerals selected for analysis were larger than the scan areas on the AFM to reduce the likelihood of AFM scans containing more than one maceral.

Coal	Maceral	Mode (GPa)		Mean (GPa)
		AFM	5μm distribution	
Immature				
New Albany Shale	Alginite	2.91*	3.09*	6.19*
Paper Coal	Cutinite	2.97	9.76	9.27
Cannel and Paper Coals	Inertinite	3.21	3.81	3.72
Cannel Coal	Sporinite	1.35	2.85	3.19
Mature				
Northumberland Coal	Bituminite	6.27	6.79	7.11
	Inertinite	4.59	4.62	5.91
	Cutinite	6.99	7.81	8.43

Table 3.2: Modal an mean values of AFM QI^{TM}on each coal maceral. *Values for Alginite are affected by the interaction of the alginite/tip with the resin.

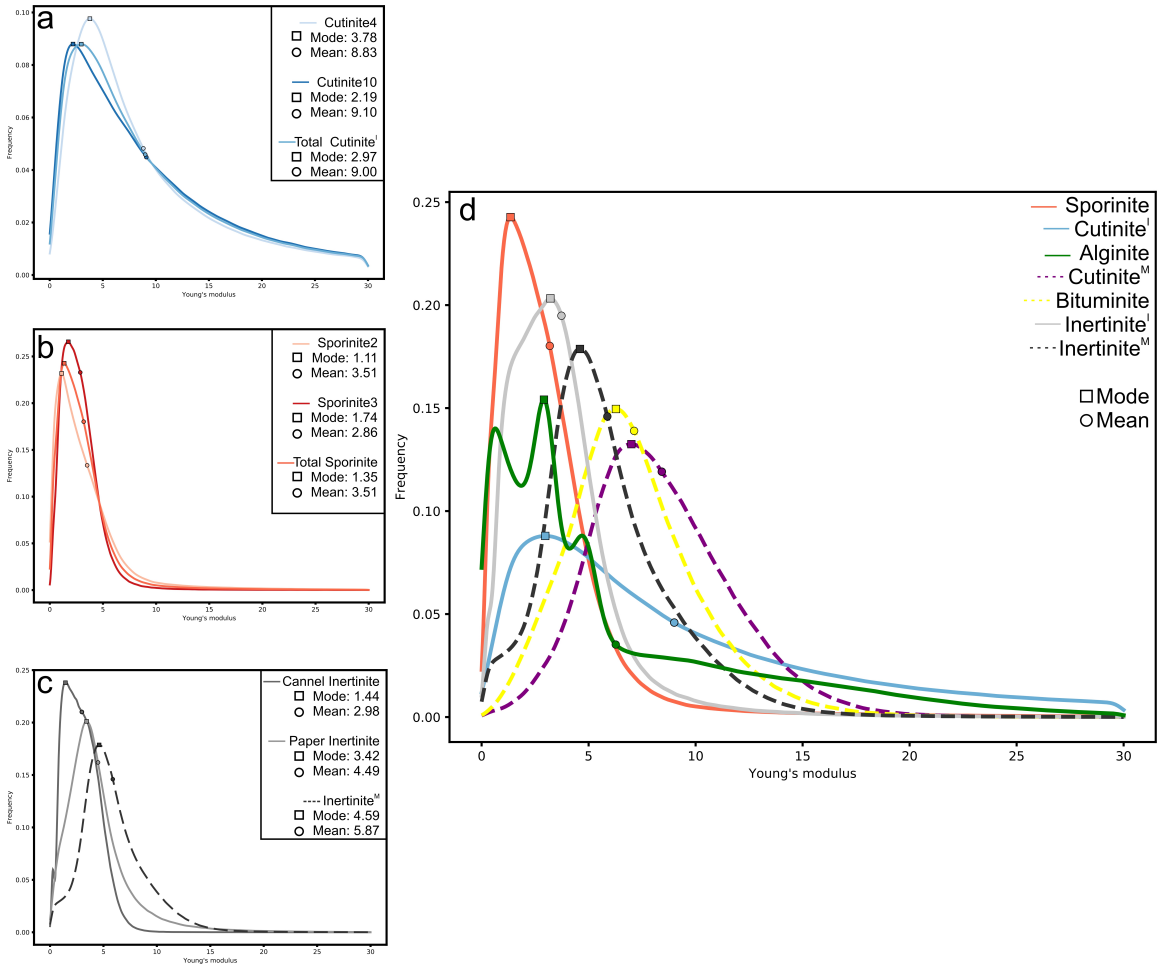

Figure 3.5: Probability distributions of each of the macerals studied, (a) is the distributions of immature cutinite from the Paper coal, (b) is the distributions of immature sporinite form the cannel coal, (c) is the distributions of inertinite in all three coals and (d) is a composite chart of all macerals studied. Block lines are from immature coals (paper and cannel), dashed lines are from the Northumberland Coal. Boxes indicate the modal value of each distribution, circles are the locations of the mean values from each distribution. In the immature shales the liptinite macerals have a lower modulus than their inertinite counterpart, a relationship which inverts with maturity. Liptinite macerals increase in stiffness drastically with maturity, as well as becoming more Normally distributed. Inertinite also becomes stiffer with maturity, although to a lesser extent than liptinite, which may be due to the oxidized state in which the inertinite was deposited. n.b. ^{I} denotes immature macerals, ^{M} denotes mature macerals.

Liptinite Macerals

The Young's modulus of alginite in the New Albany Shale is tri-modally distributed, with peaks at $\sim 2.5, 4.5$ and 5.5GPa. The reason for this trimodal distribution is likely a reflection of the limits of polishing a kerogen isolate in terms of the smoothness required for AFM. This makes it difficult to adequately differentiate between the scanned alginite (E=3-7GPa) and the resin in

which the particles of alginite are set. AFM analysis of the resin indicates a modal modulus value of $\sim$ 5.0GPa. Only limited research has been undertaken using AFM on isolated kerogen; which may be due to the preparation and mounting method for kerogen isolation not being optimal for AFM analysis. Therefore the alginite values described here are not considered further.

The two sporinite rich areas scanned in the cannel coal have the lowest modal and mean Young's modulus values of the macerals studied, with modes of 1.1GPa and 1.74GPa, and means of 3.51GPa and 2.86GPa (Figure 3.5a). The modal value within the sporinite rich scans also have the highest probability frequency ($\sim$ 0.245). The cutinite-rich scans in the paper coal have the highest mean modulus values of all studied macerals (8.83GPa and 9.10GPa) (Figure 3.5b), the largest difference between these aforementioned mean values, and the equivalent modal value (3.78GPa, and 2.19GPa). The comparably thermally mature cutinite has a similar mean modulus (8.43GPa), which is the third highest modulus studied, but with a mode of 6.99GPa (Figure 3.5d)., which is closer to the mean than in the immature equivalent. The modal value of bituminite is 6.27GPa and a mean of 7.11GPa. This is the second highest modal value within the macerals measured (Figure 3.5d).

There is a clear trend in reduced Young's modulus distribution within the liptinite macerals sampled; with immature macerals being less stiff than their mature counterparts. There is also a generally larger difference between the mean and modal values of E' in the immature sporinite and cutinite macerals, which is indicative of a non-normal distribution (Table 3.2).

When comparing the frequency of the distributions of immature macerals, it is obvious that the sporinite measured is extremely homogeneous. In contrast, the cutinite has a large degree of heterogeneity, indicated by the difference in modal frequencies in Figure 3.5 and appearance in Figure 3.6. It may be that sporinite is more homogeneous than cutinite in general, indicative of the mechano-chemical compositional differences. Another possibility for the difference is the size of the macerals. As already noted the macerals of cutinite in the paper coal are larger than the sporinite in the cannel coal (Figure 3.4a,b vs Figure 3.4c,d), which may allow for the measurement of more internal heterogeneity within the cutinite, causing a more varied modulus distribution. Another possible explanation for this difference is the interaction between mineral matter/groundmass and the cutinite macerals in the form of mechanical layering. There appears

to be relatively little mineral matter ($E' > 15$GPa) in the vicinity of the sporinite measured in comparison to the different colours and larger portions of masked out modulus in the immature cutinite scans (Figure 3.6). This would cause a spread distribution in the cutinite, as many measurements would be made of cutinite/mineral matter contributing to a higher mean modulus value and a lower frequency of the modal modulus.

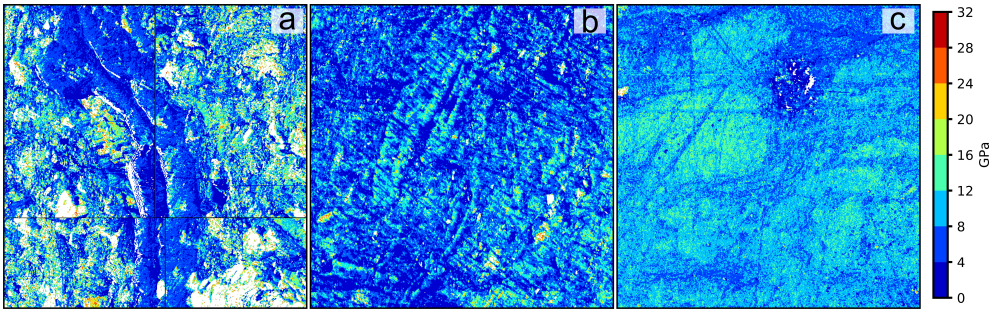

Figure 3.6: A selection of AFM Young's modulus scans including (a) immature cutininte from the Paper coal, (b) immature sporinite from the Cannel coal and (c) mature cutinite from the Northumberland Coal. Areas of white in the scans are places where the reduced Young's modulus is greater than 30GPa. It is obvious from both these scans and Figure 3.5 that there is far more heterogeneity associated with immature cutinite (a) than either the immature sporinite (b) or mature cutinite (c).

There is clear evidence for a transition in modulus mode and mean values of liptinite macerals with maturity. The bituminite and cutinite from the Northumberland coal have modal values between twice and five times greater than the immature sporinite and cutinite. These modal values are also similar to the mean value, suggesting a more gaussian distribution. This most likely reflects a transition in mechanical properties related to chemical changes in the macerals with maturity. Hydrogen-rich macerals are known to lose a lot of aliphatic and nitrogen, sulphur and oxygen-rich compounds in the oil window and become more aromatic by the gas window (Pan et al., 2013), which may be reflected in the stiffer, more normal distribution exhibited by the Northumberland coal liptinite.

Inertinite

The inertinite in the cannel coal shows two distributions, which are not observed between two different scans in any of the other macerals. One piece of inertinite has a mode and mean similar to the sporinite (mode: 1.23GPa, mean: 2.36GPa) (Figure 3.5a).The second distribution,

however, is almost twice as stiff and unlike any of the other immature sample distributions is approximately normally distributed with a mode of 3.69GPa and a mean of 3.60GPa.

The modal (2.49GPa and 3.72GPa) and mean values (4.05GPa and 4.92GPa) for the inertinite within the paper coal are similar too, albeit slightly stiffer than that observed within the more normally distributed cannel (Figure 3.5c). The reduced Young's modulus values of the inertinites scanned from the mature Northumberland coal are larger than the immature equivalent with a modal value of 4.59 and mean of 5.87GPa. The distribution of the mature inertinite appears to be almost normal, although with a limb between 0-1.5GPa, where values of modulus in this range are relatively infrequent. This limb appears in a similar region to the modal value of the cannel coal inertinite, which may be indicative of a transformation from immature inertinite to another more mature form or from the loss of this mechanical element during primary oxidation, which formed the inertinite.

A trend of slightly higher modal values of modulus in the inertinite macerals measured within the immature cannel coal than the equivalent inertinite in the paper coal most likely represents regular heterogeneities exhibited between coals of similar maturity, but with different burial histories and associated stress fields. This could be a result of: 1) differences in the type of inertinite (i.e. different source organic matter), 2) different amounts of oxidation prior to burial or 3) differences in the orientation of the maceral regarding any internal structure.

Trends in Modulus Values

The most obvious trend in Young's modulus of coal macerals is the aforementioned evolution with maturity, whereby macerals appear to become stiffer, more normally distributed and more heterogeneous. Figure 3.5 demonstrates this trend, with the mode and mean values generally increasing and becoming less separated with maturity. The frequency of the mode also appears to generally decrease with maturity, indicating that in general the macerals are becoming more mechanically heterogeneous. The exception to this is the immature cutinite macerals, which have the highest mean modulus and lowest frequency mode. These macerals are as mentioned previously influenced by mineral/groundmass which is stiffer than the maceral itself.

A notable trend is the amount of stiffening in the liptinite macerals relative to the inertinite

macerals with maturity. Liptinite macerals modal moduli increases by a factor between two and five with maturity, whereas the modal value for inertinite only increases by approximately 42% (Figure 3.5c., Table 3.2). The modal value of inertinite increased by 1.17GPa from the Paper coal to the Northumberland coal, whereas cutinite increased by 4.02GPa in the same two coals. This trend indicates that thermal maturity is almost certainly the main drive in the transition of modulus values and distribution. The inertinite which is most likely thermally matured or oxidised at surface, is less affected than the hydrogen rich liptinite macerals. This may therefore only represent the mechanical 'maturation' with increased burial depth. This change in liptinite macerals may be associated with the transition in chemistry from chaotic to an ordered aromatic structure (Pan et al., 2013) along with the same mechanical maturation associated with the inertinites.

It appears from the results obtained here that the analysed macerals show a larger variability than in previous AFM studies on coals (Li et al., 2020), and are in general notably less stiff. The modulus results are closer to those found within nanoindentation literature (Kossovich et al., 2016; Zhang et al., 2018c,b; Borodich et al., 2015). However, it is not prudent to directly compare effective reduced Young's modulus with local reduced Young's modulus. The reasons for this are linked to both internal porosity at length scales between the AFM and nanoindentation measurements (Table 3.3). This porosity would certainly decrease the effective modulus, but may not significantly affect the AFM measured local modulus. Studies on the distribution of porosity in coals indicate that vitrinite contains a large number of mesopores (2-50nm in diameter), liptinite macerals contain some mesopores with inertinite appearing to contain very few mesopores (and dominance of larger pores) that may affect the AFM readings (Teng et al., 2017). These fine pores, would reduce Young's modulus and could be a reason as to why the inertinite in the immature coal is stiffer than the equivalent liptinite (sporininte/cutinite). Studies into the development of organic porosity using FIB-SEM (Focussed Ion Beam Milled-Scanning Electron Microscopy) in shales have found that organic porosity increases from immature organic matter through to the gas window in the Woodford Shale (Curtis et al., 2012), however, the overall porosity in the New Albany shale at similar maturity intervals measured by helium and mercury porosimetry decreases (Mastalerz et al., 2013).

Lu et al. (2018) used mercury injection porosimetry to measure the pore volumes in 18 middle rank coals (VR_o 0.71-1.14%) from the Huaibei coal field, reporting no issues with the use of mercury injection values. Zhou et al. (2017) used NMR and mercury injection porosimetry to measure the porosity of coals, but found that a significant portion of pores are below the limit of mercury injection (<1nm). Roslin et al. (2020b,a) found the modal poresize within an intermediate coal was between 1-25nm, which may be observed partially be mercury injection porosimetry, however, there were still a significant proportion of pores (approximately 42%) between 25nm-50μm, which will be readily resolved by mercury injection. Mastalerz et al. (2021) used mercury injection porosimetry to determine the pore size distribution of a mature organic rich shale, which suggests that this similar technique is adequate for use on similarly organic rich deposits such as coal. Although it is noted that mercury injection may have inaccuracies due to the compressibility of coal (Yao and Liu, 2012).

Whilst the mercury porosimetry data acquired here gives an insight into the likely pore size distribution and overall porosity of these coals, these measurements come with some error due to the aforementioned compressibility of coal and likely deformation during injection(Spitzer, 1981). Li et al. (2018c) indicate that MICP measurements on samples of a similar maturity to the Northumberland Coal are similar to those obtained by NMR. However, any impacts of mercury injection deforming coals are more likely to affect the less thermally mature samples. As such, the pore size distribution and overall porosity of the cannel and paper coals should be considered to have a greater margin of error. The effect of compressibility on mercury injection porosimetry in heated lignites has been reported by Bergins et al. (2007), reporting that the corrected porosimetry is lower, with a lower proportion of meso-pores. This indicates that the mean pore throat diameter of the cannel and paper coals are likely an underestimate, and the overall porosity of these coals is likely an overestimate.

The mercury injection porosimetry results from this study suggest that the median poresize is within the resolution of the AFM. However, a large proportion of coal porosity is unmeasurable by mercury injection with the modal poresize determined to be <10nm in many coals (Mastalerz et al., 2021; Raza et al., 2019). This suggests that there may be an impact of porosity in this study, whereby the porosity data is incomplete, and gives no suggestion of the pores <6nm in

diameter. The porosimetry data also doesn't give a representation of the different porosities in each maceral, as the technique used bulk coal samples. The overall porosity of a coal is known to evolve during thermal maturation. Porosity initially decreases in coals through the oil window, where pores are saturated with liquid hydrocarbons. Then in the late oil early gas window porosity increases, and continues to increase with the production of gaseous hydrocarbons (Zhang et al., 2018a; Yan et al., 2020). The adsorption capacity of coals follows a similar trend with Langmuir Volume shown to initially decrease during the oil window, before increasing with increased thermal maturity thereafter (Laxminarayana and Crosdale, 1999; Yan et al., 2020).

Whilst the porosity of each maceral is known to be different at a similar maturity, with vitrinite macerals exhibiting a large amount of meso and microporosity relative to liptinite macerals, and liptinite macerals exhibiting more meso/microporosity than inertinite macerals (Teng et al., 2017). A study by Cardott and Curtis (2018) suggest that the porosity in thermally immature coals is dominated by nanoporosity, which is all but absent in bituminous rank coals, with microporosity only present within woody cell lumens in vitrinite. This trend was observed in bituminous rank coals, which are significantly more mature than the cannel and paper coals tested here, and much less mature than the Northumberland coal. As such, due to the likely differential development of porosity across these macerals, the pore size distribution and median porosity obtained from the mercury injection porosimetry is the most reliable information currently available, and literature values of porosity for each maceral, may be misleading. Further work could entail using helium porosimetry/ NMR porosimetry along with SEM images to identify the poresize distribution in each of the macerals within this study.

Whilst further investigation is required into the evolution of coal maceral porosity, it is likely to follow a similar mechanism to the evolution in shale organic matter, due to similar thermal processes occurring particularly in hydrogen rich (liptinite) macerals. As such we expect the porosity of liptinite macerals to increase with maturity as a result of generation of hydrocarbons, which, in turn, which would in turn decrease the modulus if porosity was the major factor in the difference between the liptinite and inertinite macerals. Although with increasing maturity much of the hydrogen rich liptinite macerals are converted into inertinite macerals as their reactive hydrogen is produced as hydrocarbons. The porosity measurements in Table 3.3 appear to show

little trend with maturity. If porosity was a defining factor on the stiffness trends observed in each maceral, then the macerals of immature cannel coal would generally appear stiffer than the macerals from the more porous paper coal. This trend is not observed as both the liptinite and inertinite macerals in the paper coal are stiffer than those in the cannel (Figure 3.5).

Another reason for caution in comparing AFM and nanoindentation is the effect of the central limit theorem, which indicates that the collection of means of any distribution are normally distributed(Bauer, 2011). As the nanoindenter measures the mean modulus at a scale of $\sim 25\mu m^2$, any collection of nanoindentation curves should be normally distributed. However, the actual modulus of each component, measured by AFM may be entirely non-normally distributed. A further analysis of this to attempt to contrast AFM and nanoindentation is undertaken in Section 3.3.5.

Coal	Porosity (%)	Mean Throat Diameter (nm)
Cannel	3.19	6.34
Paper	7.45	16.83
Northumberland	9.88	7.39

Table 3.3: Mercury injection porosimetry derived total porosity and mean pore radius size values for each coal.

When analysing for the CCUS potential of a coal it is common to undertake a point count analysis for the maceral content of the coal. As well as this, a key method to estimate the effects of CO_2 injection on the physical properties of coals is the use of models derived from laboratory based experiments. These models take the bulk coal modulus and any maceral variability is not accounted for. Recent modelling work which has attempted to estimate swelling from injection pressure of CO_2 uses Young's modulus of the coal medium as a key input (Pan and Connell, 2007; Zhang et al., 2008; Connell and Detournay, 2009; Liu et al., 2010; Ma et al., 2011; Liu et al., 2019). However, the variability exhibited within the macerals analysed may be of even greater importance. The highest modal value of Young's modulus is more than 500% of the lowest modal value between two liptinite moduli (sporinite and mature cutinite).

3.3.4 Organic Matter Distribution Analysis

A key feature of each maceral Young's modulus is the distribution shape. This is reflected as a transition to a more normally distribution with maturity, shown by a smaller proportional gap between modal and mean values of Young's modulus. Previous studies use the volume averaging properties of nanoindentation tests to estimate the Young's modulus and hardness values for minerals within rock (Bobko and Ulm, 2008; Ulm et al., 2007; Ulm and Abousleiman, 2006; Liu et al., 2018; Li et al., 2019). This technique is a form of multi-scale modelling, whereby the distribution of the nanoindenation results is a composite of normal distributions for each phase multiplied by its respective proportion in the rock indented. This deconvolution based approach is successful due to the central limit theorem mentioned above, as the mean of the nanoindentation moduli will always be normal even if the distributions themselves are not. Deconvolution by normal distribution works when a single indent can be considered to sample the representative elemental volume for a mineral phase without coupling to other neighbouring phases and aren't mechanically coupled with other phases (calcite, quartz, pyrite etc.), therefore produce a sharp noticeable normally distributed peak. At higher resolutions of mechanical measurement, or with increased testing, the volume sampled by the testing probe is less than that of the required effective volume, leading to the measurement of the true statistical distribution of the mechanical data. Our results show that these are inherently non-normal.. In the coals and shale studied here the Young's modulus distribution of the organic matter appears to be non-normal. As such it is important to identify which distribution may be more appropriate to add to the deconvolution model for organic matter.

In order to facilitate this, each maceral was analysed against a set of distributions (Normal, Lognormal, Gamma) to minimize the error between the proposed distribution and the observed distribution (Equation 3.6). The minimization was carried out initially a by the Python based scipy.distribution.fit program for each of the distributions shown. The fitted parameters were then used as an initial guess to undertake a single phase deconvolution, using a method similar to that presented in Bobko and Ulm (2008). The N observations were sorted and the Experimental Cumulative Density Function (ECDF) was then formed by the F_M of these N points using

Equation 3.5.

$$F_M(M_i) = \frac{i}{N} - \frac{1}{2N} \quad \text{for i} \in [1; \text{N}] \tag{3.5}$$

The ECDF was then minimized for root mean square error against a CDF generated the fitting parameters of each of the three distributions in order to obtain the minimum error (Equation 3.6). The minimization was undertaken using scipy optimize least squares package, which uses the Levenberg-Marquardt Algorithm, for information on this package readers are directed to Virtanen et al. (2020) & (cf. More, 1977). For each of the distributions μ and σ correspond to the mean and standard deviation respectively, whereas k is a shape parameter of the gamma distribution and θ is a fitting parameter.

$$\begin{aligned} \min\left[(\text{CDF}(\text{X} \sim \text{N}(\mu, \sigma)) - \text{ECDF})^2\right] \\ \min\left[(\text{CDF}(\text{X} \sim \Gamma(\text{k}, \theta)) - \text{ECDF})^2\right] \\ \min\left[(\text{CDF}(\text{X} \sim \text{LogNorm}(\mu, \sigma)) - \text{ECDF})^2\right] \\ \text{Where} : \mu > 0.0 \end{aligned} \tag{3.6}$$

The results of the minimization are shown in Figure 3.7, which indicate that although no single distribution matches the maceral distribution absolutely. It appears that for sporinite, cutinite (immature and mature) and Northumberland inertinite the Gamma distribution appears to fit the most accurately. For the bituminite and inertinite from the immature coals the Normal distribution appears visually to fit as well as the Gamma distribution. The Normal distribution shows the best fit for inertinite from the thermally immature Cannel and Paper coals. Although it should be noted that some of these distributions (mature cutinite, mature inertinite, bituminite) appear to be a mixture between Gamma and Normal distributions. The Lognormal distribution, although selected for this comparison due to its visual similarity to some of the maceral distributions performs poorest out of all the distributions. Further investigation indicates that the constraint of a positive mean (as negative mean Modulus is unrealistic) causes the Lognormal distribution to lose the fitting capacity for almost all the macerals.

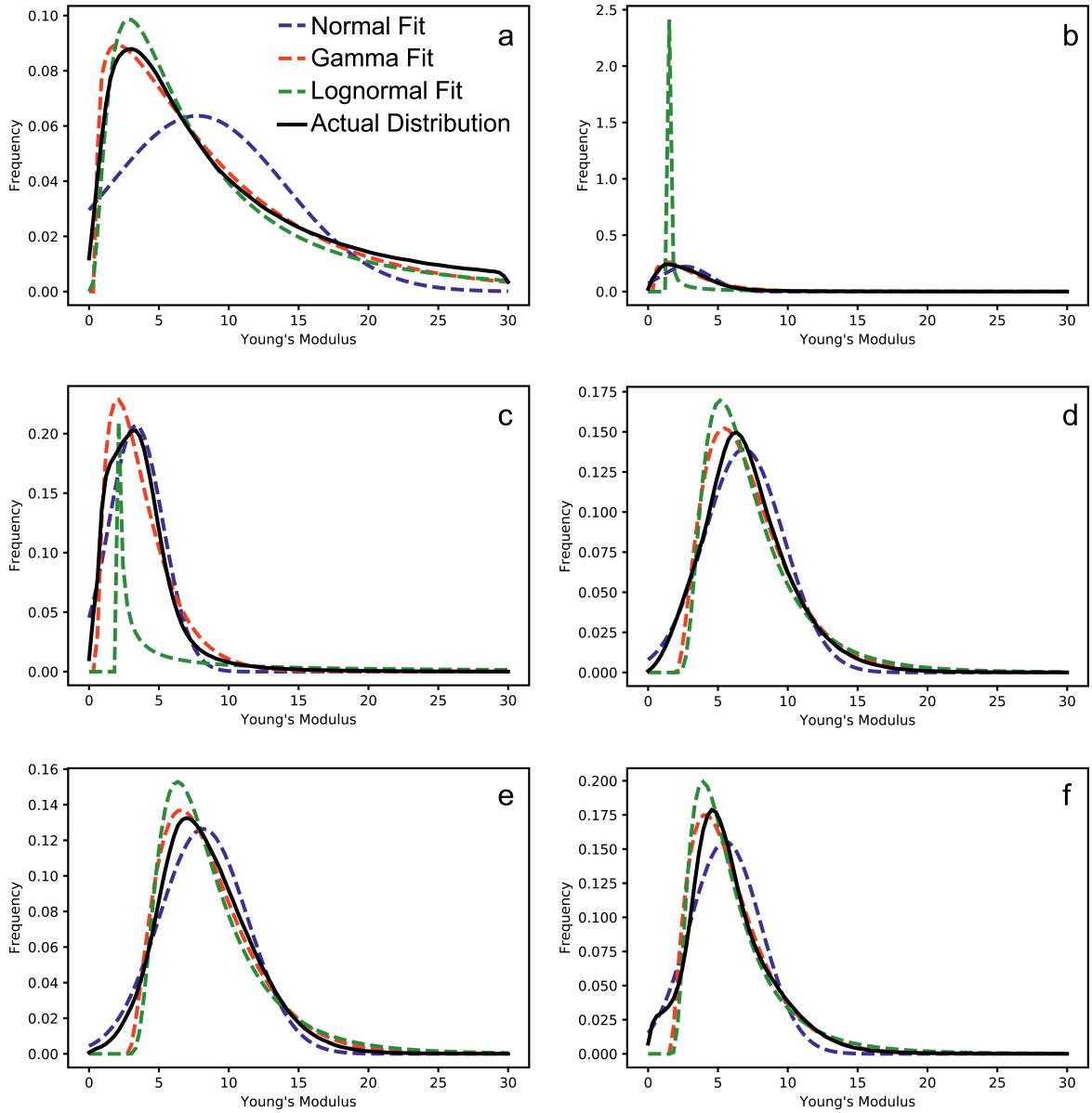

Figure 3.7: A comparison of the AFM distribution with the optimum Normal, Gamma and Lognormal Distribution for immature cutinite (a), sporinite (B), immature inertinite (c), Bituminite (d), mature Cutinite (e) and mature inertinite (f). The Gamma distribution appears to be the best fit for all macerals apart from immature inertinite. The Normal distribution is the next best fit visually aside from the immature cutinite distribution. The Lognormal distribution is the poorest fit for each distribution and is particularly poor for sporinite.

Detailed analysis of Figures 3.7 & 3.8 and Table 3.4 suggests that the normal distribution used for deconvolution is less appropriate for immature hydrogen rich macerals, with the highest error values associated with immature cutinite and sporinite (Figure 3.7a,b), which have twice the error of fit when compared to the mature liptinite macerals (Figure 3.7d,e). The Gamma

distribution actually shows the opposite error trend, whereby the least fit error is associated with the immature cutinite and sporinite distributions (Table 3.4).

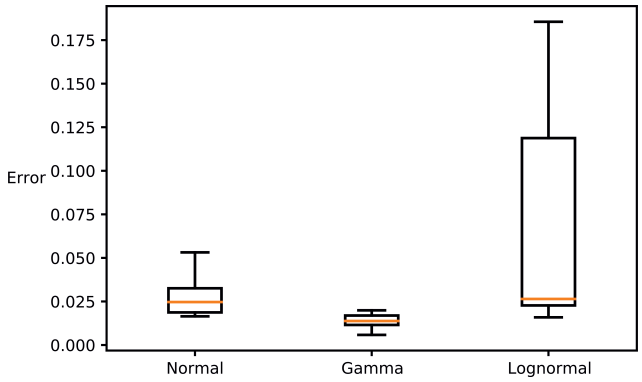

Figure 3.8: The Root-Mean-Squared-Error associated with fitting each distribution on all the macerals studied. The Gamma distribution has a low error value for each maceral and a relatively small standard deviation in error. The Lognormal error is high, partly due to the poor fit on Sporinite.

Maceral	Normal Error	Gamma Error	Lognormal Error
Cutinite^{I}	0.053	0.006	0.015
Sporinite	0.034	0.011	0.149
Inertinite^{I}	0.022	0.020	0.186
Bituminite	0.016	0.018	0.028
Cutinite^{M}	0.018	0.013	0.024
Inertinite^{M}	0.027	0.014	0.022

Table 3.4: Root-Mean-Squared-Error for each distribution fit for each Maceral. ^{I} denotes from an immature coal, whilst ^{M} denotes from a mature coal

Figure 3.8 displays the error associated with fitting each distribution, which clearly demonstrates that the Gamma distribution is the most likely fit for the analysed coal macerals. This distribution has a maximum error below the mean error for the Normal distribution. These findings suggest that any homogenisation using coal macerals at this scale should be performed using a Gamma distribution. This relationship may assist in attempts to upscale and homogenize coal Young's modulus measurements, which in turn may help assist injection models at core scale.

Results from the minimization indicate that the shape parameter k is in the range of 1.20 (immature cutinite) to 2.87 (mature cutinite). A scale parameter (θ) is required along with the shape parameter k to fit the Gamma distribution. The calculated values of θ range from 1.70

in immature inertinite to 7.26 in immature cutinite.

Furthermore, shale organic matter should be analysed to identify if the Gamma distribution is a better fit for all organic matter. This may also inform as to whether a normal distribution is most prudent for deconvolution of shales at higher resolutions than nanoindentation or if other distributions may offer greater accuracy.

3.3.5 Mean Analysis

In order to attempt a comparison between the AFM results reported here and the literature, nanoindentation values of the AFM scans were analysed to gather mean values across a 5μm $\times$ 5μm area with a 2.5μm overlap with the adjacent means (dashed line in Figure 3.9). This upscaling gives a square of similar size to the 2D zone of influence of a nanoindent (Figure 3.9). These are reported in this literature as effective moduli values with the effective size of 5μm.

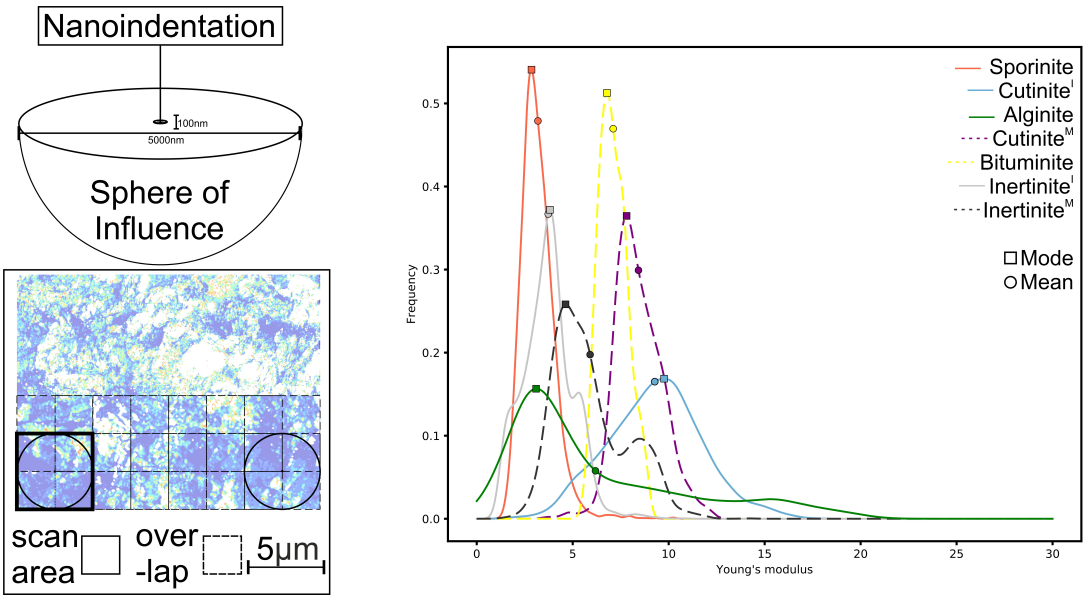

Figure 3.9: The distribution of mean values for AFM when analysed at $25\mu m^2$ increments. This gives a total of 361 mean measurements for each $50\mu m \times 50\mu m$ area. The left of the figure indicates the approximate area of influence for a nanoindentation scan 100nm deep, which is a hemisphere of radius $\sim 5\mu$m. The figure on the right indicates the probability distributions of the means. Each of the modal values are greater than those in the overall local AFM population (Figure 3.5), the modal value of the immature cutinite means is significantly greater than the local AFM distributions indicated in Table 3.2. n.b. ^{I} denotes immature macerals, ^{M} denotes mature macerals.

Figure 3.9 displays the effective modulus distribution acquired from 5μm means for each set of macerals, indicating a distinct increase in modal value when compared to the overall distribution of each maceral. Table 3.2 indicates the modal values for each of the macerals in this format, mean values are the same as the mean for the overall distributions. The increase in modal value from this technique is widest in the immature cutinite where the Young's modulus increases by more than 325% (2.97GPa to 9.76GPa). The smallest increase is $\sim 0.5\%$ within the mature inertinite. This increase with 5μm averaging is greatest in macerals with the highest degree of non-normality (Table 3.4). This absolute increase in coal Young's modulus with maturity has been indicated at higher length scales with UCS/uniaxial or triaxial compression tests by other studies (Pan et al., 2013; Morcote et al., 2010). The increase in modulus observed by AFM is greater than that observed in literature and may be a result of the decreased effect of the mineral proportion on the AFM modulus distribution. The mineral phase in these coals is unlikely to evolve or stiffen with maturity to the same extent that the organic matter in coal does within the maturities measured here.

It is noted that these results more likely represent the appearance of macerals at higher length scales, which is indicated by Figure 3.9. This increase in modal modulus is to be expected considering the distributions will conform to the central limit theorem (Bauer, 2011). This is due to each of the distributions being most similar to a Gamma distribution with a mean greater than the mode, which will combine to a Normal distribution with a mode close to the mean of these distributions.

The effective modulus distributions are generally normally distributed with the exception of alginite, and inertinite. As mentioned previously, there is significant interference between the alginite and the resin encapsulating it, which explains the bimodal distribution of the 5μm distributions. It does however appear that there is more than one phase within both the mature and immature inertinite. This is particularly interesting as there is little to no groundmass in these scans due to the particle size of the inertinite. A primary reason for this also could be the difference between two individual macerals of inertinite, however, two individual macerals were scanned of both immature cutininte and sporinite and resulted in a normal distribution.

The effective modulus distributions of the mature coal fit closer to the distributions acquired

by Li et al. (2020), which are at a similar length scales, albeit somewhat softer than the modulus values obtained in that study. Their study also implies that the average modulus of the 'mineral' content of a coal, most likely quartz, carbonate, pyrite and clay minerals have an average Young's modulus <20GPa, which appears to be unlikely.

The effective modulus distributions of organic matter appear to be within the ranges of those stated within nanoindentation (Figure 3.10) the literature (Yu et al., 2018; Zhang et al., 2018c, 2017) (Figure 3.10), although slightly lower than some values. The reason for this could be the difference in maturity between the samples analysed and those in the aforementioned literature, or the influence of mineral inclusions which may bolster the effective Young's modulus at the length scale of nanoindenation, which are masked out in this form of AFM due to being stiffer than the tip used. If mineral matter were to be a major contributing factor, then the increased porosity measured at nanoindation would decrease modulus readings by similar amounts. Results of nanoindentation from Kossovich et al. (2016); Zhang et al. (2018c,b); Borodich et al. (2015) give modulus values of coal between 3-9GPa, which are within the ranges exhibited here (Figure 3.10), suggesting that this averaging technique may be applicable to upscale modulus values from AFM length scales to Nanoindentation length scales in simplistic three phase systems (maceral, porespace, mineral matter).

It is not always prudent to further upscale these AFM results to the region of triaxial experiments due to the formation of cleats and fractures within the coal, which are not captured by the AFM. However, Gentzis et al. (2007) found static Young's moduli values of between 1.1-5.1GPa with no pore pressure and Poisson's ratios of between 0.26-0.48. The equivalent Young's moduli values of our maceral means when analysed with Poisson's ratios of 0.26 are 2.97-8.65GPa and with $\nu = 0.48$ are 2.45-7.14GPa, which although slightly stiffer than the triaxial values are not significantly different.

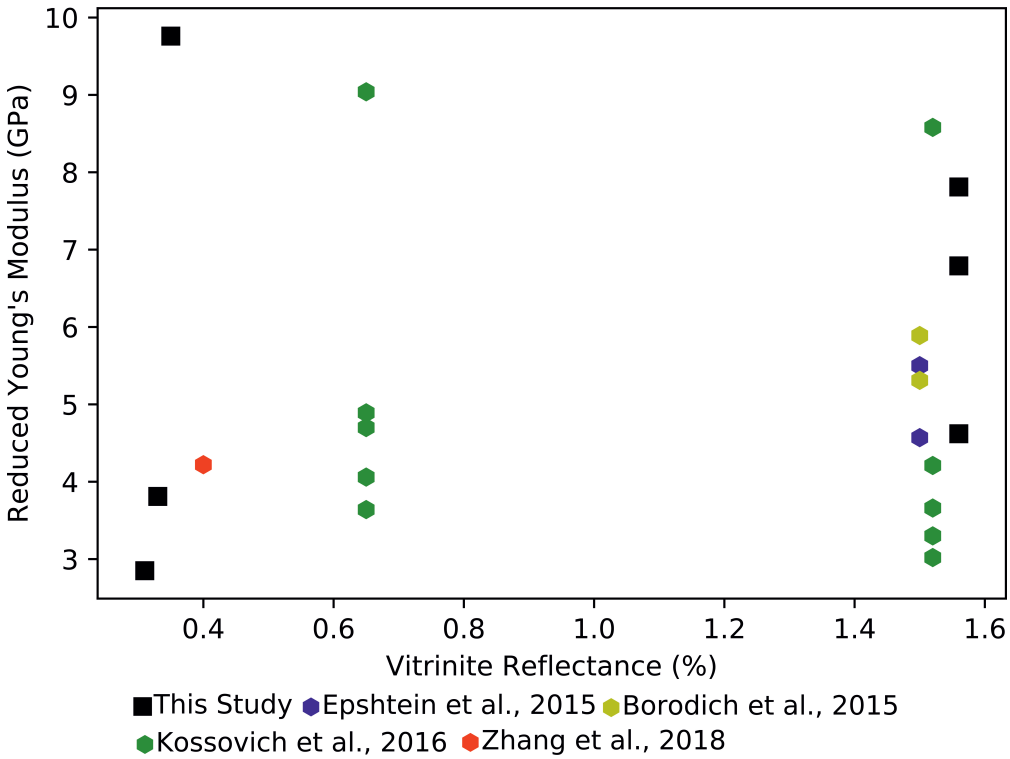

Figure 3.10: A comparison of the mean distributions of AFM from this paper with nanoindentation values from other literature, at the maturities measured. The means of the AFM distributions are within the range of literature values acquired from nanoindentation at the maturities measured. The mean of the immature cutinite may be marginally above the literature reported but is most likely due to the interaction with mineral matter/groundmass.

3.3.6 CO_2 Injection Modelling

The difference in modulus values within a single coal is crucial when investigating the deformation potential with regards to CO_2, as open phase fractures may readily form due to the differential swelling associated with different macerals. Figure 3.11 indicates how the modal modulus value of each maceral affects the swelling associated with gas injection using the Pan and Connell (2007) model (Equation 3.7).

In this study the Langmuir Constants determine the rate of adsorption onto the coal surface, and are taken from Fruitland coal adsorption of CO_2 from Levine (1996). This is in order to compare the results of this modelling to those obtained by Pan and Connell (2007), who also used the Levine (1996) data for their model. These chosen values assume that CO_2 behaves as an ideal gas for simplicity. x and c within equation 3.7 (Table 3.5), relate to the values used in

the Scherer (1986) pore structure model which has been used to describe the maceral structure. x is the length to width ratio of the maceral and is kept constant at 0.5 for a theoretical maceral, for ease of comparison. $c(= 8\sqrt{3/\pi})$ is a constant in the Scherer (1986) model and describes the morphology of the adsorption sites. Maceral density within the model has been kept constant, but realistically will be 1.3 ± 0.1 (Walker Jr et al., 1988). The modal values of each distribution were chosen as the Young's modulus within this model. Poisson's ratio (ν) has also been kept at the value used by Pan and Connell (2007) within the model (equation 3.7), due to the difficulty measuring Poisson's ratio at this length scale, but is likely to alter in a similar manner to the Young's modulus. The simulation was undertaken using low pressure and a Langmuir adsorption isotherm, and assuming isotropic elastic behavior using the the equation below and parameters in Table 3.5.

$$\epsilon = \mathrm{RTL}\ln(1+\mathrm{BP})\frac{\rho_s}{E_s}f(x,\nu_s) - \frac{P}{E_s}(1-2\nu_s)$$

$$\text{Where :} \tag{3.7}$$

$$f(x,\nu_s) = \frac{[2(1-\nu_s)-(1+\nu_s)cx][3-5\nu_s-4(1-2\nu_s)cx]}{(3-5\nu_s)(2-3cx)}$$

Symbol	Value	Description	Symbol	Value	Description
T	295(K)	Temperature	ρ	1.3($\mathrm{gcm^{-3}}$)	Coal Density
R	8.314(J $\mathrm{mol^{-1}K^{-1}}$)	Ideal Gas Constant	E_s	Table 3.2 (GPa)	Coal Young's modulus
L	1.257,1.488 ($\mathrm{molkg^{-1}}$)	Langmuir Constants (CH_4,CO_2	x	0.5	Diameter to length ratio of coal sample
B	0.294,0.953 ($\mathrm{Pa^{-1}}$)		c	1.2	Pore structure model constant
P	0-5(MPa)	Injection Pressure	ν_s	0.372	Coal Poisson's Ratio

Table 3.5: Input parameters used in this study for Equation 3.7. E_s values are the modal modulus value of each maceral within this study. The remaining mechanical and thermodynamic properties are adopted from Scherer (1986); Levine (1996); Pan and Connell (2007).

Results of this modelling approach indicate that the linear strain exhibited in a maceral is directly linked to the Young's modulus, in an inverse manner, assuming a constant value of Poisson's ratio. This indicates that differential swelling may open fractures between macerals of different moduli, and thus different precursors. However, the differential swelling of macerals, may cause the higher swelling macerals to fill in the existing fracture network. The proposed opening of microfractures from differential swelling may assist in the percolation of CO_2 through the coal during sequestration, or cause seepage into pre-existing fractures causing unwanted leakage upwards of the CO_2 being sequestered.

The increase in modal Young's modulus at higher length scales affect the strain associated with injection in immature macerals. In particular the strain associated with the local modal value of cutinite three times greater than that if the cutinite is modelled from the effective modulus of 5 micron squares (Figure 3.11). This possible increased stiffening of coal at microscopic (nanoindentation) length scales may cause misinterpretation regarding strains from CO_2 injection.

Figure 3.5 indicates that the modal Young's modulus values increase in all macerals with maturity. This increase in modulus represents a decrease of approximately 30% in linear strain in the Pan and Connell (2007) model with maturity (Figure 3.11. The increase in liptinite maceral modulus is even more significant, with the modal values increasing from 1.35/2.97GPa in immature coals, to >6GPa in the bituminite and cutinite of the Northumberland coal. This represents strains 2-4 times greater than that observed in the immature sporinite and cutinite macerals compared to the mature bituminite and cutinite macerals under the Pan and Connell (2007) model.

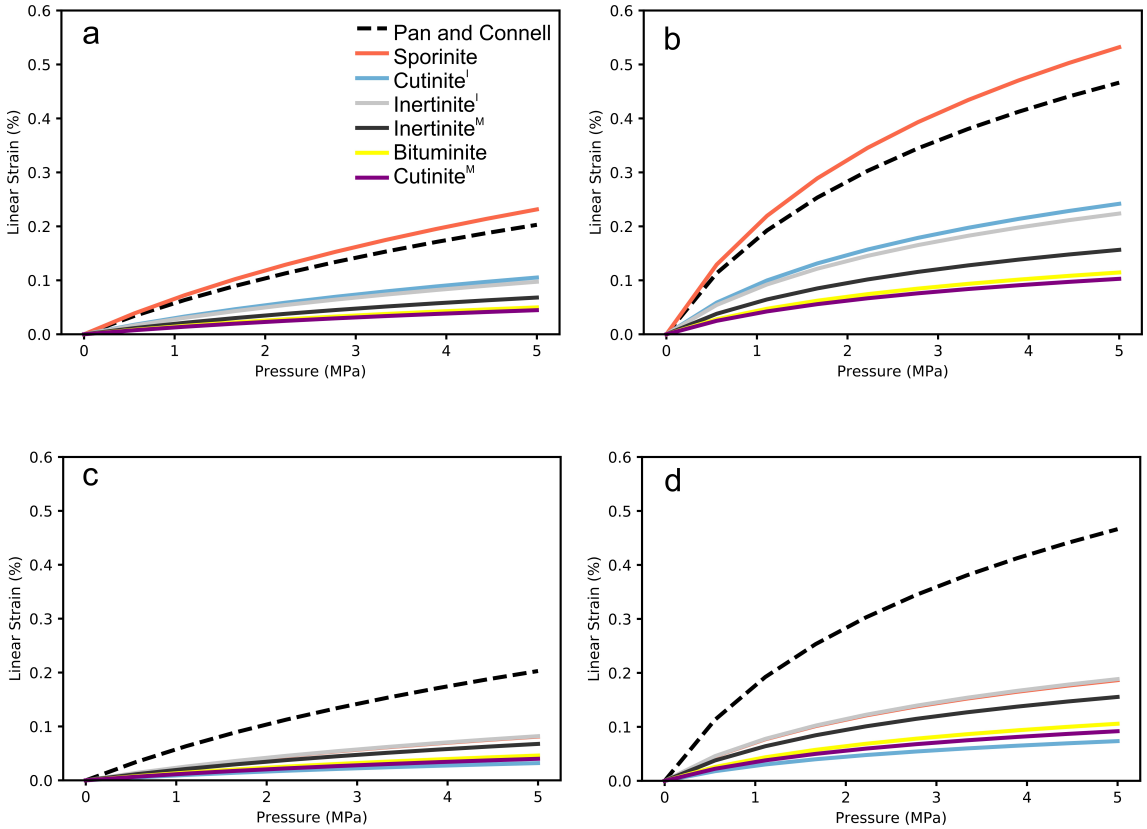

Figure 3.11: Gas injection pressure comparison with linear strain generated on each of the coal macerals using the Pan and Connell (2007) model and data from Table 3.5. The modal value of modulus was used to compute the results The strain related to each maceral from CH_4 (a), CO_2 (b) indicates that a lower Young's modulus causes greater linear strain upon injection. (c) and (d) are CH_4 and CO_2 injection into the macerals defined by their effective Young's modulus modal values (Table 3.2) from the 5μm mean analysis.

The results of this modelling approach differ to the experimental approach undertaken by Mastalerz et al. (2009) on the cannel and paper coals analysed within this study. Mastalerz et al. (2009) indicate strains of between 0.42-1.05%. The differences in result are likely due to a combination of different length scales used: macerals in this study vs whole coals in Mastalerz et al. (2009), the need to update to macerals specific Langmuir inputs for the Pan and Connell (2007) model, and the higher maximum injection pressure in the experimental procedure than used in this study.

The overall outcome of injection modelling at a maceral scale further indicates the need to undertake detailed coal petrology prior to injection design. The permeability of the coal will evolve during injection, and has been observed to initially decrease (Niu et al., 2019). This

occurs as the coal matrix begins to strain, causing filling of porespace and cleats (Mazumder and Wolf, 2008; Liu and Harpalani, 2013; Zhang et al., 2016; Niu et al., 2019). The modelling demonstrated here indicated from the results presented here indicate that the macerals within the matrix strain will strain with injection (Figure 3.11). As this strain occurs, cleats are infilled, causing a reduction in permeability in the short term(Liu et al., 2013; Vishal et al., 2013; Niu et al., 2019). However, coals comprise a variety of macerals, which have been shown in this study to have different Young's moduli and thus different strain rates under injection. If these macerals strain at different rates, this may facilitate the opening of microfractures, through differential strain. This phenomenon was observed by Hol et al. (2012); Sampath et al. (2019), where during initial CO_2 injection microfractures were opened. These microfractures led a permeability increase, although not likely to offset the blocking of cleats during an initial phase of sequestration (Zhang et al., 2016). However, if multiple injection phases were introduced, this would cause multiple phases of differential stress and could lead to these microfractures becoming more significant, and allowing larger amounts of CO_2 to be stored in the homogenised coal.

The results of this study indicate that this differential swelling is much more evident in less thermally mature coals. However, the lignites chosen for this study, due to ease of maceral identification, and enrichment in a particular type of liptinite, would not make suitable candidates for CO_2 storage. The principal of differential swelling between macerals is still evident within the mature Northumberland Coal but to a much lesser extent (Figure 3.11). This means that when injecting into a similarly mature coal, the swelling of individual macerals will be more homogeneous, and thus the formation of microfractures between the macerals may be less likely. In contrast to this, the mineral phases in these coals will not swell and so microfractures may form between uniformly between the mineral phases and the adjacent macerals. The observations of Hol et al. (2012); Zhang et al. (2016); Sampath et al. (2019) suggest similar occurrences, whereby microfractures occurred along bedding planes and between macerals and mineral phases. This modelling approach would be significantly improved by constraining the variation in Poisson's ratio with maceral type and maturity.

The water content of the coals studied here has not been measured, however, previous re-

search on cubes of coal indicate a Young's modulus decrease of approximately 25% between moisture contents of 3.8% and 12% (White and Mazurkiewicz, 1989), whilst Yao et al. (2015) found a negative exponential correlation between moisture content and Young's modulus on coal samples. This reduction in modulus accompanies an increased likelihood of microfracture with increasing water content (Yao et al., 2019). Despite this, little research has been conducted onto the effects of water content, particularly that hosted within organic pores, on maceral Young's moduli or any other associated mechanical properties. Therefore, further investigation should be conducted at different moisture contents to understand if there are any effects on individual maceral Young's moduli. Or, if the moisture content impact is limited to the non-organic phases in the coal, as observed within shales(Gensterblum et al., 2013; Merkel et al., 2015).

3.3.7 Nanoindentation Comparison

The results of nanoindentation experiments undertaken on each of the coals and macerals are presented in Figure 3.12. The modulus values of cutinite are displayed in Figure 3.12a, which are all less than 30GPa. Two different distributions can be seen, a softer distribution in the Cutinite10 scan (modal value: 5.1GPa) than the stiffer distributions in Cutinite4 (modal value: 12.6GPa) and the mature cutinite sample (modal value: 11.5GPa). The frequencies of the Cutinite4 and mature cutinite are also much lower than that in Cutinite10, suggesting a more heterogeneous material. The distribution of the Cutinite4 nanoindentation modulus is the broadest of any of the macerals scanned, with the lowest maximum frequency.

Unlike the cutinite scans, the modulus values of the two sporinite areas scanned have a very similar modulus distribution, with the only small difference being a slightly increased frequency of modulus values at around 10GPa in the Sporinite2 scan (Figure 3.12b). The modal modulus of the sporinite macerals is much higher than either the cutinite or the inertinite with modal values 15.7 and 16.0GPa.

The inertinite modulus values are all almost completely normally distributed, but similar to the cutinite has multiple different distributions. The inertinite from the cannel coal has modal value of 5GPa, which is considerably lower than that from the paper coal (modal modulus: 13.3GPa) and the shotton coal (modal modulus: 10.3GPa). The inertinite modulus profile from

the cannel coal is almost identical to the Cutinite10 scan, which is also from the cannel coal. The reasons for this are discussed later in Section 3.3.9.

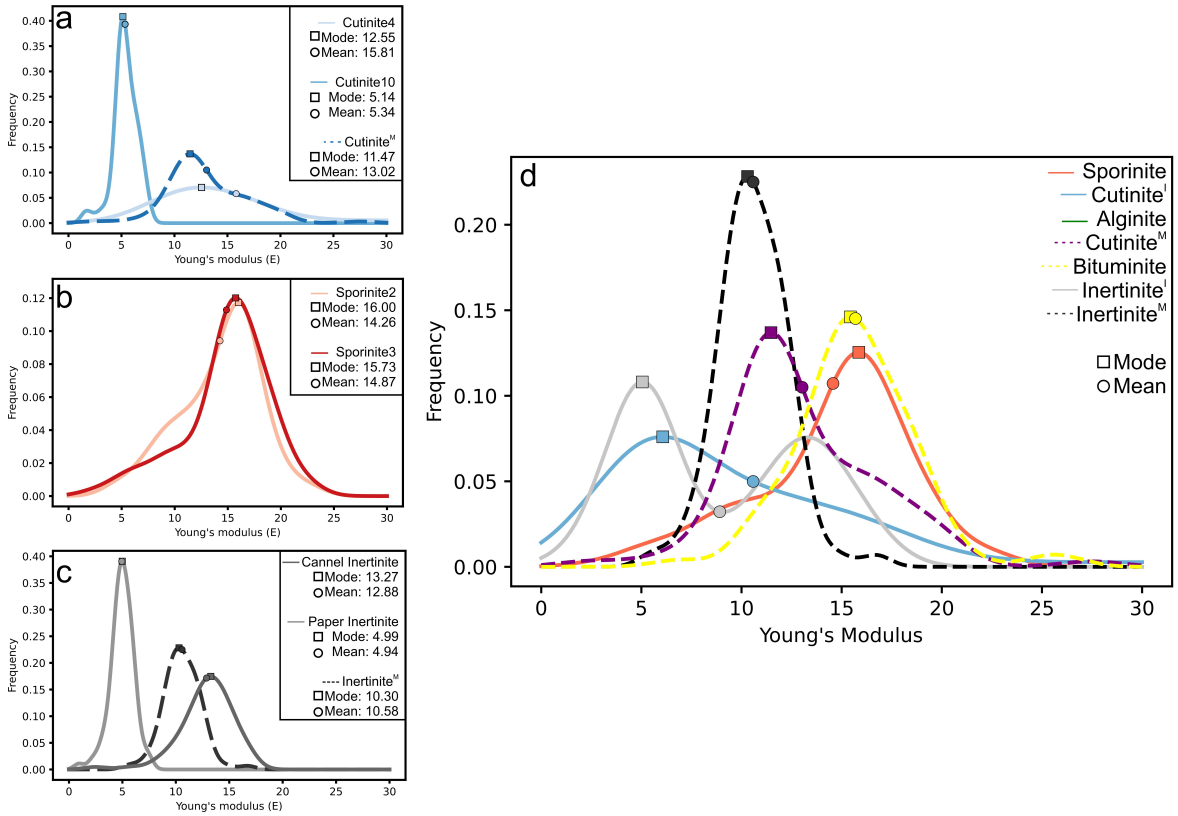

Figure 3.12: Probability density functions of Nanoindentation data collected on each coal maceral. Figure a indicates the modulus distribution of cutinite in the immature and mature coals, b indicates the distribution of sporinite within the paper coal, c, the distribution of inertinite measured and d, the overall distribution of all macerals across each coal. ^{I} and ^{M} indicate immature and mature coals macerals.

Neither the inertinite or cutinite show any signs of evolution with maturity as in both cases the mature sample has a modal modulus between the modal moduli of the two immature samples. This is in contrast to what is observed in the AFM scans on the same coal samples, where there was a general trend of increasing Young's modulus between immature coal macerals and mature coal macerals. The same trend is not observed in Figure 3.12d, where the modal moduli of the mature macerals (inertinite mode: 10.3GPa, cutinite mode: 11.5GPa & bituminite mode: 15.4GPa) are in the same region as the modal moduli of sporinite and of the stiffer peak in immature inertinite.

All scans apart from mature cutinite and sporinite are normally distributed, which is due to

the averaging effect of the central limit theorem of multiple components mentioned previously. It is likely that the mature cutinite and the sporinite scans have multiple normally distributed components, which are significantly different in terms of mean and standard deviation, which in turn, would lead to a non-normal distribution as two statistically different normal distributions merge.

3.3.8 Comparisons Between AFM and Nanoindentation Results

Figure 3.13 presents a comparison of the modulus distribution of each maceral when analysed by AFM, a 5 micron AFM mean (Section 3.3.5) and nanoindentation. It is notable that the nanoindentation results appear to be significantly different to the results acquired by AFM in all macerals apart from immature cutinite and immature inertinite. Aside from this, there is a clear and obvious similarity in the AFM data in most macerals, with the same means, albeit slightly different modal values. In spite of an increase in the modal value of the distributions when the 5μm average is used, these values are generally lower, and in some cases considerably lower than the modal value obtained by nanoindentation. The reason for this could be two fold: firstly, due to the modulus of the tip, the nanoindenter is capable of measuring Young's modulus values of the mineral inclusions in any of the coals, which would naturally increase the effective modulus measured. Secondly, the nanoindenter measures a 3-dimenional modulus around the indent, rather than just the surface 2-D modulus measured by the AFM, as such the effect of any mineral matter would most likely be exaggerated in this method.

While this theory is a possible explanation, there appears to be relatively little mineral matter, or areas above the limit of the AFM tip in the immature sporinite or mature cutinite in Figure 3.6. The optical microscopy images (Figure 3.1) also show relatively little mineral matter. Therefore, the increases in modulus, particularly in the sporinite, are unlikely to be caused by fluctuations in mineralogy.

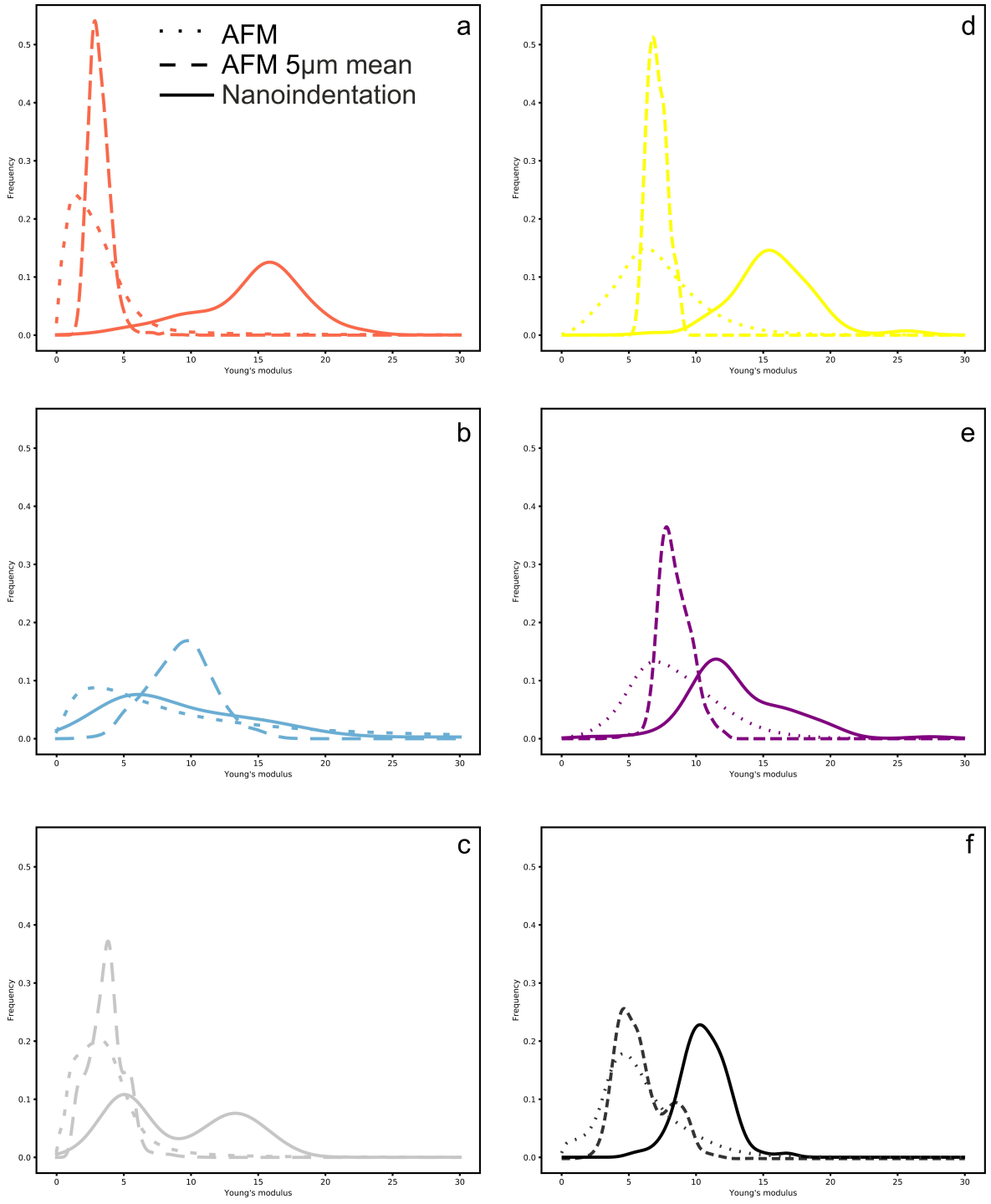

Figure 3.13: Young's modulus distributions of each maceral when analysed with AFM (spotted line), AFM 5μm^2 area (dashed line) and nanoindentation (solid line). The scans recorded are a.) immature sporinite, b.) immature cutinite, c.) immature inertinite, d.) mature bituminite, e.) mature cutinite and f.) mature inertinite.

3.3.9 Limitations of this Nanoindentation Dataset

As mentioned previously, there are clearly two distributions within the cutinite nanoindentation dataset and three distributions in the inertinite dataset. This same bi/trimodality is not readily observed in the AFM data. The influence of other minerals whilst not discounted, is believed to be unlikely to cause this distribution anomaly. Further reference to the data indicates a situation where the nanoindenter assemblage/ tip have been altered significantly between the two sets of measurements. Figure 3.14 indicates the modulus distributions of each maceral scanned within this study, as well as a related MSc project; Tyson (2019), which used nanoindentation on an area of the same Northumberland Coal sample used for this study. As can be seen in the figure the distributions of Young's modulus of Cutinite10 and the paper coal inertinite are intrinsically similar to the modulus distribution obtained by Tyson (2019). The nanoindentation tests done at a later date are stiffer, and less Normally distributed. It is not apparently obvious as to which of the results are correct, but the AFM distributions in Figure 3.13 indicate that the softer distributions from the earlier date are more likely to be representative. The reason for this abrupt change is most likely due to damage to the Berkovich indenter, changing the properties of the indentation. Further research may involve using SEM to locate the indentations and look for abnormalities, although conventional SEM techniques may not be optimal for this due to the mono-mineralogic nature of the sample surface, and difficulties locating the indentations. The stiffer nanoindentation results presented here are stiffer in comparison to the literature values, with the reported modulus of <10GPa (Borodich et al., 2015; Kossovich et al., 2016) in similar samples of mostly higher maturities.

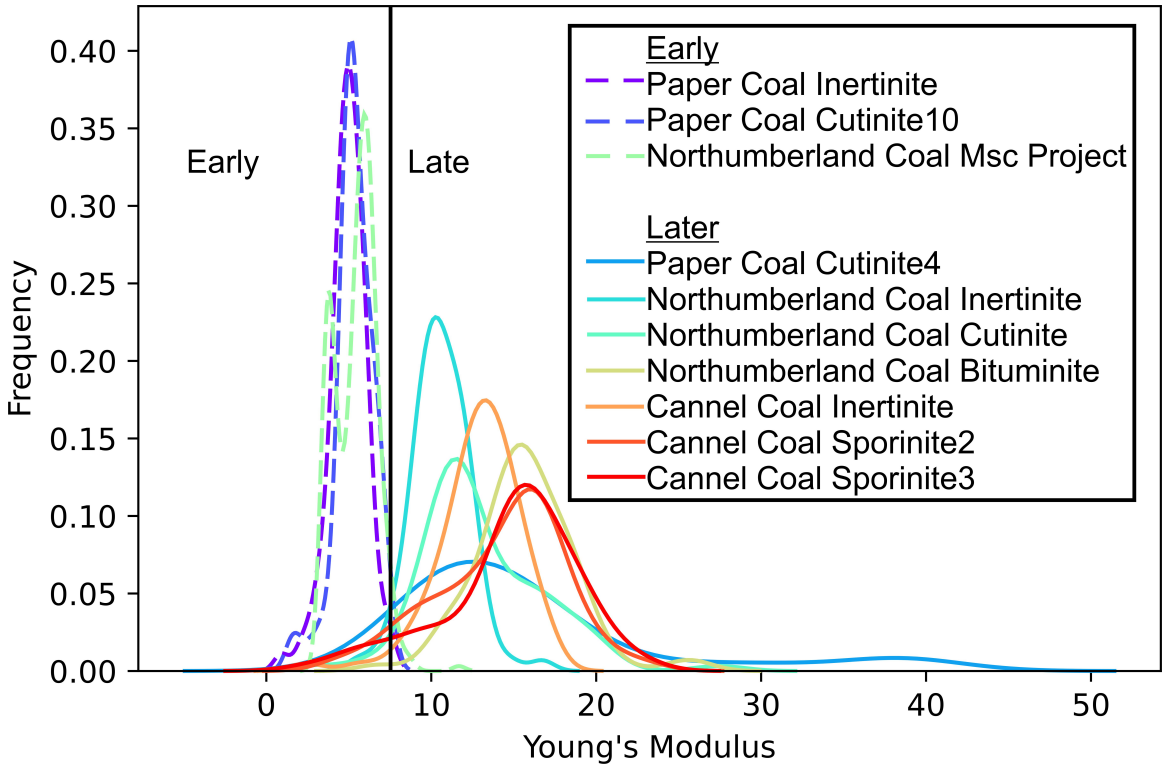

Figure 3.14: Young's modulus distributions of macerals analysed through nanoindentation. The distributions are coded in the form of initial nanoindentation (dashed line), which include the inertinite and Cutinite10 scans from the paper coal and the scans undertaken on the Northumberland coal during an MSc project. The solid line scans are undertaken at a later date and are much stiffer than the nanoindentation results from earlier. The cause of this unknown but is most likely due to either damage to the indenter tip or the machine used to run the nanoindentation.

Studies in the field of materials science have used correction factors to correct for "pile-up", whereby the original surface is displaced into piles around the outside of the nanoidentor, or "sink-in", where the surface around the nanoindenter subsides under the strain (McElhaney et al., 1998; Kese and Li, 2006; Lee et al., 2008). Both "pile-up" and "sink-in" can lead to overestimation of modulus, and possibilities here due to the porous and soft nature of the coal relative to the indenter. Detailed SEM analysis could ascertain as to whether these increased modulus values later are related to pile-up/sink-in, or an odd shape indentation indicating some damage to the tip. It has been noted that the same indentation apparatus was used by Kossovich et al. (2016) on a similar coal sample with no signs of pile-up or sink-in.

3.4 Conclusions

Geomechanical properties of coals are a key determinant as to whether a deep coal seam is suitable for CCUS. Geomechanical properties including Young's modulus determine the yield strength of a coal under injection but also indicate whether a coal will retain permeability during the injection process or swell reducing permeability. As such these properties determine the reservoir quality of a coal for CO_2.

Cutinite, sporinite, bituminite and inertinite macerals were analysed for reduced Young's moudulus using Atomic Force Microscopy. Cutinte and sporinite were tested from immature Paper (0.38%VR_o) and annel (0.39%VR_o) coals from Indiana. Alginite was analysed from the early thermally mature New Albany Shale (0.65%R_o). A thermally mature (1.56%R_o) coal from the Northumberland coal field containing cutinite, bituminite and inertinite was also analysed.

The reduced Young's modulus of the liptinite and inertinite macerals were less than 10GPa, and were found to be non-normally distributed. The liptinite macerals from immature coals had the lowest reduced Young's modulus, with modal values between $1.4 - 3.0$GPa. The equivalent inertinites in each coal have a modal modulus of $1.4 - 3.4$GPa. The Young's modulus of alginite appears to be influenced by the encapsulating resin in which a kerogen isolate slide is traditionally mounted. It appears that the commonly used kerogen preparation technique is an unsuitable for samples for AFM testing. There is a general trend of stiffening with maturity in all macerals. However, this is greatly exaggerated in the hydrogen-rich macerals. The modal modulus value of cutinite increased by 135%, but in comparison, inertinite only increased by 40%, in samples that had %VR_o values between 0.4% and 1.6%.

Analysis of the modulus distributions acquired from each maceral show a degree of non-normality. The immature liptinite macerals were the least normally distributed, with the mature liptinite macerals being the most normally distributed. Distribution matching indicates that a Gamma distribution is the most likely fit for organic matter local Young's modulus in coals. This finding allows classical deconvolution models to be adapted to account for smaller length scales where phases are described by their local modulus distribution.

When upscaling local Young's modulus values to a $25\mu m^2$ area, there were significant in-

creases in the modal Young's modulus values. This is observed due to the inherent shape of the Gamma distribution, where the mean value is greater than the modal value in all macerals. The modal values across each maceral after this $25\mu m^2$ averaging between 2.9GPa in immature sporinite to 9.8GPa in immature cutinite. These values fall within the range of previously observed Young's modulus values of nanoindentation on coal. Therefore this simple homogenisation model represents an effective method of upscaling in mechanically homogeneous systems with only three main phases (maceral organics, mineral matter, porosity).

The macerals were also analysed using nanoindentation, which found an increase in modal and mean effective Young's modulus values for most macerals. However, due a believed fault with the nanoindenation equipment these results appear unreliable. It is not currently clear whether the nanoindentation measured stiffer values than those by the AFM or if the nanoindentation measured the moduli at equivalent stiffness. Further studies should focus on indicating if these two techniques (Nanoindentation and AFM) yield similar results in this relatively homogeneous medium.

The modal Young's modulus values obtained in this study have been applied to the numerical Pan and Connell (2007) model, with all other attributes remaining standard from Levine (1996). This modelling approach indicates a direct inverse relationship between reduced Young's modulus and adsorption related strain. As such the maturity related relationships mentioned previously are also inverse to strain, whereby an immature maceral is likely to swell more than a mature maceral. Swelling of the macerals can either enhance porosity by creating open microfractures where macerals strain relative to the mineral groundmass, or reduce porosity by filling of cleats and existing fractures within the coal decreasing overall permeability. At higher maturities the difference in strain between inertinite macerals and liptinite macerals is less pronounced. Homogeneous mature coals therefore require much less sophistication when modelling, than a system with many differentially swelling components, and most likely reflect a more favourable CCUS target.

Nanoindentation data obtained within this study in general suggests a stiffer modulus distribution than the AFM, which may be due to the intenters ability to capture some of the mineral matter. However, when investigated further there appears to be some form of experimental error

during the acquisition of this data which would leave it unreliable. Literature nanoindentation is generally softer than that obtained within this study, suggesting that the AFM measurements are more likely representative of the macerals studied.

This study provides a first insight into the nanomechanical properties of individual coal macerals at a length scale of approximately 10nm. The results from this study have only been obtained on a small selection of macerals on three coals, therefore future research should focus on broadening the scope beyond this, providing a systematic check of each major maceral subgroups' mechanical evolution with maturity. Any efforts to constrain the variation in Poisson's ratio and organic porosity of coal macerals with maturity and hydrogen content at the length scale below the resolution of a typical nanoindentor, would allow further insight into the effects of gas adsorption/desorption at the nanoscale.

3.5 Contributions

The contributors to this chapter are as follows.

Name/ Institution	Contribution
Jan Hennissen (British Geological Survey)	Palynology advice and assistance
Maria Mastalerz (University of Indiana)	Provided cannel coal, paper coal and New Albany Shale samples. Palynology advice and assistance. Maturity data for New Albany Shale
Aberdeen University	Mercury Injection Capillary Porosity measurements
Ian Chaplin (Durham University)	Thin section and polished block sample preparation
Hassan Gonabadi (Newcastle University)	Nanoindentation assistance
Matthew German (Newcastle University)	Atomic Force Microscopy assistance and advice
Cees Van Der Land (Newcastle University)	Academic support
Mohamed Rouainia (Newcastle University)	Academic support
Martin Jones (Newcastle University)	Academic support
Thomas Wagner (Heriot-Watt University)	Academic support

Table 3.6: List of contributors to this chapter

Chapter 4

An Assessment of the Viability of Different Machine Learning Algorithms for Predicting Shale Young's Modulus Data

4.1 Introduction

The advances in computing technology and processing power since the turn of the millennium has led to significant improvements in the fields of cloud computing, artificial intelligence and machine learning. This leap forward has been particularly significant in the 2010s with the release of a vast array of cloud computing, such as the Google Cloud which first launched in 2008. In the 2010s the energy industry began to utilise machine learning in order to streamline typically expensive procedures such as seismic interpretation (Wang et al., 2018), facies classification (Hall, 2016) and even the reservoir characterisation (Demyanov et al., 2019). Machine learning is important in geoscience as it can be used to make predictions on areas where data isn't available or is limited, which is commonplace in the subsurface.

Machine learning algorithms can be classified into two types, supervised and unsupervised;

supervised models have the classification labels included within the training dataset (e.g. Random Forest), whereas unsupervised models classify without any knowledge of the classification labels (e.g. Principal Component Analysis). There is another classification of machine learning models- instance vs model based learning. The difference between these categories is that the instance based learner saves a subset of the training data to compare to the new data, which allows adaptability, but can lead to overfitting. A common example of this classifier is K-Nearest Neighbour. The model based learner fits a mathematical formula around the training data and then predicts based off the test data. An advantage of this model type is that with large data inputs the model doesn't need to save large amounts of training data, however, on smaller datasets these models can be prone to overfitting. An example of a model based learner is an Artificial-Neural-Network (ANN).

One of the fields of geoscience in which machine learning has been widely applied and highly useful is pattern recognition. This has been used at many levels to identify geologic features, from detecting outcrops in the field (Francis et al., 2014; Shu et al., 2017), to the composition of grains in a sandstone (Maitre et al., 2019), and most significantly characterisation of microscale mineralogy and textures (Wu et al., 2019; Duarte-Coronado et al., 2019; Tang et al., 2017; Su et al., 2020). Studies of petrographic classification have used a wide range of machine learning algorithms and models, from Random Forest (Wu et al., 2019) to Convolutional Neural Networks (CNN) (de Lima et al., 2020), with varying success.

This field of machine learning is particularly important due to the amount of data required for a petrographic study, where hundreds of thin sections may need to be analyzed using both optical microscopy and scanning electron microscopy (SEM). This process is particularly time consuming and leads to petrographic studies routinely requiring more than 1000 man-hours. Therefore efficiency gains that can be made using machine learning are extremely important. Machine learning in the form of pattern recognition is particularly useful as a first pass with initial basic classifications allowing the man-hours to be spent on more specialised interpretations.

Along with being used to make first pass observations, machine learning is important to make predictions on incomplete datasets, which is important with the need for CCUS. Many of the most viable CCUS reservoirs are in conventional oil and gas plays, as such there is a large

amount known about the reservoir, and to some extent the seal. Machine learning can be applied to regions where the seal integrity and geological conditions are less well constrained. This is mainly due to the absence of core material acquired during the initial prospecting or production. The use of machine learning here can be a deal breaker for some less well explored conventional seals, allowing an extrapolation of seal conditions from a mixture of seismic interpretation and analysis of cuttings.

Whilst it is convenient to characterise poorly constrained data using analogue studies, it may be that on the scale of a prospective top-seal that even analogue studies leave large amounts of uncertainty. Therefore using machine learning data to train, test and validate on the information available can leave a model capable of making inferences of the the likely top seal conditions where significantly less data is available. Machine learning algorithms are also capable of dealing with multiple types of data and drawing inferences from them, such as utilising petrophysical data in combination with wellbore data and geochemical data. This leaves machine learning as a valuable asset for potential top-seal leakage modelling, and may be combined with fluid flow models or lithological models readily.

4.1.1 Previous uses of Machine Learning Algorithms for Rock/Mineral Classification

Decision Trees/ Random Forest, which are intrinsically related, have been applied in the fields of shale and coal petrography. A decision tree algorithm classifies the information given based on the amount of information gained, until either it's no longer possible to split the data, or until the maximum branches are reached. More informtation is available in section 4.3.3. Wu et al. (2019) found mean F_1 score accuracies of >0.86 for classification of organic matter, fractures, pyrite and matrix in a single SEM image of shale, using Random Forest. A model's F_1 score is a measure of accuracy that includes the precision and recall of the model. Wu et al. (2019) used Gaussian blur to enhance the segmentation capacity of the Random Forest, which greatly helped in the classification of the 'transition zone' between two phases. Gaussian blur involves convolving data (generally an image) with a gaussian function, to reduce the effects of noise, and make the data 'more seperable'. Rubo et al. (2019) used Random Forest to predict the mineralogy

of reservoir rocks from the Santos Basin. The thin sections were first segmented using Weka Segmentation (for further information on Weka Segmentation readers are directed to Arganda-Carreras et al. (2017)). The segmented images were then passed through convolutional filters before being classified. The resulting Random Forest classification achieved reported accuracies between 90.13-99.97% on a large dataset, comprising over 2,000,000 datapoints. Decision Trees were used by Akkaş et al. (2015) to identify some common igneous minerals using SEM and EDX with accuracies in excess of 96% reported. The study found that boosted Decision Trees were incrementally more accurate than standard Decision Trees, although the increase in accuracy in most reported cases amounted to <1%. A boosted Decision Tree complex, is where single Decision Trees are used as iterative weak learners, which then combine to fit to the residual error from the previous tree. Random Forest algorithms have also been used in ore geology to assess the prospectivity of gold in south east Spain (Rodriguez-Galiano et al., 2015).

Multi-Layer-Perceptron (MLP) and Artificial Neural Networks (ANN) have also been used to assist in many petrographic studies. Saporetti et al. (2018) have used MLP with 10 Fold Cross Validation, along with Decision Trees, and Random Forest to classify carbonate and sillciclastic rocks from well logs, with maximum accuracies of 87% using a Decision Tree algorithm. They have shown that in geological datasets, balancing of the data may be required, whereby minority classes are artificially enhanced in the training data. This led to a significant increase in accuracy in all the models used, but in particular a >20% increase in the accuracy of the MLP. Wang and Carr (2012) showed the potential use of a classical MLP with stochastic gradient descent to predict facies across the Marcellus Shale. Rubo et al. (2019) reported a high accuracy of 97-99%, using ANN for mineral recognition in the Santos Basin. This accuracy can be attributed to the large training dataset along with the previously mentioned convolutional filters. ANN has also been successfully used on wellbore scale data with R values of 85-86% from petrographic characterisation of a well from the South Provence Basin, France, using elastic, petrographic and mineralogic data (Silva et al., 2015). This data was preprocessed with the Waikato Environment for Knowledge Analysis (WEKA) tool, which implements a variety of preprocessing and data mining tools to assist in obtaining the 85-86% R values.

Deep learning Convolutional Neural Networks (CNN) have been used recently as a method

for classifying mineralogy in shales from SEM. This method has been shown to be useful at estimating porosity from thin sections in unconventional reservoirs, although only reporting accuracies between 64-78% in the method used by Duarte-Coronado et al. (2019) using a series of CNN models, with the major misclassifications occurring between similar porosities. An array of different CNN algorithms have been shown to also be useful in identifying fossils as well as simple differentiation between lithotypes (de Lima et al., 2019). This study reported the highest accuracies on fossil, core and rock sample identification (all >97%). The accuracies reported are significantly lower in petrographic thin section samples (81%). Similar CNN models have also been used to classify igneous minerals from microscope images in plain and cross polarized light, with accuracies of >99% on a selection of igneous rocks (Su et al., 2020). The major inaccuracy in the study being a misclassification of diorite and granite, which are both course grained and similar in mineralogy.

It is important to separate the models above from the results obtained by Support Vector Machines (SVM) and K-Nearest Neighbours (KNN), as these methods of machine learning, do not apply a mathematical model to the data, but fit each dataset by statistical parameters, generally measuring the euclidean distance between points for classification. Nevertheless these methods have been shown to be effective at classifying rock fabrics and mineralogies (Saporetti et al., 2018; Wang et al., 2014).

All of these methods report high accuracies on similar data, i.e. SEM scans of the same shale/ reservoir from one particular well, or from one formation. There has been little attempt to combine the feature classification models used on SEM with geomechanical predictive models. Li et al. (2019) used a combination of finite element modelling and ANN by Li et al. (2019) to attempt this where few else have. Their efforts combining CNN with a stochastic finite element model to generate effective modulus data produces cross validation error <3%. The modulus values are generated from a nanoindenation, and the CNN used on SEM images, and classified into silicate, carbonate, clay, kerogen and other.

4.1.2 Machine Learning for Geomechanical Prediction

Geomechanical prediction through machine learning has been less well studied in the petroleum industry, as such there is significantly less literature on this use of machine learning. Machine learning has been used to predict and interpret wellbore/wireline logs. A Long-Short-Term-Memory ANN has been used to learn and predict the geomechanical properties from wellbore wireline logs in North Dakota's Williston Basin, specifically focussing on the physical possibility of the results, to avoid impossible results (Chen and Zhang, 2020). (Khatibi and Aghajanpour, 2020) used an ANN to predict shear and sonic logs in an gas field in southern Iran, with an R^2 value of 0.89, across multiple lithologies. Random Forest has been used in coal geomechanical prediction, with Matin et al. (2016) obtaining a predictive R^2 of 0.9 when predicting the Hardgrove Grindability Index on coal samples, with 1000 trees providing peak accuracy.

MLP and ANN have been used to a greater extent in predicting the geomechanical properties of shales and other rocks in comparison to other machine learning algorithms. Armaghani et al. (2014) used an particle swarm optimization ANN to predict shale shear stress with R^2 values between 0.88 and 0.96. Moshrefi et al. (2018) use a regular ANN to predict the ultimate strength of an Iranian shale with an R^2 of 0.92. Genetic algorithm-ANN has also been used to estimate the friction angle of Malaysian black shales with R^2 values >0.9 (Shao et al., 2019). The ANN has been used to predict geomechanical properties of shale reservoirs from wireline data by Li et al. (2018b), using a network of two hidden layers comprising 9 and 5 neurons in each layer. This study reported an R^2 value of 0.85 in one well. MLP has been also been used as an alternative to the Random Forest method to predict grindability of coals (Bagherieh et al., 2008; Chelgani et al., 2008).

4.1.3 Aims of this Study

Many machine learning algorithms have been used for SEM classification, and to a lesser extent, geomechanical prediction. Here we present the first study combining the two, at the resolution of an AFM, allowing prediction of individual phases and crystals within the shale. Mechanical properties linked to phase prediction are important for CCUS seal integrity studies, giving insight

into the most likely fracture propagation routes in a complex shale and highlighting where soft and stiff phases are juxtaposed. As part of this study we aim to use a detailed dataset comprising over 11,000,000 individual pixels in 10 dimensions, to train and test the accuracy of a series of machine learning algorithms.

Although it may be useful to train an algorithm on a large dataset to produce high accuracies, there is a tendency in more complex models to overfit to this data. As such we aim to use an unrelated dataset from Goodarzi et al. (2016, 2017), which comprises a fundamentally different shale to indicate the generalizability of these models, and to therefore suggest, which model is best suited for a wider spread of data. A key factor in which model is most accurate, is not only the accuracy of phase prediction, but also the accuracy of Young's modulus distribution prediction for each phase. These measurements are most likely related, but the overall test is modulus prediction.

A series of algorithms that can accurately predict the Young's modulus and phase distributions within a rock cutting can readily assist in upscaling. This could be undertaken as a first pass to a more complex homogenization model, providing the geomechanical, geochemical and grain size data for the model. This combination of pattern recognition machine learning and homogenisation may combine to increase accuracy of geomechanical predictions in cap rocks where triaxial experiments are not possible.

4.2 Shale Data and Depositional Environment

The data used for machine learning in the study are from three shales; Eagle Ford, Green River and Posidonia. In total twenty three AFM scans and associated SEM/ EDX images are used for model training and testing. These comprise sixteen scans from the Eagle Ford shale and four from the Green River shale. Three scans of the Posidonia shale are used for further validation. Details of the depositional environment and likely mineralogy of the Green River and Eagle Ford shales are included in Section 2.2. SEM and AFM scans of the Eagle Ford and Green River shale used here are included in an online repository at `https://figshare.com/s/2c5d0b1235068bc38c6e`

4.2.1 Posidonia Shale

The Posidonia shale was deposited in a marine setting during the Toarcian epoch of the Jurassic. The data used here are from a previous study by Goodarzi et al. (2016, 2017) and are indicated to comprise between 28-50% calcite, 7-16% quartz and 19-31% clay minerals (Mathia, 2015). This is a similar mineralogy to the Eagle Ford and Green River, however initial SEM (Figure 4.1) indicate that the fabric of the Posidonia is very different to the other shales. SEM analysis indicates the Posidona contains an increased amount of clay minerals than the other two shales, and two of the three scans have appear to have little to no calcite, instead the non organic, non phylosilicate fraction is dominated by quartz. The AFM scans and SEM images of these samples are also taken at higher resolution than those within the other two shales. Further differences regarding the preparation methods and analytical techniques are mentioned in the section below.

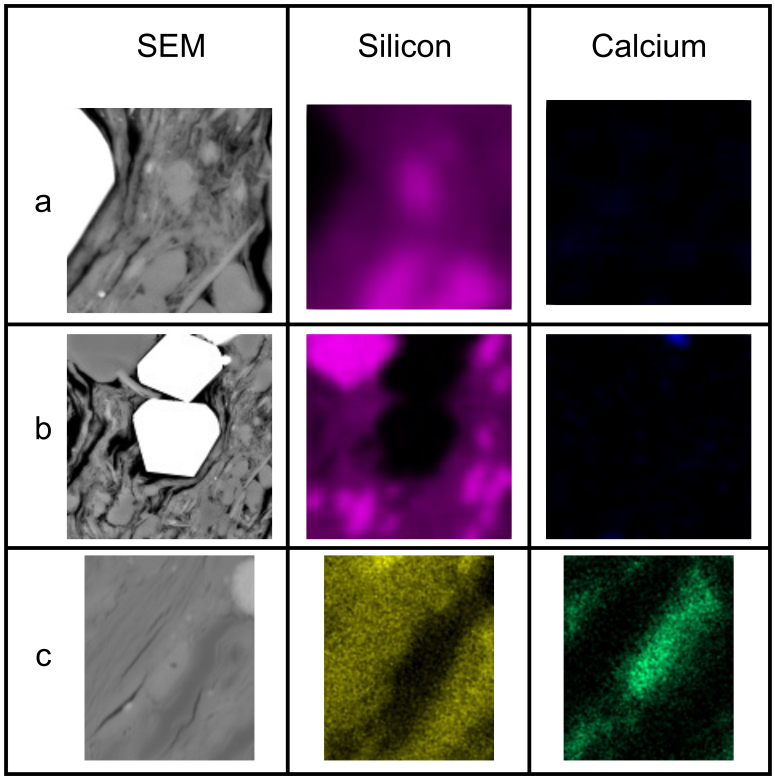

Figure 4.1: SEM and EDX images of the Posidonia scans used in this study. Scan *a* is referred to as 24/2-007, Scan *b* referred to as 24/2-010 and Scan *c* is referred to as 29/2-008 in later sections of this study. There is a notable lack of Calcite in scan *a* and *b*, whilst scan *c* shows an a few calcite crystals in the scan. Scan *c* is notably less clear than the other scans.

Figure 4.1 includes the SEM and EDX scans of the Posidonia used for validation. There is an obvious lack of calcite in the samples 24/2-007 and 24/2-010 with no calcium peak in the equivalent EDX scan, however, sample 29/2-009 has a calcium peak in the EDX where there are calcite crystals. The other major observation is the difference in SEM quality between the very clear scans of samples 24/2-007 and 24/2-010 and the poor exposure of the sample 29/2-009 scan. This may affect the ability of the machine learning algorithms discussed later.

4.2.2 Shale Data Acquisition (Techniques and Methods)

The shale samples from the Eagle Ford and Green River were prepared as thick sections, and mechanically polished with Alumina crystals with a minimum size of 0.5μm. These samples were then subjected to broad ion beam milling using a GATAN PECS II^{TM}(Precision Etching and Coating System) at Sheffield University to produce a flat surface.

In contrast to the Green River and Eagle Ford the Posidonia samples were prepared as a transmitted electron microscopy (TEM) disk, which are thinner than the thick sections made from the Eagle Ford and Green River. These TEM sections were polished using a GATAN 691 PIPS^{TM}(Precision Ion Polishing System) at Durham University.

The SEM/EDX images on the Eagle Ford/Green River were taken using an FEI Quanta FEG 650 SEM at a vacuum of 0.82 torr and a beam acceleration of 15-20Kv.

The AFM measurements on the Eagle Ford/ Green River samples were taken using a silicon nitride RTESPA-525 with a working limit of 30GPa using a JPK AFM QI^{TM}, further details of which can be found in Section 2.3. The comparative measurements on the Posidonia were made using a DNISP diamond tip with a working limit >1TPa, on a Bruker PeakForce^{TM}. As such, only the Posidonia sample Young's moduli distributions will be compared later in this study.

4.3 Methods and Models

4.3.1 Data Preparation

The sample dataset comprises 23 SEM images and complimentary EDX and AFM data. Each SEM image/ AFM scan has a pixel size of approximately 100x100nm in the Eagle Ford and

Green River, with the pixel size varying between approximately 62.5x62.5nm and 78x78nm in the Posidonia samples. The data for each image (SEM, AFM and EDX) were categorised into the eight most common components across all of the shales: porespace, organic matter, clay, dolomite, quartz, calcite, feldspar and pyrite. Fortunately during this study there were no other minerals in large quantities across the shale SEM scans. The minimum elemental data required for this process are Aluminium, Carbon, Calcium, Iron, Magnesium, Oxygen, Potassium, Silicon and Sulphur. Two of the samples from the Posidonia contained no carbon EDX signal and as such there were only seven phases in the classification, with porespace and organic matter combined. Details of the number of pixels and classification are included as Tables 4.1 & 4.2.

Total Number of Training Pixels	5,375,488
Number of Green River Pixel	919,040
Number of Eagle Ford Carol Pixels	2,359,296
Number of Eagle Ford Cinco Saus Pixels	2,097,152
Number of Posidonia Pixels	136,192
Number of Pixels Unclassified from Initial Segmentation	180,613

Table 4.1: The number of pixels associated with each shale sample set, the Eagle Ford is common and comprises over 75% of the training dataset, whereas the validation dataset is small in comparison.

Phase	Training/ Test Dataset	Validation Dataset
Number of Organic Pixels	101,884	1,181
Number of Porespace Pixels	119,669	9,448
Number of Organo-Pore Pixels	N/A	8,799
Number of Clay Pixels	1,808,020	67,407
Number of Dolomite Pixels	318,291	0
Number of Calcite Pixels	2,864,917	2,078
Number of Quartz Pixels	5,953	33,232
Number of Feldspar Pixels	68,687	0
Number of Pyrite Pixels	88,067	14,047

Table 4.2: The total number of datapoints classified as each phase post segmentation. There is an obvious enrichment in calcite and clay within the training dataset, which is different to the large amount of quartz in the validation dataset.

Due to the mixed appearance of the SEM images from different shales, due to different voltages and vacuums, it is important to attempt to normalise the reflection of the shales in order to assist the machine learning algorithm in its determination of each phase. Normalising the reflectivity of the SEM scans also assists in the initial segmentation procedure documented

below.

The upper and lower greyscale bounds (where applicable) for each phase present in all of the 20 scans of the training data (Eagle Ford and Green River), were standardized using the following Equations:

$$x_{min-max} = \frac{x_i - x_{min}}{x_{max} - x_{min}} \tag{4.1}$$

Equation 4.1 is the minimum-maximum scaling where x_{min} is the minimum value of x and x_{max} the maximum value of x.

$$x_{standard} = \frac{x_i - \mu}{\sigma} \tag{4.2}$$

Equation 4.2 is a standardization where μ represents the mean of the data and σ the standard deviation.

$$x_{robust} = \frac{x_i - Q_1(x)}{Q_3(x) - Q_1(x)} \tag{4.3}$$

Lastly, Equation 4.3 is a normalisation using the robust scaler, which scales according the interquartile range, as such $Q_1(x)$ refers to the first interquartile of x and $Q_3(x)$ the third interquartile of x.

It is notable that organic matter and porespace were combined into one phase for this standardization as both have similar greyscale values across the SEM scans analysed. Each of these techniques was analysed across the range of SEM scans with the results displayed as Figure 4.2. It is clear that the min-max scaler is the poorest technique to standardize the SEM dataset, with large standard deviations in calcite and pyrite, along with a large amount of outliers (circles in Figure 4.2). Equations 4.2 and 4.3 give similar results, but for this study we use the standard scaler (Equation 4.2) due to the large error on the organic matter and porespace upper limits when using Equation 4.3, which could lead to misclassification under most models.

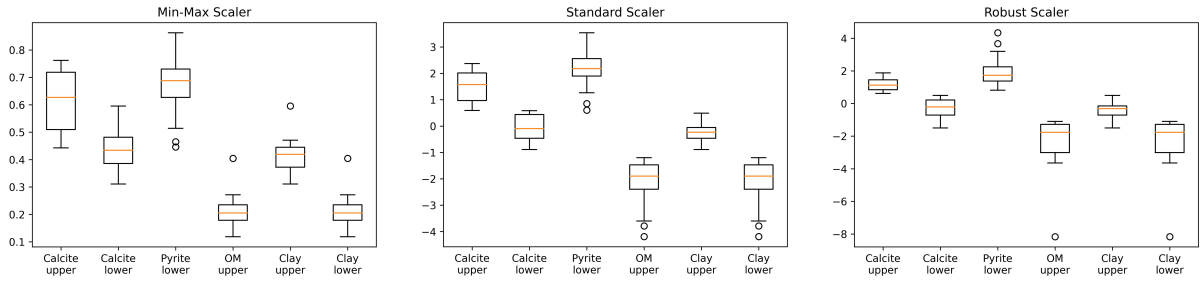

Figure 4.2: Analysis of the possible scaler distributions for use with this data. The graphs show the mean boundaries of each phase on each of the scalers. The standard scaler and robust scaler are similar apart from the outlier in the organic matter upper phase boundary on the robust scaler. Feldspar was not included in this as it did not appear in every SEM scan. Organic matter and porespace are combined as organics, due to having a similar greyscale value under SEM.

The min-max scaler has been used to standardise the EDX data in order to identify enrichments in elements. The min-max scaler appeared to be more consistent when comparing elements with different absolute minimum and maximum intensities, and gave greater consistency when used for mineral thresholding and classification. This theoretically would assist in the machine learning classification of each phase, by reducing the inherent variability between a single phase across multiple SEM scans, and between the different shales.

4.3.2 Segmentation

The data was segmented to give each pixel a probable phase value. This was achieved by first determining the minimum and maximum (where appropriate) greyscale pixel value for each individual mineral on each SEM scan. Efforts were made to avoid overlap between the pixel values of different minerals, but with a greyscale image this is unavoidable. An indication of the rank of SEM greyscale pixels along with further information on EDX enrichments is included as Figure 4.3.

Each individual pixel was therefore given one possible phase name, at which point the EDX values were filtered through a min-max scaler, and were compared to a series of thresholds for segmentation. Details of each mineral threshold are included in Table 4.3. In this, organic matter and porespace are differentiated based on the abundance of carbon, clay and dolomite are segmented on the bases of an enrichment of either aluminium or magnesium, calcite and quartz are separated from either other based on an enrichment of calcium or silicon respectively.

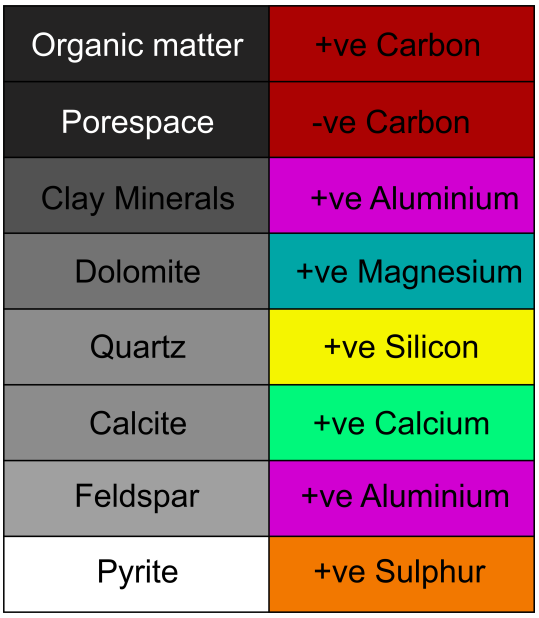

Figure 4.3: Relative brightness in ranks of segmentation and mineral enrichment for classification

Feldspar is generally brighter than calcite but is segmented from calcite by an enrichment in aluminium and pyrite requires relatively little EDX for segmentation but is enriched in iron and sulphur.

Mineral	SEM colour	EDX value (after min-max scaling)
Organic Matter	Dark/Black	C >0.5
Porespace	Dark/Black	C <0.5
Clay	Dark Grey	Al >0.5 & Al>Mg
Dolomite	Dark Grey-Grey	Mg >Al
Calcite	Grey-Light Grey	Ca >0.5 & Ca>Si
Quartz	Grey-Light Grey	Si>Ca
Feldspar	Light Grey	Al>0.5
Pyrite	Light Grey-White	Fe & S>0.5

Table 4.3: The criteria for segmentation for each mineral

The method above allowed classification of most pixels, and any remaining pixels were unclassified. In order to generalize this process and reduce the amount of time required, particularly at edges in low resolution SEM images, a K-Nearest Neighbours unsupervised classifier (for further information see Section 4.3.3 below) was used to draw in the grain boundaries. The total number of pixels left unclassified that required classification using the KNN algorithm was 180,613, which represents approximately 3% of the overall training/testing dataset.

The low resolution used in these images is due to the limited relative resolution of the AFM data, and the need to keep the SEM/EDX data at the same resolution as that AFM data. This method avoids the need for pooling when using models later on, which may in turn lead to overlapping pixel values across multiple AFM results.

Segmentation of quartz in these scans was difficult, primarily due to the high proportion of calcite and therefore calcium within the samples, which combined with the relatively low resolution EDX data, meant that the silicon EDX distribution was generally not greater than the calcium across areas comprising more than one crystal.

4.3.3 Machine Learning Models

Within this study, six major machine learning models were used. Details of each are found within the following sections. These models were selected primarily on their previous use in the literature for other discriminant classifications. The models range from the basic perceptron to a complex series of neural networks. As such a range of both computational complexities but also classifiers are used. Details of each model are found in the following sections.

K-Nearest Neighbours

K-Nearest Neighbours (KNN) memorises the entire dataset in order to make new predictions and as such, doesn't use a discriminant function in order to analyse the data. What the algorithm does is plot the data in n-dimensional space and use the number of nearest neighbours to assign a class to that data point. The KNN algorithm uses a majority vote on the nearest neighbours in order to assign a class to the data point. In the event of a draw, the class is defined by a distance measurement, choosing the closest of the two (or more) drawing classes.

The hyperparameters used with the KNN are; the number of neighbours selected and the distance measurement used. In both segmentation and data prediction five nearest neighbours were used. The distance measurement used in all KNN algorithms is Euclidean Distance (Equation 4.4).

$$D(x, y) = \sqrt{\sum_{j-1}^{d}(x_j - y_j)^2} \tag{4.4}$$

Where D is determined as the distance between points x and y in a series j.

Logistic Regression

Logistic Regression is used as a base case model in the sense that it may be used in a node in a Multi-Layer-Perceptron. The model itself uses as probabilistic classification, with the aim of finding the maximum likelihood of an instance forming into a class, in order to learn the model parameters (Aggarwal, 2018). As the current model has many classes (minerals), multinomial logistic regression must be used, this form of model is commonly known as the *Softmax Classifier*. The multinomial logistic regression actually uses a log-likelihood loss function in order to feedback into the model.

This model requires each training datapoint to be represented as ($\bar{X}_i$, $c(i)$), where $\bar{X}_i$ is a vector of the SEM pixel value, EDX values and AFM pixel value for the particular datapoint (i) and $c(i)$ is the class of that datapoint, which is a value between $1 - k$, where k is the number of classes (minerals), in this case eight. This method achieves training by finding k separators (weights), $\bar{W}_1 ... \bar{W}_k$ simultaneously, so that the value of $\bar{W}_{c(i)} \cdot \bar{X}_i$ is larger than $\bar{W}_r \cdot \bar{X}_i$ for $r \neq c(i)$. The label r that has the largest value of $\bar{W}_r \cdot \bar{X}_i$ will be given the class label.

Due to the this method being a probabilistic classification, the class membership is probabilistic and so much have a posterior probability ($P(r)$), which can be attributed through the *Softmax Function* using Equation 4.5 (adapted from Aggarwal, 2018).

$$P(r|\bar{X}_i) = \frac{exp(\bar{W}_r \cdot \bar{X}_i)}{\sum_{j=1}^{k} exp(\bar{W}_j \cdot \bar{X}_i)} \tag{4.5}$$

In order to iteratively refine the model, the stochastic averaging gradient descent (SAGD) method is used, for more information readers are directed toward Schmidt et al. (2017). Cross-entropy loss, which is the negative logarithm of the probability of the true class being chosen, is used by this model in order to backpropagate loss and amend weights accordingly. The equation

for cross entropy loss is as follows:

$$\begin{aligned} L_i &= log[P(c(i))|\bar{X}_i] \\ &= \bar{W}_{c(i)} \cdot \bar{X}_i + log[\sum_{j=1}^{k} exp(\bar{W}_j \cdot \bar{X}_i)] \end{aligned} \tag{4.6}$$

Equation 4.6 was adapted from Aggarwal (2018) and indicates the basic formula for calculating cross-entropy loss (L_i) using the softmax function. However, in order to adjust the weights $\bar{W}_i$, the partial derivative of the softmax function is required, which is included in Equation 4.7 (adapted from Aggarwal, 2018), where $\upsilon_r = \bar{W}_i \cdot \bar{X}_i$.

$$\frac{\partial L_i}{\partial \upsilon_r} = \begin{cases} -(1 - P(r|\bar{X}_i) & \text{if r = c(i)} \\ P(r|\bar{X}_i) & \text{if r} \neq \text{c(i)} \end{cases} \tag{4.7}$$

This gradient descent partial derivative can be used to adjust the weights, using the partial derivative of the probability of the data being labelled with the incorrect class. The above Equation (Eqn 4.7) is used with the regularization parameter (λ) and learning rate (α) to adapt the separator (weights) for the r'th class using the following Equation (adapted from Aggarwal, 2018):

$$\bar{W}_r \Leftarrow \bar{W}_r(1 - \alpha\lambda) + \alpha \begin{cases} \bar{X}_i \cdot (1 - P(r|\bar{X}_i)) & \text{if r = c(i)} \\ -\bar{X}_i \cdot P(r|\bar{X}_i) & \text{if r} \neq \text{c(i)} \end{cases} \tag{4.8}$$

Perceptron

The simple single layer perceptron model is designed in the form of a single neuron in the brain, and was first published by Rosenblatt (1957). In this study, we use a binary perceptron, without an activation function as the most simplistic case for what a perceptron based algorithm is capable of, on the given data. This model comprises k individual perceptrons trained to

recognise one mineral in a *one vs rest* manner. Similar to the multinomial logistic regression model, the perceptron uses the i'th set of values $\bar{X}i$ and initialises weights ($\bar{W}i$) accordingly. The loss function for a perceptron is as follows:

$$\begin{aligned} x &= (\bar{W} \cdot \bar{X}_i) \\ error_i &= \phi(x) - y_i \end{aligned} \tag{4.9}$$

Where $error_i$ is the error, y_i is the binary class of the individual perceptron, ϕ is an activation function (Eqn. 4.10). The error is then backpropagated in order to train the model using Equation 4.11.

$$\phi(x) = \begin{cases} 1 & if\ x \geq 0 \\ -1 & \text{otherwise} \end{cases} \tag{4.10}$$

$$\bar{W} \Leftarrow \bar{W}(1 - \alpha\lambda) + \alpha(error_i \cdot \bar{X_i}^T) \tag{4.11}$$

Where α is the learning rate and λ is the regularization parameter. The model is updated by stochastic gradient descent (SGD), whereby the update of each weight is proportional to its contribution to the final result. This leads to a series of perceptrons, which allow a calculation in a *one vs all* for each of the k classes. It is noted that as the number of classes increases, this model of one vs all for each class would become computationally expensive.

Decision Tree

Decision Tree analyses are done in a similar manner to the thought process of a human when categorising data, the model uses a series of decisions at branches and maximise the information gained (IG) at each branch. For a binary problem (e.g. whether a pixel is black or white) the information gained is indicated in Equation 4.12 adapted from Raschka (2015).

$$IG(D_p, f) = I(D) - \sum_{\nu \in values(A)} \frac{|D_\nu|}{|D|} I(D_\nu) \tag{4.12}$$

Where f represents the feature to split (e.g. Carbon pixel value in EDX), D_p represents the total values entering a node and D_ν is the total number of values that are positive or negative for that classification at that point. An example of this is indicated in Figure 4.4, I in this Equation represents function to generate the impurity at a node, which is the GINI impurity (Equation 4.13), which aims to minimize the probability of mis-classification.

$$I_{GINI} = 1 - \sum_{i=1}^{c} p(i|t)^2 \tag{4.13}$$

Equation 4.13 above indicates the impurity of a proportion of examples $p(i|t)$ belonging a class i at a node t.

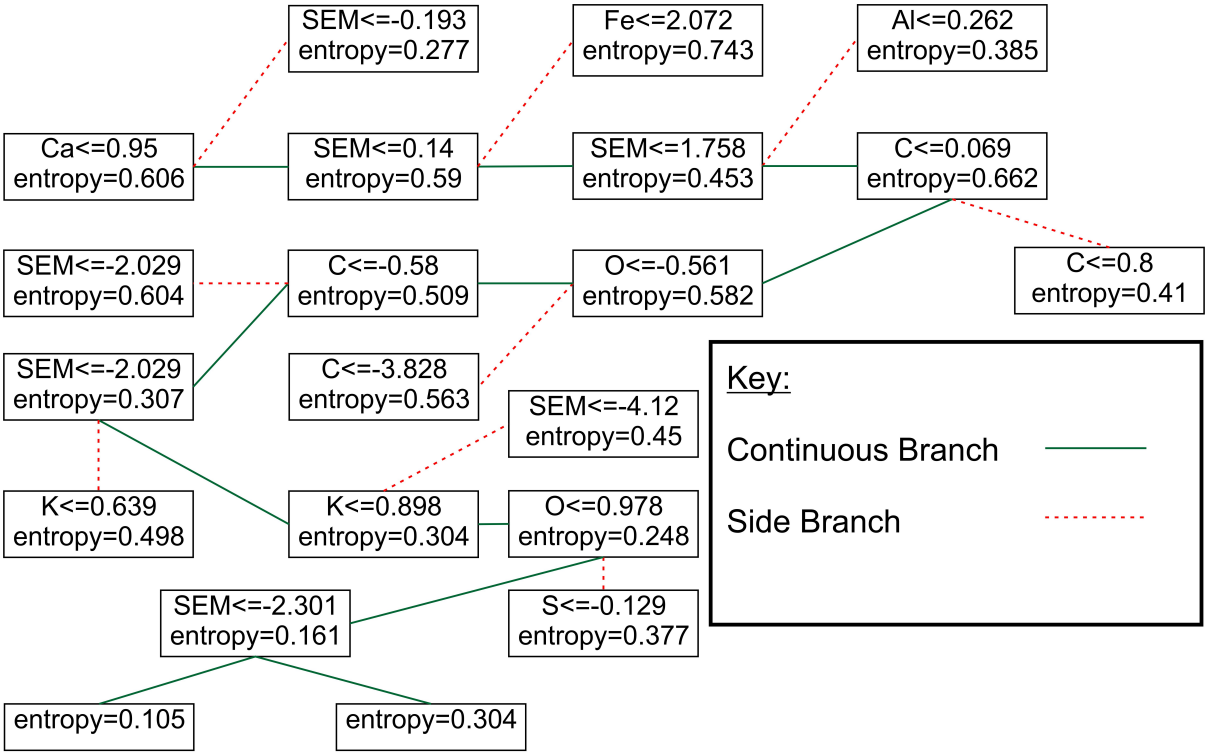

Figure 4.4: An indication of one single stem in the Decision Tree used for this study. Ten separate branches are shown with the alternate path for one branch also indicated. The sorting criteria for each node is also shown along with the entropy.

The core advantage of the Decision Tree and the Random Forest mentioned later is that these

models don't require the data to be normalized or standardized prior to learning or testing. The hyperparameter of Decision Trees not discussed so far is the maximum number of branches, which in this study has been set at 10 to be similar to the Random Forest, meaning the Decision Trees must end after 10 branches as indicated in Figure 4.4.

Random Forest

Random Forest involves the stochastic iteration of Decision Trees to reduce bias and increase generalization. As such the Random Forest is similar in architecture to a Decision Tree whereby decision is made based on information gained from Equation 4.12, to satisfy the GINI impurity (Equation 4.13).

Random Forest uses an ensemble of Decision Tree classifiers $h(x, \Theta_k), \quad k = 1...$ (Breiman, 2001), where Θ_k are independent variables in vector form and each Decision Tree casts a vote for the most popular class at x (Breiman, 2001). A training set of data (d_j) is then drawn in a bootstrap manner from the total data ($d = (x_1, y_2), ..., (x_N, y_N)$), with $(x_i, 1), ..., (x_j, p)$ representing the input prediction pairs of training data (adapted from Cutler et al., 2012). This bootstrap is then run through j Decision Trees and the the response ($\hat{h}_j(x)$) is compared across the trees giving a most popular class prediction of value x (Breiman, 2001; Cutler et al., 2012). The hyperparameters required for Random Forests are the number of Decision Trees that are simultaneously linked (h), for this study 100 has been selected as the optimal amount obtained by cross validation through gridsearch. A second hyperparameter is the depth of Decision Tree required, which in this study has been set to be a value of 10 for computational efficiency.

Multi-Layer-Perceptron (MLP)

Multi-Layer-Perceptron (MLP), often referred to as a type of Artificial Neural Network (ANN), and is a model defined by a series of layers, of perceptrons, which give a traditionally 2D classifier the ability to deal with non linear multidimensional data. The means by which this is achieved is to use multiple layers of perceptrons, each with a non-linear activation function and feedback error using backpropagation, whereby the magnitude of the error backpropagated is proportional to the weight of the activation function at that neuron. Further details of this are included in

Figure 4.5.

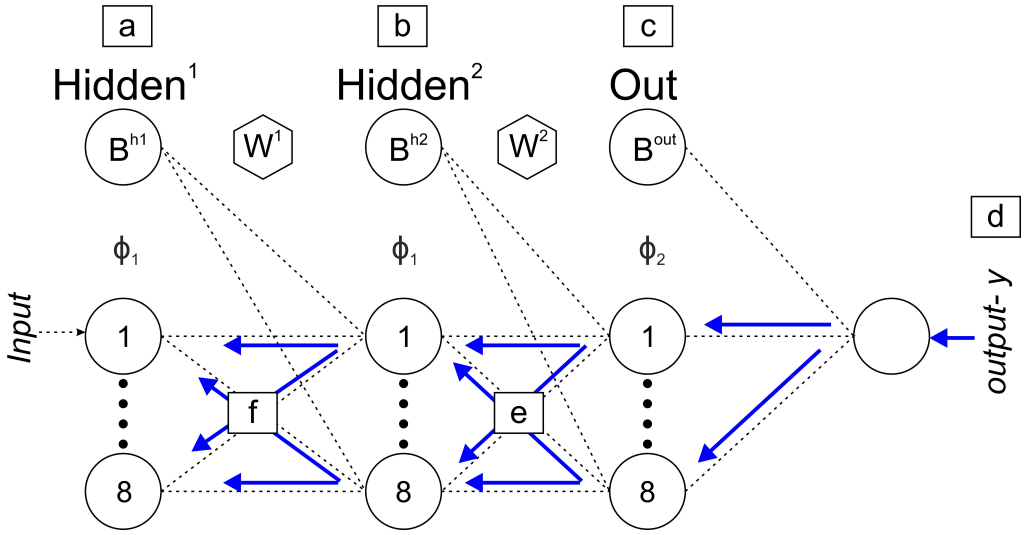

Figure 4.5: The Multi Layer Perceptron used in this study, comprising of two hidden layers with eight neurons in each. In this study ϕ_1 is the tanh function (Equation 4.14) and ϕ_2 is the softmax function (Equation 4.5). Black dashed lines represent the travel of data in the feedforward loop in Equation 4.16, blue arrows indicate the back propagation of the error in Equation 4.17.

For the neural network used in this study, a network of two hidden layers with eight neurons in each layer has been chosen empirically, each with a seperate bias neuron added to prevent the network being stuck in a local minima. For this, a cross validation gridsearch has been used to identify the most appropriate combination of activation functions from common functions used for multidimensional data (sigmoid, tanh, softmax). The activation functions used in this MLP are indicated in Figure 4.5, whereby the tanh function is used for the hidden layers (ϕ_1), and the softmax function (ϕ_2) is used for the output nodes.

The method for feeding forward through a neural network is demonstrated in Equation 4.16 (adapted from Raschka, 2015) and Figure 4.5. This process involves passing the initial standardized data through the *tanh* activation function (Equation 4.14) (Figure 4.5 point a). The results of this are then multiplied again using the dot product with another set of weights and bias and fed through another *tanh* activation function (Figure 4.5 point b). This final product is then passed through a final *softmax* function (Equation 4.5) (Figure 4.5 point c). The output is then compared with the actual segmented results (Figure 4.5 point d) and the cost is calculated using the *Adam* loss function due to it's computational efficiency, and well

established viability to produce superior results to classical stochastic gradient descent (Kingma and Ba, 2014).

Once the error has been obtained, the neural network can adjust the weights using back-propagation (Equation 4.17). The resulting error ($\delta^{(out)}$) is combined in the dot product with the weights from the output ($W^{(out)}$) and multiplied element wise with the first derivative of the softmax activation (Equation 4.6), of the data produced at the second hidden layer (Figure 4.5 point e). The resulting vector, is then multiplied with the transposed matrix of the weights from the second hidden layer, which are multiplied element-wise with the partial derivative of the tanh function (Equation 4.15); the output of the first hidden layer passed as the function data (Figure 4.5 point f). These backpropagated errors are the results of the partial derivative of the cost function, and as such gives the gradient change (Δ). This is combined with the regularization function of the weight, to give an overall change of weight, which is subsequently subtracted from the initial weight.

The following are the documentation of each activation function used in this MLP and the Adam loss function. The tanh function is defined as:

$$tanh(x) = \frac{\exp^{(x)} - \exp^{(-x)}}{\exp^{(x)} + \exp^{(-x)}} \tag{4.14}$$

With the partial differential:

$$\frac{\partial}{\partial x} tanh(x) = 1 - \frac{(\exp^{(x)} - \exp^{(-x)})^2}{(\exp^{(x)} + \exp^{(-x)})^2} \tag{4.15}$$

The softmax function is implemented in the output layer of the MLP in a similar manner to which is is in the simple perceptron through Equations 4.5, 4.6 and 4.8.

The following Equations 4.16 and 4.17 demonstrate the mathematical representation of feed-forward and backpropagate respectively.

$$
\begin{aligned}
a^{(in)} &= \phi_1(input) \\
z^{(h1)} &= a^{(in)} \cdot W^{(h1)} + B^{(h1)} \\
a^{(h1)} &= \phi_1(z^{(h1)}) \\
z^{(h2)} &= a^{(h1)} \cdot W^{(h2)} + B^{(h2)} \\
a^{(h2)} &= \phi_1(z^{(h1)}) \\
z^{(out)} &= a^{(h2)} \cdot W^{(out)} + B^{(out)} \\
a^{(out)} &= \phi_2(z^{(out)})
\end{aligned}
\tag{4.16}
$$

Where $^{(in)}$, $^{(h1)}$, $^{(h2)}$ and $^{(out)}$ represent the layers of the MLP from Figure 4.5. W and B represent the weights and bias at a given layer, ϕ_1 and ϕ_2 represent the activation functions tanh and softmax respectively.

$$\begin{aligned}
\delta^{(out)} &= a^{(out)} - y \\
\delta^{(h2)} &= \delta^{(out)} \cdot (W^{(out)})^T \times \frac{\partial \phi_2(z^{(h2)})}{\partial z^{(h2)}} \\
\delta^{(h1)} &= \delta^{(h2)} \cdot (W^{(h2)})^T \times \frac{\partial \phi_1(z^{(h1)})}{\partial z^{(h1)}}
\end{aligned}$$

$$\begin{aligned}
\frac{\partial}{\partial W_{i,j}^{(out)}} J(W) &= a_j^{(h2)} \cdot \delta_i^{(out)} \\
\frac{\partial}{\partial W_{i,j}^{(h2)}} J(W) &= a_j^{(h1)} \cdot \delta_i^{(h2)} \\
\frac{\partial}{\partial W_{i,j}^{(h1)}} J(W) &= a_j^{(in)} \cdot \delta_i^{(h1)}
\end{aligned} \tag{4.17}$$

$$\begin{aligned}
\Delta^{(h1)} &= ((a^{(in)})^T \cdot \delta^{(h1)}) + \lambda W^{(h1)} \\
\Delta^{(h2)} &= ((a^{(h1)})^T \cdot \delta^{(h2)}) + \lambda W^{(h2)} \\
\Delta^{(out)} &= ((a^{(h2)})^T \cdot \delta^{(out)}) + \lambda W^{(out)}
\end{aligned}$$

$$\begin{aligned}
W^{(h1)} &= W^{(h1)} - \eta \Delta^{(h1)} \\
W^{(h2)} &= W^{(h2)} - \eta \Delta^{(h2)} \\
W^{(out)} &= W^{(out)} - \eta \Delta^{(out)}
\end{aligned}$$

Where y is the classes to be tested against, ∂ represents the partial derivative of each activation function ($\phi_{1/2}$), $J(W)$ represents the cost function which in this model is crossentropy (Equation4.6), Δ represents the weight adjustment at a given layer, λ is the Level 2 regularization term and η represents the learning rate.

4.3.4 Model Training

The aforementioned models were trained in two different ways. The first method of training involves using 2,500,000 random data points obtained from the entire shale training dataset,

each of which comprise an SEM pixel with the associated EDX pixel for each element and a Young's modulus. These are then randomly shuffled using shuffle algorithm from the Sci-kit Learn (Pedregosa et al., 2011). These 2.5 million datapoints were selected using three random seeds (123, 555 and 999) to estimate the difference in shuffling methods. The data was then split into a train/test data split using the sci-kit learn package train_test_split (Pedregosa et al., 2011), with a 4:1 ratio of training to test data, resulting in a training dataset 2 million pixels in size and a test dataset of 500k pixels in size.

Due to the Green River Shale being poorly represented in the dataset ($\approx$ 900k SEM pixels vs $\approx$ 4million SEM pixels between the two Eagle Ford wells) (Tables 4.1 & 4.2), a second method of selecting the training and test data was also used for comparison. In this method two scans of the Green River Shale and two scanned areas from each well of the Eagle Ford Shale were used as the training and test data. This data was shuffled and drawn in a 4:1 ratio, as with the other method described above. This should remove some degree of bias from the training dataset, which would likely be a majority carbonate in the random seed method due to the majority of Eagle Ford scans comprising carbonate (57% of the overall database).

Cross Validation

As mentioned previously the hyperparameters for all machine learning models have been tuned using 5-fold cross validation. A diagram indicating this procedure is included as Figure 4.6. The principal of this method is to use the entire dataset given (in this case 2,500,000 points) as test and training data. The data is split into 5 folds, each of which is used as the test data for validation once. This process is used to test the accuracy of each model with a series of hyperparameters.



Figure 4.6: A diagram of 5-fold cross validation. The train/test data is split into 5 composite parts each of 500,000 points, which are tested with each hyperparameter to be tuned, using each dataset as the test data once and a part of the train data 5 times.

A list of optimal hyperparameters for each machine learning algorithm obtained through cross validation is included below as Table 4.4. It is notable that the maximum depth of the Decision Tree/ Random Forest along with the number of estimators for the Random Forest were chosen to fulfil both optimal accuracy but also computational efficiency, 500 estimators led to an $\approx 10\times$ increase in run time, with marginal gains ($<1\%$) in overall accuracy.

Model	Hyperparameter	Value
Multinomial Logistic Regression	C	0.1
	Solver	sag
	Penalty	Level 2
Perceptron	Learning rate	0.01
	Penalty	Level 1
	Stopping Criterion	0.01
KNN	Neighbours	5
	Weights	Distance
	Metric	Minkowski
Decision Tree	Crierion	GINI
	Maximum depth	10
Random Forest	No of estimators	100
	Criterion	GINI
	Maximum depth	10
MLP	Hidden Layer 1	8 Nodes
	Hidden Layer 2	8 Nodes
	Activation Function 1	Tanh
	Activation Function 2	Softmax
	Dropout Rate	0.1
	Learning Rate	0.01
	Loss Measurement	Categorical Crossentropy
	Optimizer	ADAM

Table 4.4: Optimal hyperparameters from 5-fold cross validation testing. Further detailed information on these hyperparameters can be found in sklearn/ tensorflow documentation (Pedregosa et al., 2011; Abadi et al., 2015)

4.4 Results and Discussion

4.4.1 Individual Shale Accuracies

Figures 4.7, 4.8 and 4.9 demonstrate the output of the each of the machine learning algorithms on a example scan from each of the Eagle Ford wells and the Green River sample. These figures also indicate the segmented appearance of a the same scan for comparison. Figures of the overall accuracies on the other 20 scans of Eagle Ford and Green River shale are included online at `https://figshare.com/s/2c5d0b1235068bc38c6e`. Tables 4.5, 4.6 & 4.7 indicate the ability of each of the models to predict the individual phases in each shale sample.

Figure 4.7 indicates the perceptron has a poor capacity to correctly identify any of the phases in the Green River, with none of the major mineral boundaries identified. The perceptron model trained on the random seed data classifies most of the sample as either calcite or dolomite. The

perceptron trained on the two-scans of each sample is slightly more accurate, classifying more of the sample as clay.

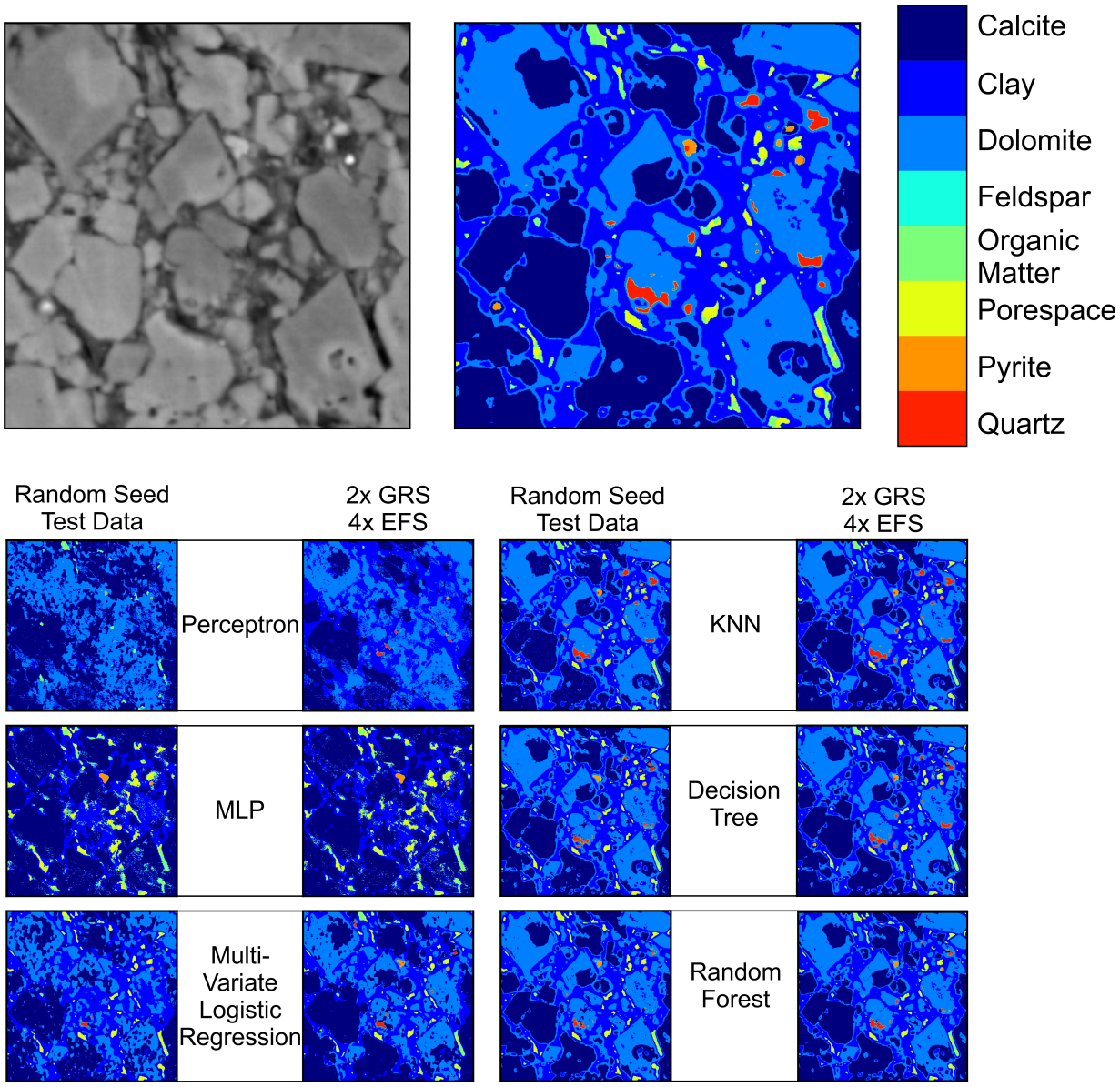

Figure 4.7: An SEM image (a) of the Green River shale with the equivalent initial segmentation (b). The images below indicate the predicted phases of the Green River scan from each of the six machine learning models. Models shown are trained on 2,000,000 random training data (Random Seed Test Data) or trained on 2 scans of each shale as mentioned previously in Figure 4.10 (2x Each Shale).

Model	Relative Fit							
	Organic Matter	Porespace	Clay Minerals	Dolomite	Calcite	Quartz	Feldspar	Pyrite
Decision Tree	Good	Good	Good	Good	Good	Poor	N/A	Good
Multivariate Logistic Regression	Good	Good	Average	Poor	Poor	Poor	N/A	Average
Perceptron	Average	Poor	Poor	Poor	Poor	Poor	N/A	Average
KNN	Good	Good	Good	Good	Good	Good	N/A	Good
MLP	Good	Good	Poor	Poor	Poor	Poor	N/A	Good
Random Forest	Good	Good	Good	Good	Good	Good	N/A	Good

Table 4.5: A description of the capacity of each machine learning algorithm's ability to predict each of the phases in Green River Shale Sample

The MLP classification is also relatively poor, underestimating the dolomite content and misclassifying the majority of dolomite as calcite. This may be due to an over-reliance on the calcium value of each pixel. The MLP does appear to classify the grain boundaries accurately in both the random seed and two-scan methods. The MLP well classifies the organic matter, porespace and pyrite content in the sample, in both the random seed and two-scan methods, suggesting that MLP classifies the 'end member' phases well, i.e. the darkest and lightest on SEM, the softest and stiffest on AFM. This may indicate that the MLP may be over reliant on the SEM greyscale value, and doesn't train as readily on the EDX values.

The multi-variate logistic regression classification is mixed, with the calcite, organic matter and porespace well classified, but with the dolomite and clay often misclassified for each other. The grain boundary classification appears more accurate in the model trained on the two-scan method than the random seed method, most likely due to the relatively higher proportion of Green River pixels in the training data in the two-scan method. This is most notable in the classification of the pyrite using the two-scan training method is good, which again is most likely due to the increased proportion of Green River pixels in the training data, further highlighting the need for a well rounded training dataset.

The KNN classification of the Green River is excellent, correctly classifying all key phases, with only minor inacurracies around the edge of some phases. There is also relatively little difference in the classification between the two training methods. The accuracy of the KNN may be due to the large amount of data saved within the algorithm, and could identify that using Euclidean distances on classification may be a suitable method.

The Decision Tree and Random Forest are both excellent classifiers of the Green River shale dataset, with relatively little between these methods and the KNN. These methods are grouped

together due to being related classifiers and appear approximately equally effective on classifying the Green River scan presented, using both the training methods. The biggest difference between these models is the shape of the quartz in the centre of the segmented image.

The phase prediction of the Eagle Ford Carol (Figure 4.8) scan is more accurate than the Green River, most likely due to this shale being mineralogically less complex. The only discretion with the prediction and initial segmentation revolves around another topographic related defect with a clear peak in the calcite crystal identified as Feldspar. Despite the most accurate prediction of this sample being more accurate than the Green River prediction, there is a large disparity in the range of model predictive accuracies.

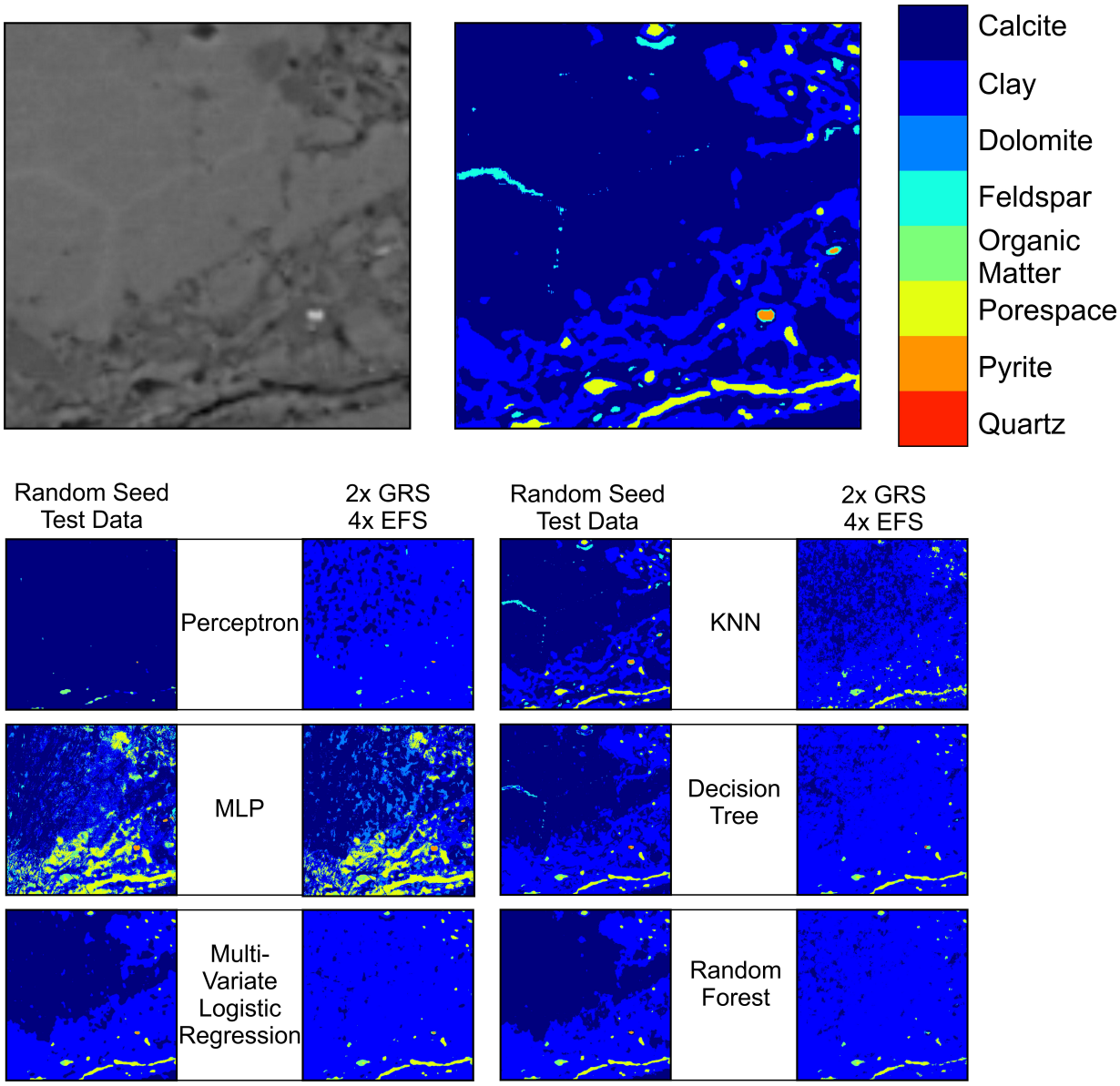

Figure 4.8: An SEM image of the Eagle Ford Shale Carol Well with the equivalent mask. The images below indicate the predicted mask of the Green River scan from each of the six machine learning models. Models shown are trained on 2,000,000 random training data (Random Seed Test Data) or trained on 2 scans of each shale as mentioned previously in Figure 4.10 (Shale Split Test Data).

The perceptron accuracy is very poor on this particular scan, predicting no grain boundaries and failing to predict the fracture in the bottom right of the sample. The two-times scan and random seed methods resulted in similar inaccuracies. The MLP accuracy is also relatively poor, and misinterprets much of the calcite crystal as clay or dolomite in each of the training methods. The MLP trained on both methods does identify the fracture at the base of the image, but also

Model	Relative Fit							
	Organic Matter	Porespace	Clay Minerals	Dolomite	Calcite	Quartz	Feldspar	Pyrite
Decision Tree	Good	Good	Good	N/A	Average	N/A	Average	Good
Multivariate Logistic Regression	Good	Good	Good	N/A	Poor	N/A	Poor	Average
Perceptron	Average	Average	Poor	N/A	Poor	N/A	Poor	Poor
KNN	Good	Good	Good	N/A	Average	N/A	Average	Average
MLP	Good	Good	Poor	N/A	Poor	N/A	Poor	Good
Random Forest	Good	Good	Good	N/A	Average	N/A	Average	Good

Table 4.6: A description of the capacity of each machine learning algorithm's ability to predict each of the phases in Eagle Ford Carol Sample

overestimates the amount of the scan which is comprised of porespace/organic matter. This would have a devastating effect on potential sealing properties of a mudrock if you increased the fracture related porespace by approximately 100%. The MLP does identify the small pyrite crystal in the bottom right of the image and is one of the few algorithms to identify the shape and size of the crystal accurately.

The multi-variate logistic regression prediction is quite accurate when trained on the random seed data, successfully predicting the fracture in the bottom right of the scan as well as predicting the general shape of the large calcite crystal that covers most of the top of the scan. However, the intricacies of the matrix surrounding this crystal are less well predicted, with the model trained on the random dataset predicting the majority of the matrix to be clay, much more so than indicated by the SEM. The multi-variate logistic regression model trained on the two-scan method is comparatively worse at predicting the mineralogy in this sample than that trained on the random seed dataset. The two-scan model does successfully highlight the fracture in the bottom right, but fails to identify any of the other complex mineralogy in the scan, instead predicting that the remainder of the sample is mainly clay minerals.

The KNN model trained on the random seed data is very accurate.Identifying the key fracture, the shape of the calcite crystal and much of the heterogeneity in the matrix, whilst also identifying the pyrite crystal and feldspar misclassification in the large calcite crystal. This model when trained on the two-scan method is considerably less accurate, only accurately classifying the fracture.

The random seed decision tree model is also very accurate. The difference between this model and the random seed KNN is the lower accuracy classification of the matrix around the large calcite crystal. The difference is that the decision tree is much less computationally expensive

than the KNN. The two-scan trained decision tree is again, similar to the equivalent KNN model, less accurate in its classification than the random seed equivalent. The two-scan decision tree only accurately predicts the fracture and some of the associated porosity just above the fracture. The two-scan decision tree doesn't identify the calcite mineral at all in the sample. The random forest trained on the random seed, is almost as accurate as the decision tree/KNN, but doesn't identify the feldspar classified defect in the calcite mineral. Other than that the random forest trained on the random seed only misrepresents the matrix complexity, the small pyrite crystal and some of the porespace, which is mis-classified as feldspar.

It is immediately notable from Figure 4.8 that the models trained under the random seed method are more accurate than those trained under the 2x each shale, due the abundance of Eagle Ford in the random seed data, which means that this relatively simple Eagle Ford scan will be well fitted.

The phase prediction of the Eagle Ford Cinco Saus scan presented in Figure 4.9. This scan is mineralogically more complex than the previous Eagle Ford scan, comprising a larger proportion of pyrite and feldspar.

The perceptron classification using the random seed method is average, correctly predicting the pyrite crystal in the centre, but mispredicting the feldspar below as pyrite. This model also poorly predicts the calcite filled foram in the scan, and underestimates the matrix complexity in the left side of the scan, underestimating the amount of porespace and organic matter. The two-scan trained perceptron prediction is poor, only predicting the pyrite crystals with any accuracy. This model predicts much of the porespace in the matrix to be organic matter, and predicts almost all of remainder of the scan to comprise calcite, when in reality there is a strong mix of calcite and clay minerals.

The MLP prediction is marginally better than the basic perceptron when trained using the random seed method, correctly identifying more of the organic matter in the matrix. However, the MLP trained in this manner still underestimates the amount of calcite in the sample, and miscassifies feldspar as pyrite, along with missing some of the intricacy in foram. The MLP trained in the two-scan method is poor at classifying the scan, overestimating the amount of porespace and organic matter, and fails to correctly predict the foram at all. This model mainly

misclassifies clay minerals as organic or porespace, which would be heavily detrimental to any geological model based off this going forward.

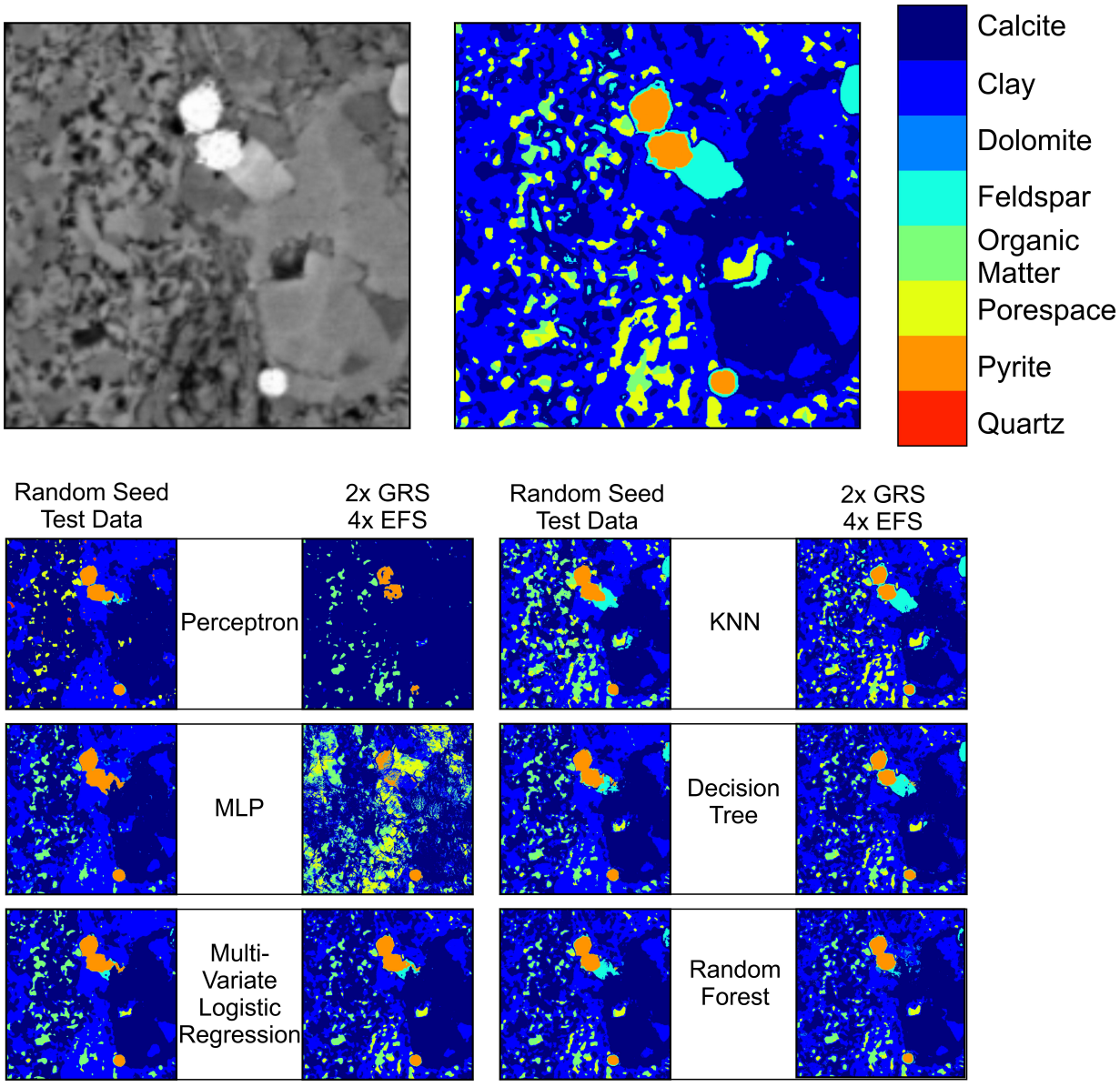

Figure 4.9: An SEM image of the Eagle Ford Shale Cinco Saus Well with the equivalent mask. The images below indicate the predicted mask of the Green River scan from each of the six machine learning models. Models shown are trained on 2,000,000 random training data (Random Seed Test Data) or trained on 2 scans of each shale as mentioned previously in Figure 4.10 (Shale Split Test Data).

The fit of the multi-variate logistic regression model is far superior in both the random seed and two-scan method to either perceptron based model. This model when trained on the random seed data accurately predicts the foram, the clay and calcite matrix and the small pore in the

Model	Relative Fit							
	Organic Matter	Porespace	Clay Minerals	Dolomite	Calcite	Quartz	Feldspar	Pyrite
Decision Tree	Good	Good	Good	N/A	Good	N/A	Average	Good
Multivariate Logistic Regression	Good	Good	Average	N/A	Average	N/A	Poor	Good
Perceptron	Poor	Average	Poor	N/A	Poor	N/A	Poor	Good
KNN	Good	Good	Good	N/A	Good	N/A	Good	Good
MLP	Average	Average	Average	N/A	Average	N/A	Poor	Good
Random Forest	Good	Good	Good	N/A	Good	N/A	Average	Good

Table 4.7: A description of the capacity of each machine learning algorithm's ability to predict each of the phases in Eagle Ford Cinco Saus sample

centre of the foram. However, the model overestimates the amount of organic matter in the matrix, misclassifying porespace as organics, and also misclassifies the feldspar as pyrite. The two-scan trained equivalent model, is similarly accurate, and also misclassifies similar minerals, again misclassifying porespace as organic matter and feldspar as pyrite.

The KNN models are very accurate on this sample, both predicting every mineral phase well. The small differences in accuracy between the two training methods relate to the shape of the pyrite/feldspar crystals, and the composition of the poro-organic component of the matrix. The random seed trained KNN has a marginally better classification, more accurately identifying the boundary of the pyrite and feldspar crystals and also more accurately distributing the poro-organic component in the matrix and is overall the most accurate classifier of this scan.

The decision tree is also relatively accurate, correctly classifying the clay and calcite content of this scan. The random seed decision tree poorly classifies the outline of the pyrite crystal and associated feldspar, along with misclassifying some of the porespace as organic matter. The two-scan trained decision tree is marginally better at classifying this scan than the random seed method, only marginally underestimating the organic and porespace component, whilst maintaining high accuracy on the other phases.

The random forest model is similar in accuracy to the decision tree and misclassifes similar components, namely feldspar and pyrite and some of the organo-pore component. The two-scan method is marginally more accurate for training within the random forest, but the differences are minor.

There are some obvious trends from the results presented here, notably that the KNN, Decision Tree and Random Forest models are more accurate than the other models, accurately predicting most phases. The KNN accuracy is due to the model incorporating some of the

training data into the model, training data is also part of the test dataset in this element of the study. The KNN is also the most complex of the models requiring approximately three times more memory than the next largest model, as such this method would become very computationally expensive if hundreds/thousands of thin section classifications are required rather than the 23 from this study. The reason for the Decision Tree and Random Forest models having the next highest accuracies is most likely due to the processing method of data. The process of the Decision Tree, mirrors somewhat the process of mineral identification by an inexperienced mineralogist, effectively running through a *checklist of points* to establish the correct mineral identification.

Another notable trend is the superior performance of the majority models trained on the random seed across the Eagle Ford scans. The models trained using the random seed and the two-scan methods were approximately equal in accuracy in the Green River, and in some cases the two-scan trained model was more accurate. It is notable in the Eagle Ford Cinco Saus scan that the two-scan trained KNN, Random Forest and Decision tree models were more adept at predicting the phases. These models were also adept at predicting the Green River shale, which indicates that these models trained by the two-scan method predict more complex mineralogies at a higher accuracy. It may be that these models excel when trained on a more rounded dataset, and predicting more difficult mineralogies.

4.4.2 Overall Mean Accuracy

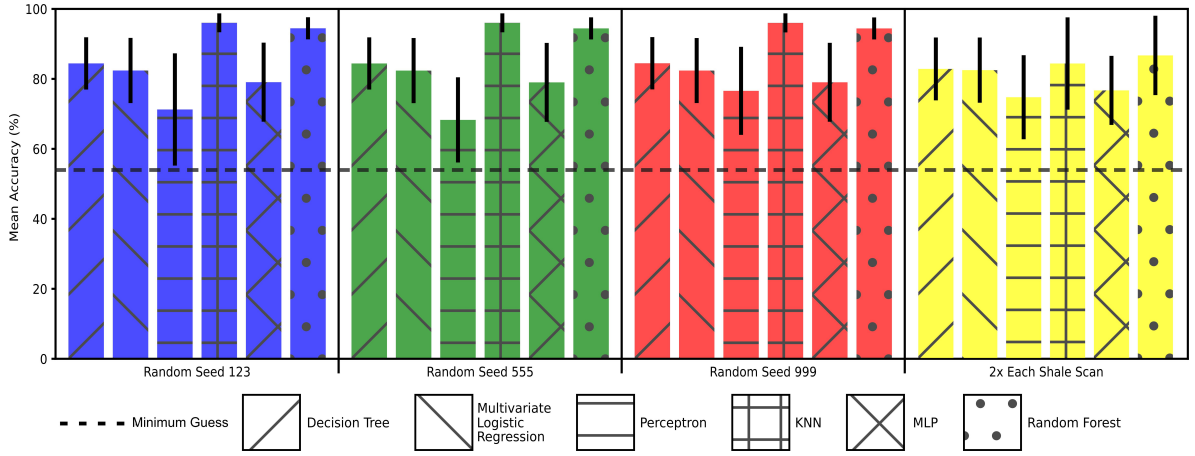

Figure 4.10: A bar plot indicating the mean accuracy of each method across the entire database. The different colours represent different random seeds of the 2,500,000 train/test data for model initialization in the red, blue and green. The results in yellow were from models trained and tested on data from 2 scans of each shale (Eagle Ford Cinco Saus, Eagle Ford Carol and Green River Shale). The grey dashed line is the minimum possible accuracy of any model, i.e. the accuracy acquired if the model selected the same mineral for every pixel on every scan. The black lines at the top of each bar represents the standard deviation.

The mean accuracy associated with each method across the 20 Eagle Ford and Green River SEM/AFM/EDX combinations is displayed in Figure 4.10. The accuracy is lowest in the simple Perceptron model, which is the most basic of the models used. This model also has the highest standard deviation in accuracy suggesting that it has the least generalizability. The MLP has the second lowest accuracy at approximately 80% on all the samples, and has the second highest standard deviation. The most accurate fit on all data were the KNN and Random Forest algorithms. These algorithms achieve a mean accuracy of >95% across the entire training/testing dataset. The Multivariate Logistic Regression and Decision Tree have intermediate mean accuracies of 85-90%. The minimum guess line at approximately 57% indicates the accuracy of a model which classifies all of the data as the most common class, in this case calcite.

Comparisons With Other Studies

The model accuracies reported within this study are similar to those found from other machine learning algorithms. The average accuracy of the KNN and Random Forest algorithms were

>95%, when trained with two million datapoints, an accuracy similar to some of the most accurate models on SEM identification in the literature, and is very similar to the outcomes of machine learning models by Rubo et al. (2019) and Akkaş et al. (2015). Rubo et al. (2019) also first segmented the images, however, then used convolutional filters to enhance classification. This implies that incorporating convolutional filters into this machine learning protocol, most likely after segmentation, could also lead to further increases in accuracy. A convolutional filter involves convolving several pixels into one pixel value, A similar approach could be adopted in this study, but would be dependent on the method used to average the AFM results which contribute the pixels on that image. This could be accomplished using a moving average, or using statistical deconvolution.

The accuracy of the Decision Tree model ($\approx 83 - 88\%$) for classification were similar to that obtained in Saporetti et al. (2018), and suggest that further incremental improvement could be made by enhancing minority classes. In some respects, this has been indirectly attempted by training the model on two scans from each shale in order to give a more balanced training dataset. It may be prudent to statistically enhance the training dataset to ensure the models are generalizable, which may lead to improvements on unseen data. This may give rise to an increase in the MLP accuracy, which is lower than that reported in the majority of other studies, with accuracy increases of approximately 20% made in other by Saporetti et al. (2018) from balancing the training dataset. It would appear that accurate prediction of shale mineralogy using machine learning is variable with CNN models, which in theory should be best placed to analyse minerals by appearance, having a great degree of variability in accuracy; as low as 64% (Duarte-Coronado et al., 2019) and high as >99% (Su et al., 2020).

The random forest model had the second highest accuracies in this study, and was more accurate than that presented by Wu et al. (2019) on a similar shale segmentation problem. The KNN and random forest methods presented here are more accurate than many of the facies prediction models presented within the literature, which generally have an accuracy of 80-90% (Bhattacharya and Mishra, 2018; Wang and Carr, 2012; Wang and Krupnick, 2015). Therefore, if machine learning is used to bridge the gap between dynamic logs and facies prediction in active exploratory operations, then pattern recognition on the cuttings returned during drilling could

help supplement this. This could be achieved by combining the machine learning models used to scale dynamic logs to facies, with the models presented here, which allow an upscaling and automatic facies description from cuttings. It is evident that the random forest and to a lesser extent the KNN could be readily incorporated into an algorithm which uses dynamic logs, SEM images and XRD to give an exceptional understanding of the shale seal across the wellbore. This information could then be used within the iterative process of refining geomechanical models at the wellbore scale.

It is obviously important that the training data and test datasets are similar to allow an accurate prediction. However, this may be considered overfitting the model, which is mentioned below when the models are used on validation data from the Posidonia, which is mineralogically completely different to the Eagle Ford, which makes up the bulk of the training data.

4.4.3 Model Validation

Whilst it is convenient to use the same dataset (16 Eagle Ford scans and 4 Green River scans) used to train the data for testing and validation, this can lead to low generalization as the model locally overfits to the training data, causing bias on any new datasets observed. In this case the bias may be the over-population of calcite and dolomite in the dataset, along with a small variability in the composition of the clay fraction. Therefore, in order to test how well each of the models generalize to other data, scans of Posidonia shale from Goodarzi et al. (2016, 2017) were used. This shale is significantly different to the Eagle Ford, in being particularly calcite lean in two SEM scans, immature, and with a higher clay content. The shale sections were also prepared in a different method, whereby they were polished as TEM sections using a similar ion beam mill but for a longer period of time. The SEM on these samples was also undertaken using a different machine and at different pressures.

This data therefore presents a great test of generalization for each of the models. The data obtained from Goodarzi et al. (2016, 2017) was segmented using a the same approach for the training and test data where appropriate on sample 29-2-Scan008. Samples 24-2-Scan007 and 24-2-Scan010 were segmented in a similar manner but, due to the EDX signature of carbon not being collected we were unable to accurately segment between organic matter and porespace,

as such these categories were combined. This meant that during the training and testing of the model the phases of organic matter and porespace were combined in the train and test datasets.

Validation Accuracy

The accuracies of each model on the Posidonia data are presented in Figures 4.11 and 4.12. The results in Figure 4.11 indicate the accuracy of each model trained by using the two million datapoint method and a random seed (in this case 555). Using this training method, 24-2Scan007 has the highest individual model accuracy (60.7%-KNN) and mean accuracy (51.15%). The lowest accuracy on the two scans of 24-2 is the MLP with an average of 41.3%. There is a notable dip in accuracy in the non-Decision Tree related models between Scan007 and Scan010, with the Decision Tree and Random Forest inversely increasing in accuracy. This change in accuracy appears to be related to the relative abundance and correct/incorrect identification of pyrite within Scan010 (Figure 4.15).

The lowest accuracies overall are within the 29-2 sample. It is notable that in Figures 4.11 and 4.12 that the accuracy scale on the 29-2 sample is double than that on the 24-2 graphs. The MLP is actually the most accurate predictive model on this sample, which is related to the correct prediction of a clay band in the centre of the image, and the correct identification of the pyrite framboid in the top right of Figure 4.13. The accuracy of the Decision Tree and Random Forest are incredibly low with predictions $<2\%$ accuracy.

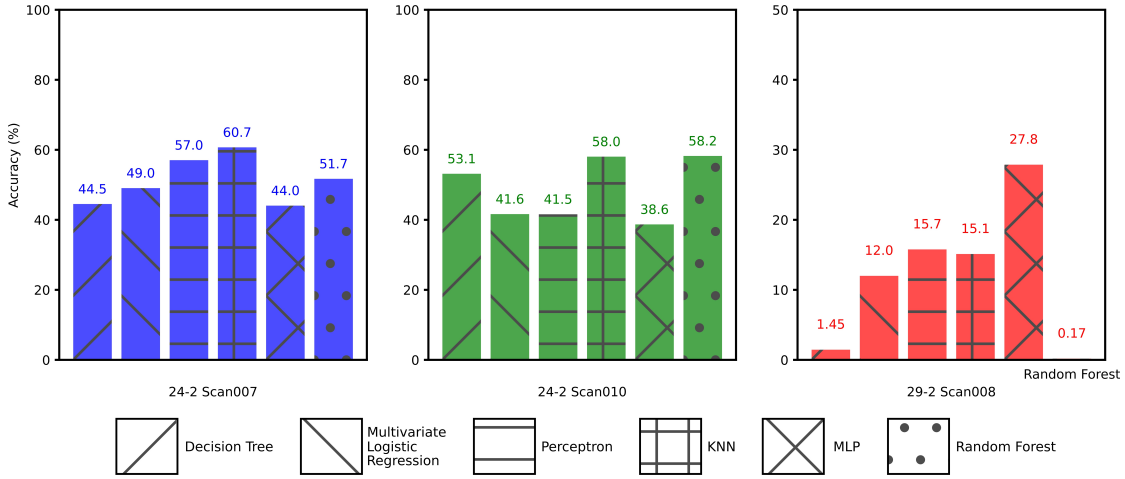

Figure 4.11: Bar graph indicating the accuracy associated with each model on the Posidonia shale scans. These accuracies are obtained with models trained on random seeded 2,000,000 datapoints as mentioned in section 4.3.4. It is notable that the accuracy of all models when fitting the scan from sample 29-2 is at double the scale in order to show bars with lower accuracies. The accuracy of each model is included above the bar on the chart.

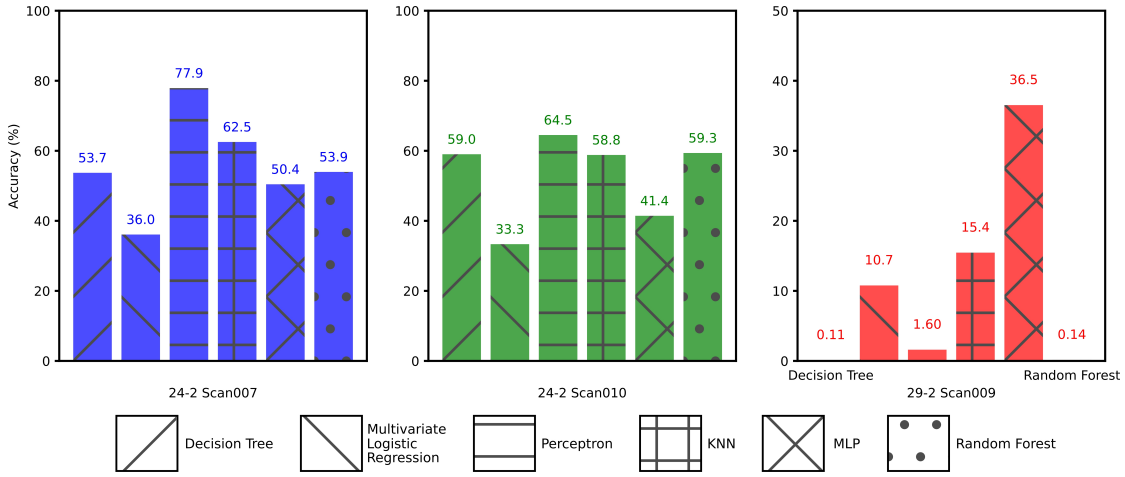

Figure 4.12: Bar graph indicating the accuracy associated with each model on the Posidonia shale scans. These accuracies are obtained with models trained on two scans of each shale as mentioned in section 4.3.4. It is notable that the accuracy of all models when fitting the scan from sample 29-2 is at double the scale in order to show bars with lower accuracies. The accuracy of each model is included above the bar on the chart.

The accuracies of the models trained on the 2x shale scans method from each Posidonia scan are indicated in Figure 4.12. The accuracies are different than those trained by the two million point method, with a significant increase in the accuracy of the Perceptron model in the 24-2 sample (77.9 & 64.5% up from 57 & 41.5% respectively). In comparison the Multinomial

Logistic Regression accuracy has decreased drastically with accuracy losses of 13% and 8.3%. The remainder of models have relatively similar accuracies, with the KNN being the second most accurate followed by the Random Forest and Decision Tree. The increase in the Decision Tree and Random Forest accuracies between Scan007 and Scan010 observed in the random seed trained models is not exhibited to the same extent in the model trained on the 2x each shale method. The massive decrease in accuracy between the 24-2 and 29-2 samples is also observed in the predictions made by models trained by the 2x each shale method.

Scan by Scan Validation Accuracy

The predictions of the 29-Scan008 by each of the machine learning algorithms is displayed in Figure 4.13. As can be seen the prediction of all phases is poor, which most likely links to the difficulties in segmenting this image mentioned later. The segmentation of this image is difficult due to the difference in exposure of this SEM image to the images obtained within this study and the other images from Goodarzi et al. (2016). As such, only the pyrite, organic matter and porespace were accurately segmented. The interspaced clay minerals, quartz and calcite are poorly segmented due to the area being enriched in all of Al, Ca and Si in the EDX scans from from Goodarzi et al. (2016), which are included in the online repository at `https://figshare.com/s/2c5d0b1235068bc38c6e`.

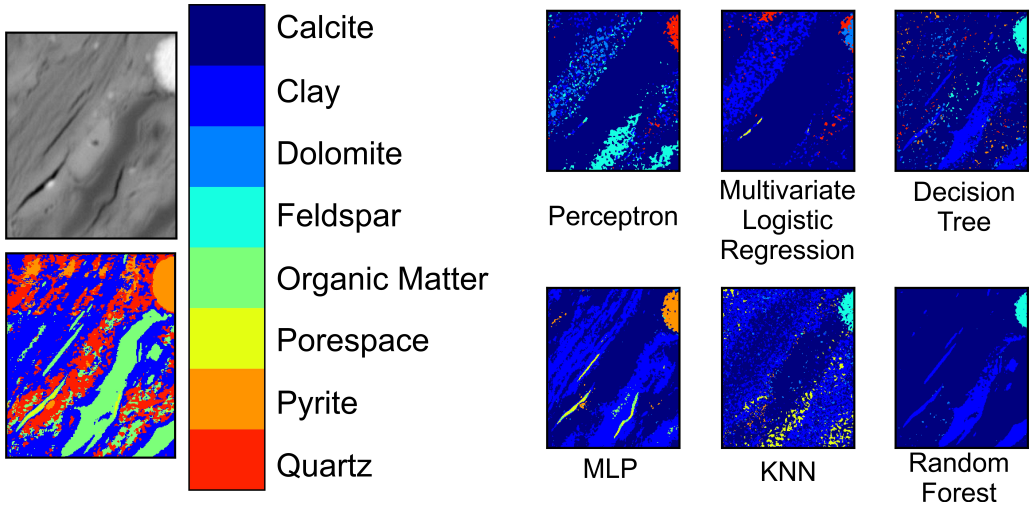

Figure 4.13: An indication of the accuracy of each model when predicting data on the Posidonia 29-2-Scan008.

Model	Relative Fit							
	Organic Matter	Porespace	Clay Minerals	Dolomite	Calcite	Quartz	Feldspar	Pyrite
Decision Tree	Poor	Poor	Poor	N/A	N/A	Poor	N/A	Good
Multivariate Logistic Regression	Poor	Poor	Poor	N/A	N/A	Poor	N/A	Poor
Perceptron	Poor	Poor	Poor	N/A	N/A	Poor	N/A	Poor
KNN	Poor	Poor	Poor	N/A	N/A	Poor	N/A	Poor
MLP	Average	Average	Average	N/A	N/A	Poor	N/A	Good
Random Forest	Poor	Poor	Poor	N/A	N/A	Poor	N/A	Poor

Table 4.8: A description of the capacity of each machine learning algorithm's ability to predict each of the phases in Eagle Ford Cinco Saus sample

The perceptron poorly differentiates the key phases in this image, misclassifying the pyrite as quartz, the organic matter as feldspar, and determining that the intermixed clay/quartz/calcite was intermixed calcite and dolomite. As this is the most basic model, it has struggled with the complexity of this fundamentally different dataset. This itself would cause issues if this model were to be chosen, for any geological purpose as this lack of flexibility would inhibit any prediction.

The accuracy of the multivariate logistic regression is no better than the perceptron, misclassifying the organic matter, pyrite and quartz within this sample. This technique does predict a level of clay content within the matrix, which is actually unclassified by the segmentation process. Although this model predicts the clay mineral content, more similar to the likely real-life mineralogy, this prediction is still inaccurate is it is measured off the variance from the segmentation.

The decision tree and random forest accuracy is similar, both predicting the pyrite framboid to be feldspar. This is likely due to the SEM greyscale value of this framboid being lower than any observed within the training data and as would be classified as the next brightest mineral observed (feldspar). These models also predict the shape of the organic matter and porespace accurately, but misclassify them as clay within this sample. This again relates to the greyscale of the SEM image, which indicates that these models put a large emphasis on classifying from the greyscale image, rather than the associated EDX scans.

The MLP visually appears quite accurate in terms of recognising the outline of individual features. However, similar to the previously mentioned models, many of these features are misclassified mineralogically. The MLP successfully classifies the Pyrite, and porespace within the sample, but misclassifies much of the matrix as clay and calcite, not identifying any of the

quartz within the sample. This does indicate that the MLP may be the most flexible model chosen here, which has the capacity to adapt to lesser quality data. This indicates that the MLP may be a useful tool for an initial first pass at segmenting SEM images into their component phases, if that is most important. This could a useful process if the fraction of a phase within an image is required, such as for an input to a homogenisation model.

The KNN classification here is poor, especially in comparison to that achieved on the training dataset. The KNN doesn't accurately predict any phase outline correctly, and misclassifies most phases, most notably not predicting the organic matter or porespace and classifying the pyrite as feldspar. This inaccuracy is caused by the KNN saving a selection of training data, which is fundamentally different to this test data. It may be that a more rounded training dataset may improve this model.

The segmentation of the Posidonia 24-2Scan007 and 24-2-Scan010- scans are far superior to that from the 29-Scan008 (Figures 4.14 and 4.15). The figures also indicate the model predictions on these scans. A first pass of these predictions indicates a greater accuracy than that within the Posidonia 29-Scan008.

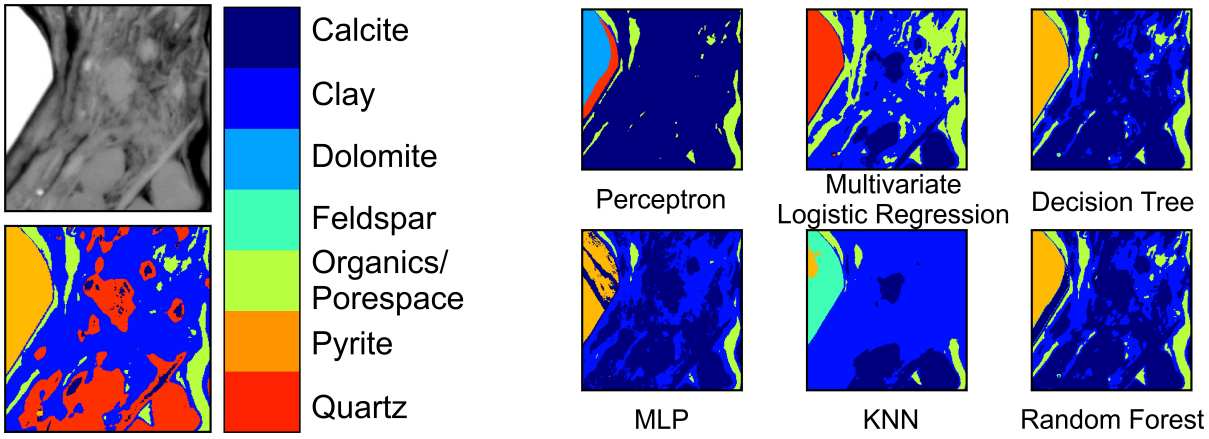

Figure 4.14: Indications of the accuracy of each model when predicting the data on the Posidonia scan 24-2-Scan007.

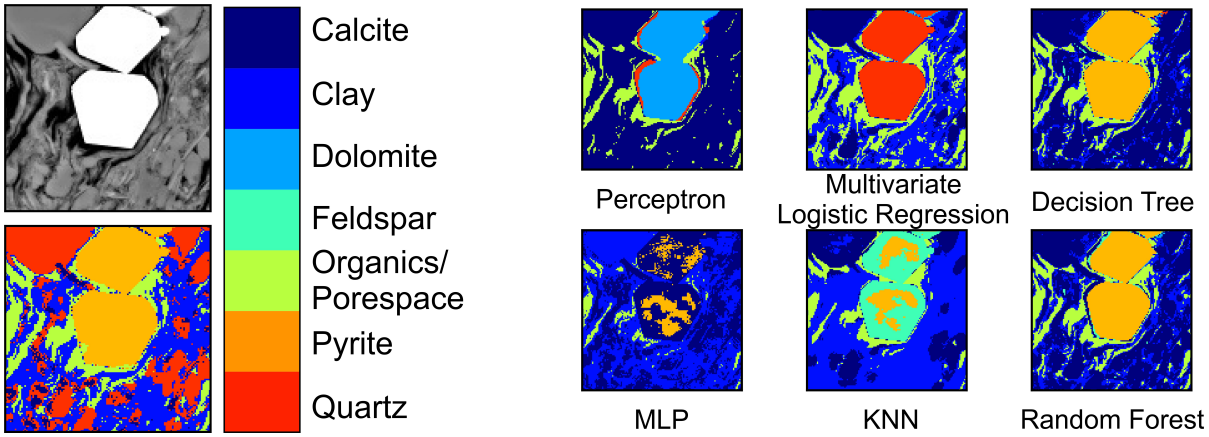

Figure 4.15: Indications of the accuracy of each model when predicting the data on the Posidonia scan 24-2-Scan010.

Model	Relative Fit						
	Organic Matter/Porespace	Clay Minerals	Dolomite	Calcite	Quartz	Feldspar	Pyrite
Decision Tree	Good	Poor	N/A	N/A	Poor	N/A	Good
Multivariate Logistic Regression	Good	Poor	N/A	N/A	Poor	N/A	Poor
Perceptron	Good	Poor	N/A	N/A	Poor	N/A	Poor
KNN	Poor	Good	N/A	N/A	Poor	N/A	Poor
MLP	Average	Average	N/A	N/A	Poor	N/A	Average
Random Forest	Good	Poor	N/A	N/A	Poor	N/A	Good

Table 4.9: A description of the capacity of each machine learning algorithm's ability to predict each of the phases in the Posidonia 24-2-Scan007 sample

Model	Relative Fit						
	Organic Matter/Porespace	Clay Minerals	Dolomite	Calcite	Quartz	Feldspar	Pyrite
Decision Tree	Good	Poor	N/A	N/A	Poor	N/A	Good
Multivariate Logistic Regression	Good	Average	N/A	N/A	Poor	N/A	Poor
Perceptron	Good	Poor	N/A	N/A	Poor	N/A	Poor
KNN	Poor	Good	N/A	N/A	Poor	N/A	Poor
MLP	Average	Average	N/A	N/A	Poor	N/A	Average
Random Forest	Good	Poor	N/A	N/A	Poor	N/A	Good

Table 4.10: A description of the capacity of each machine learning algorithm's ability to predict each of the phases in the Posidonia 24-2-Scan010 sample

The perceptron has the poorest visual accuracy in Figures 4.14 and 4.15, misclassifying the obvious pyrite as dolomite, and the clay as calcite. The perceptron does classify the organic matter accurately within this scan. This dataset further emphasises that a more complex model should be used.

The multivariate logistic regression classification of this sample is quite accurate in terms of identifying the key different components in the sample. However, the actual classification of these components is less accurate, misclassifying the pyrite as quartz and the matrix quartz and

calcite. The organic component was well classified by this model.

The decision tree and random forest classifications are both similar. Both models classify the outline of the different phases well, and well classify the organic, clay and pyrite component of this scan. Both models misclassify the quartz content as calcite. These models have the most accurate prediction of this samples mineralogy, and are both incredibly similar.

The MLP classification of this sample is poor, with no accurate outline of the key phases, and misclassification of most phases within the sample. The only phase that is accurately outlined is the pyrite, but this is misclassified as a mixture of pyrite and calcite. The inability of the MLP to correctly identify the outline of these phases in a sample, much less complex and visually more obvious to classify than the previous 29-Scan008 sample is interesting. In that previous sample, the MLP was the best model at identifying the overall phase outlines, but here is easily the poorest. It is unclear as to why this is the case, but may be that the ability of the MLP to correctly outline the phases has not decreased, but that the other models have increased drastically.

The KNN poorly classifies the sample, not identifying any of the complexity in the matrix, and also misclassifying much of the pyrite as feldspar. The KNN also underestimates the amount of organic matter within the sample and the heterogeneity of the matrix. Like many of the models, the KNN misclassifies all of the quartz in the matrix as calcite.

One of the most notable consistencies within these classifications on the Posidonia 24-2 scans is the incorrect classification of quartz as calcite. This error most likely arises due to the inherent bias in the training dataset, as most minerals with a similar greyscale value and modulus value to the quartz here were classified as calcite, due to the Eagle Ford shale (a marl) comprising approximately 83% of the training dataset. The Green River shale images also had more calcite than quartz, which meant that the number of calcite pixels in the training dataset was approximately 480 times the number of quartz pixels (Table 4.2). The models were trained on two scans of each shale, but this did little to offset this bias, which could be improved in the future by use of minority class enhancement, such as that undertaken by Saporetti et al. (2018).

If minority enhancement allowed the decision tree and random forest to classify the calcite as quartz, then these models would be ideal for predicting mineralogy, with accuracies that would

reduce the time required for petrophysical analysis. The random forest and decision tree analyses could automate mineral classification, which would allow the user to identify where particular phases juxtapose. This would be useful when undertaking geochemical analyses of samples, assisting in identifying the areas of concern for porosity development, oil and gas migration and clay mineral transformation.

There is a clear disparity between the statistical accuracy in Figures 4.11 and 4.12 and the visual accuracy of the techniques from Figures 4.14 and 4.15. The perceptron and KNN accuracies are statistically higher than or in the same region as the random forest and decision tree. However, visually the perceptron and KNN model predictions appear far less accurate than the decision tree or random forest, as the perceptron/KNN captures much less of the heterogeneity. With minority enhancement, the perceptron in particular would remain at this accuracy or decrease, the KNN may increase in accuracy, but the random forest and decision tree would most likely become the most accurate models. This is a clear indication that reporting statistical model accuracy is not sufficient alone to understand the output of a machine learning algorithm. It is important to understand whether the inaccuracy is through misclassification (in this case of calcite-quartz) or non-identification (in this case not identifying the quartz phase at all). Both result in statistical misclassification and statistically similar accuracies, but to misclassify a phase is more useful than to not identify it.

4.4.4 Validation Young's Modulus Analysis

The aim of modelling phases from SEM in this study is to assist geomechanical prediction, particularly in terms of automating the preprocessing of many of the current homogenization and rock upscaling methods. Therefore, in order to truly test the accuracy of the models used in this study, Young's modulus data from the Posidonia Shale has been used as validation data. Each model has predicted the Young's modulus distribution of each phase in the Posidonia scans relative to the segmentation predictions. The predicted modulus distributions of each mineral using the different machine learning models, along with the segmentation prediction of the three Posidonia shale scans, are included as Figures 4.16, 4.17 and 4.18. The accuracy of each model to predict each phase is included in Tables 4.9 & 4.10.

Before discussing the predicted model modulus values, it is notable that the modulus distributions obtained using the segmentation are lower than expected. This reflects on the overall modulus distribution in the sample being lower than expected, especially in Sample 24-2 where a large proportion of each scan comprised pyrite with a reported modulus >100GPa. However, as displayed below the majority of modulus distributions have a modal peak between 40-60GPa. It is beyond the scope of this study to investigate the Young's modulus distributions obtained by the AFM from Goodarzi et al. (2017), which most likely relates to the standard used to calibrate the AFM. These AFM scans were calibrated to a standard with a modal value of approximately 18GPa, and it may be that the modulus value obtained becomes increasingly inaccurate, the further away from the standard's modulus value.

Posidonia Sample 24-2

The modulus distributions for this scan are included as Figure 4.16 and 4.17.

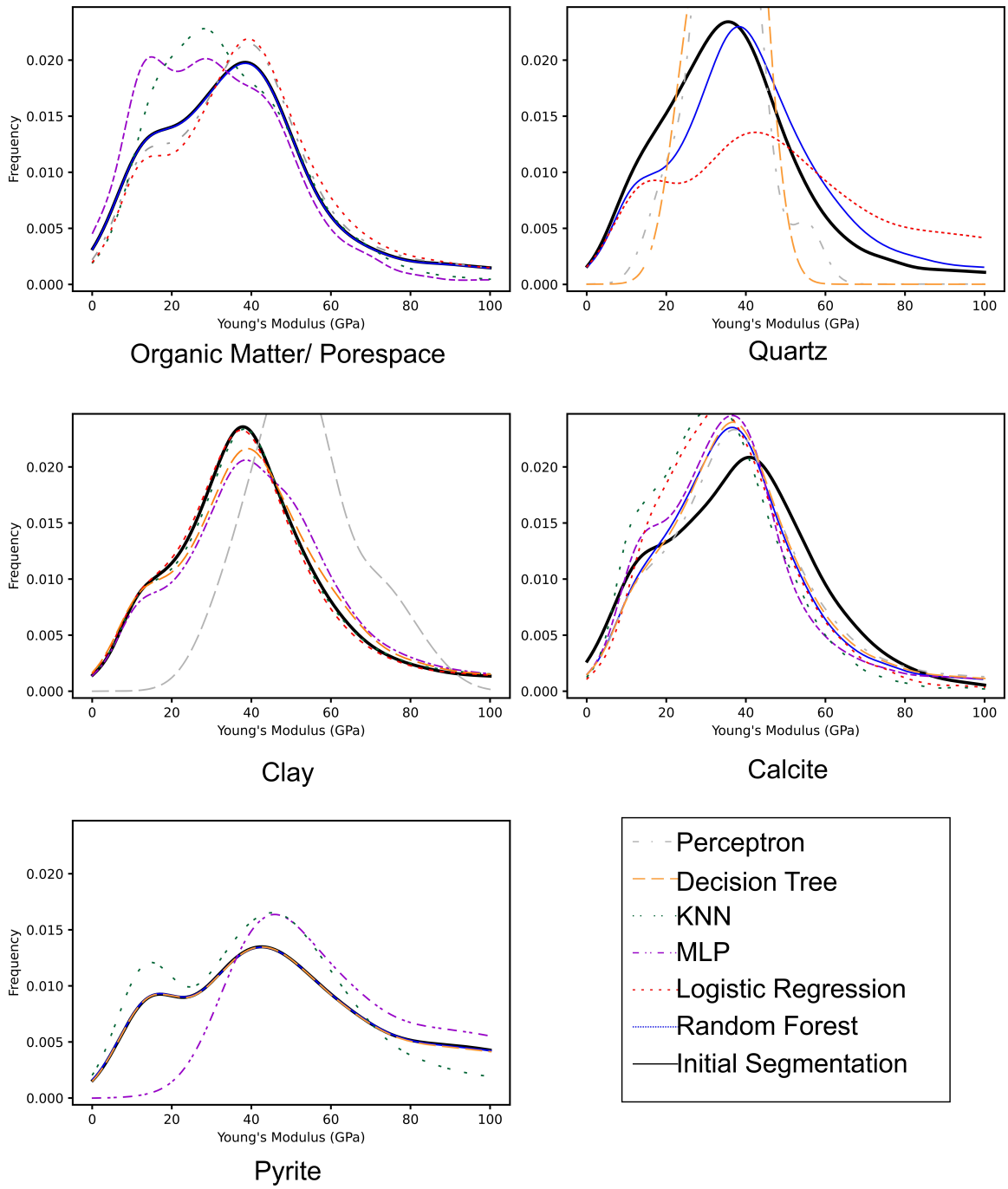

Figure 4.16: Probability density functions of Young's modulus for each of the major mineral phases from Posidonia shale sample 24-2 Scan007 as classified as the initial segmentation and each of the machine learning models used.

The organic matter/porespace in this sample could not be interpreted from each other due to the lack of Carbon in the EDX obtained by Goodarzi et al. (2017), and as such are combined

into one phase. The fit accuracy of this phase is relatively high in both scans, with the random forest and decision tree algorithms fitting exceptionally. All of the algorithms fit the organo-pore phase well in Scan010 (Figure 4.17 apart from the MLP which incorporates a second peak at approximately 10GPa. This second peak offsets the mean and modal modulus, indicating a lower value than reported by the segmentation. The organo-pore phase fitting is generally worse in the Scan007 (Figure 4.16), with only the random forest fitting this with great accuracy, as mentioned previously. The multinomial logistic regression and perceptron fit the overall distribution relatively well, only slightly overestimating the mean by <5%. This overestimation would not be a massive concern, as would most likely would fall within the range sample variance. The KNN and MLP underestimate the mean and modal modulus values by up to 30GPa, which would cause a massive impact on any forward modelling of rock competence under stress, leading to an underestimate the sealing potential of this particular shale.

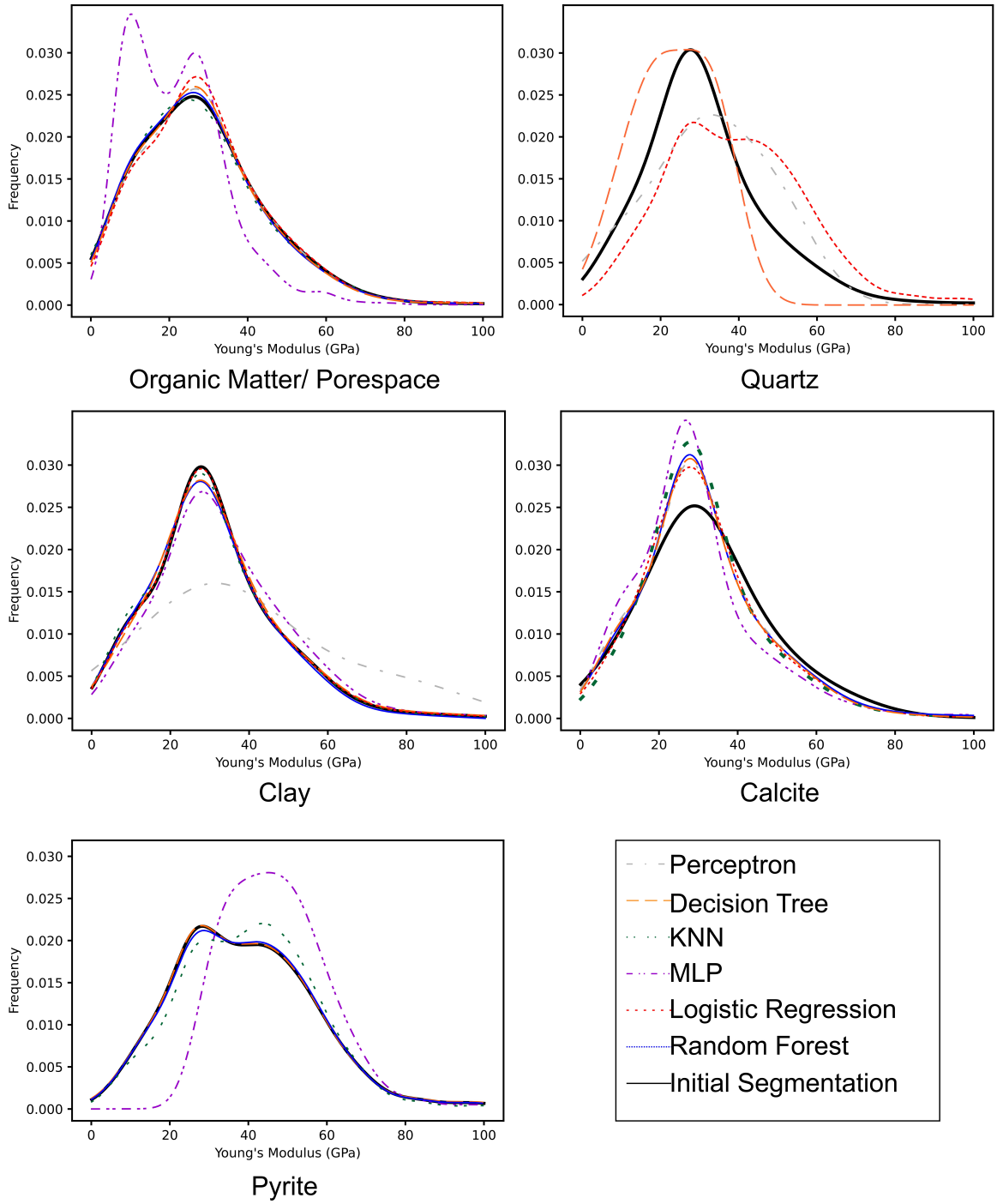

Figure 4.17: Probability density functions of Young's modulus for each of the major mineral phases from Posidonia shale sample 24-2 Scan010 as classified by the initial segmentation and each of the machine learning models used.

The modulus fit of clay in both scans is relatively accurate in most models, with only the perceptron not fitting the segmented distribution closely. The most accurate models across the

two scans are the KNN and multinomial logistic regression. One reason for this could be the fact that the properties (Young's modulus, SEM brightness and EDX composition) of the clay minerals within these scans is relatively similar to those within the training dataset, which make models with a high dependency on the training data, such as the KNN (which saves some of the training data), more accurate. Clay minerals comprise a major phase in both the training and validation datasets, and this could be a reason for the overall accuracy of prediction. This observation could be key when looking at enhancing minority classes. It may be prudent to also enhance minority classes in the validation data to ensure that the phases are all fit as accurately as possible. The approach of enhancing minority classes in the validation dataset could be used to assist in the segmentation of individual clay minerals. For example, where, determining, illite/smecite/chlorite/kaolinite etc. is important when looking at porespace creation or creep. The inaccuracy of the perceptron was due to the inability of the model to predict clay, instead misclassifying as calcite in figures 4.14 and 4.15.

The prediction of pyrite Young's modulus values is only adequately achieved by the random forest and decision tree algorithms. This is due to the misclassification of pyrite by many of the models as mentioned in Section 4.4.3. The perceptron and multinomial logistic regression algorithms fail to predict any of the pyrite. This would be disastrous in terms of sequestering fluid, as although pyrite and feldspar have similar modulus values, they have inherently different chemical compositions. Pyrite is soluble in acidic porewaters and would be dissolved upon injection (Tang et al., 2021), therefore an accurate estimation of the occurrence of pyrite is important, more so that an estimate of its Young's modulus distribution. The distribution of pyrite in these two scans is interesting with a relatively low modal modulus, indicating the possibility of porespace associated with these crystals at a higher resolution that that observed within the SEM. This porespace could be the result of either inherent porespace within pyrite framboids, dissolution, or preferential milling during sample preparation. Further investigation into this is beyond the scope of this study, but could be undertaken by means of higher resolution SEM.

The model predictions of quartz and calcite are inherently linked, due to these two phases being most commonly misidentified in Figures 4.14 and 4.15. In general, as most of the models

misclassify quartz as calcite, the predicted calcite modulus distribution is more similar to the segmented quartz modulus distribution. The random forest fits these two phases as a pseudo-gaussian mixture. In figure 4.16 this model fits the quartz phase with a similar modal modulus, but includes the 'hump' at approximately 20GPa, which is observed in the segmentation of the calcite distribution. The random forest also underestimates the modal modulus in the calcite distribution (42GPa), fitting a modal value more similar to the segmented quartz (36GPa). However, in Figure 4.17 the random forest fits the calcite with the quartz modulus distribution, in a similar manner to all the other models. This misclassification and poor fit is due to the aforementioned absence of quartz from the training dataset, indicating the need to have a mixed marl and shale dataset to train. This could be assisted by minority class enhancement, but most likely would be eliminated by a rounded high quality training dataset, including accurate EDX data. Using XRD as a means of testing the model output may also assist in this, to quickly identify which phases are being under/overestimated.

Posidonia Sample 29-2

Figure 4.18 indicates the predicted modulus distributions for each mineral phase in the Posidonia 29-2 Scan008 and the overall accuracy of each model at predicting each phase is included below as Table 4.8. There are individual measurements for organic matter and porespace within these predictions due to the initial EDX data having a measurement of carbon, which enables accurate classification between organic matter and porespace.

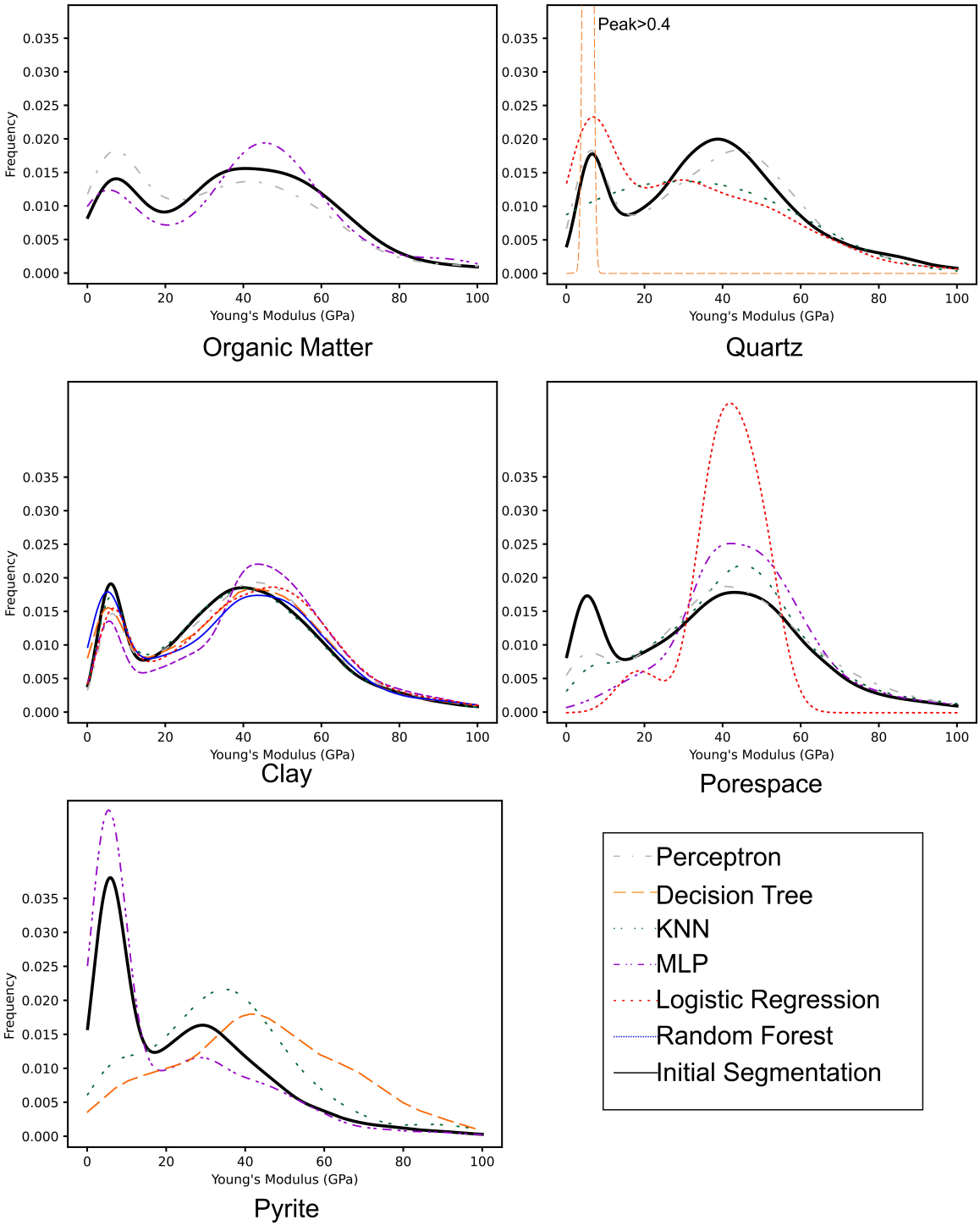

Figure 4.18: Probability density functions of Young's modulus for each of the major mineral phases from Posidonia shale sample 29-2 Scan008 as classified by the initial segmentation and each of the machine learning models used.

The modulus distribution predictions of these phases are mostly inaccurate, representing the

poor classifications indicated in Section 4.4.3. The only phase predicted with any accuracy is the clay mineral phase, which is predicted with reasonable precision by all the models, but with the MLP being least accurate.

It is notable that the modulus distributions of segmented phases within this scan are mostly similar, with all but pyrite exhibiting a bimodal distribution, with peaks at approximately 10GPa and 50GPa. The MLP fits the organic matter and pyrite relatively well, whilst the perceptron fits the porespace and quartz relatively well. These are the only models which fit any phase aside from clay to any extent. This further highlights the need for high quality data both within the training and validation datasets.

4.4.5 Overall Modulus Prediction

The prediction of the modulus values from all of the models is not good when initially analysed, this is mostly due to the significant bias within the training/testing data. The train/test dataset is made up of >50% calcite, with a sparsity of quartz. In comparison, the validation dataset is rich in quartz and calcite is almost absent. This is one of the key reasons for the low accuracies of the models on the validation dataset, as we commonly observe quartz misclassified as calcite. This itself could be improved upon by using a less biased dataset during the training of the model, which was planned by using SEM images of the Bowland and Barnett Shales, each richer in quartz than the Eagle Ford and Green River. However, due to the COVID-19 pandemic the acquisition of this SEM data could not be completed, which has left the model, biased towards carbonate minerals.

Despite calcite and quartz being chemically different, the Young's modulus of these phases, including dolomite are similar (calcite: 79-87GPa Kumar et al. (2012), quartz: 99GPa Kumar et al. (2012), dolomite: 51-67GPa Austin and Kennedy (2005)). As such, these minerals may be geomechanically grouped together into intermediate stiff minerals. This grouping is helped, as all these minerals occupy a similar character within each of the shales; comprising the highly abundant non-clay matrix element, and also the largest clasts.

The same principal applies for geomechanical purposes to feldspar and pyrite, which can be grouped into one class as stiff minerals; both having Young's moduli commonly in excess of

100GPa (feldspar: 201.4GPa Brown et al. (2016), pyrite: 297GPa Kumar et al. (2012)), whilst also comprising low quantities of individual crystals in the shale and thus, are unlikely to be load bearing.

4.4.6 Four-Phase Classification

The mudstones presented here can be adequately split into four geomechanical phases, organo-pore, clay, intermediate stiff and stiff minerals. The overall accuracy of this four-phase classification for the train/test data and the Posidonia validation data are included as Figures 4.19, 4.20 and 4.21. It is noted that no hyperparameters were adjusted in any of the machine learning models when undertaking this four phase learning approach. There is a reduction in accuracy on the random seeded approach using four phases. Nonetheless, a mean accuracy of 96% was achieved by the KNN algorithm using seeded data. This is the only mean accuracy above 90%. The accuracy of the Perceptron has also increased significantly to that observed in Figure 4.10, which is to be expected of a simple model in a simplified dataset. The MLP has exhibited a drop in accuracy, becoming the least accurate model. The accuracy of the Random Forest has also dropped but not significantly with a mean accuracy of 87%. The accuracy of the Multinomial Logistic Regression and Decision Trees have remained very similar at or around 82-87%.

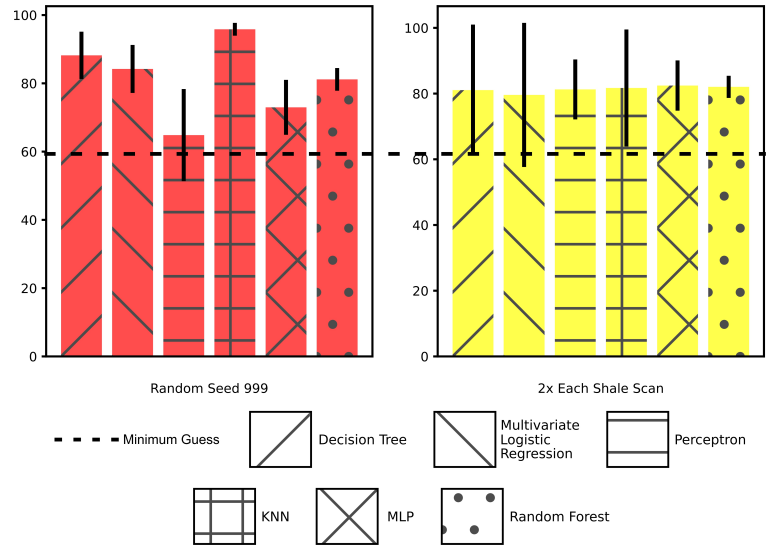

Figure 4.19: Accuracies for learning in a four phase system. The dashed line represents the minimum possible guess which in this case would be guessing everything to be intermediate-stiff phase

These accuracies are somewhat disappointing from a simplified database. If the task required a simplified database such as this, the likelihood is the margin for error would be very low, such as when trying to forward model mechanical interactions of different phases. The >10% error on most models would be significant when trying to predict the outcome of stress upon a sample at this scale.

The models trained on two scans of each shale are similar in accuracy at around 80%. The models which showed a notable decrease in accuracy in the random seed trained models, are the two most accurate when trained in this manner (MLP and Random Forest). The standard deviation for the algorithms when trained this way are generally larger than those trained on the random seeded data. This is to be expected due to the difference in size of the train/ test data, and over-representation of certain minerals (particularly quartz and feldspar) in the training data when compared to the datasets which are to be predicted.

The more complicated algorithms trained on the random seed data are struggling with the possible lack of complexity in the datasets, as the Random Forest and MLP's mean accuracy is significantly lower than that where all mineral phases were preserved. It is likely that the accuracy of these complex models could be further enhanced through hyperparameter tuning for this dataset. This would be useful information to research in order to establish a best suit of hyperparameters for a less complicated dataset. This trade-off between model complexity, which directly affects size and CPU time, and the outcomes required is a vital point for using machine learning within any aspect of geoscience where datasets are large. If the aim of the study is to infer a single Young's modulus value from a set of samples, such as to correlate cuttings with an equivalent triaxial or dynamic measurement, then a simple four-phase model may be more efficient, requiring a less complicated algorithm. To the same end, if a complicated understanding of the geomechanical interactions is required for a specific task, such as homogenisation and accurate upscaling, then a complicated algorithm, with a large and variable training dataset is required to reach useful accuracies. An example of where a high resolution and complex dataset may be required is predicting the changes in mechanical properties around an injection well during CO_2 sequestration, where the stress is variable on a metre scale. This would likely involve analysing a small amount of core or cuttings at very high resolution to understand the

likely fracture propagation within the seal. However, if looking to establish the overall sealing capacity of a kilometre wide seal, then a lower resolution 4-phase system would be useful to analyse the amount of cuttings available in a timely manner.

Four-Phase Validation

Figures 4.20 and 4.21 indicate the prediction accuracy of each model on the Posidonia scans. There is a significant increase in accuracy of all of the models mineral phase predictions in the Posidonia, when trained using the random seeded two million datapoints, compared to the predictions of all eight phases. In all methods the accuracy on this validation data is similar to that achieved on the training data. This increase in accuracy is further indication that a more rounded training dataset would enable significantly greater accuracies in the previous methods. The MLP is the least accurate again in this more simple classification, suggesting that further tuning of hyperparameters may be necessary. The KNN is on the other end of the accuracy scale, with accuracies on both 24-2 scans >95%. There is a notable drop off in accuracies when validating with the 29-2 sample. This is as mentioned previously due to the low contrast of the SEM image, which causes many of the phases to be misclassifed, either organics as clay or pyrite as intermediate-stiff. This non-ideal data may require preprocessing with Gaussian blur or other convolutional techniques prior to validation to increase accuracy.

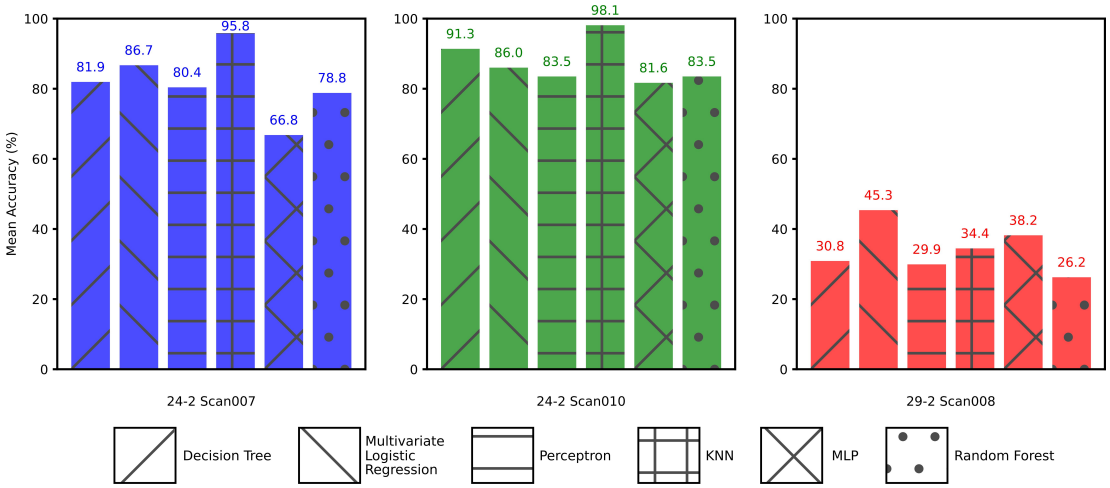

Figure 4.20: Accuracy of each model on the validation dataset under a four-phase system when trained with the random seed method.

The overall accuracy of the KNN to predict these four phase systems is most likely in the region required for accurate geomechanical prediction for forward modelling, and equivalent to some of the most accurate machine learning results in the literature (Wang and Carr, 2012; Saporetti et al., 2018; Bhattacharya and Mishra, 2018; Wu et al., 2019).This technique would be ideally suited for use on simpler systems, as these would also not overwhelm the CPU by having to save a large amount of data within the KNN model.

The accuracy of the decision tree and random forest models has not increased to the levels of the KNN. As such these models may not be usable as 'stand alone', but may be combined or used as a first pass, before refining. The random forest is also less accurate on this 4-phase system, as well as being more computationally expensive, therefore, if a simple outcome is required there is no reason to use the random forest over a well cross validated decision tree.

The ability to classify the 29-2 sample is almost equal among the models using this training datset, with only the MLP having a significantly increased accuracy prediction, although still only 55%. This further emphasises the need to preprocess this data set to enable more accurate predictions.

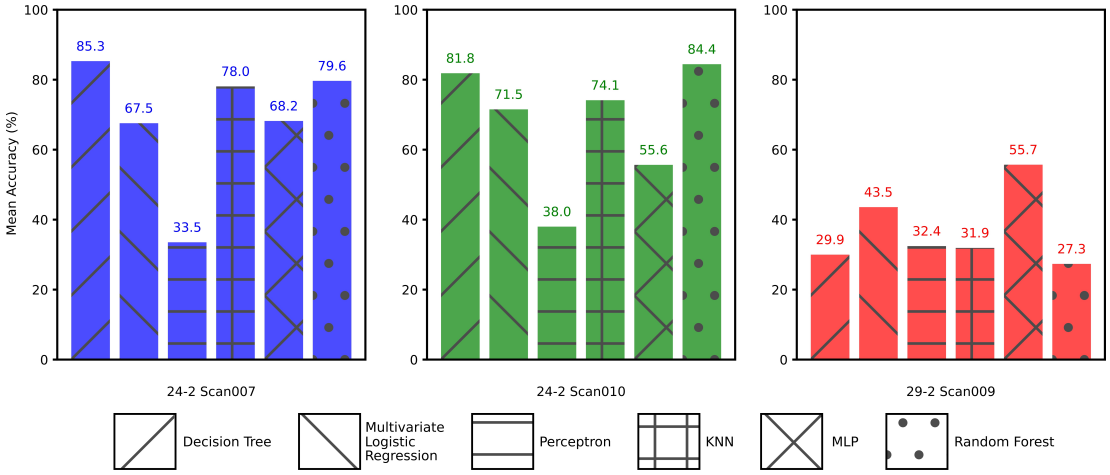

Figure 4.21: Accuracy of each model on the validation dataset under a four-phase system when trained with the two scan from each shale method

The drastic increase in predictive accuracy in most models when simplifying the data indicates that in order to have a model that predicts new shale data accurately it is important to either have a large but balanced training dataset for optimal high accuracy, or have a simple

mineralogic model with relatively few phases. The random forest method has the largest upside in this study on complicated mineralogies, being almost as accurate as the KNN, but with a fraction of the computational cost. As mentioned previously this is most likely due to the fact that the *"thought process"* of the algorithm is similar to that of a human identifying these minerals, by identifying if a mineral has a bright or dark SEM profile and then a high or low value of each element in an EDX profile. The random forest would therefore most likely be useful if trying to identify trends on the sub metre scale with mineralogy, which could not be readily computed by using dynamic logs.

The best technique for the four phase predictions was the KNN, which although computationally expensive, would be much less so in a simpler system. This KNN could easily help match up cuttings from different wells and identify trends in these, against trends observed in sonic logs.

The major use for these machine learning algorithms in CCUS may be to help infer more information from a potential caprock, which is unlikely to have been cored at all locations during the exploration. As such it is key to establish a relationship between the information that can be obtained from cuttings; SEM, EDX, AFM, Nanoindentation, XRD, XRF, and macroscale geomechanical properties, such as Young's modulus derived from Triaxial experiments. Machine learning can be a key tool in this by both; reducing the time required to analyse the high resolution data, but also acting as the start of a homogenization scheme, whereby the modulus distributions, grain sizes and proportions of each mineral phase can be accurately predicted from the SEM data, which form the backbone of any successful homogenization based upscaling scheme.

4.5 Conclusions

A series of six machine learning algorithms were used to classify eight major mineralogic components across 23 samples of three shales. Two of the shales (two wells in the Eagle Ford and a sample of Green River) were used as the test/ train data split for the machine learning algorithms. The machine learning algorithms used ranged from the relatively simple Perceptron

to the complicated and highly flexible MLP. The Random Forest and Decision Tree algorithms were also chosen as examples of machine learning which require relatively little preprocessing of data. A Multinomial Logistic Regression was also chosen as an alternative to the simple perceptron. All of these models are supervised and fit algorithmically to the train dataset looking for patterns. The last model used is an instance based KNN model, which uses the known points to identify other points in the data on a hyperplane.

The train and test dataset were classified with EDX and SEM pixel value segmentation to split into eight major phases. Where segmentation was not possible a KNN was implemented to assist in drawing grain boundaries. This method appears to work relatively well with only some grain boundaries misplaced, most notably between feldspar and pyrite.

The models were then trained using two separate methods; a random seed method, where the entire training dataset was shuffled and 2,000,000 points were used for training and 500,000 for testing, and a shale split method, where two scans of Green River Shale and two scans from each well of the Eagle Ford Shale were used for the train/test data in order to attempt to balance the training data and ensure increased generalization of the machine learning models.

The accuracies of the machine learning methods vary largely on both the training datasets, however, the KNN and Random Forest algorithms proved to be the most accurate overall, particularly in the random seed training data, where mean accuracies were >95%. The MLP, multinomial logistic regression and Decision Tree classifiers were similar in accuracy at between 80-90%. The perceptron was the poorest fitting model only reaching a peak accuracy of 78%.

In order to assess the predictive potential of each model a second set of data from the Posidonia was introduced as validation data. The mineralogy of this shale is significantly different to the shales the model has trained on, being enriched in silicates and carbonate lean. As such the models struggled to correctly predict the validation data, with peak accuracies of 60.7% in the models trained using the random seed method. The accuracies on the two scans per shale/well trained models were generally higher, indicating that this method may be preferable to avoid overfitting, but aside from a peak accuracy of 77% in the KNN most other models accuracies were <60%. The models were used to fit a scan of Posidonia, which appeared to have poor contrast in the SEM image, with poor results. The peak accuracy amongst all models at

predicting this data were 36%, which demonstrates the need to have a high quality SEM image, preferably from the same conditions as the training dataset.

An aspect of this prediction, was the ability of the models to accurately predict the Young's modulus of each phase from the AFM dataset. This ability was limited due to the poor predictions on the validation data. The most inaccurate prediction was for quartz, which was mainly classified as calcite. However, the modulus prediction for clay, calcite and in some models, organic matter and pyrite was good, suggesting that further training data would allow an accurate prediction of mineral Young's modulus. The Random Forest algorithm had the best overall modulus predictions across the dataset predicting most phases accurately, suggesting that the modulus prediction of this model was superior to its mineral prediction. Further research could therefore be undertaken at combining this machine learning algorithm to attempt to upscale between AFM resolution data and nanoindentation.

In order to assess overall generalization of these models, the training and validation datasets were re-categorised into four classifications; organo-pore, clay, intermediate-stiff and stiff minerals. This reclassification decreased the predictive accuracy of all models on the training data, however, the accuracy on the validation data (and thus generalizability) of each model increased drastically, with most predictive accuracies in the random seed trained models >80%. This indicates a biased training dataset may be able to train models capable of predicting a simple four phase distribution, which may be useful when predicting reservoir scale properties. However, a highly detailed prediction requires a large balanced training dataset, which would be necessary where predictions must be accurate or at higher resolutions, e.g. around a wellbore.

The outcome of this comparison is that the machine learning model should be selected, with the output in mind. If the desired output is complex mineralogy, then the Random Forest achieves a high accuracy (2nd to the KNN) but is much less computationally expensive than the KNN. If a less complex outcome is required, such as in the four-phase system, for uses such as overall mechanical prediction, then the KNN is the most useful algorithm as the model size would be lower. These two algorithms could become the backbone of further complex homogenization models, which require information on the proportion, size, distribution and modulus of each phase. As such machine learning algorithms that can accurately predict and estimate this

information are useful to streamline and improve the upscaling from the nano/micro scale to the scale of a triaxial.

The poor predictive accuracy on the validation dataset suggests that, although these models work, a more rounded training dataset would be required in order to accurately predict the mineralogy of a shale which is dissimilar to the training data. As such further research should focus on collecting a highly variable, large training dataset, which comprises clay rich, silica rich and calcite rich shales.

4.6 Contributions

The contributors to this chapter are as follows.

Name/ Institution	Contribution
Mohamed Rouainia (Newcastle University)	2016 study results and academic support
Majid Goodarzi	2016 study results
Yu Guan (Newcastle University)	Academic support
Cees Van Der Land (Newcastle University)	Academic support
Martin Jones (Newcastle University)	Academic support
Thomas Wagner (Heriot-Watt University)	Academic support

Table 4.11: List of contributors to this chapter

Chapter 5

Conclusions and Future Work

The need to bring anthropogenic climate change under control in the next twenty years has brought about a large amount of research into CO_2 sequestration in a variety of underground reservoirs. The quantification of risk in underground reservoirs needs on include the risk of shale seal failure, of which the mechanical properties, in particular Young's modulus are a key constraint. Owing to the key role that organic pores and organic matter plays in many of these shale seals, further knowledge of the organic matter Young's modulus, including associated trends, are integral to conducting CCUS safely. Organic geochemistry defines organic matter primarily by its precursor and depositional environment, loosely into four categories: lacustrine/bacterial, marine/algal, terrestrial/higher plant and oxidised. A second principle of organic geochemistry is the evolution of organic matter with thermal maturity. In this study we present the effect of depositional environment between lacustrine and marine organic matter on its Young's modulus, along with addressing the link between geochemical maturity and modulus change using marine shales.

Here we use the atomic force microscope to analyse the Young's modulus, at a resolution that can capture the internal heterogeneity of larger organic matter particles, and capture smaller lenses of organic matter independently of the neighbouring minerals. Four marine shales, covering a range of maturities, from immature to early gas window have been analysed, with subtly different organic matter types, mineralogies and depositional environments. These shales are; the immature sulphur rich Cretaceous Tarfaya marly-shale, comprising solely amorphous organic

matter, the early-late oil window Cretaceous Eagle Ford marly-shale, with a small terrestrial content, the peak-late oil window Mississippian, quartz rich Barnett Shale, only comprising amorphous organic matter and lastly the early gas window Mississippian Bowland shale, most rich in terrestrial organic matter. A sample of immature lacustrine Green River shale which has a similar terrestrial maceral content to the Bowland Shale has been used as a Type I kerogen comparison.

Organic matter Young's modulus analysis results on the marine shales, indicates that the samples share a bimodal Young's modulus distribution, comprising a softer peak with a mode at around 7-10GPa and a stiffer peak with a modal value of between 19-24GPa. This bimodal distribution also evolves with maturity; the immature Tarfaya distribution is dominated by the softer peak, which becomes roughly equal in size with the stiffer peak in the early/peak oil window Barnett and Eagle Ford Shale samples, after which the stiffer peak dominates the distribution in the late oil Eagle Ford and gas window Barnett and Bowland Shale samples. ^{13}C solid state NMR analysis indicates that this increase in the stiffer distribution coincides with an increase in aromatic carbon within the organic matter. This well known geochemical transition therefore appears to affect the organic matter's geomechanical properties, indicating that at least some of the other key transitions in organic geochemistry may affect organic geomechanics.

With this in mind the modulus distribution of the immature Tarfaya shale was analysed against the organic distribution of the Green River shale which contains Type I kerogen, deposited in a lacustrine setting. Palynofacies analysis undertaken on these two samples suggest minimal difference, with both comprising >95% amorphous organic matter. However, when the Young's modulus distributions are analysed it is clear that the lacustrine organics in the Green River do not share a bimodal distribution with the other marine shales, instead exhibiting a unimodal distribution centered around a value of 12.4GPa. This is unique amongst the shales studied, despite the NMR results of the Tarfaya and Green River being very similar. This suggests that further research into the modulus distributions and maturity paths of lacustrine organic matter is necessary before an adequate upsclaing model can be established.

Along with organic matter in shales being important for potential seals, coals represent a valuable potential CO_2 reservoirs for countries rich in deep coal deposits, or producing more CO_2

than feasibly stored in saline aquifers or depleted hydrocarbon reservoirs. As such understanding the mechanical response of a coal to CO_2 injection is necessary to determine the suitability of a seam for CCUS and enhanced coalbed methane recovery. The bulk elastic properties of a coal or shale, which determine its mechanical response, are controlled by the elastic properties of its individual components, i.e. macerals and minerals. The elastic properties of minerals are relatively well understood, and attempts have been made previously to acquire maceral elastic properties, particularly Young's modulus, by means of nanoindentation. However, due to the resolution of a nanoindent and small size of macerals, the response is likely to be from a combination of macerals.

Here atomic force microscopy is used for the first time to give a unique understanding of the local Young's modulus of individual macerals, with a precision of 10nm in both immature and mature coals/shale. Alginite, cutinite, inertinite and sporinite macerals are analysed from a samples of cannel coal (rich in cutinite), paper coal (enriched in sporinite), Northumberland coal (higher rank coal, rich in vitrinite and inertinite) and alginite rich New Albany Shale. Initial findings on the New Albany Shale indicate that kerogen isolation is not a suitable preparation technique for atomic force microscopy and as such, no alginite maceral moduli are reported. Therefore only results of the coal derived macerals (cutinite, inertinite and sporinite) are included in this study.

The results at this length scale indicate that the mean and modal Young's modulus values in all coal macerals, are less than 10GPa. This range is similar to Young's modulus values acquired by nanoindentation within previous studies. A major difference is that the modal modulus values obtained here are significantly lower than the modal values obtained within previous studies. Thermally immature liptinite macerals (cutinite/sporinite) have a lower modal modulus (1.35-2.97GPa) than the inertinites (1.44-3.42GPa) from the same coal. The modulus response is also non-normally distributed and most likely conform to a Gamma Distribution with shape parameter between 1.5-2.5.

The modal Young's modulus of all macerals increases with maturity, but not at the same rate, whereby the liptinite macerals become stiffer than the inertinites by the dry gas window (1.56%R_o in Northumberland Coal). This most likely reflects the inability of inertinite to un-

dergo major chemical transformations during maturation, and so the large proportion of the stiffening here is purely from compaction, although further research with a higher number of different maturity coals may help confirm this observation.

Upscaling of the Gamma Distributions to approximate nanoindentation results, which is simplistic but feasible, due to the relatively homogeneous nature of coals when compared with shales or other rocks, indicate that the AFM derived results are within the literature values of nanoindentation. This was achieved by taking a mean of an area equivalent, at least in 2D, to the area of influence of a nanoindent. However, these results were significantly different to the nanoindentation results acquired on some of the macerals during this study, although many of these ill-fitting results are believed to be due to calibration issues with the nanoindenter during the period of investigation. The similarity to the literature values and to those experienced on some of the coal macerals indicate that in relatively homogeneous, mechanically isotropic samples, this simple upscaling is a useful way of gaining an approximation of the Young's at a length scale higher than AFM.

Modelling of volumetric strain under CO_2 injection indicates an inversely proportionate relationship to Young's modulus, where the highest strains are predicted in the immature liptinite macerals, and lowest strains in the mature liptinite macerals. This is important, as the differential strain between macerals is most likely to cause failures under injection. It is therefore preferable to target mature coals for CCUS, as the reaction of macerals at higher maturities is more predictable across an entire coal seam.

In order to successfully sequester CO_2 into former conventional reservoirs, a detailed model of the caprock integrity is required. AFM on cuttings can help fill in some of the gaps that were left when the basin was initially drilled, however, further understanding of the seal may be required. The use of machine learning algorithms can help this by allowing inferences where data may be partial or missing, from the understanding of other areas of the same, or similar seals.

In this study we use a six of machine learning algorithms to predict the mineralogy of twenty three shale scans, each comprising SEM, EDX and AFM. The algorithms used are: Multivariate Logistic Regression, Perceptron, Random Forest, Decision Tree, K-Nearest Neighbours and

Multilayer Perceptron (also know as an artificial neural network). The training and testing data used were from the Eagle Ford and Green River shales gathered during Chapter 2. This dataset comprised approximately 4.2 million pixels of Eagle Ford and 900k pixels of Green River, each with an SEM backscatter reflectance, 10 EDX elemental datapoints and one Young's modulus value.

The models were trained in two methods, 2.5 million pixels were chosen using a random shuffle of all the training data across three random seeds, whilst the other method involved using 260,000 datapoints from the Green River and 520,000 datapoints from the Eagle Ford to give a more balanced dataset.

The predictive accuracies of these models varied across the training and test dataset, with the KNN and Random Forest having the highest mean accuracies when trained using the random seed, both in excess of 95%, with the majority of other models above 80%. These accuracies are slightly higher than those attained using the smaller training dataset. The accuracy of prediction within each mineral is slightly variable, with models best predicting the most common phases (calcite and clay), whilst struggling slightly with the identification of the least frequent phases (feldspar and dolomite), particularly in the Green River scans where some damage was present in the thin section.

Whilst these accuracies are high, it is important that a model is generalizable, as such these models were validated with three scans of Posidonia Shale, which had a significantly higher quartz content. This lead to a decrease in mineral classification accuracies, with all models apart from the KNN below 50%. The cause of this fall in accuracy was the misclassification of quartz as calcite. Although this isn't ideal, it makes little difference geomechanically, due to the similar Young's modulus of these two minerals. The Random Forest and KNN appear to be the most consistent models across the validation data, ranking in the top three accuracies on two of the validation datasets. The modulus distributions match this to an extent, but with the Random Forest modulus distributions mostly matching the predicted distribution, apart form the quartz distribution which, in turn is matched by the calcite distribution. The KNN modulus distributions are less accurate than the Random Forest suggesting a more systematic error. One of the Posidonia scans is very poorly predicted, which is related to the low contrast of the SEM

data in this scan. This demonstrates that a key component of any machine learning process is to collect the highest quality data possible.

In order to increase the accuracy on the validation dataset, the number of phases to be predicted was decreased to 4; organo-pore, clay, intermediate stiff and stiff. The accuracy on the high quality Posidonia scans when using these phases increased to approximately 80-90%, indicating that the reduction in complexity can compensate for the relatively homogeneous, and non-ideal training dataset.

Despite the progress in the field of organic matter geomechanics made during this research project, there are several research areas that could be improved upon by further work:

- Despite this study being the first to acquire the geomechanical properties of a lacustrine shale through AFM, further research should involve undertaking more analysis on the Green River Shale along with other lacustrine shales at different maturities, to identify any trends that exist within the organic matter of these shales. There are several ideal candidates such as those found in Eastern China (Ma et al., 2019), or the Ordos Basin in northern China (Tang et al., 2014) It appears at first that the organic matter is unimodally distributed with a peak completely different to the marine shales, but further data acquisition could lead to ascertain why this is.

- Along with analysing lacustrine shales further, future research should also attempt to refine some of the more common upscaling techniques to include the non-normal distributions and bimodal distributions, either by including a shape parameter similar to that used in the interpretation of many probability distributions (e.g. Gamma). Another option for this would be to increase the complexity of upscaling models to include two different organic phases in order to account for the bimodal distribution.

- The use of AFM to measure the mechanical properties of coal macerals is in its infancy, and as such there are large areas that future research should focus on. The main focus of research should be to increase the amount of different coal macerals and different maturities studied. This could involve undertaking a systematic approach of different coal fields in a similar manner to that undertaken on the shales in this study, or by analysing many

similar macerals from the same coal field in order to gain a greater understanding of the intrafield heterogeneity, which may help to better constrain the change with maturity. Another avenue for future research is significantly more complex, and should entail further constraining and developing the relationship between the thermodynamic properties of the coal macerals and their mechanical properties, with the aim of improving the Pan and Connell (2007) model used in this study.

- The basic machine learning techniques used here can be further improved by using a more detailed and varied dataset, which should allow models to be more generalizable, whilst still retaining accuracy. An improved model could allow detailed modulus prediction through AFM, which could readily combine with SEM and nanoindentation data for an alternative method to upscale between these two techniques.

- Along with improving the training dataset, the major improvement and future research regarding machine learning should focus upon using machine learning algorithms as a backbone for homogenization schemes and upscaling. This can be accomplished by using the machine learning algorithms to accurately predict the mechanical properties of each phase, along with its proportion and role in the shale. An example of this would be to use machine learning to assign a Young's modulus distribution of calcite, which may encompass multiple peaks, which could be due to matrix and grain calcite. These phases may have different moduli due to the variance in porosity between a calcite grain and calcite within the matrix, as well as the form of the calcite crystals within these two phases. This could allow a model to use a proportion of calcite within the shale matrix but also separately as grains, and then determine elastic stiffness based upon the modulus distribution of the phase which is load bearing. It may be that in this example, that the modulus distribution of the calcite grains becomes irrelevant as they are not load bearing, and thus the upscaling model can be changed from the observations during machine learning.

Appendix A

Appendix 1: Well Logs

Log Symbology

Lithology


Mudstone

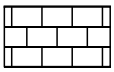
Marl

Sample


Sample Location

Pervasive Features


Bioturbation


Clast-rich Layer


Fossil

Fluid Escape Structure



Fracture

Laminations


Organic-Rich Laminae

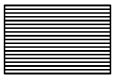
Parallel Laminations

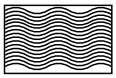
Undulating Laminations


Sparsely Laminated


Sparsely Laminated Marl

Vein

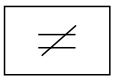
Massive/ Featureles

A.1 Barnett Lake Davis Well

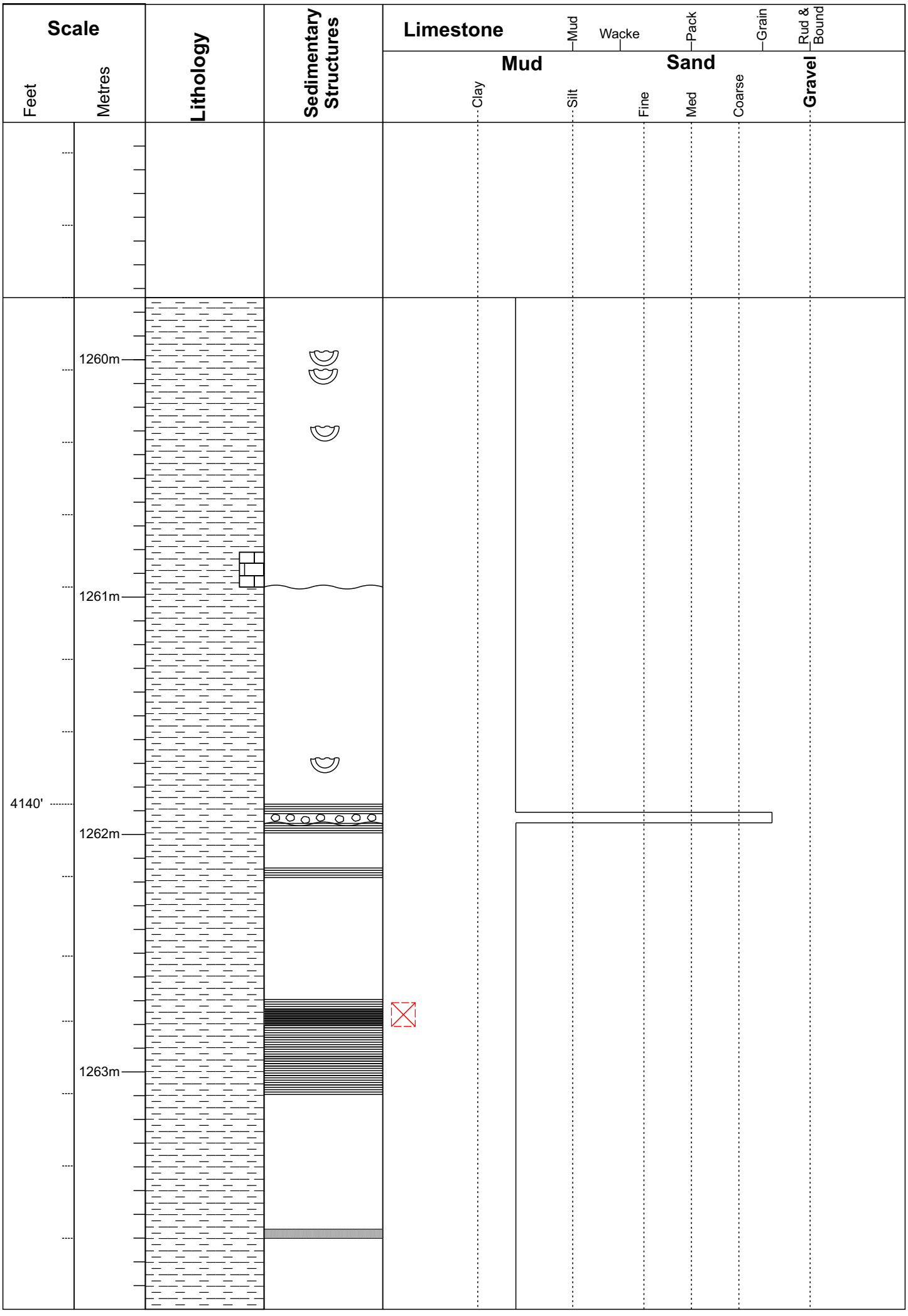
Scale
Feet
Metres
Lithology
Sedimentary Structures
Limestone
Mud
Wacke
Pack
Grain
Rud & Bound
Mud
Sand
Clay
Silt
Fine
Med
Coarse
Gravel
1260m
1261m
4140'
1262m
1263m

A.2 Barnett TP Sims Well

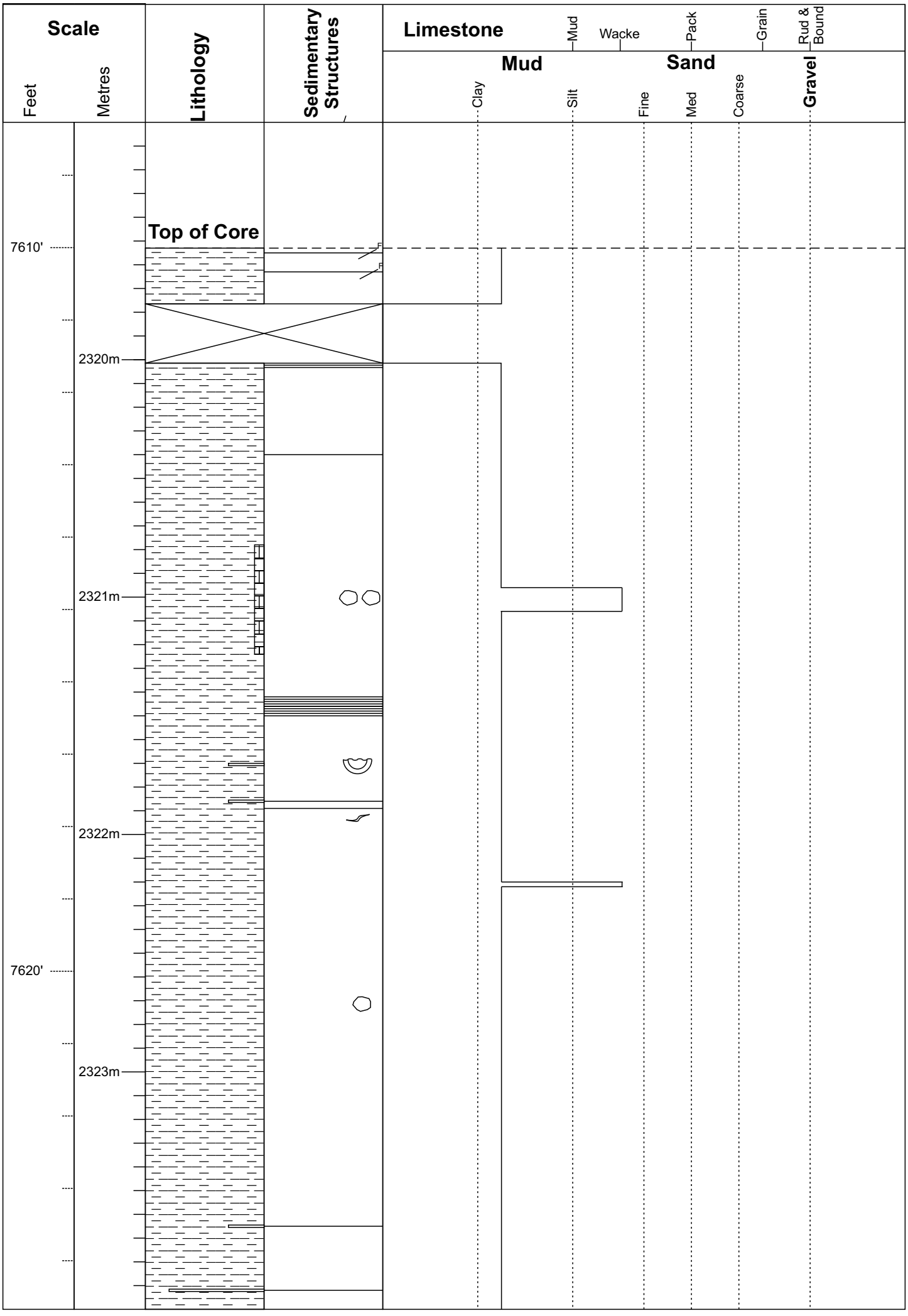
Scale
Feet
Metres
Lithology
Sedimentary Structures
Limestone
Mud
Wacke
Pack
Grain
Rud & Bound
Mud
Sand
Clay
Silt
Fine
Med
Coarse
Gravel
Top of Core
7610'
2320m
2321m
2322m
7620'
2323m

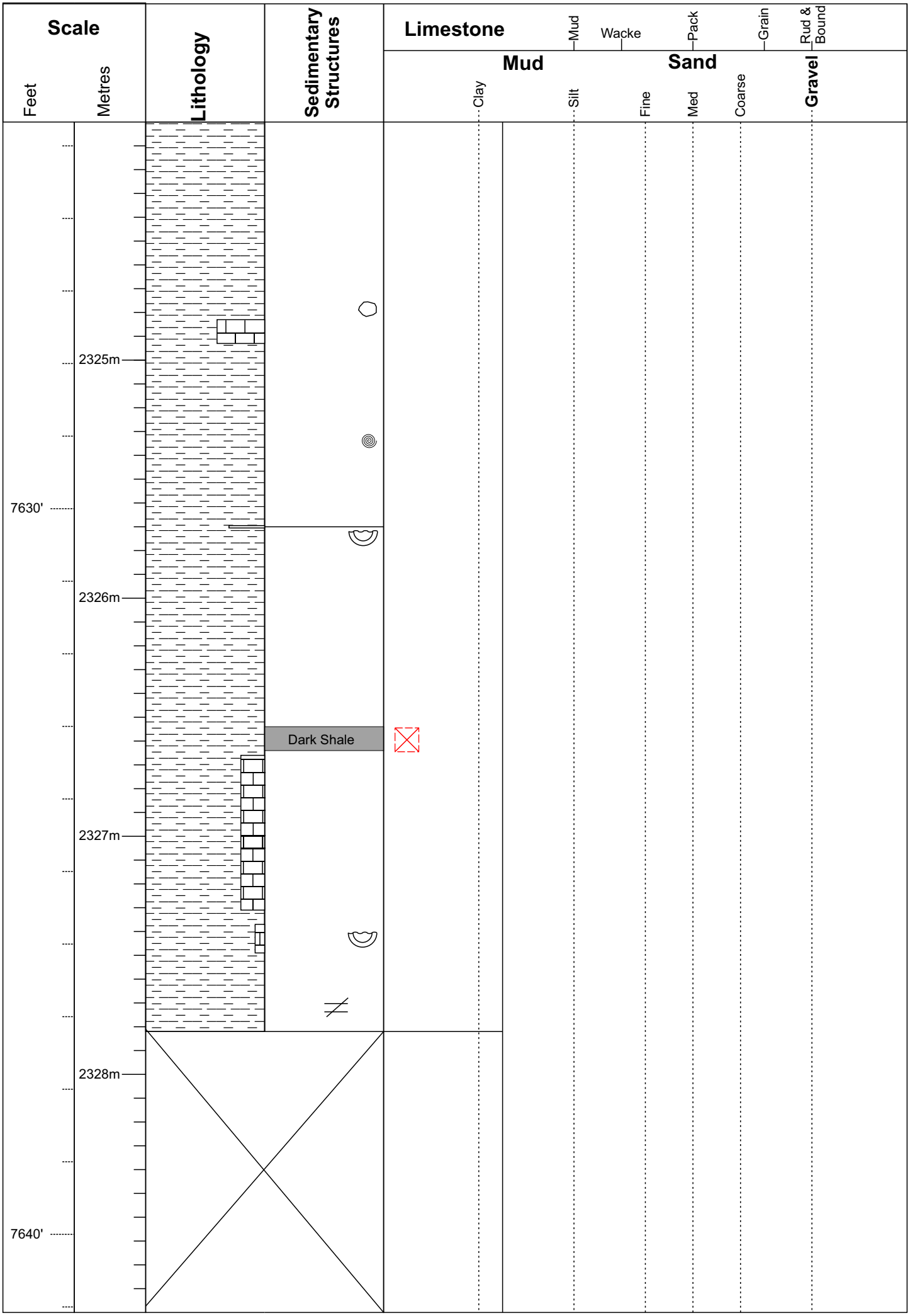
Scale
Feet
Metres
Lithology
Sedimentary Structures
Limestone
Mud
Wacke
Pack
Grain
Rud & Bound
Mud
Sand
Clay
Silt
Fine
Med
Coarse
Gravel
2325m
7630'
2326m
Dark Shale
2327m
2328m
7640'

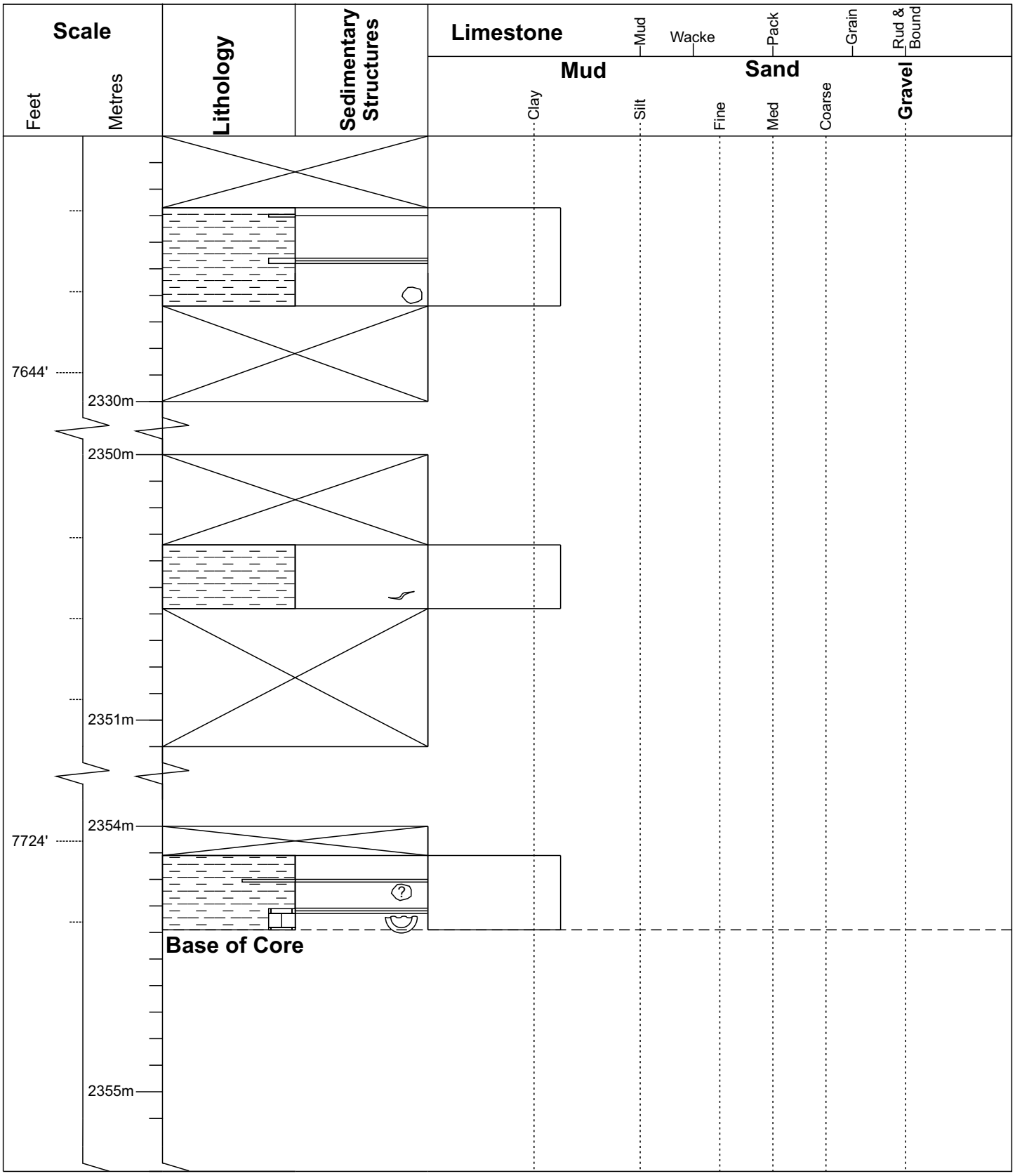
Scale
Feet
Metres
Lithology
Sedimentary Structures
Limestone
Mud
Wacke
Pack
Grain
Rud & Bound
Mud
Sand
Clay
Silt
Fine
Med
Coarse
Gravel
7644'
2330m
2350m
2351m
2354m
7724'
2355m
Base of Core

A.3 Bowland Preese Hall #1

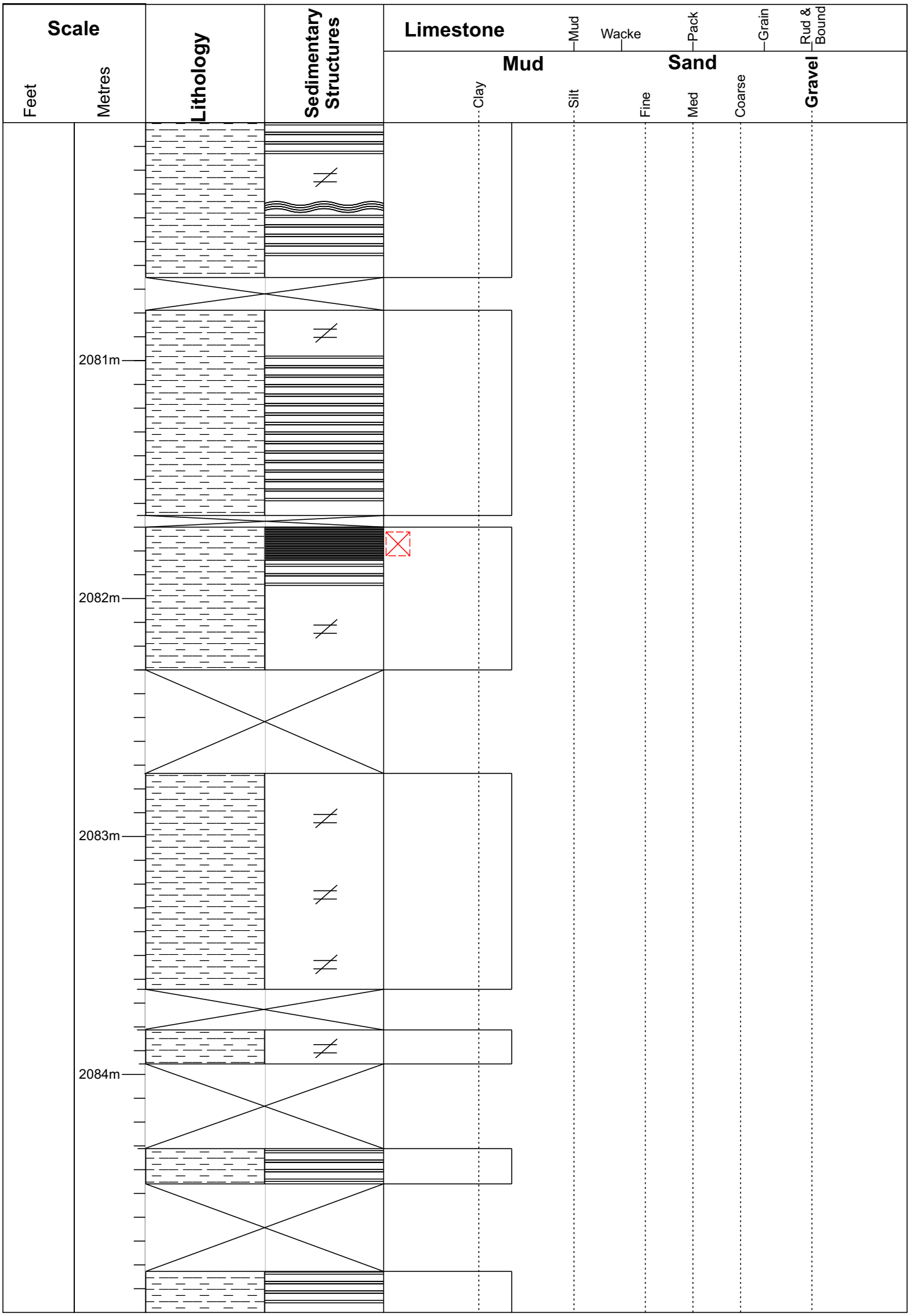
Scale
Feet
Metres
Lithology
Sedimentary Structures
Limestone
Mud
Wacke
Pack
Grain
Rud & Bound
Mud
Sand
Clay
Silt
Fine
Med
Coarse
Gravel
2081m
2082m
2083m
2084m

A.4 Eagle Ford Cinco Saus

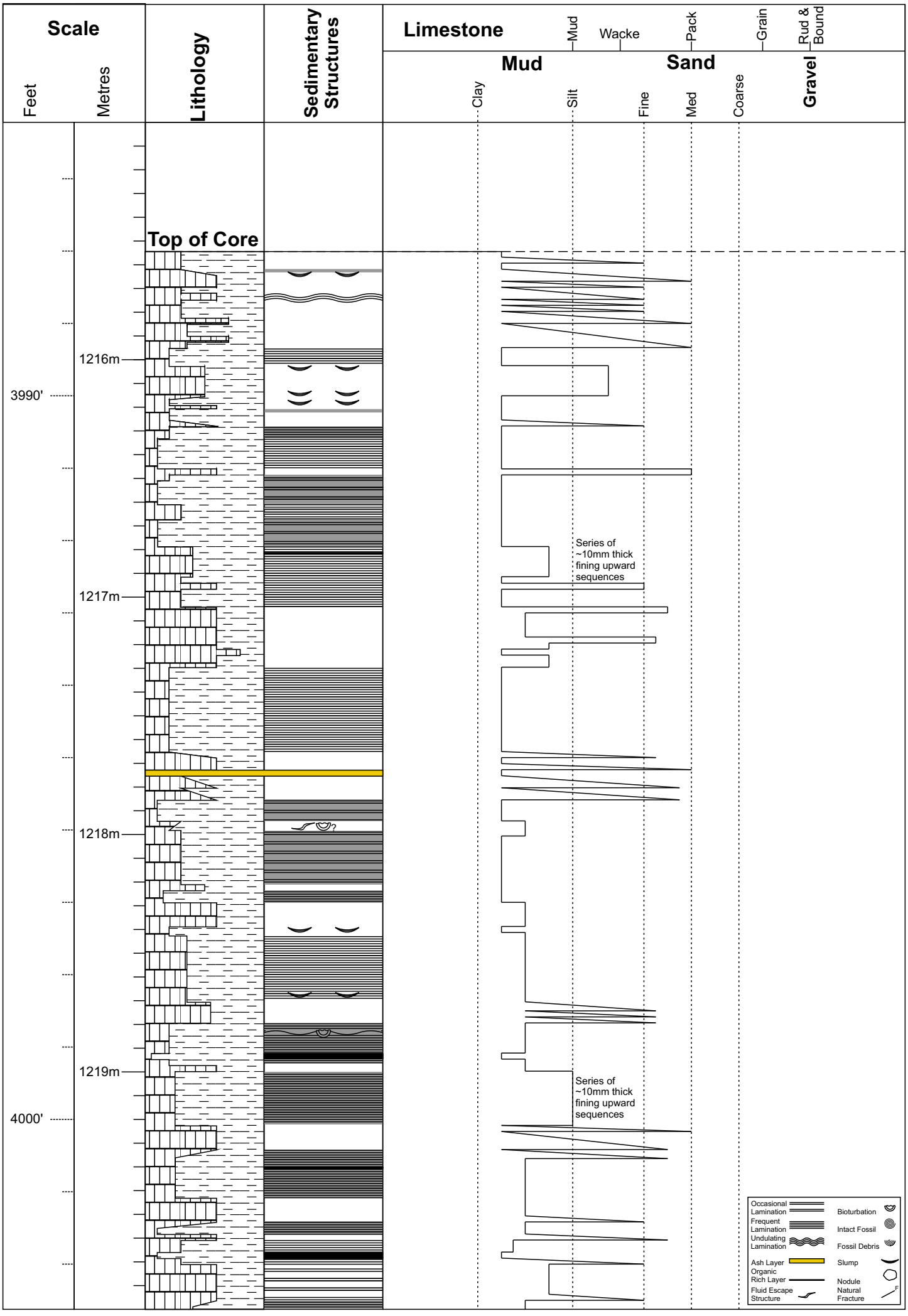
Scale
Feet
Metres
Lithology
Sedimentary Structures
Limestone
Mud
Wacke
Pack
Grain
Rud & Bound
Mud
Sand
Clay
Silt
Fine
Med
Coarse
Gravel
Top of Core
1216m
3990'
1217m
1218m
1219m
4000'
Series of ~10mm thick fining upward sequences
Series of ~10mm thick fining upward sequences
Occasional Lamination
Frequent Lamination
Undulating Lamination
Ash Layer
Organic Rich Layer
Fluid Escape Structure
Bioturbation
Intact Fossil
Fossil Debris
Slump
Nodule
Natural Fracture

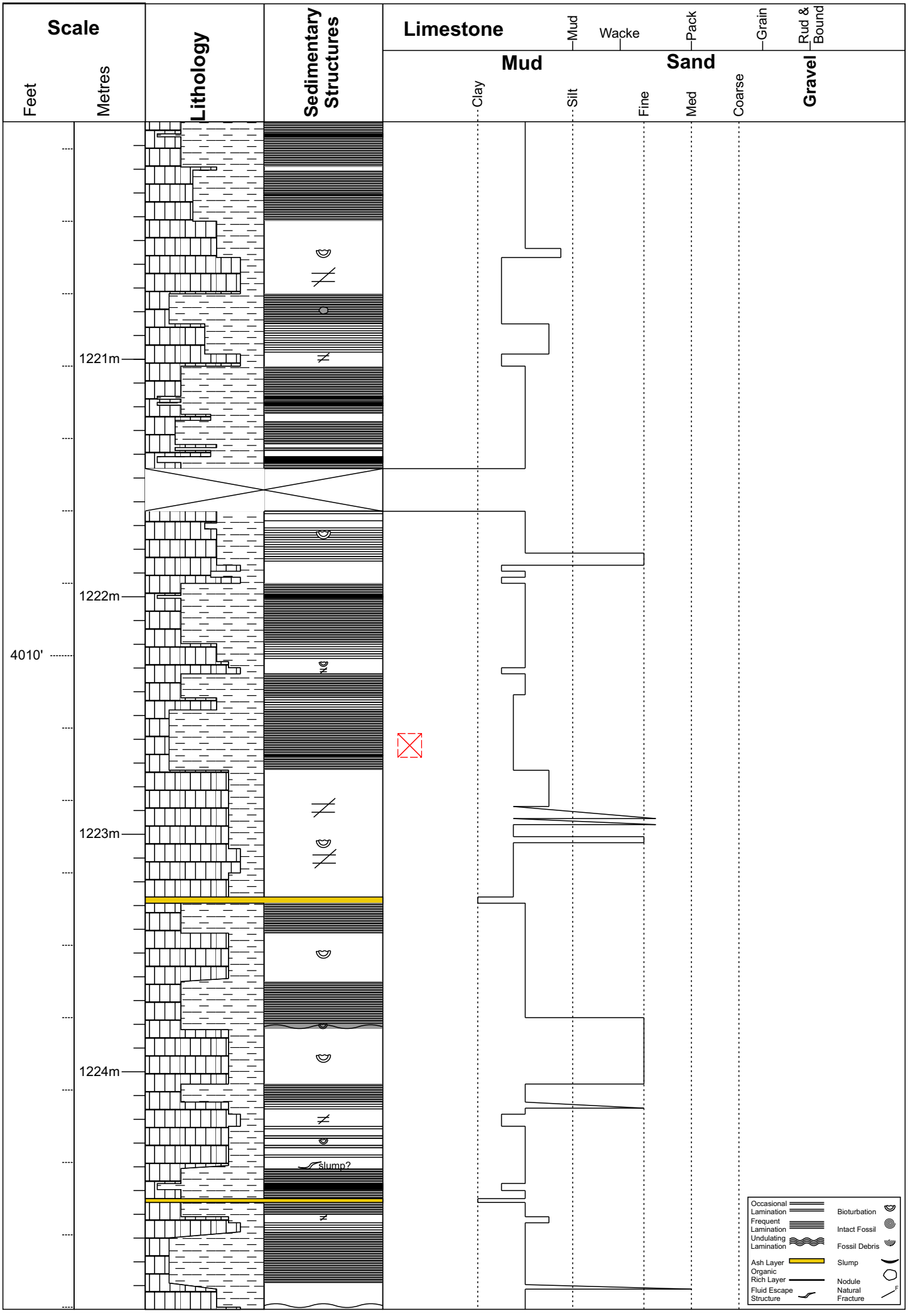
Scale
Feet
Metres
Lithology
Sedimentary Structures
Limestone
Mud
Wacke
Pack
Grain
Rud & Bound
Mud
Sand
Gravel
Clay
Silt
Fine
Med
Coarse
1221m
1222m
4010'
1223m
1224m
slump?
Occasional Lamination
Frequent Lamination
Undulating Lamination
Ash Layer
Organic Rich Layer
Fluid Escape Structure
Bioturbation
Intact Fossil
Fossil Debris
Slump
Nodule
Natural Fracture

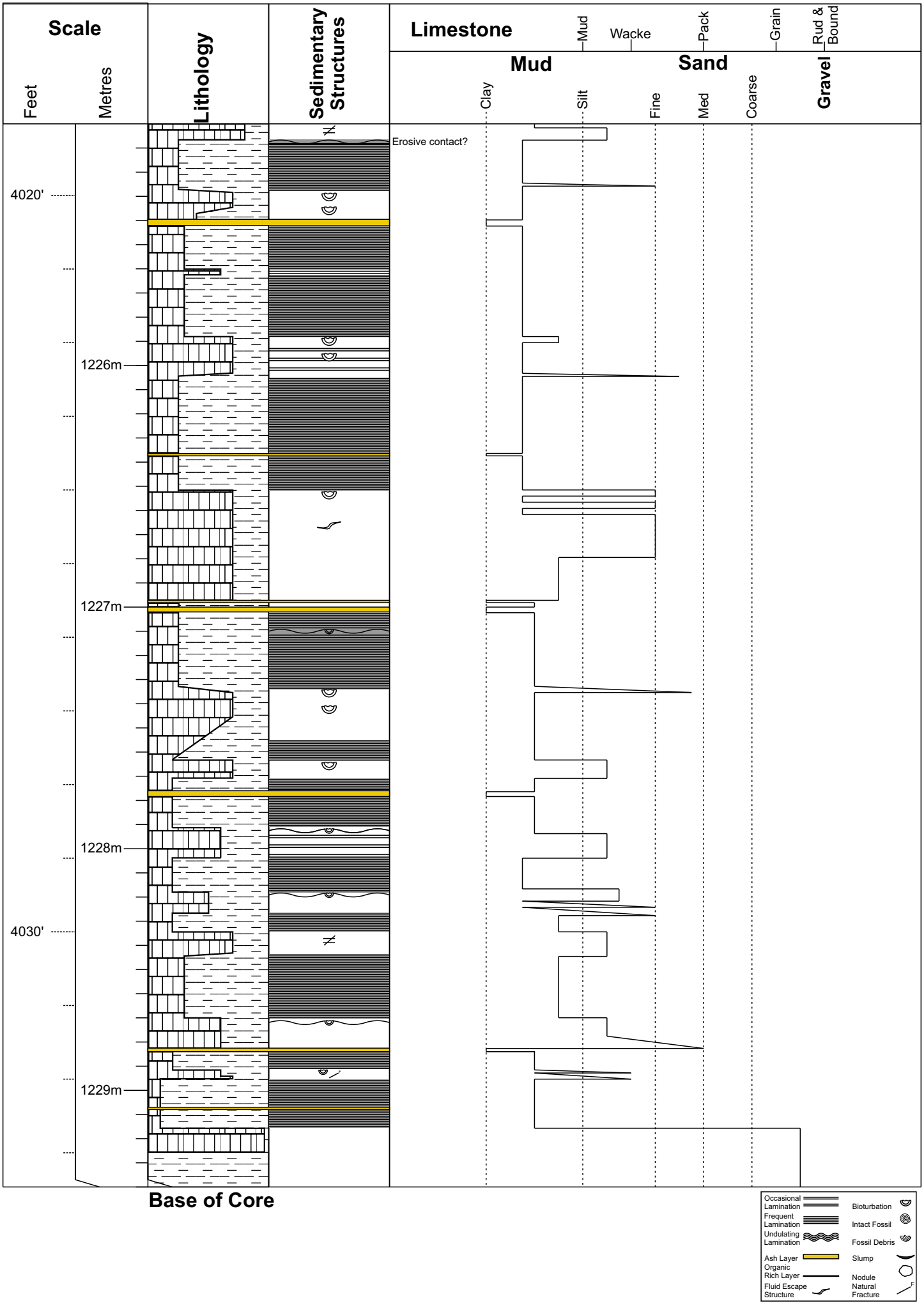
Scale
Feet
Metres
Lithology
Sedimentary Structures
Limestone
Mud
Wacke
Pack
Grain
Rud & Bound
Mud
Sand
Gravel
Clay
Silt
Fine
Med
Coarse
Erosive contact?
4020'
1226m
1227m
1228m
4030'
1229m
Base of Core
Occasional Lamination
Frequent Lamination
Undulating Lamination
Ash Layer
Organic Rich Layer
Fluid Escape Structure
Bioturbation
Intact Fossil
Fossil Debris
Slump
Nodule
Natural Fracture

A.5 Eagle Ford Carol

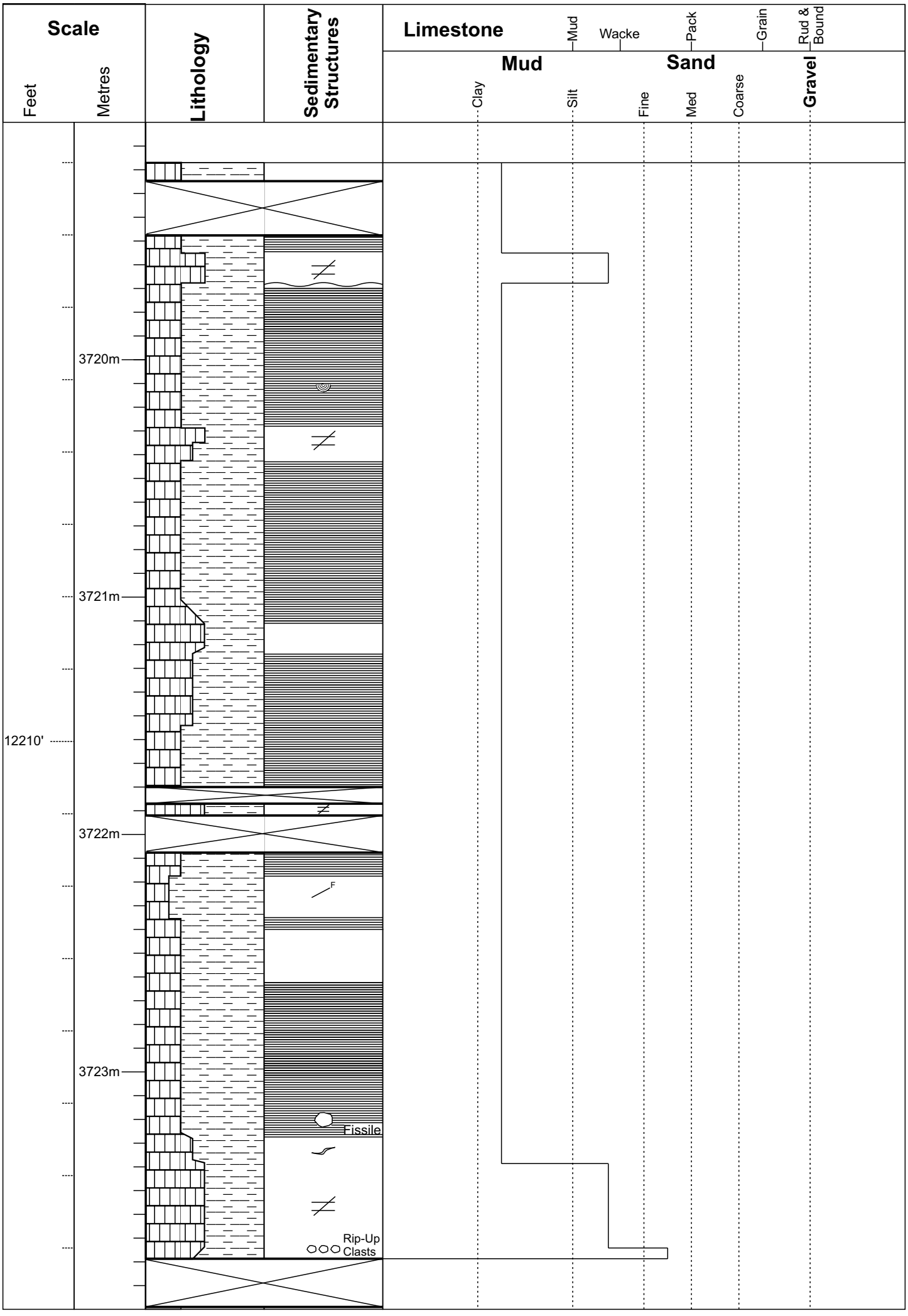
Scale
Feet
Metres
Lithology
Sedimentary Structures
Limestone
Mud
Wacke
Pack
Grain
Rud & Bound
Mud
Sand
Clay
Silt
Fine
Med
Coarse
Gravel
3720m
3721m
12210'
3722m
3723m
F
Fissile
Rip-Up Clasts

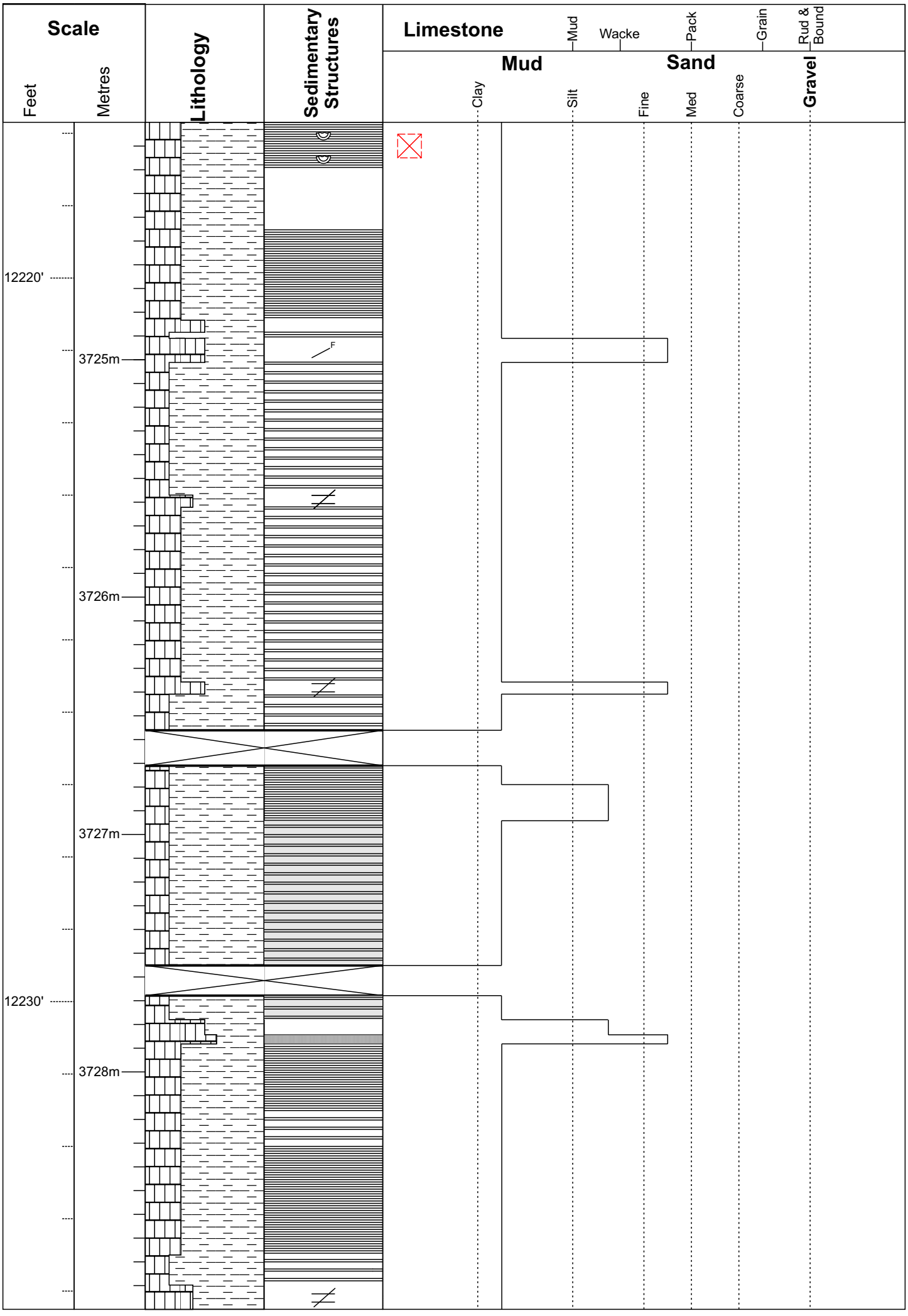
Scale
Feet
Metres
Lithology
Sedimentary Structures
Limestone
Mud
Wacke
Pack
Grain
Rud & Bound
Mud
Sand
Clay
Silt
Fine
Med
Coarse
Gravel
12220'
3725m
3726m
3727m
12230'
3728m
F

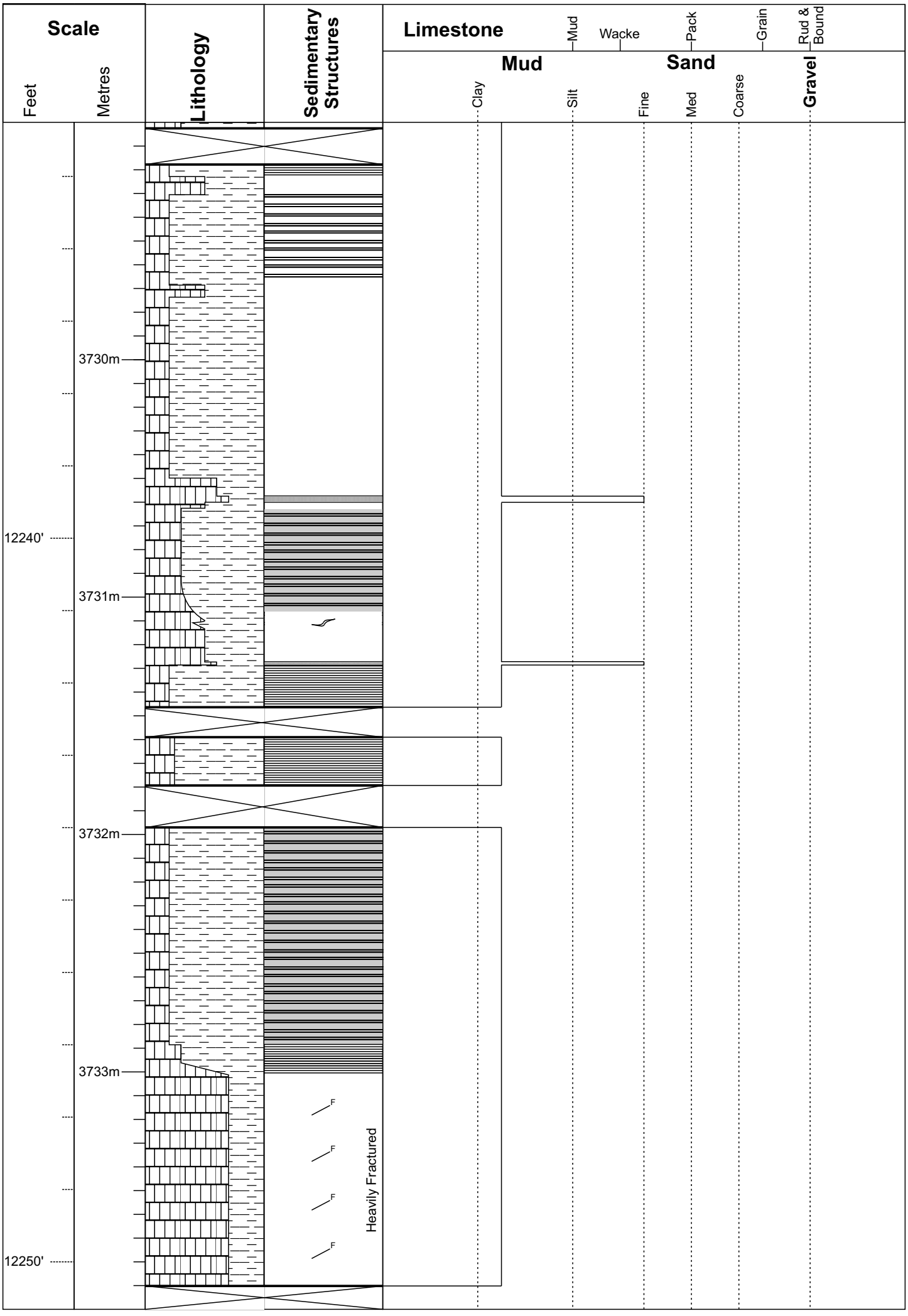
Scale
Feet
Metres
Lithology
Sedimentary Structures
Limestone
Mud
Wacke
Pack
Grain
Rud & Bound
Mud
Sand
Clay
Silt
Fine
Med
Coarse
Gravel
3730m
12240'
3731m
3732m
3733m
12250'
F
F
F
F
Heavily Fractured

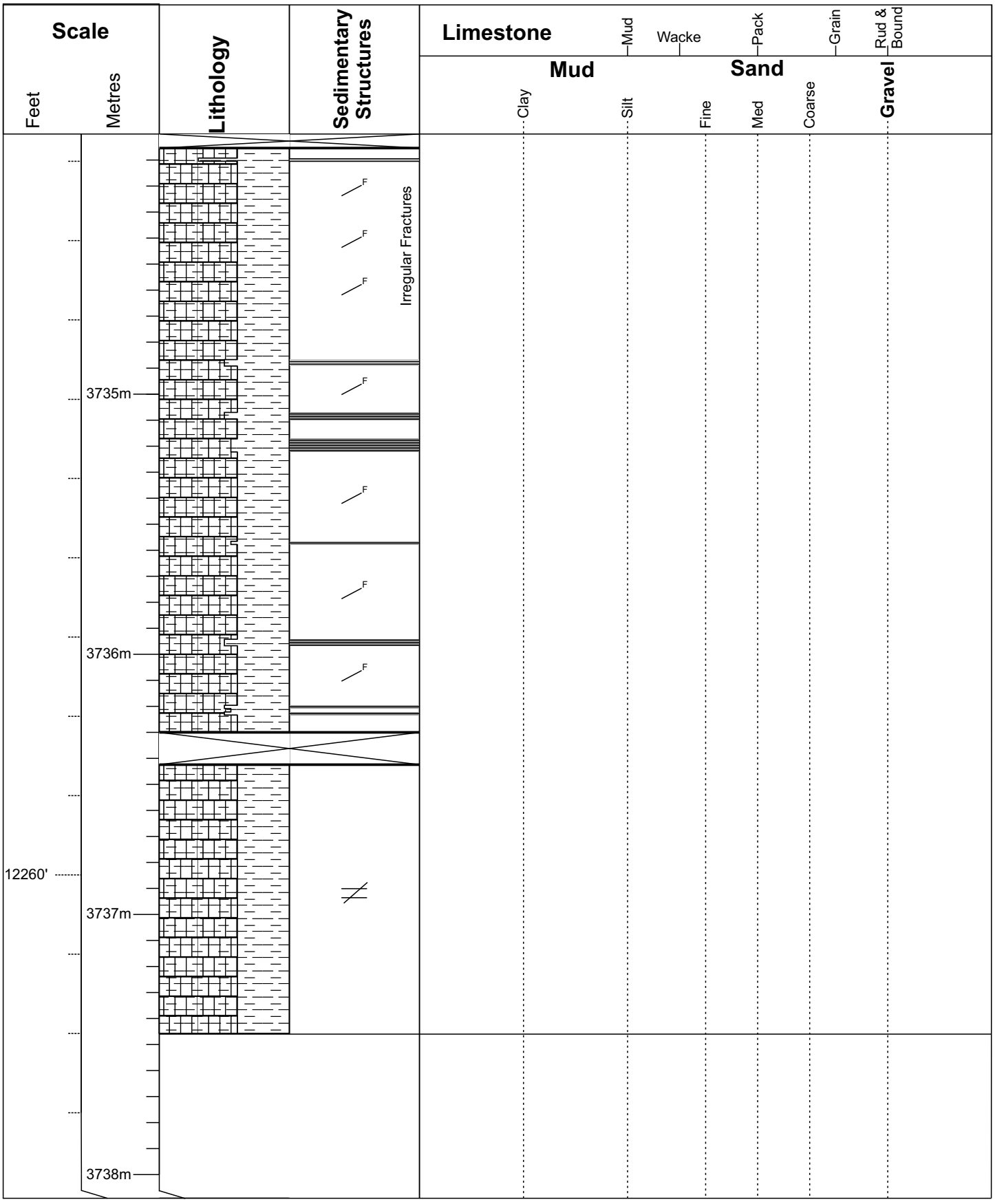
Scale
Feet
Metres
Lithology
Sedimentary Structures
Limestone
Mud
Wacke
Pack
Grain
Rud & Bound
Mud
Sand
Clay
Silt
Fine
Med
Coarse
Gravel
Irregular Fractures
F
3735m
3736m
3737m
3738m
12260'

A.6 Tarfaya, S57

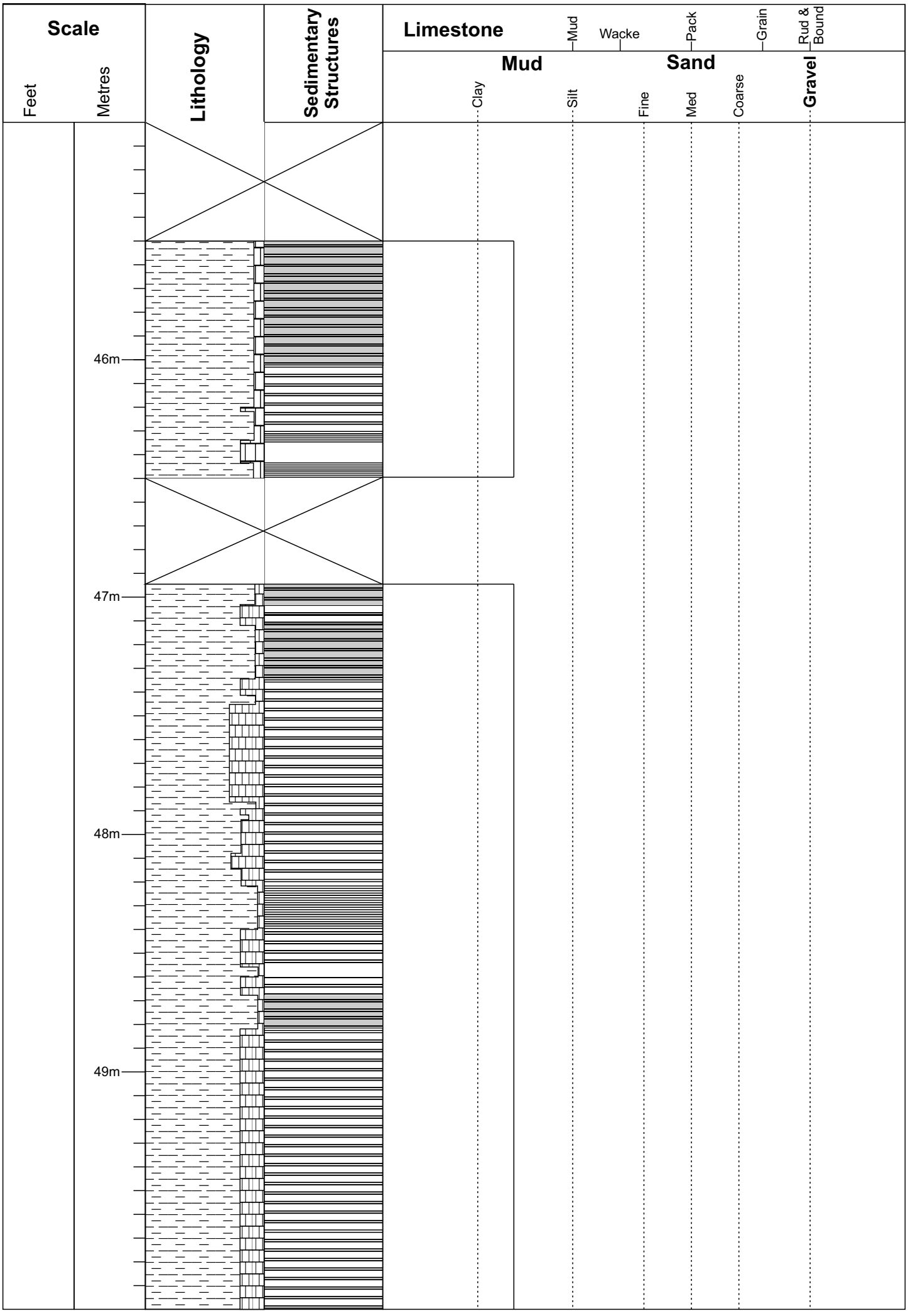
Scale
Feet
Metres
Lithology
Sedimentary Structures
Limestone
Mud
Wacke
Pack
Grain
Rud & Bound
Mud
Sand
Clay
Silt
Fine
Med
Coarse
Gravel
46m
47m
48m
49m

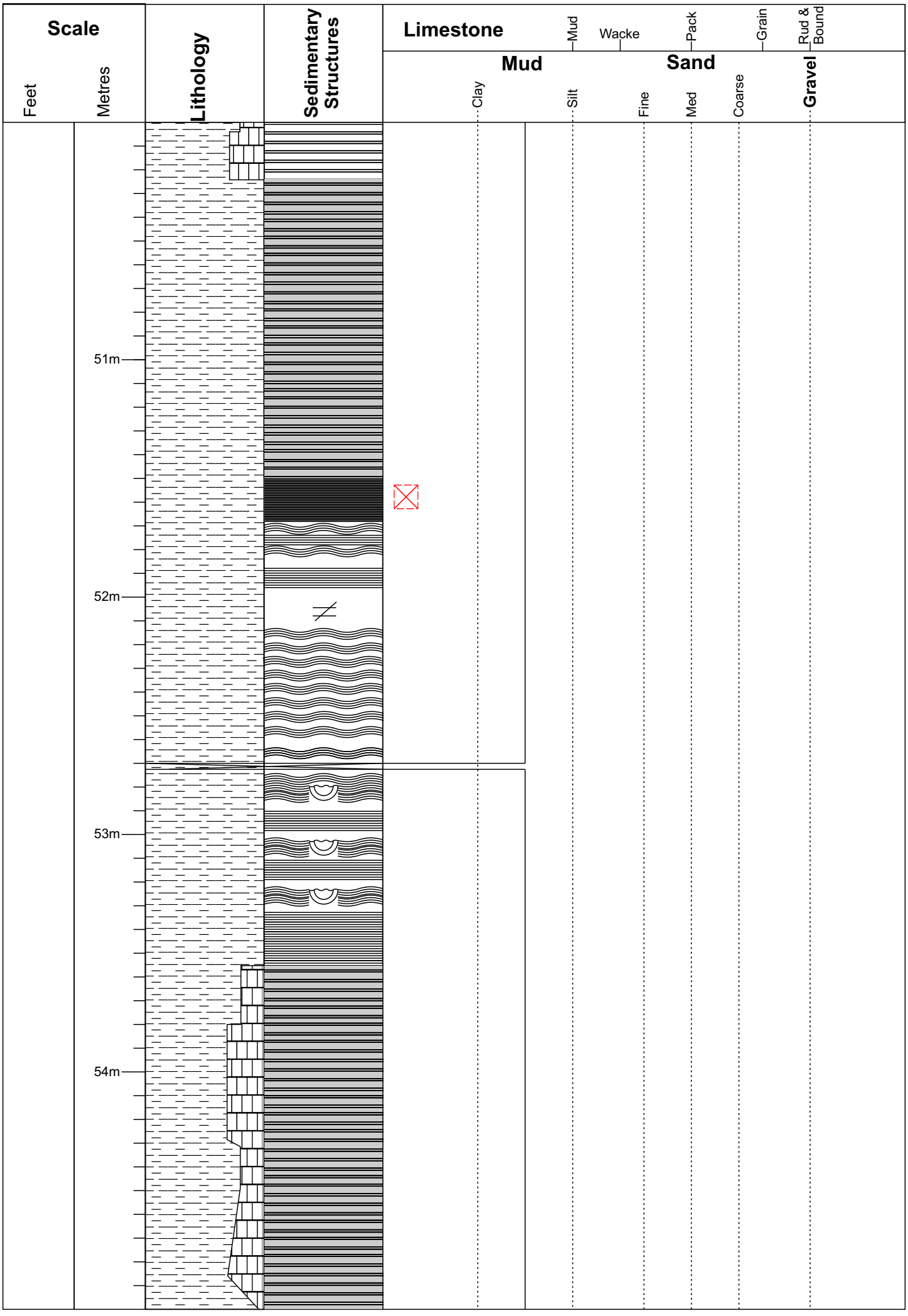
Scale
Feet
Metres
Lithology
Sedimentary Structures
Limestone
Mud
Wacke
Pack
Grain
Rud & Bound
Mud
Sand
Clay
Silt
Fine
Med
Coarse
Gravel
51m
52m
53m
54m

Bibliography

, .

Abadi, M., Agarwal, A., Barham, P., Brevdo, E., Chen, Z., Citro, C., Corrado, G.S., Davis, A., Dean, J., Devin, M., Ghemawat, S., Goodfellow, I., Harp, A., Irving, G., Isard, M., Jia, Y., Jozefowicz, R., Kaiser, L., Kudlur, M., Levenberg, J., Mané, D., Monga, R., Moore, S., Murray, D., Olah, C., Schuster, M., Shlens, J., Steiner, B., Sutskever, I., Talwar, K., Tucker, P., Vanhoucke, V., Vasudevan, V., Viégas, F., Vinyals, O., Warden, P., Wattenberg, M., Wicke, M., Yu, Y., Zheng, X., 2015. TensorFlow: Large-scale machine learning on heterogeneous systems. URL: `https://www.tensorflow.org/`. software available from tensorflow.org.

Aggarwal, C.C., 2018. Neural networks and deep learning. Springer 10, 978–3.

Akkaş, E., Akin, L., Çubukçu, H.E., Artuner, H., 2015. Application of decision tree algorithm for classification and identification of natural minerals using SEM–EDS. Computers & Geosciences 80, 38–48.

Alexeev, A., Revva, V., Alyshev, N., Zhitlyonok, D., 2004. True triaxial loading apparatus and its application to coal outburst prediction. International Journal of Coal Geology 58, 245–250.

Allan, A.M., Clark, A.C., Vanorio, T., Kanitpanyacharoen, W., Wenk, H.R., 2016. On the evolution of the elastic properties of organic-rich shale upon pyrolysis-induced thermal maturation elasticity of pyrolyzed shale. Geophysics 81, D263–D281.

Allan, A.M., Vanorio, T., Dahl, J.E., 2014. Pyrolysis-induced P-wave velocity anisotropy in organic-rich shales. Geophysics 79, D41–D53.

Ambrose, J., 2014. Failure of anisotropic shales under triaxial stress conditions .

Andrews, I.J., 2013. The Carboniferous Bowland Shale gas study: geology and resource estimation .

Aplin, A.C., Macquaker, J.H., 2011. Mudstone diversity: Origin and implications for source, seal, and reservoir properties in petroleum systems. AAPG bulletin 95, 2031–2059.

Arganda-Carreras, I., Kaynig, V., Rueden, C., Eliceiri, K.W., Schindelin, J., Cardona, A., Sebastian Seung, H., 2017. Trainable Weka Segmentation: a machine learning tool for microscopy pixel classification. Bioinformatics 33, 2424–2426.

Armaghani, D.J., Hajihassani, M., Bejarbaneh, B.Y., Marto, A., Mohamad, E.T., 2014. Indirect measure of shale shear strength parameters by means of rock index tests through an optimized artificial neural network. Measurement 55, 487–498.

Armitage, P., Faulkner, D., Worden, R., Aplin, A., Butcher, A., Iliffe, J., 2011. Experimental measurement of, and controls on, permeability and permeability anisotropy of caprocks from the co_2 storage project at the Krechba Field, Algeria. Journal of Geophysical Research: Solid Earth 116.

Austin, N., Kennedy, L., 2005. Textural controls on the brittle deformation of dolomite: variations in peak strength. Geological Society, London, Special Publications 243, 37–49.

Bagherieh, A., Hower, J.C., Bagherieh, A., Jorjani, E., 2008. Studies of the relationship between petrography and grindability for kentucky coals using artificial neural network. International Journal of Coal Geology 73, 130–138.

Baihly, J., Malpani, R., Altman, R., Lindsay, G., Clayton, R., 2015. Shale gas production decline trend comparison over time and basins—revisited, in: Unconventional Resources Technology Conference, San Antonio, Texas, 20-22 July 2015, Society of Exploration Geophysicists, American Association of Petroleum .... pp. 1080–1107.

Barron, J., . China surpassed the United States as the world's largest crude oil importer in

2017. US Energy Information Administration URL: https://www.eia.gov/todayinenergy/detail.php?id=34812.

Barrows, M.H., Cluff, R.M., 1984. New Albany Shale Group (Devonian-Mississippian) source rocks and hydrocarbon generation in the Illinois Basin .

Bauer, H., 2011. Measure and integration theory. volume 26. Walter de Gruyter.

Behar, F., Vandenbroucke, M., 1987. Chemical modelling of kerogens. Organic Geochemistry 11, 15–24.

Beil, S., Kuhnt, W., Holbourn, A.E., Aquit, M., Flögel, S., Chellai, E.H., Jabour, H., 2018. New insights into Cenomanian paleoceanography and climate evolution from the Tarfaya Basin, southern Morocco. Cretaceous Research 84, 451–473.

Bennett, K.C., Berla, L.A., Nix, W.D., Borja, R.I., 2015. Instrumented nanoindentation and 3D mechanistic modeling of a shale at multiple scales. Acta Geotechnica 10, 1–14.

Bentham, M., Kirby, M., 2005. CO_2 storage in saline aquifers. Oil & gas science and technology 60, 559–567.

Bergins, C., Hulston, J., Strauss, K., Chaffee, A.L., 2007. Mechanical/thermal dewatering of lignite. Part 3: Physical properties and pore structure of MTE product coals. Fuel 86, 3–16.

Bernard, S., Wirth, R., Schreiber, A., Schulz, H.M., Horsfield, B., 2012. Formation of nanoporous pyrobitumen residues during maturation of the Barnett Shale (Fort Worth Basin). International Journal of Coal Geology 103, 3–11.

Bhattacharya, S., Mishra, S., 2018. Applications of machine learning for facies and fracture prediction using Bayesian Network Theory and Random Forest: Case studies from the Appalachian basin, USA. Journal of Petroleum Science and Engineering 170, 1005–1017.

Bickle, M.J., 2009. Geological carbon storage. Nature Geoscience 2, 815–818.

Bjørlykke, K., Aagaard, P., 1992. Clay minerals in North Sea sandstones .

Bobko, C., Ulm, F.J., 2008. The nano-mechanical morphology of shale. Mechanics of Materials 40, 318–337.

Boles, J.R., Franks, S.G., 1979. Clay diagenesis in Wilcox sandstones of Southwest Texas; implications of smectite diagenesis on sandstone cementation. Journal of Sedimentary Research 49, 55–70.

Borodich, F.M., Bull, S., Epshtein, S., 2015. Nanoindentation in studying mechanical properties of heterogeneous materials. Journal of Mining Science 51, 470–476.

Bowker, K.A., 2007. Barnett Shale gas production, Fort Worth Basin: Issues and discussion. AAPG Bulletin 91, 523–533.

Bradley, W.H., 1964. Geology of the Green River Formation and associated Eocene rocks in southwestern Wyoming and adjacent parts of Colorado and Utah, United States Geological Survey professional paper 496-A. US Government Printing Office, Washington, DC 57.

Breiman, L., 2001. Random forests. Machine learning 45, 5–32.

Britt, L.K., Schoeffler, J., et al., 2009. The geomechanics of a shale play: what makes a shale prospective, in: SPE eastern regional meeting, Society of Petroleum Engineers.

Brown, J.M., Angel, R.J., Ross, N.L., 2016. Elasticity of plagioclase feldspars. Journal of Geophysical Research: Solid Earth 121, 663–675.

Bullock, L.A., Parnell, J., Perez, M., Armstrong, J.G., Feldmann, J., Boyce, A.J., 2018. High selenium in the Carboniferous Coal Measures of Northumberland, North East England. International Journal of Coal Geology 195, 61–74.

Busch, A., Gensterblum, Y., 2011. Cbm and CO_2-ECBM related sorption processes in coal: a review. International Journal of Coal Geology 87, 49–71.

Camp, W.K., 2013. Enhancing SEM grayscale images through pseudocolor conversion: examples from Eagle Ford, Haynesville, and Marcellus Shales, in: Unconventional Resources Technology

Conference, Society of Exploration Geophysicists, American Association of Petroleum .... pp. 2300–2307.

Cardott, B.J., Curtis, M.E., 2018. Identification and nanoporosity of macerals in coal by scanning electron microscopy. International Journal of Coal Geology 190, 205–217.

Cardott, B.J., Landis, C.R., Curtis, M.E., 2015. Post-oil solid bitumen network in the Woodford shale, USA—a potential primary migration pathway. International Journal of Coal Geology 139, 106–113.

Cavanagh, A., Ringrose, P., 2014. Improving oil recovery and enabling CCS: a comparison of offshore gas-recycling in Europe to CCUS in North America. Energy Procedia 63, 7677–7684.

Chadwick, A., Arts, R., Bernstone, C., May, F., Thibeau, S., Zweigel, P., 2008. Best practice for the storage of CO_2 in saline aquifers-observations and guidelines from the SACS and CO_2STORE projects. volume 14. British Geological Survey.

Chadwick, O.A., Masiello, C.A., Baldock, J., Smernik, R., Randerson, J., 2004. The oxidation state of soil organic carbon: A new proxy for carbon storage mechanisms and land use change. Kearney Foundation of Soil Science, UC Davis .

Chelgani, S.C., Hower, J.C., Jorjani, E., Mesroghli, S., Bagherieh, A., 2008. Prediction of coal grindability based on petrography, proximate and ultimate analysis using multiple regression and artificial neural network models. Fuel Processing Technology 89, 13–20.

Chen, Y., Zhang, D., 2020. Physics-constrained deep learning of geomechanical logs. IEEE Transactions on Geoscience and Remote Sensing .

Cheng, P., Xiao, X., Wang, X., Sun, J., Wei, Q., 2019. Evolution of water content in organic-rich shales with increasing maturity and its controlling factors: Implications from a pyrolysis experiment on a water-saturated shale core sample. Marine and Petroleum Geology 109, 291–303.

Chopinet, L., Roduit, C., Rols, M.P., Dague, E., 2013. Destabilization induced by electropermeabilization analyzed by atomic force microscopy. Biochimica et Biophysica Acta (BBA)-Biomembranes 1828, 2223–2229.

Collister, J.W., Summons, R.E., Lichtfouse, E., Hayes, J.M., 1992. An isotopic biogeochemical study of the Green River Oil Shale. Organic Geochemistry 19, 265–276.

Condon, S., Dyman, T., 2006. 2003 geologic assessment of undiscovered conventional oil and gas resources in the Upper Cretaceous Navarro and Taylor Groups, Western Gulf Province, Texas. Technical Report. US Geological Survey.

Connell, L., Detournay, C., 2009. Coupled flow and geomechanical processes during enhanced coal seam methane recovery through co_2 sequestration. International Journal of Coal Geology 77, 222–233.

Constantinides, G., Ulm, F.J., 2007. The nanogranular nature of C–S–H. Journal of the Mechanics and Physics of Solids 55, 64–90.

Cornford, C., Morrow, J., Turrington, A., Miles, J., Brooks, J., 1983. Some geological controls on oil composition in the UK North Sea. Geological Society, London, Special Publications 12, 175–194.

Craddock, P.R., Le Doan, T.V., Bake, K., Polyakov, M., Charsky, A.M., Pomerantz, A.E., 2015. Evolution of kerogen and bitumen during thermal maturation via semi-open pyrolysis investigated by infrared spectroscopy. Energy & Fuels 29, 2197–2210.

Curtis, C.D., 1985. Clay mineral precipitation and transformation during burial diagenesis. Philosophical Transactions of the Royal Society of London. Series A, Mathematical and Physical Sciences 315, 91–105.

Curtis, M.E., Cardott, B.J., Sondergeld, C.H., Rai, C.S., 2012. Development of organic porosity in the Woodford Shale with increasing thermal maturity. International Journal of Coal Geology 103, 26–31.

Cutler, A., Cutler, D.R., Stevens, J.R., 2012. Random forests, in: Ensemble machine learning. Springer, pp. 157–175.

D2798-11a, 2014. Standard test method for microscopical determination of the reflectance of vitrinite dispersed in sedimentary rocks .

Datta, A., Krishnamoorti, R., 2019. Opportunities for a low carbon transition-deploying carbon capture, utilization, and storage in northeast India. Frontiers in Energy Research 7, 12.

Dehua, Z., Fangzheng, J., 2012. Evaluation and prediction of shale gas sweet spots: A case study in jurassic of Jiannan area, Sichuan Basin. Petroleum Geology & Experiment 34, 109–114.

Demyanov, V., Reesink, A.J.H., Arnold, D.P., 2019. Can machine learning reveal sedimentological patterns in river deposits? Geological Society, London, Special Publications 488, 221–235.

Derjaguin, B.V., Muller, V.M., Toporov, Y.P., 1975. Effect of contact deformations on the adhesion of particles. Journal of Colloid and interface science 53, 314–326.

DiMichele, W.A., Rischbieter, M.O., Eggert, D.L., Gastaldo, R.A., 1984. Stem and leaf cuticle of Karinopteris: source of cuticles from the Indiana "paper" coal. American Journal of Botany 71, 626–637.

Duarte-Coronado, D., Tellez-Rodriguez, J., Pires de Lima, R., Marfurt, K., Slatt, R., et al., 2019. Deep convolutional neural networks as an estimator of porosity in thin-section images for unconventional reservoirs, in: SEG International Exposition and Annual Meeting, Society of Exploration Geophysicists.

Eliyahu, M., Emmanuel, S., Day-Stirrat, R.J., Macaulay, C.I., 2015. Mechanical properties of organic matter in shales mapped at the nanometer scale. Marine and Petroleum Geology 59, 294–304.

Emmanuel, S., Eliyahu, M., Day-Stirrat, R.J., Hofmann, R., Macaulay, C.I., 2016. Impact of thermal maturation on nano-scale elastic properties of organic matter in shales. Marine and Petroleum Geology 70, 175–184.

Emmanuel, S., Eliyahu, M., Day-Stirrat, R.J., Hofmann, R., Macaulay, C.I., 2017. Softening of organic matter in shales at reservoir temperatures. Petroleum Geoscience 23, 262–269.

Epshtein, S.A., Borodich, F.M., Bull, S.J., 2015. Evaluation of elastic modulus and hardness of highly inhomogeneous materials by nanoindentation. Applied Physics A 119, 325–335.

Espinoza, D.N., Pereira, J.M., Vandamme, M., Dangla, P., Vidal-Gilbert, S., 2015. Desorption-induced shear failure of coal bed seams during gas depletion. International Journal of Coal Geology 137, 142–151.

Fan, L., Martin, R.B., Thompson, J.W., Atwood, K., Robinson, J.R., Lindsay, G.J., et al., 2011. An integrated approach for understanding oil and gas reserves potential in Eagle Ford shale formation, in: Canadian Unconventional Resources Conference, Society of Petroleum Engineers.

Fauchille, A.L., Ma, L., Rutter, E., Chandler, M., Lee, P.D., Taylor, K.G., 2017. An enhanced understanding of the Basinal Bowland shale in Lancashire (UK), through microtextural and mineralogical observations. Marine and Petroleum Geology 86, 1374–1390.

Fender, T., Rouainia, M., Van Der Land, C., Jones, D.M., Mastalerz, M., Hennisen, J.A., Graham, S.P., Wagner, T., 2020. Geomechanical properties of coal macerals; measurements applicable to modelling swelling of coal seams during CO_2 sequestration. International Journal of Coal Geology , 103528.

Francis, R., McIsaac, K., Thompson, D., Osinski, G., 2014. Autonomous mapping of outcrops using Multiclass Linear Discriminant Analysis, in: Proceedings of the International Symposium on Artificial Intelligence, Robotics and Automation in Space, Montreal, Canada.

Fraser, A., Nash, D., Steele, R., Ebdon, C., 1990. A regional assessment of the intra-Carboniferous play of Northern England. Geological Society, London, Special Publications 50, 417–440.

Furre, A.K., Eiken, O., Alnes, H., Vevatne, J.N., Kiær, A.F., 2017. 20 years of monitoring CO_2-injection at Sleipner. Energy procedia 114, 3916–3926.

Gawthorpe, R.L., 1987. Tectono-sedimentary evolution of the Bowland Basin, N England, during the Dinantian. Journal of the Geological Society 144, 59–71.

Gensterblum, Y., Merkel, A., Busch, A., Krooss, B.M., 2013. High-pressure CH4 and CO2 sorption isotherms as a function of coal maturity and the influence of moisture. International Journal of Coal Geology 118, 45–57.

Gensterblum, Y., Van Hemert, P., Billemont, P., Battistutta, E., Busch, A., Krooss, B., De Weireld, G., Wolf, K.H., 2010. European inter-laboratory comparison of high pressure CO_2 sorption isotherms II: Natural coals. International Journal of Coal Geology 84, 115–124.

Gentzis, T., 2000. Subsurface sequestration of carbon dioxide—an overview from an Alberta (Canada) perspective. International Journal of Coal Geology 43, 287–305.

Gentzis, T., Deisman, N., Chalaturnyk, R.J., 2007. Geomechanical properties and permeability of coals from the foothills and mountain regions of western Canada. International Journal of Coal Geology 69, 153–164.

Goodarzi, M., Rouainia, M., Aplin, A., 2016. Numerical evaluation of mean-field homogenisation methods for predicting shale elastic response. Computational Geosciences 20, 1109–1122.

Goodarzi, M., Rouainia, M., Aplin, A., Cubillas, P., de Block, M., 2017. Predicting the elastic response of organic-rich shale using nanoscale measurements and homogenisation methods. Geophysical prospecting 65, 1597–1614.

Goodman, A., Favors, R., Hill, M., Larsen, J.W., 2005. Structure changes in Pittsburgh No. 8 coal caused by sorption of CO_2 gas. Energy & fuels 19, 1759–1760.

Graham, S., Rouainia, M., Aplin, A., Cubillas, P., Fender, T., Armitage, P., 2020. Geomechanical characterisation of organic-rich calcareous shale using AFM and nanoindentation. Rock Mechanics and Rock Engineering , 1–18.

Hall, B., 2016. Facies classification using machine learning. The Leading Edge 35, 906–909.

Hebblewhite, B., Lu, T., 2004. Geomechanical behaviour of laminated, weak coal mine roof strata and the implications for a ground reinforcement strategy. International Journal of Rock Mechanics and Mining Sciences 41, 147–157.

Hol, S., Spiers, C.J., Peach, C.J., 2012. Microfracturing of coal due to interaction with $/rmCO_2$ under unconfined conditions. Fuel 97, 569–584.

Horsfield, B., Curry, D., Bohacs, K., Littke, R., Rullkötter, J., Schenk, H., Radke, M., Schaefer, R., Carroll, A., Isaksen, G., et al., 1994. Organic geochemistry of freshwater and alkaline lacustrine sediments in the Green River Formation of the Washakie Basin, Wyoming, USA. Organic Geochemistry 22, 415–440.

Hower, J.C., Trinkle, E.J., Raione, R.P., 2008. Vickers microhardness of telovitrinite and pseudovitrinite from high volatile bituminous kentucky coals. International Journal of Coal Geology 75, 76–80.

Huaqing, X., Shangwen, Z., JIANG, Y., ZHANG, F., Zhen, D., Wei, G., 2018. Effects of hydration on the microstructure and physical properties of shale. Petroleum Exploration and Development 45, 1146–1153.

Iferobia, C.C., Ahmad, M., 2020. A review on the experimental techniques and applications in the geomechanical evaluation of shale gas reservoirs. Journal of Natural Gas Science and Engineering 74, 103090.

Ingram, G.M., Urai, J.L., 1999. Top-seal leakage through faults and fractures: the role of mudrock properties. Geological Society, London, Special Publications 158, 125–135.

Ingram, L., Ellis, J., Crisp, P., Cook, A., 1983. Comparative study of oil shales and shale oils from the Mahogany Zone, Green River Formation (USA) and Kerosene Creek Seam, Rundle Formation (Australia). Chemical Geology 38, 185–212.

Jarvie, D., Pollastro, R., Hill, R., Bowker, K., Claxton, B., Burgess, J., 2004. Evaluation of hydrocarbon generation and storage in the Barnett Shale, Fort Worth Basin, Texas, in: Ellison Miles Memorial Symposium, Farmers Branch, Texas, USA, pp. 22–23.

Jarvie, D.M., Hill, R.J., Pollastro, R.M., 2005. Assessment of the gas potential and yields from shales: The Barnett Shale model. Oklahoma Geological Survey Circular 110, 37–50.

Jarvie, D.M., Hill, R.J., Ruble, T.E., Pollastro, R.M., 2007. Unconventional shale-gas systems: The Mississippian Barnett Shale of north-central Texas as one model for thermogenic shale-gas assessment. AAPG Bulletin 91, 475–499.

Jennings, D.S., Antia, J., Camp, W., Diaz, E., Wawak, B., 2013. Petrographic characterization of the Eagle Ford Shale, South Texas: Mineralogy, common constituents, and distribution of nanometer-scale pore types. Electron microscopy of shale hydrocarbon reservoirs: AAPG Memoir 102, 101–113.

Josh, M., Esteban, L., Delle Piane, C., Sarout, J., Dewhurst, D., Clennell, M., 2012. Laboratory characterisation of shale properties. Journal of Petroleum Science and Engineering 88, 107–124.

JPK-Instruments, 2011. QI^{TM}mode-quantitative imaging with the NanoWizard 3 AFM. Tech. Note (JPK Instruments) , 1–7.

Karacan, C.Ö., 2007. Swelling-induced volumetric strains internal to a stressed coal associated with CO_2 sorption. International Journal of Coal Geology 72, 209–220.

Kese, K., Li, Z.C., 2006. Semi-ellipse method for accounting for the pile-up contact area during nanoindentation with the Berkovich indenter. Scripta materialia 55, 699–702.

Khair, H.A., Cooke, D., Hand, M., 2013. The effect of present day in situ stresses and paleo-stresses on locating sweet spots in unconventional reservoirs, a case study from Moomba-Big Lake fields, Cooper Basin, south Australia. Journal of Petroleum Exploration and Production Technology 3, 207–221.

Khatibi, S., Aghajanpour, A., 2020. Machine learning: A useful tool in geomechanical studies, a case study from an offshore gas field. Energies 13, 3528.

Khatibi, S., Ostadhassan, M., Tuschel, D., Gentzis, T., Bubach, B., Carvajal-Ortiz, H., 2018.

Raman spectroscopy to study thermal maturity and elastic modulus of kerogen. International Journal of Coal Geology 185, 103–118.

Kingma, D.P., Ba, J., 2014. Adam: A method for stochastic optimization. arXiv preprint arXiv:1412.6980 .

Klaver, J., Desbois, G., Littke, R., Urai, J.L., 2015. BIB-SEM characterization of pore space morphology and distribution in postmature to overmature samples from the Haynesville and Bossier Shales. Marine and petroleum Geology 59, 451–466.

Ko, L.T., Loucks, R.G., Zhang, T., Ruppel, S.C., Shao, D., 2016. Pore and pore network evolution of Upper Cretaceous Boquillas (Eagle Ford–equivalent) mudrocks: Results from gold tube pyrolysis experiments. AAPG Bulletin 100, 1693–1722.

Ko, L.T., Ruppel, S.C., Loucks, R.G., Hackley, P.C., Zhang, T., Shao, D., 2018. Pore-types and pore-network evolution in Upper Devonian-Lower Mississippian Woodford and Mississippian Barnett mudstones: Insights from laboratory thermal maturation and organic petrology. International Journal of Coal Geology 190, 3–28.

Kolonic, S., Sinninghe Damsté, J., Böttcher, M., Kuypers, M., Kuhnt, W., Beckmann, B., Scheeder, G., Wagner, T., 2002. Gerchemical characterization of Cenomanian/Turonian black shales from the tarfaya basin (SW Morocco) relationships between palaeoenvironmental conditions and early sulphurization of sedimentary organic matter. Journal of Petroleum Geology 25, 325–350.

Kolonic, S., Wagner, T., Forster, A., Sinninghe Damsté, J.S., Walsworth-Bell, B., Erba, E., Turgeon, S., Brumsack, H.J., Chellai, E.H., Tsikos, H., et al., 2005. Black shale deposition on the northwest African Shelf during the Cenomanian/Turonian oceanic anoxic event: Climate coupling and global organic carbon burial. Paleoceanography 20.

Kongsjorden, H., Kårstad, O., Torp, T.A., 1998. Saline aquifer storage of carbon dioxide in the Sleipner project. Waste management 17, 303–308.

Kossovich, E., Dobryakova, N., Epshtein, S., Belov, D., 2016. Mechanical properties of coal microcomponents under continuous indentation. Journal of Mining Science 52, 906–912.

Kumar, V., Sondergeld, C.H., Rai, C.S., et al., 2012. Nano to macro mechanical characterization of shale, in: SPE Annual Technical Conference and Exhibition, Society of Petroleum Engineers.

Lai, B., Li, H., Zhang, J., Jacobi, D., Georgi, D., 2016. Water-content effects on dynamic elastic properties of organic-rich shale. SPE Journal 21, 635–647.

Laxminarayana, C., Crosdale, P.J., 1999. Role of coal type and rank on methane sorption characteristics of bowen basin, australia coals. International Journal of Coal Geology 40, 309–325.

Lee, Y., Hahn, J., Nahm, S., Jang, J., Kwon, D., 2008. Investigations on indentation size effects using a pile-up corrected hardness. Journal of Physics D: Applied Physics 41, 074027.

Levine, J.R., 1996. Model study of the influence of matrix shrinkage on absolute permeability of coal bed reservoirs. Geological Society, London, Special Publications 109, 197–212.

Lewis, A., 2019. GetDist: a Python package for analysing Monte Carlo samples URL: `https://getdist.readthedocs.io`, `arXiv:1910.13970`.

Li, C., Ostadhassan, M., Gentzis, T., Kong, L., Carvajal-Ortiz, H., Bubach, B., 2018a. Nanomechanical characterization of organic matter in the Bakken Formation by microscopy-based method. Marine and Petroleum Geology 96, 128–138.

Li, C., Ostadhassan, M., Kong, L., Bubach, B., 2019. Multi-scale assessment of mechanical properties of organic-rich shales: A coupled nanoindentation, deconvolution analysis, and homogenization method. Journal of Petroleum Science and Engineering 174, 80–91.

Li, H., He, J., Misra, S., et al., 2018b. Data-driven in-situ geomechanical characterization in shale reservoirs, in: SPE Annual Technical Conference and Exhibition, Society of Petroleum Engineers.

Li, W., Cheng, Y.p., Wang, L., Zhou, H.x., Wang, H.f., Wang, L.g., 2013. Evaluating the security of geological coalbed sequestration of supercritical co_2 reservoirs: the Haishiwan Coalfield, China as a natural analogue. International Journal of Greenhouse Gas Control 13, 102–111.

Li, X., Kang, Y., Haghighi, M., 2018c. Investigation of pore size distributions of coals with different structures by nuclear magnetic resonance (NMR) and mercury intrusion porosimetry (MIP). Measurement 116, 122–128.

Li, Y., Yang, J., Pan, Z., Tong, W., 2020. Nanoscale pore structure and mechanical property analysis of coal: An insight combining AFM and SEM images. Fuel 260, 116352.

de Lima, R.P., Bonar, A., Coronado, D.D., Marfurt, K., Nicholson, C., 2019. Deep convolutional neural networks as a geological image classification tool. Sediment. Rec 17, 4–9.

de Lima, R.P., Duarte, D., Nicholson, C., Slatt, R., Marfurt, K.J., 2020. Petrographic microfacies classification with deep convolutional neural networks. Computers & Geosciences , 104481.

Liu, F., Ellett, K., Xiao, Y., Rupp, J.A., 2013. Assessing the feasibility of co_2 storage in the New Albany Shale (Devonian–Mississippian) with potential enhanced gas recovery using reservoir simulation. International Journal of Greenhouse Gas Control 17, 111–126.

Liu, H., Lin, B., Yang, W., 2019. Theoretical models for gas adsorption-induced coal deformation under coal seam field conditions. Energy Science & Engineering 7, 1504–1513.

Liu, J., Chen, Z., Elsworth, D., Miao, X., Mao, X., 2010. Linking gas-sorption induced changes in coal permeability to directional strains through a modulus reduction ratio. International Journal of Coal Geology 83, 21–30.

Liu, S., Harpalani, S., 2013. A new theoretical approach to model sorption-induced coal shrinkage or swelling. AAPG bulletin 97, 1033–1049.

Liu, Y., Xiong, Y., Li, Y., et al., 2018. Effect of thermal maturation on chemical structure and nanomechanical properties of solid bitumen. Marine and Petroleum Geology 92, 780–793.

Loucks, R.G., Reed, R.M., 2014. Scanning-electron-microscope petrographic evidence for distinguishing organic-matter pores associated with depositional organic matter versus migrated organic matter in mudrock .

Loucks, R.G., Reed, R.M., Ruppel, S.C., Jarvie, D.M., 2009. Morphology, genesis, and distribution of nanometer-scale pores in siliceous mudstones of the Mississippian Barnett Shale. Journal of Sedimentary Research 79, 848–861.

Loucks, R.G., Ruppel, S.C., 2007. Mississippian Barnett Shale: Lithofacies and depositional setting of a deep-water shale-gas succession in the Fort Worth Basin, Texas. AAPG Bulletin 91, 579–601.

Lu, G., Wang, J., Wei, C., Song, Y., Yan, G., Zhang, J., Chen, G., 2018. Pore fractal model applicability and fractal characteristics of seepage and adsorption pores in middle rank tectonic deformed coals from the Huaibei coal field. Journal of Petroleum Science and Engineering 171, 808–817.

Ma, C., Dong, C., Lin, C., Elsworth, D., Luan, G., Sun, X., Liu, X., 2019. Influencing factors and fracability of lacustrine shale oil reservoirs. Marine and Petroleum Geology 110, 463–471.

Ma, Q., Harpalani, S., Liu, S., 2011. A simplified permeability model for coalbed methane reservoirs based on matchstick strain and constant volume theory. International Journal of Coal Geology 85, 43–48.

Maitre, J., Bouchard, K., Bédard, L.P., 2019. Mineral grains recognition using computer vision and machine learning. Computers & Geosciences 130, 84–93.

Mason, G.M., Surdam, R.C., 1992. Carbonate mineral distribution and isotope-fractionation: An approach to depositional environment interpretation, Green River Formation, Wyoming, USA. Chemical Geology: Isotope Geoscience section 101, 311–321.

Masoudian, M.S., 2016. Multiphysics of carbon dioxide sequestration in coalbeds: A review with a focus on geomechanical characteristics of coal. Journal of Rock Mechanics and Geotechnical Engineering 8, 93–112.

Mastalerz, M., Drobniak, A., Hower, J.C., 2021. Controls on reservoir properties in organic-matter-rich shales: Insights from MICP analysis. Journal of Petroleum Science and Engineering 196, 107775.

Mastalerz, M., Karayigit, A., Hampton, L., Drobniak, A., 2016. Variations in gas content in organic matter-rich low maturity shale; example from the New Albany Shale in the Illinois Basin. Jacobs Journal of Petroleum and Natural Gas 1, 005.

Mastalerz, M., Rupp, J., Drobniak, A., Harpalani, S., Anderson, A., Korose, C., Frailey, S., Morse, D., 2009. Assessment of co_2 sequestration and enhanced coalbed methane potential in unminable coal seams of the Illinois Basin .

Mastalerz, M., Schieber, J., 2017. Effect of ion milling on the perceived maturity of shale samples: implications for organic petrography and SEM analysis. International Journal of Coal Geology 183, 110–119.

Mastalerz, M., Schimmelmann, A., Drobniak, A., Chen, Y., 2013. Porosity of Devonian and Mississippian New Albany Shale across a maturation gradient: Insights from organic petrology, gas adsorption, and mercury intrusion. AAPG bulletin 97, 1621–1643.

Mathia, E.J., 2015. Geological Evaluation of Posidonia and Wealden organic-rich shales: Geochemical and diagenetic controls on pore system evolution. Ph.D. thesis. Newcastle University.

Mathieson, A., Midgley, J., Dodds, K., Wright, I., Ringrose, P., Saoul, N., 2010. Co 2 sequestration monitoring and verification technologies applied at Krechba, Algeria. The Leading Edge 29, 216–222.

Matin, S., Hower, J.C., Farahzadi, L., Chelgani, S.C., 2016. Explaining relationships among various coal analyses with coal grindability index by Random Forest. International Journal of Mineral Processing 155, 140–146.

Mazumder, S., Wolf, K.H., 2008. Differential swelling and permeability change of coal in response to co_2 injection for ECBM. International Journal of Coal Geology 74, 123–138.

McArthur, A., Gamberi, F., Kneller, B., Wakefield, M., Souza, P., Kuchle, J., 2017. Palynofacies classification of submarine fan depositional environments: Outcrop examples from the Marnoso-Arenacea formation, Italy. Marine and Petroleum Geology 88, 181–199.

McElhaney, K., Vlassak, J.J., Nix, W.D., 1998. Determination of indenter tip geometry and indentation contact area for depth-sensing indentation experiments. Journal of Materials research 13, 1300–1306.

Merkel, A., Fink, R., Littke, R., 2015. The role of pre-adsorbed water on methane sorption capacity of Bossier and Haynesville shales. International Journal of Coal Geology 147, 1–8.

Middleton, M., 1982. Tectonic history from vitrinite reflectance. Geophysical Journal International 68, 121–132.

Milner, M., McLin, R., Petriello, J., et al., 2010. Imaging texture and porosity in mudstones and shales: comparison of secondary and ion-milled backscatter SEM methods, in: Canadian unconventional resources and international petroleum conference, Society of Petroleum Engineers.

Montgomery, S.L., Jarvie, D.M., Bowker, K.A., Pollastro, R.M., 2005. Mississippian Barnett Shale, Fort Worth basin, north-central Texas: Gas-shale play with multi–trillion cubic foot potential. AAPG bulletin 89, 155–175.

Morales, A., Zhang, K., Gakhar, K., Marongiu Porcu, M., Lee, D., Shan, D., Malpani, R., Pope, T., Sobernheim, D., Acock, A., et al., 2016. Advanced modeling of interwell fracturing interference: An Eagle Ford shale oil study-refracturing, in: SPE Hydraulic Fracturing Technology Conference, Society of Petroleum Engineers.

Morcote, A., Mavko, G., Prasad, M., 2010. Dynamic elastic properties of coal. Geophysics 75, E227–E234.

More, J., 1977. The Levenberg-Marquardt algorithm: implementation and theory Numerical Analysis.

Moshrefi, S., Shahriar, K., Ramezanzadeh, A., Goshtasbi, K., 2018. Prediction of ultimate strength of shale using artificial neural network. Journal of Mining and Environment 9, 91–105.

NASA, 2019a. The Atmosphere: Getting a handle on Carbon Dioxide. URL: `https://climate.nasa.gov/news/2915/the-atmosphere-getting-a-handle-on-carbon-dioxide`. accessed:20-08-2020.

NASA, 2019b. Climate Change: Vital Signs of the Planet. URL: `https://climate.nasa.gov/vital-signs/global-temperature/`. accessed:20-08-2020.

Niu, Q., Cao, L., Sang, S., Zhou, X., Liu, S., 2019. Experimental study of permeability changes and its influencing factors with CO2 injection in coal. Journal of Natural Gas Science and Engineering 61, 215–225.

Oceanic, N., Adiministration, A., 2019. Trends in Atmospheric Carbon Dioxide. URL: `https://www.esrl.noaa.gov/gmd/ccgg/trends/`. accessed:20-08-2020.

O'Keefe, J.M., Bechtel, A., Christanis, K., Dai, S., DiMichele, W.A., Eble, C.F., Esterle, J.S., Mastalerz, M., Raymond, A.L., Valentim, B.V., et al., 2013. On the fundamental difference between coal rank and coal type. International Journal of Coal Geology 118, 58–87.

Okiongbo, K.S., Aplin, A.C., Larter, S.R., 2005. Changes in type ii kerogen density as a function of maturity: Evidence from the Kimmeridge Clay formation. Energy & fuels 19, 2495–2499.

Oliver, W.C., Pharr, G.M., 1992. An improved technique for determining hardness and elastic modulus using load and displacement sensing indentation experiments. Journal of materials research 7, 1564–1583.

Palmer, I., Mansoori, J., et al., 1996. How permeability depends on stress and pore pressure in coalbeds: a new model, in: SPE annual technical conference and exhibition, Society of Petroleum Engineers.

Pan, J., Meng, Z., Hou, Q., Ju, Y., Cao, Y., 2013. Coal strength and young's modulus related

to coal rank, compressional velocity and maceral composition. Journal of Structural Geology 54, 129–135.

Pan, Y., Hui, D., Luo, P., Zhang, Y., Sun, L., Wang, K., 2018. Experimental investigation of the geochemical interactions between supercritical CO_2 and shale: implications for CO_2 storage in gas-bearing shale formations. Energy & Fuels 32, 1963–1978.

Pan, Z., Connell, L.D., 2007. A theoretical model for gas adsorption-induced coal swelling. International Journal of Coal Geology 69, 243–252.

Pan, Z., Connell, L.D., Camilleri, M., 2010. Laboratory characterisation of coal reservoir permeability for primary and enhanced coalbed methane recovery. International Journal of Coal Geology 82, 252–261.

Pedregosa, F., Varoquaux, G., Gramfort, A., Michel, V., Thirion, B., Grisel, O., Blondel, M., Prettenhofer, P., Weiss, R., Dubourg, V., Vanderplas, J., Passos, A., Cournapeau, D., Brucher, M., Perrot, M., Duchesnay, E., 2011. Scikit-learn: Machine learning in Python. Journal of Machine Learning Research 12, 2825–2830.

Pepper, A.S., Corvi, P.J., 1995a. Simple kinetic models of petroleum formation. Part I: oil and gas generation from kerogen. Marine and Petroleum Geology 12, 291–319.

Pepper, A.S., Corvi, P.J., 1995b. Simple kinetic models of petroleum formation. Part III: Modelling an open system. Marine and Petroleum Geology 12, 417–452.

Pepper, A.S., Dodd, T.A., 1995. Simple kinetic models of petroleum formation. Part II: oil-gas cracking. Marine and Petroleum Geology 12, 321–340.

Peters, K., 1986. Guidelines for evaluating petroleum source rock using programmed pyrolysis. AAPG Bulletin 70, 318–329.

Pittenger, B., Erina, N., Su, C., 2014. Mechanical property mapping at the nanoscale using Peakforce QNM scanning probe technique, in: Nanomechanical analysis of high performance materials. Springer, pp. 31–51.

Pollastro, R.M., Jarvie, D.M., Hill, R.J., Adams, C.W., 2007. Geologic framework of the mississippian Barnett Shale, Barnett-paleozoic total petroleum system, Bend Arch– Fort Worth Basin, Texas. AAPG Bulletin 91, 405–436.

Poulsen, B., Shen, B., Williams, D., Huddlestone-Holmes, C., Erarslan, N., Qin, J., 2014. Strength reduction on saturation of coal and coal measures rocks with implications for coal pillar strength. International Journal of Rock Mechanics and Mining Sciences 71, 41–52.

Poulton, S.W., Henkel, S., März, C., Urquhart, H., Flögel, S., Kasten, S., Sinninghe Damsté, J.S., Wagner, T., 2015. A continental-weathering control on orbitally driven redox-nutrient cycling during Cretaceous Oceanic Anoxic Event 2. Geology 43, 963–966.

Protocol, K., 1997. Report of the conference of the parties, in: United Nations Framework Convention on Climate Change (UNFCCC).

PTI, . India's oil import dependence jumps to 84 percent. The Economic Times India, url=https://economictimes.indiatimes.com/industry/energy/oil-gas/indias-oil-import-dependence-jumps-to-84-pc/articleshow/69183923.cms?from=mdr, urldate=2019-05-05 .

Pytte, A., Reynolds, R., 1989. The thermal transformation of smectite to illite, in: Thermal history of sedimentary basins. Springer, pp. 133–140.

Ranathunga, A.S., Perera, M.S.A., Ranjith, P., Bui, H., 2016. Super-critical co_2 saturation-induced mechanical property alterations in low rank coal: An experimental study. The Journal of Supercritical Fluids 109, 134–140.

Ranjith, P., Perera, M.S.A., 2012. Effects of cleat performance on strength reduction of coal in co_2 sequestration. Energy 45, 1069–1075.

Raschka, S., 2015. Python machine learning. Packt Publishing Ltd.

Raza, S.S., Ge, L., Rufford, T.E., Chen, Z., Rudolph, V., 2019. Anisotropic coal permeability estimation by determining cleat compressibility using mercury intrusion porosimetry and stress-strain measurements. International Journal of Coal Geology 205, 75–86.

Rexer, T.F., Mathia, E.J., Aplin, A.C., Thomas, K.M., 2014. High-pressure methane adsorption and characterization of pores in Posidonia Shales and isolated kerogens. Energy & Fuels 28, 2886–2901.

Ringrose, P., Atbi, M., Mason, D., Espinassous, M., Myhrer, Ø., Iding, M., Mathieson, A., Wright, I., 2009. Plume development around well KB-502 at the In Salah co_2 storage site. First break 27.

Robertson, E.P., 2005. Measurement and modeling of sorption-induced strain and permeability changes in coal. Technical Report. Idaho National Laboratory (INL).

Rodrigues, C.F., De Sousa, M.L., 2002. The measurement of coal porosity with different gases. International Journal of Coal Geology 48, 245–251.

Rodriguez-Galiano, V., Sanchez-Castillo, M., Chica-Olmo, M., Chica-Rivas, M., 2015. Machine learning predictive models for mineral prospectivity: An evaluation of neural networks, random forest, regression trees and support vector machines. Ore Geology Reviews 71, 804–818.

Rosenblatt, F., 1957. The perceptron, a perceiving and recognizing automaton Project Para. Cornell Aeronautical Laboratory.

Roslin, A., Pokrajac, D., Wu, K., Zhou, Y., 2020a. 3d pore system reconstruction using nanoscale 2D SEM images and pore size distribution analysis for intermediate rank coal matrix. Fuel 275, 117934.

Roslin, A., Pokrajac, D., Zhou, Y., 2020b. Coal matrix pore analysis using nanoscale scanning electron microscopy and direct capillary pressure curve simulation. Energy & Fuels 34, 6761–6767.

Rubin, E., De Coninck, H., 2005. Ipcc special report on carbon dioxide capture and storage. UK: Cambridge University Press. TNO (2004): Cost Curves for CO2 Storage, Part 2, 14.

Rubo, R.A., de Carvalho Carneiro, C., Michelon, M.F., dos Santos Gioria, R., 2019. Digital petrography: Mineralogy and porosity identification using machine learning algorithms in petrographic thin section images. Journal of Petroleum Science and Engineering 183, 106382.

Rutqvist, J., 2012. The geomechanics of CO_2 storage in deep sedimentary formations. Geotechnical and Geological Engineering 30, 525–551.

Rybacki, E., Reinicke, A., Meier, T., Makasi, M., Dresen, G., 2015. What controls the mechanical properties of shale rocks?–Part I: Strength and Young's modulus. Journal of Petroleum Science and Engineering 135, 702–722.

Sachse, V.F., Littke, R., Heim, S., Kluth, O., Schober, J., Boutib, L., Jabour, H., Perssen, F., Sindern, S., 2011. Petroleum source rocks of the Tarfaya Basin and adjacent areas, Morocco. Organic Geochemistry 42, 209–227.

Sampath, K., Perera, M., Ranjith, P., Matthai, S., Dong-yin, L., 2019. Qualitative and quantitative evaluation of the alteration of micro-fracture characteristics of supercritical CO2-interacted coal. The Journal of Supercritical Fluids 147, 90–101.

Saporetti, C.M., da Fonseca, L.G., Pereira, E., de Oliveira, L.C., 2018. Machine learning approaches for petrographic classification of carbonate-siliciclastic rocks using well logs and textural information. Journal of Applied Geophysics 155, 217–225.

Scherer, G.W., 1986. Dilatation of porous glass. Journal of the American Ceramic Society 69, 473–480.

Schmidt, M., Le Roux, N., Bach, F., 2017. Minimizing finite sums with the stochastic average gradient. Mathematical Programming 162, 83–112.

Schopf, J.M., 1956. A definition of coal. Economic geology 51, 521–527.

Scott, V., Gilfillan, S., Markusson, N., Chalmers, H., Haszeldine, R.S., 2013. Last chance for carbon capture and storage. Nature Climate Change 3, 105–111.

Shao, Z., Armaghani, D.J., Bejarbaneh, B.Y., Mu'azu, M., Mohamad, E.T., 2019. Estimating the friction angle of black shale core specimens with hybrid-ANN approaches. Measurement 145, 744–755.

Shi, J., Durucan, S., 2004. Drawdown induced changes in permeability of coalbeds: a new interpretation of the reservoir response to primary recovery. Transport in porous media 56, 1–16.

Shu, L., McIsaac, K., Osinski, G.R., Francis, R., 2017. Unsupervised feature learning for autonomous rock image classification. Computers & Geosciences 106, 10–17.

Shukla, P., Kumar, V., Curtis, M., Sondergeld, C.H., Rai, C.S., et al., 2013. Nanoindentation studies on shales, in: 47th US Rock Mechanics/Geomechanics Symposium, American Rock Mechanics Association.

Shukman, D., . Sir david Attenborough warns of climate 'crisis moment'. British Broadcasting Company URL: `https://www.bbc.co.uk/news/science-environment-51123638`.

Silva, A.A., Neto, I.A.L., Misságia, R.M., Ceia, M.A., Carrasquilla, A.G., Archilha, N.L., 2015. Artificial neural networks to support petrographic classification of carbonate-siliciclastic rocks using well logs and textural information. Journal of Applied Geophysics 117, 118–125.

Słowakiewicz, M., Tucker, M.E., Vane, C., Harding, R., Collins, A., Pancost, R., 2015. Shale-gas potential of the mid-Carboniferous Bowland-Hodder unit in the Cleveland Basin (Yorkshire), central Britain. Journal of Petroleum Geology 38, 59–75.

Sneddon, I.N., 1965. The relation between load and penetration in the axisymmetric Boussinesq problem for a punch of arbitrary profile. International journal of engineering science 3, 47–57.

Sone, H., Zoback, M.D., 2013. Mechanical properties of shale-gas reservoir rocks—Part 1: Static and dynamic elastic properties and anisotropy. Geophysics 78, D381–D392.

Song, D., Tuo, J., Wu, C., Zhang, M., Su, L., 2020. Comparison of pore evolution for a Mesoproterozoic marine shale and a Triassic terrestrial mudstone during artificial maturation experiments. Journal of Natural Gas Science and Engineering 75, 103153.

Spitzer, Z., 1981. Mercury porosimetry and its application to the analysis of coal pore structure. Powder Technology 29, 177–186.

Stach, E., Murchison, D., Taylor, G.H., Zierke, F., 1982. Stach's textbook of coal petrology. volume 535. Borntraeger Berlin.

Stephen, C., Passey, Q.R., 1993. Recurring patterns of total organic carbon and source rock quality within a sequence stratigraphic framework. AAPG bulletin 77, 386–401.

Strapoc, D., Mastalerz, M., Schimmelmann, A., Drobniak, A., Hasenmueller, N.R., 2010. Geochemical constraints on the origin and volume of gas in the New Albany Shale (Devonian–Mississippian), eastern Illinois Basin. AAPG bulletin 94, 1713–1740.

Su, C., Xu, S.j., Zhu, K.y., Zhang, X.c., 2020. Rock classification in petrographic thin section images based on concatenated convolutional neural networks. arXiv preprint arXiv:2003.10437 .

Suggate, R., 1998. Relations between depth of burial, vitrinite reflectance and geothermal gradient. Journal of Petroleum Geology 21, 5–32.

Suwannasri, K., Vanorio, T., Clark, A., 2018. Monitoring the changes in the microstructure and the elastic and transport properties of Eagle Ford marl during maturation. Geophysics 83, MR263–MR281.

Suwannasri, K., Vanorio, T., Clark, A., 2019. Data-driven elastic modeling of organic-rich marl during maturation. Geophysics 85, 1–62.

Tang, D., Spikes, K., et al., 2017. Segmentation of shale SEM images using machine learning, in: 2017 SEG International Exposition and Annual Meeting, Society of Exploration Geophysicists.

Tang, X., Zhang, J., Wang, X., Yu, B., Ding, W., Xiong, J., Yang, Y., Wang, L., Yang, C., 2014. Shale characteristics in the southeastern Ordos Basin, China: Implications for hydrocarbon accumulation conditions and the potential of continental shales. International Journal of Coal Geology 128, 32–46.

Tang, Y., Hu, S., He, Y., Wang, Y., Wan, X., Cui, S., Long, K., 2021. Experiment on co2-brine-rock interaction during co2 injection and storage in gas reservoirs with aquifer. Chemical Engineering Journal 413, 127567.

Taylor, G.H., Teichmüller, M., Davis, A., Diessel, C., Littke, R., Robert, P., 1998. Organic petrology .

Teichmüller, M., 1989. The genesis of coal from the viewpoint of coal petrology. International Journal of Coal Geology 12, 1 – 87. URL: http://www.sciencedirect.com/science/article/pii/0166516289900475, doi:https://doi.org/10.1016/0166-5162(89)90047-5.

Teng, J., Mastalerz, M., Hampton, L., 2017. Maceral controls on porosity characteristics of lithotypes of Pennsylvanian high volatile bituminous coal: Example from the Illinois Basin. International Journal of Coal Geology 172, 80–94.

Tissot, B.P., Welte, D.H., 1978. Petroleum formation and occurrence. Springer Science & Business Media.

Trtik, P., Kaufmann, J., Volz, U., 2012. On the use of peak-force tapping atomic force microscopy for quantification of the local elastic modulus in hardened cement paste. Cement and concrete Research 42, 215–221.

Tyson, J., 2019. The effect of thermal maturity on the nanomechanical properties of coal and its impact on carbon capture storage (CCS). Master's thesis. Newcastle University.

Tyson, R., 2012. Sedimentary organic matter: Organic facies and palynofacies. Springer Science & Business Media.

Tyson, R.V., 2006. Calibration of hydrogen indices with microscopy: A review, reanalysis and new results using the fluorescence scale. Organic Geochemistry 37, 45–63.

Ulm, F.J., Abousleiman, Y., 2006. The nanogranular nature of shale. Acta Geotechnica 1, 77–88.

Ulm, F.J., Vandamme, M., Bobko, C., Alberto Ortega, J., Tai, K., Ortiz, C., 2007. Statistical indentation techniques for hydrated nanocomposites: concrete, bone, and shale. Journal of the American Ceramic Society 90, 2677–2692.

Vandamme, M., Ulm, F.J., 2009. Nanogranular origin of concrete creep. Proceedings of the National Academy of Sciences 106, 10552–10557.

Vandenbroucke, M., Largeau, C., 2007. Kerogen origin, evolution and structure. Organic Geochemistry 38, 719–833.

Viete, D.R., Ranjith, P.G., 2006. The effect of co_2 on the geomechanical and permeability behaviour of brown coal: implications for coal seam co_2 sequestration. International Journal of Coal Geology 66, 204–216.

Virtanen, P., Gommers, R., Oliphant, T.E., Haberland, M., Reddy, T., Cournapeau, D., Burovski, E., Peterson, P., Weckesser, W., Bright, J., van der Walt, S.J., Brett, M., Wilson, J., Millman, K.J., Mayorov, N., Nelson, A.R.J., Jones, E., Kern, R., Larson, E., Carey, C.J., Polat, İ., Feng, Y., Moore, E.W., VanderPlas, J., Laxalde, D., Perktold, J., Cimrman, R., Henriksen, I., Quintero, E.A., Harris, C.R., Archibald, A.M., Ribeiro, A.H., Pedregosa, F., van Mulbregt, P., SciPy 1.0 Contributors, 2020. SciPy 1.0: Fundamental Algorithms for Scientific Computing in Python. Nature Methods 17, 261–272. doi:10.1038/s41592-019-0686-2.

Vishal, V., Ranjith, P., Singh, T.N., 2013. CO2 permeability of Indian bituminous coals: implications for carbon sequestration. International Journal of Coal Geology 105, 36–47.

Wagner, T., Hofmann, P., Flögel, S., 2013. Marine black shale deposition and Hadley Cell dynamics: A conceptual framework for the Cretaceous Atlantic ocean. Marine and Petroleum Geology 43, 222–238.

Walker, J., 2020. Geochemical processes assoiated with 'marine band' formation in the Lower Carboniferous Bowland Shale Formation, Northern England. Newcastle University.

Walker Jr, P.L., Verma, S.K., Rivera-Utrilla, J., Davis, A., 1988. Densities, porosities and surface areas of coal macerals as measured by their interaction with gases, vapours and liquids. Fuel 67, 1615–1623.

Wang, F., Guo, S., 2019. Influential factors and model of shale pore evolution: A case study of a continental shale from the Ordos Basin. Marine and Petroleum Geology 102, 271–282.

Wang, F.P., Reed, R.M., et al., 2009. Pore networks and fluid flow in gas shales, in: SPE annual technical conference and exhibition, Society of Petroleum Engineers.

Wang, G., Carr, T.R., 2012. Marcellus shale lithofacies prediction by multiclass neural network classification in the Appalachian Basin. Mathematical Geosciences 44, 975–1004.

Wang, G., Carr, T.R., Ju, Y., Li, C., 2014. Identifying organic-rich Marcellus Shale lithofacies by support vector machine classifier in the Appalachian Basin. Computers & Geosciences 64, 52–60.

Wang, K., Xu, T., Wang, F., Tian, H., 2016. Experimental study of co_2–brine–rock interaction during co_2 sequestration in deep coal seams. International Journal of Coal Geology 154, 265–274.

Wang, X., Zeng, F., Gao, R., Zhao, X., Hao, S., Liang, Q., Jiang, S., 2017. Cleaner coal and greener oil production: An integrated CCUS approach in Yanchang Petroleum Group. International Journal of Greenhouse Gas Control 62, 13–22.

Wang, Z., Di, H., Shafiq, M.A., Alaudah, Y., AlRegib, G., 2018. Successful leveraging of image processing and machine learning in seismic structural interpretation: A review. The Leading Edge 37, 451–461.

Wang, Z., Krupnick, A., 2015. A retrospective review of shale gas development in the United States: What led to the boom? Economics of Energy & Environmental Policy 4, 5–18.

Waters, C., Waters, R., Barclay, W., Davies, J., 2009. A lithostratigraphical framework for the Carboniferous successions of southern Great Britain (Onshore). British Geological Survey.

Weber, M., Wilson, T.H., Akwari, B., Wells, A.W., Koperna, G., 2012. Impact of geological complexity of the Fruitland Formation on combined co_2 enhanced recovery/sequestration at San Juan Basin pilot site. International Journal of Coal Geology 104, 46–58.

West, L.M., 2014. A regional assessment of residual oil zones in the Permian Basin and their potential for carbon dioxide capture usage and storage. Energy Procedia 63, 7884–7890.

White, J.M., Mazurkiewicz, M., 1989. Effect of moisture content on mechanical properties of Nemo coal, Moberly, Missouri USA. Mining Science and Technology 9, 181–185.

Wilkinson, T.M., Zargari, S., Prasad, M., Packard, C.E., 2015. Optimizing nano-dynamic mechanical analysis for high-resolution, elastic modulus mapping in organic-rich shales. Journal of Materials Science 50, 1041–1049.

Wu, Y., Misra, S., Sondergeld, C., Curtis, M., Jernigen, J., 2019. Machine learning for locating organic matter and pores in scanning electron microscopy images of organic-rich shales. Fuel 253, 662–676.

Yan, J., Meng, Z., Zhang, K., Yao, H., Hao, H., 2020. Pore distribution characteristics of various rank coals matrix and their influences on gas adsorption. Journal of Petroleum Science and Engineering 189, 107041.

Yang, Y., Yao, J., Wang, C., Gao, Y., Zhang, Q., An, S., Song, W., 2015. New pore space characterization method of shale matrix formation by considering organic and inorganic pores. Journal of Natural Gas Science and Engineering 27, 496–503.

Yao, Q., Chen, T., Tang, C., Sedighi, M., Wang, S., Huang, Q., 2019. Influence of moisture on crack propagation in coal and its failure modes. Engineering Geology 258, 105156.

Yao, Q., Li, X., Zhou, J., Ju, M., Chong, Z., Zhao, B., 2015. Experimental study of strength characteristics of coal specimens after water intrusion. Arabian Journal of Geosciences 8, 6779–6789.

Yao, Y., Liu, D., 2012. Comparison of low-field NMR and mercury intrusion porosimetry in characterizing pore size distributions of coals. Fuel 95, 152–158.

Yu, H., Zhang, Y., Lebedev, M., Han, T., Verrall, M., Wang, Z., Al-Khdheeawi, E., Al-Yaseri, A., Iglauer, S., 2018. Nanoscale geomechanical properties of Western Australian coal. Journal of Petroleum Science and Engineering 162, 736–746.

Zaluski, W., El-Kaseeh, G., Lee, S.Y., Piercey, M., Duguid, A., 2016. Monitoring technology

ranking methodology for co_2-EOR sites using the Weyburn-Midale Field as a case study. International Journal of Greenhouse Gas Control 54, 466–478.

Zargari, S., Prasad, M., Mba, K.C., Mattson, E., et al., 2011. Organic maturity, hydrous pyrolysis, and elastic property in shales, in: Canadian Unconventional Resources Conference, Society of Petroleum Engineers.

Zargari, S., Wilkinson, T.M., Packard, C.E., Prasad, M., 2016. Effect of thermal maturity on elastic properties of kerogen. Geophysics 81, M1–M6.

Zeng, K., Jiang, P., Lun, Z., Xu, R., 2018. Molecular simulation of carbon dioxide and methane adsorption in shale organic nanopores. Energy & Fuels 33, 1785–1796.

Zeszotarski, J.C., Chromik, R.R., Vinci, R.P., Messmer, M.C., Michels, R., Larsen, J.W., 2004. Imaging and mechanical property measurements of kerogen via nanoindentation. Geochimica et cosmochimica acta 68, 4113–4119.

Zhang, H., Liu, J., Elsworth, D., 2008. How sorption-induced matrix deformation affects gas flow in coal seams: a new FE model. International Journal of Rock Mechanics and Mining Sciences 45, 1226–1236.

Zhang, M., Fu, X., Wang, H., 2018a. Analysis of physical properties and influencing factors of middle-rank coal reservoirs in China. Journal of Natural Gas Science and Engineering 50, 351–363.

Zhang, T., Yang, R., Milliken, K.L., Ruppel, S.C., Pottorf, R.J., Sun, X., 2014. Chemical and isotopic composition of gases released by crush methods from organic rich mudrocks. Organic Geochemistry 73, 16–28.

Zhang, Y., Lebedev, M., Al-Yaseri, A., Yu, H., Xu, X., Iglauer, S., 2018b. Characterization of nanoscale rockmechanical properties and microstructures of a Chinese sub-bituminous coal. Journal of Natural Gas Science and Engineering 52, 106–116.

Zhang, Y., Lebedev, M., Al-Yaseri, A., Yu, H., Xu, X., Sarmadivaleh, M., Barifcani, A., Iglauer,

S., 2018c. Nanoscale rock mechanical property changes in heterogeneous coal after water adsorption. Fuel 218, 23–32.

Zhang, Y., Lebedev, M., Sarmadivaleh, M., Barifcani, A., Iglauer, S., 2016. Swelling-induced changes in coal microstructure due to supercritical co_2 injection. Geophysical Research Letters 43, 9077–9083.

Zhang, Y., Zhang, Z., Sarmadivaleh, M., Lebedev, M., Barifcani, A., Yu, H., Iglauer, S., 2017. Micro-scale fracturing mechanisms in coal induced by adsorption of supercritical co_2. International Journal of Coal Geology 175, 40–50.

Zheng, Z., Khodaverdian, M., McLennan, J., 1991. Static and dynamic testing of coal specimens, in: 1991 SCA Conference.

Zhiltsov, S.S., Semenov, A., 2016. Shale gas: History of development, in: Shale Gas: Ecology, Politics, Economy. Springer, pp. 9–16.

Zhou, S., Liu, D., Cai, Y., Yao, Y., Che, Y., Liu, Z., 2017. Multi-scale fractal characterizations of lignite, subbituminous and high-volatile bituminous coals pores by mercury intrusion porosimetry. Journal of Natural Gas Science and Engineering 44, 338–350.

Zoback, M.D., 2010. Reservoir geomechanics. Cambridge University Press.